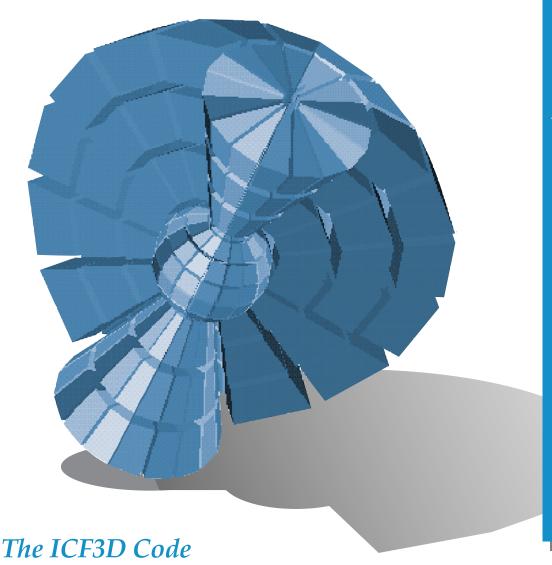
ICF Quarterly Report

July-September 1996, Volume 6, Number 4

# Special Issue: Computational Advances in ICF



3-D PIC Code for High-Current HIF Ion-Beam Propagation

3-D Nonlinear Hydrodynamics Code for Laser-Plasma Interactions

3-D Simulations of NIF Capsule Implosions

LASNEX—a 2-D Physics Code for Modeling ICF

NIF Design Optimization

Laser Optimization Techniques

Frequency-Conversion Modeling

The PROP92 Fourier Beam Propagation Code **The Cover:** A subdomain given to one processing element (PE) when discretizing a spherical domain and running in Cartesian coordinates. This image includes both ghost and owned cells. ICF3D requires that a PE be given all cells that share one or more vertices with owned cells. The original domain is decomposed in both radial and azimuthal directions. This example has poor surface-to-volume ratio; there are 96 owned and 236 ghost cells. The subdomain contains all allowable cell types. There are 108 hexahedra (48 owned), 96 prisms (16 owned), 96 pyramids (24 owned), and 32 tetrahedra (8 owned).

UCRL-LR-105821-96-4 Distribution Category UC-712 July-September 1996

Printed in the United States of America Available from National Technical Information Service U.S. Department of Commerce 5285 Port Royal Road Springfield, Virginia 22161 Price codes: printed copy A03, microfiche A01.

This document was prepared as an account of work sponsored by an agency of the United States Government. Neither the United States Government nor the University of California nor any of their employees makes any warranty, express or implied, or assumes any legal liability or responsibility for the accuracy, completeness, or usefulness of any information, apparatus, product, or process disclosed, or represents that its use would not infringe privately owned rights. Reference herein to any specific commercial products, process, or service by trade name, trademark, manufacturer, or otherwise, does not necessarily constitute or imply its endorsement, recommendation, or favoring by the United States Government or the University of California. The views and opinions of authors expressed herein do not necessarily state or reflect those of the United States Government or the University of California and shall not be used for advertising or product endorsement purposes.

The ICF Quarterly Report is published four times each fiscal year by the Inertial Confinement Fusion Program at the Lawrence Livermore National Laboratory. The ICF Quarterly Report is also on the Web at http://lasers.llnl.gov/lasers/pubs/icfq.html. The journal summarizes selected current research achievements of the LLNL ICF Program. The underlying theme for LLNL's ICF Program research is defined within DOE's Defense Programs missions and goals. In support of these missions and goals, the ICF Program advances research and technology development in major interrelated areas that include fusion target theory and design, target fabrication, target experiments, and laser and optical science and technology.

While in pursuit of its goal of demonstrating thermonuclear fusion ignition and energy gain in the laboratory, the ICF Program provides research and development opportunities in fundmental high-energy-density physics and supports the necessary research base for the possible long-term application of inertial fusion energy for civilian power production. ICF technologies continue to have spin-off applications for additional government and industrial use. In addition to these topics, the *ICF Quarterly Report* covers non-ICF funded, but related, laser research and development and associated applications. We also provide a short summary of the quarterly activities within Nova laser operations, Beamlet laser operations, and National Ignition Facility laser design.

LLNL's ICF Program falls within DOE's national ICF program that includes the Nova and Beamlet (LLNL), OMEGA (University of Rochester Laboratory for Laser Energetics), Nike (Naval Research Laboratory), and Trident (Los Alamos National Laboratory) laser facilities. The Particle Beam Fusion Accelerator and Saturn pulsed power facilities are at Sandia National Laboratories. General Atomics, Inc., develops and provides many of the targets for the above experimental facilities. Many of the *Quarterly Report* articles are co-authored with our colleagues from these other ICF institutions.

Questions and comments relating to the technical content of the journal should be addressed to the ICF Program Office, Lawrence Livermore National Laboratory, P.O. Box 808, Livermore, CA, 94551.

Work performed under the auspices of the U.S. Department of Energy by Lawrence Livermore National Laboratory under Contract W-7405–Eng–48.



ICF Quarterly Report

July-September 1996, Volume 6, Number 4

### In this issue:

Foreword

# WARP3d, a Three-Dimensional PIC Code for High-Current Ion-Beam Propagation Developed for Heavy-Ion Fusion

WARP3d is a three-dimensional electrostatic particle-in-cell simulation code developed to study beam behavior from first principles in realistic geometries. The code has been used to examine high-current, space-charge-dominated beams for heavy-ion fusion and will be developed further for future applications.

#### Three-Dimensional Nonlinear Hydrodynamics Code to Study 138 Laser-Plasma Interactions

This article describes a fully nonlinear, three-dimensional, time-dependent hydrodynamics and heat transport code. The code has proven to be very robust, and extends our ability to model experiments far beyond the limits of earlier treatments.

# Three-Dimensional Simulations of National Ignition Facility Capsule Implosions with HYDRA

The HYDRA radiation hydrodynamics code was used to perform the first direct three-dimensional simulations of the National Ignition Facility point-design capsule. Direct three-dimensional numerical simulations most accurately treat saturation effects and multimode coupling for capsules with realistic surface perturbations in the presence of multiple shocks, ablation, convergence, and finite shell thickness.

#### LASNEX—A 2-D Physics Code for Modeling ICF

The LASNEX code represents the spatial variation of many physical quantities on a twodimensional, axially symmetric mesh composed of arbitrarily shaped quadrilaterals. This article describes LASNEX, its physics models, the code structure, its equation-solving methods, and the user interface.

#### The ICF3D Code 165

ICF3D is a three-dimensional, inertial confinement fusion code that is based on unstructured grids and discretized using finite elements. It is portable, running on uniprocessor and massively parallel architectures. This article provides an overview of the code's modules, discusses the physics packages and how they are coupled, and presents some results.

#### NIF Design Optimization

The design of the National Ignition Facility is based on cost/performance optimization studies done in a zero-dimensional performance model and a one-dimensional propagation model. The optimization efforts give us confidence that we are designing the least expensive system that meets the facility's functional requirements.

Scientific Editor Michael Marinak

**Publication Editor** Jason Carpenter

## Technical Editors

Al Miguel Ann Parker Joy Perez Dabbie Schleich

**Classification Editor** Roy Johnson

# Managing Editor Don Correll

**Design Staff**Daniel Moore

#### Art Staff

Pamela Davis Sandra Lynn Linda Wiseman 129

150

181

Laser Optimization Techniques This article describes the techniques developed to optimize the design of large laser systems, such as the National Ignition Facility, using realistic components and realistic laser light propagation.  Frequency-Conversion Modeling Frequency conversion is a complex nonlinear process requiring precise tolerances for optimum results. Newly developed frequency-conversion codes have aided the designers of the Beamlet and National Ignition Facility lasers in specifying the correct converter designs needed for a variety of operating scenarios.  The PROP92 Fourier Beam Propagation Code PROP92 is a full-featured Fourier optics laser modeling, design, and optimization tool, with integrated models for optical elements and effects and sophisticated risk-assessment algorithms. We describe the physical basis for and numerical implementation of PROP92's most important modules.	192 199 207		
		Nova/Beamlet/NIF Updates	U-1
		Publications	P-1

111 11110 1000L =

# **FOREWORD**

This issue of the *ICF Quarterly* is dedicated to the ICF Program's calculational capabilities and accomplishments. Computer codes are an integral part of the collection of research tools and activities that are used to investigate target physics and laser science and technology. With the advent of the Accelerated Strategic Computing Initiative (ASCI), a new emphasis has been placed upon computing as a core Laboratory competency. The ICF Program has long depended upon sophisticated computer codes to model in detail physical processes important in hardware and experiments. Currently, the emphasis is on extending simulations to three dimensions and on the use of high-performance computing platforms. Most of the codes in this issue exploit some form of parallel processing.

Two articles discuss codes used to simulate plasma behavior. The first is "WARP3D, a Three-Dimensional PIC Code for High-Current Ion Beam Propagation Developed for Heavy-Ion Fusion." WARP3D combines the particle-in-cell technique used for plasma modeling with a description of a "lattice" of accelerator components. It can simulate space-charge-dominated beams in realistic accelerator geometries. A detailed understanding of beam behavior as it propagates through the accelerator is necessary to maintain the low temperatures required to achieve a small focal spot size. In the second article, "Three-Dimensional Nonlinear Hydrodynamics Code to Study Laser–Plasma Interactions," direct numerical simulations examine ponderomotive filamentation produced by intense laser beams. Ponderomotive self-focusing and filamentation are important because they can prevent laser energy from being deposited at the desired location or with the required uniformity. The code solves the two-temperature fluid equations, coupled to the paraxial equation for light-wave propagation.

Radiation hydrodynamics codes are used to design ICF experiments and to analyze target evolution. The two-dimensional (2-D) axisymmetric code LASNEX has helped to improve our understanding of ICF targets for 25 years. The article "LASNEX—a 2-D Physics Code for Modeling ICF" describes the broad variety of physics packages and capabilities that have been incorporated into the code. Specific examples illustrate the code's success in simulating hydrodynamic instability evolution of 2-D perturbations as well as spectroscopic emission in Nova targets. Experiments and numerical simulations have shown that three-dimensional (3-D) surface perturbations saturate at larger amplitudes than axisymmetric or 2-D structures. Two radiation hydrodynamics codes are being developed in the ICF Program to examine 3-D effects. HYDRA, which is based upon a block structured mesh, can perform direct 3-D numerical simulations of portions of ICF capsules, carrying the evolution of multimode perturbations through ignition and burn. The article "Three-Dimensional Simulations of National Ignition Facility Capsule Implosions with HYDRA" describes early results from the first 3-D simulations of the NIF baseline capsule design. "The ICF3D Code" outlines the development of the 3-D hydro code based upon an unstructured grid that uses discontinuous finite-element hydrodynamics. ICF3D is written using object-oriented programming and can presently run on massively parallel computers. Results from several test problems are also presented.

Computer codes have been used to design high-power lasers both previously in the ICF Program and for the National Ignition Facility (NIF). Four articles describe a suite of codes used to optimize the NIF laser design. In the article "The PROP92 Fourier Beam Propagation Code," the author describes the code used to model the

propagation of the laser beam through a comprehensive set of optical elements. Algorithms assess the risk of damage to optical elements from high beam fluence or filamentation. The detailed fields calculated with PROP92 are input into the code, which models the process of nonlinear frequency conversion, as described in the article "Frequency-Conversion Modeling." The article "Laser Optimization Techniques" describes a set of codes that employ various quadratic methods for locating the constrained nonlinear optimum of a multivariate system. To perform an iteration, the optimization code runs both the PROP92 and frequency conversion codes in parallel on a cluster of workstations. The article "NIF Design Optimization" outlines the modeling procedures used in the aforementioned laser design codes. It also presents results from the optimization that resulted in the current NIF design.

Michael M. Marinak Scientific Editor

# WARP3D, A THREE-DIMENSIONAL PIC CODE FOR HIGH-CURRENT ION-BEAM PROPAGATION DEVELOPED FOR HEAVY-ION FUSION

D. P. Grote I. Haber
A. Friedman S. M. Lund

#### Introduction

Heavy-ion induction accelerators are being developed in the United States as the principal candidate "drivers" for inertial confinement fusion (ICF) power production. They also represent an attractive option for a high-yield microfusion research facility. Heavy-ion drivers are attractive in both cases because they promise high reliability, high repetition rate (several pulses per second are required), greater efficiency (up to 30%), lifetime capacity (a power plant would need to last 30 years, or  $10^{10}$  pulses), and sufficient cost savings. With indirectly driven targets, heavy-ion drivers allow a favorable fusion chamber geometry; furthermore, the final focus is accomplished with magnetic fields that are immune to damage by target debris, in contrast to the final optics for a laser.<sup>1</sup>

The requirements for high-gain ignition of the fusion targets control the design of the accelerator. A major constraint on the beam is the requirement of a small focal spot size on the target with a large distance between the final focus lens and the target, putting a tight limit on the temperature of the beam. A thorough understanding of the beam behavior as it propagates through the accelerator is necessary to maintain the required low temperatures.

Since the space-charge–dominated beams in an induction accelerator are effectively non-neutral plasmas, analysis of the beams can be performed with computational modeling techniques related to those used in both the accelerator and plasma physics fields. Because the beam resides in the accelerator for relatively few plasma oscillation periods, particle-in-cell (PIC) simulation techniques are especially effective and have proved valuable in the design and analysis of both ongoing experiments and future machines and in the study of basic physics issues. The three-dimensional (3-D) electrostatic PIC simulation code WARP3d<sup>2,3</sup> was developed to study beam behavior from first principles

in realistic geometries. This article presents an overview of the WARP3d code, describing in detail some of its major features and present applications in a number of areas, and highlighting the important results.

#### Overview of WARP3d

WARP3d was designed and optimized for heavy-ion fusion (HIF) accelerator physics studies. It combines the PIC technique commonly used for plasma modeling with a description of the "lattice" of accelerator elements. In addition to its 3-D model, a simple beam envelope, or transverse root-mean-square (rms) size, analytic equation solver was included, primarily to obtain an initial beam well matched to the accelerator lattice. The code uses the BASIS development and run-time system, which affords a flexible and powerful interpretive user interface.

The ion beam is represented by a small number (relative to the number of beam ions in the physical system) of interacting particles whose motion is controlled by the Newton–Lorentz equations of motion. The fields affecting the particles include both the selffields of the beam and the external fields from the lattice. The self-fields are assumed to be electrostatic and are calculated in the beam frame via Poisson's equation on a Cartesian grid that moves with the beam. The electrostatic assumption is valid since, with the high mass of the beam ions, the beam is nonrelativistic throughout the accelerator, its velocity only reaching roughly 10% of the speed of light at the end of the accelerator.

There are two "field solvers" to calculate the self-fields: (1) The fastest field solver, which is generally used for long-time simulations, uses Fourier decomposition with fast Fourier transforms (FFTs). (2) An iterative solver uses successive overrelaxation (SOR) with even-odd ordering<sup>4</sup> and allows inclusion of complex electrode geometry. For the FFT field solver, the 3-D transform is sine-sine-periodic, the transverse boundary is a rectangular

metal pipe, and the longitudinal boundary is periodic. Capacity matrices<sup>5</sup> can be used to include simple electrodes in the FFT field solver to handle round pipes, structures independent of the axial coordinate, and isolated internal structures. Another variant uses a tridiagonal matrix solver along the axial direction. This method is slightly faster, but at present is restricted to conducting boundaries on the longitudinal ends of the grid.

The SOR field solver, although significantly slower than the FFT field solver, allows simulation of a much broader class of problems with a more realistic model of the conductors. This field solver was implemented using a technique, described below, to obtain subgrid-scale resolution of the conductor boundaries. With both field solvers, transverse symmetry can be exploited, simulating only half or one quarter of the system.

The external fields are applied via a lattice, which is a general set of finite-length accelerator elements, including quadrupoles for focusing, dipoles for bending, induction gaps for accelerating, elements with arbitrary transverse multipole components, and curved accelerator sections (see Ref. 2). The transverse multipole components specify the applied fields, in one form, as an electrostatic or magnetostatic potential represented by an infinite sum of terms expressed in cylindrical coordinates with the direction of beam propagation along the longitudinal axis, z.

$$\phi = \sum_{n,\nu \ge 0} V_{n,\nu}(z) r^{n+2\nu} \cos(n\theta + \nu) \tag{1}$$

The  $V_{n,v}(z)$  determine the contribution of each term. The electric or magnetic fields are calculated by taking the appropriate derivatives. As an example, a quadrupole field is given by the term with n=2, and v=0. Terms with n>2 or v>0 are referred to as high-order terms.

The field from the lattice elements can be specified at one of several levels of detail—from hard-edged, axially uniform fields at the lowest level, to self-consistent inclusion of the conducting electrodes of electric elements in the field solution at the highest level.

## Aspects of WARP

A number of features and capabilities have been implemented in WARP3d to enable simulation of a broader class of accelerators, both by way of inclusion of the relevant physics and by optimization of the code to allow simulation of larger-scale problems. This article describes the most important and novel of these in detail.

#### Lattice and Fields

A hard-edged field is the lowest level of description of lattice element fields—one that is uniform axially within the extent of the element and that has a sharp cutoff at the ends of the element. As the particles enter and
exit hard-edged, axially uniform elements, the force
applied on the particles is scaled by the fraction of the
timestep spent inside the element. These "residence corrections" are used so that the particles receive the correct
impulse from the element and allow larger timesteps to
be used. Without the residence corrections, the forces
applied to the particles would depend on the number of
timesteps they spend inside the element; keeping the
resulting error small would require a small timestep.

At a higher level of detail, fields that vary axially can be applied. This allows application of realistic fields, including fringe fields and the higher-order multipole moments of a magnetic quadrupole element, for example. In both the axially uniform and nonuniform descriptions, the applied field can be an arbitrary sum of multipole components, as given by Eq. (1).

The highest level of detail is specification of the field via a 3-D grid to allow application of fields that are not amenable to a multipole description, e.g., a field with many nonlinear components. The field can be calculated outside of WARP3d; for example, the magnetic field from a complex magnet design can be obtained from TOSCA<sup>6</sup> and input into WARP3d. With electric elements, the field can be calculated self-consistently with WARP3d by inclusion of the electrodes in the field solution, thereby obtaining the realistic fields and image effects from the electrode on the beam. This highest level of description allows modeling of complex electrode geometry and electrodes with time-varying voltages.

When electrodes are included in the field solution, to avoid the problems with the jaggedness of representing tilted or curved electrodes on a Cartesian grid, the SOR field solver allows subgrid-scale resolution of the conducting boundary locations as shown in Fig. 1. For grid points just outside the surface of a conductor, the form of Poisson's equation is changed to explicitly include the location of the surface. Normally, the evaluation of Poisson's equation at these points would require the potential at grid points that are just inside the surface of the electrode. The values inside are replaced by a value that is extrapolated from the potential at the surface and at the grid point just outside the surface. The method is similar to the method used in EGUN, <sup>7</sup> extended to three dimensions and time dependence.

Subgrid-scale resolution of the conducting boundaries allows more accurate modeling of electrodes for a given grid cell size, especially ones with curved surfaces, and it does so while allowing larger grid cell sizes. As an example, the fields from an electric quadrupole are produced from four parallel cylinders with appropriate voltages. Without the subgrid-scale resolution of the cylinder surfaces, the quadrupole focusing strength is reduced significantly since the jagged surface, produced by representing the cylinder by grid points only within

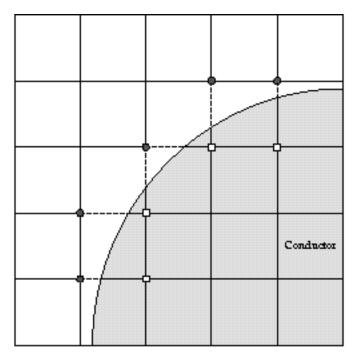


FIGURE 1. An example conductor on a grid. The numeric form of Poisson's equation is altered for the grid points at the dark circles. The equation would normally require the potentials at the nearby grid points, which are inside the conductor, marked by squares. The potential inside is replaced by a value extrapolated from the potential at the point outside and at the surface. (08-10-0896-1906pb01)

the cylinder, is effectively farther from the axis than that of the true surface. The reduced focusing changes the beam envelope on the order of 10%. A much finer grid would be needed to produce the same accurate focusing strength as that produced with the subgrid-scale resolution.

# **Beam Injection**

Several models of particle beam injection are used, all of which can model emission from planar or curved surfaces. The first model injects particles from a surface at a constant current with a specified energy, modeling a beam emerging from a wire mesh or from a plane of uniform potential. It can be used to model injection from an emitting surface if the specified energy is low compared with the diode energy.

Two self-consistent models use space-charge–limited injection and are intended only for injection directly from emission surfaces. The beam current that is injected is not predetermined, but is calculated self-consistently from the conditions near the emitting surface to give space-charge–limited injection. The first model uses the Child–Langmuir<sup>8</sup> relation in a region in front of the emitting surface to calculate the emitted current. The length of the region is small compared with the length of the diode. The Child–Langmuir relation gives

the space-charge—limited current in a 1-D diode. In the second model, the surface charge required to produce the desired zero-normal electric field on the surface is calculated assuming an infinite conducting plane. The amount of charge injected into a grid cell is then the surface charge integrated over the grid cell minus the charge already in the grid cell from earlier times.

With space-charge-limited injection, WARP3d can be run in an efficient iterative manner that captures only the steady-state behavior. The algorithm is similar to that used in the 2-D electron gun design code EGUN. At each iteration, a group of particles is tracked through the diode. Along the paths of the particles, charge is deposited on a grid to build up a representation of the charge density of a full beam. The fields are recalculated, including the new charge density, giving the new fields through which the next group of particles is tracked on the next iteration. On the initial iteration, the particles are tracked through the fields given by the solution of Laplace's equation in the diode geometry. The process converges to the correct steady-state flow in typically 10 to 20 iterations. This capability was added to the code entirely through the BASIS interpreter and required no modification of the existing code.

## Large Time-Step Algorithms

Under conditions that arise commonly in WARP3d applications, the applied focusing, bending, and accelerating fields vary rapidly with axial position, while the beam's self-fields (which are comparable in strength to the applied fields) vary smoothly. In such cases, it is desirable to employ timesteps that advance the particles over distances greater than the characteristic scales over which the applied fields vary. An example technique, used in WARP3d since the code's inception, is the residence correction described earlier. Research at Lawrence Livermore National Laboratory (LLNL) is extending this concept to cases where the effects of extended fringe fields and other smooth but rapid variations must be accurately captured, necessitating very small timesteps when a conventional "leapfrog" advance is used.9

Several related techniques are being evaluated: subcycling of the particle advance relative to the field solution (i.e., taking *N* substeps between each major timestep on which the self-consistent field is computed and applied, where *N* is a small integer); use of a higher-order time-advance algorithm; and force-averaging over the velocity-advance step by integration along approximate orbits (a generalization of the residence correction technique). The most straightforward of these techniques is particle subcycling. We are encouraged by subcycling tests that advance a particle through the extended field's quadrupole component of a pair of permanent-magnet quadrupole lenses, and we are in the process of implementing this technique in WARP3d.

Since the field solution and particle advance often use comparable amounts of computer time, subcycling with N=4 will result in roughly a twofold speedup of the code. For some problems, the field solution dominates the run time and larger speedups can be expected.

#### **Thick-Slice Model**

Several simulations have identified the existence of short longitudinal-wavelength oscillations that can occur on a long beam. These short-length phenomena have been found to be particularly significant when the beam transverse temperature is somewhat greater than the longitudinal temperature. <sup>10–13</sup> In this case, the temperature anisotropy is a source of free energy that can drive the short wavelength modes unstable, leading to an "equilibration" of the temperatures. Short longitudinal-wavelength oscillations have also been seen (in simulations) in a recirculator with external nonlinearities (see the section entitled "Recirculating" Induction Accelerator"). To investigate these phenomena numerically, therefore, it is important to examine the physics of a space-charge-dominated beam with numerical resolution in the longitudinal direction sufficiently fine to resolve phenomena that occur on the scale of the beam diameter. This requirement can be computationally expensive to satisfy if the beam is to be tracked through a realistic length of accelerator structure.

A new numerical technique currently being developed facilitates the investigation of such short longitudinal-scale phenomena. This approximation, which we call the "thick-slice" model, exploits the separation of scales that occur because of the locality of the phenomena being studied relative to the global beam variation along the accelerator structure. We assume that all the particles across a finite slice of the beam simultaneously experience the same external forces, in a manner similar to what is assumed in a single-slice (or 2-D transverse) model. However, the self-consistent beam dynamics within the slice are followed, including the longitudinal variation of the fields. The longitudinal particle and field boundaries at the ends of the slice are further assumed to be periodic.

# **Parallel Processing**

WARP3d was originally designed to run on vector supercomputers and on workstations. With the present trend toward using massively parallel processing, WARP3d was ported to a parallel environment. Currently, WARP3d can run on the CRAY T3D, using both the PVM<sup>14</sup> message passing library and the native shared memory library, and on multi-workstation clusters. In the conversion, the interactive nature of the code (through the BASIS interpreter) was maintained. The user runs the code on a local serial workstation and interacts with it through the interpreter. That code

then creates processes on the parallel machine to do the computational work. Via message passing, the user controls the progress of the simulation on the parallel machine and inquires or sets any of the code variables in a manner similar to that used when the code runs on a serial machine.

Using a model problem with up to 32 processors, timings were made by following a beam through five hard-edged lattice periods. The speedup of the code with an increasing number of processors was nearly linear. Figure 2 shows timings of the field solver and particle mover. The field solver has a slightly superlinear speedup, which is likely due to better cache memory use with the data spread out in smaller pieces on more processors.

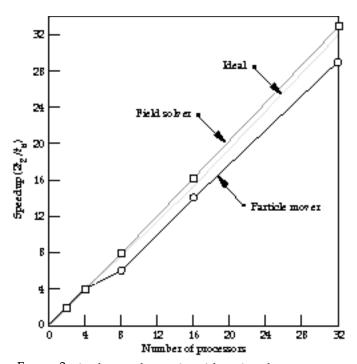


FIGURE 2. Plot showing the speedup of the code with an increasing number of processors. The speedup is twice the ratio of the time with two processors to the time with n processors, two being the fewest number of processors that the parallel code will run on. The light gray line shows the ideal linear speedup. The dark gray line with squares shows the speedup for the field solver. The black line with circles shows the speedup for the particle mover. Note that the speedup for the field solver is superlinear at first due to better use of cache memory with less data per processor. (08-10-0896-1907pb01)

# Applications of WARP3d

WARP3d has been used extensively in the design and analysis of a number of experiments within the HIF program and in the study of the basic physics of the creation and transport of space-charge—dominated beams. In the following sections, we describe several of its most recent applications within HIF and an application outside of HIF.

## **Electrostatic Quadrupole Injector**

A driver-scale injector and matching section is being built at Lawrence Berkeley Laboratory, in collaboration with LLNL, to address beam physics and technology issues. <sup>15</sup> The injector uses a sequence of electrostatic quadrupole (ESQ) lenses with a superposed voltage gradient along the axis. The net effect is to confine the beam transversely and to accelerate it. The beam is emitted from a hot-plate source and accelerated through a diode section into the quadrupole lenses. Figure 3 is an image of the injector when it is filled with the beam. Following the injector is a "matching section," a series of electric quadrupoles with decreasing aperture that reduce the transverse size of the beam down to "match" it into the following section of the accelerator.

WARP3d was used to understand a major issue in the injector design—the degradation of beam quality (brightness) by the nonlinear multipole components of the focusing fields and the so-called "energy effect." The energy effect arises from the spread transversely in the axial velocity of particles in the ESQ, which is due to the transverse variation of the electrostatic potential. Proper treatment of the beam dynamics requires detailed 3-D simulation with a realistic lattice model.

For design of the injector optics, the steady-state beam behavior was of primary interest. For efficiency, runs were made in a quasi-steady-state mode, taking several particle timesteps between each field solution and continuing until the system converged to a time-independent state. These 3-D simulations of the injector required less than 3 min on a single processor of the National Energy Research Scientific Computing Center's CRAY Y-MP C90 (at LLNL). This was fast enough to allow simulation of a large number of designs to optimize the injector, minimizing the beam degradation. Taking advantage of the ESQ's two-plane symmetry, the dimensions of the field grid were typically  $40 \times 40 \times 348$ . Typically, 100,000 particles and 500 timesteps were used.

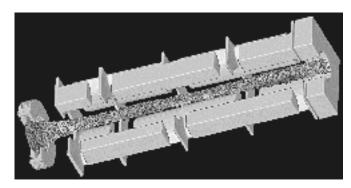


FIGURE 3. The 3-D image of the ESQ injector when filled with the beam. The shading of the beam particles is proportional to the particle energy relative to the energy at the beam center; the energy effect is evident in the darker shading of particles farther from the axis. (08-10-0896-1908pb01)

Fully time-dependent simulations of the transient behavior require several hours of C90 CPU time.

The simulations were used as a guide in the development of a scaled, proof-of-principle experiment and then a full-scale experiment. In both cases, excellent agreement was found between the experiment and simulation results. Figure 4 shows the simulated injected beam in the full-scale diode. Figure 5 shows a comparison of the phase space representations of the simulated and the full-scale experimental beams.

For the matching section, the envelope equation solver in WARP3d is used to calculate the beam transverse rms size in the presence of quadrupole and uniform focusing multipole components extracted from the field solution, including the full geometry of the electric quadrupole conductors. Good agreement between the analytic envelope solution and the results of full PIC simulation implies that the envelope solver can be used for rapid iteration of the applied voltages to achieve the desired beam state. The full simulations are conducted to evaluate possible degradations in beam quality that cannot be evaluated in the analytic envelope model.

In a full-scale driver, multiple injectors will be used and their beams will be channeled into a multiple beam transport line by the matching section, resulting in a curved matching section. This system was simulated with WARP3d, combining three of its major capabilities: injection, a bent accelerator lattice, and field solution with complex conductor geometry. The simulations found no significant degradation of beam quality, thereby validating the design concept.

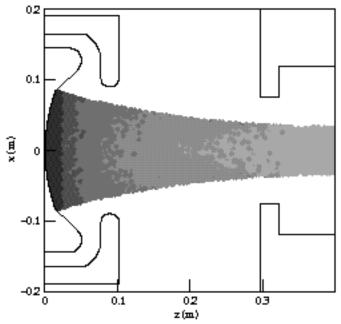
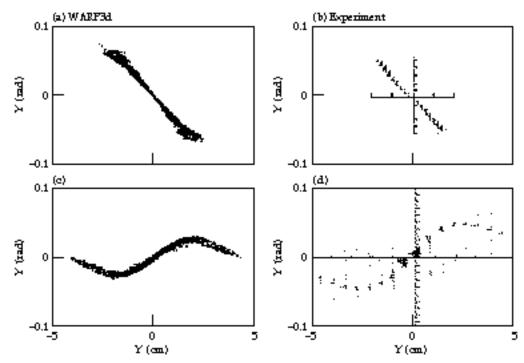


FIGURE 4. The diode of the ESQ injector filled with the beam. The outline is of the diode geometry. The shading of the beam particles is proportional to the time of injection of the particles, showing the darkest area injected last. (08-10-0896-1909pb01)

FIGURE 5. Comparison of experimental and simulation transverse phase space representations at the end of the ESQ injector. (a) and (b) compare the results at the design parameters. (c) and (d) compare the results with an increased diode voltage; in this nonoptimal case, the representations are significantly distorted from a straight line. (08-10-0896-1910pb01)



## **Recirculating Induction Accelerator**

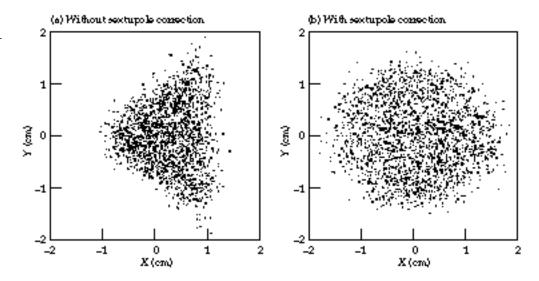
A recirculating induction accelerator, or "recirculator," offers the prospect of reduced cost relative to a conventional linear accelerator because the accelerating and focusing elements are reused many times per shot. A small recirculator is being developed at LLNL to explore the beam dynamics of a full-sized fusion driver in a scaled manner; the key dimensionless parameters that characterize the beam are similar to those of a driver-scale ring, but the physical scale is much smaller. A convenience of the second scale is much smaller.

Although a full-scale driver will use magnetic dipole elements to bend the beam, electric dipole plates were chosen for the prototype to minimize costs. The size of the plates is constrained by space considerations and voltage-holding requirements, resulting in significant high-order fields. Using WARP3d, the plate shape was adjusted to minimize 3-D field nonlinearities and their influence on beam quality. Figure 6 compares the cross section of the beam after several laps with flat dipole plates and with shaped dipole plates.

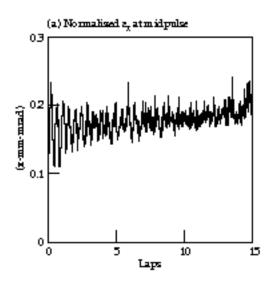
WARP3d simulations were used to follow the beam for all 15 laps. Typically, the 2- $\mu$ s-long beam is made up of 100,000 simulation particles. The field grid is a moving window covering four half-lattice periods. The grid measures 32 × 16 cells transversely (exploiting vertical symmetry) and 128 cells axially.

Figure 7 shows the time history of the normalized emittance at the midpulse for an acceleration schedule that does not compress the beam axially. The normalized emittance is a measure related to the transverse beam temperature and is given approximately by  $\varepsilon_X \approx \tilde{x}v_X$ 

FIGURE 6. The beam cross section after several laps (a) with flat dipole plates and (b) with shaped dipole plates. The triangular shape in (a) is a result of the sextupole component from the flat dipole plates. (08-10-0896-1911pb01)



- TILLE OD, A THEEL DIVILIANDONAL TIC CODE



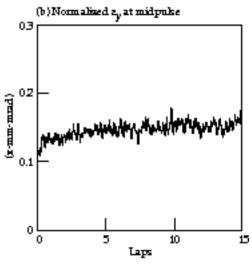


FIGURE 7. The time history of the normalized emittance and the beam midpulse show an acceptable increase. The initial oscillation and increase are due to axial thermal spread and the change from a straight to a bent lattice. (08-10-0896-1912pb01)

where x is a transverse dimension and  $\tilde{x}$  is the rms of x. The simulations show an initial transverse heating of the beam on the order of 50% as the beam "matches" itself from the straight insertion line to the bent recirculator lattice. This heating is due to radial separation of particles with differing axial velocities in the bends, which leads to nonlinearities in the space-charge forces that thermalize to produce an increase in temperature. The observed growth agrees well with theoretical analysis. After the initial heating, little further degradation in beam quality is seen over the 15 laps. The overall degradation is acceptable.

Near the end of the simulation, the emittance begins to rise due to the appearance of an instability that presents itself as a sinusoidal variation of the beam axial velocity along the beam. The variation begins to grow from the noise during laps 11 and 12 and becomes significant enough to affect the emittance during lap 15. The wavelength of the variation is on the order of the pipe radius. Numerous simulations seem to indicate that the instability is not numerical in origin; the wavelength and growth rate varied little with a wide range of numerical parameters, including timestep size and grid size. The instability requires all of the following: high space charge, bending, acceleration, and a uniform focusing force. The uniform focusing force results from the electric dipole plates. It is believed that the instability will not occur with magnetic dipoles, which will be used in a driver; the simulations made so far with magnetic dipoles have not shown the instability. The authors await the experimental results from the recirculator to see whether or not the instability indeed does occur as predicted.

## Straight and Bending Experiment

As a precursor to the full recirculator experiment just described, the beam is being examined in a straight lattice and in a lattice with an 18° bend (using WARP3d). The straight experiment is being conducted to fully characterize the beam. The bent experiment will be the first

detailed examination of a space-charge-dominated beam in a bent, alternating-gradient lattice.

The straight experiment consists of a series of electric quadrupoles and then magnetic quadrupoles. The field from the electric quadrupoles was calculated with WARP3d using the electrode geometry, and the field from the magnetic quadrupoles was calculated analytically. The quadrupole component was extracted from the fields and is used in the calculation of the envelope of the beam. Figure 8 shows a comparison of the

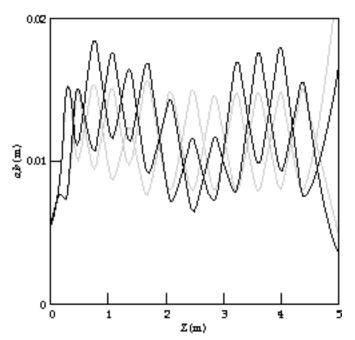


FIGURE 8. Comparison of the beam envelope as calculated with quadrupoles with hard-edged fields (gray) and with quadrupoles with calculated field profiles (black). The horizontal and vertical envelopes (*a,b*) for each case are shown in the same colors. The envelope was matched to the quadrupoles with hard-edged fields; this is seen in the nearly equal heights of the peaks in the gray curves. The significant difference shows the importance of including the correct quadrupole field profile. (08-10-0896-1913pb01)

envelope solution with hard-edge quadrupoles and with the calculated quadrupole data. Of course, given the detailed solution, it would be possible to construct a better hard-edged model.

The "simultaneous perturbation stochastic approximation" optimization algorithm was implemented with the analytic envelope solver to find a matched envelope. The algorithm varies the voltages on the electric quadrupoles to find a matched beam in the first bent-lattice period. The envelope solver is being used by the experimentalists for the determination of the voltages for the experiment.

The bent beam experiment has been simulated with WARP3d to predict the amount of emittance growth from the bend correlated with the longitudinal thermal spread. Figure 9 shows the emittance growth for up to a 45° bend with a straight lattice afterward. Figure 10

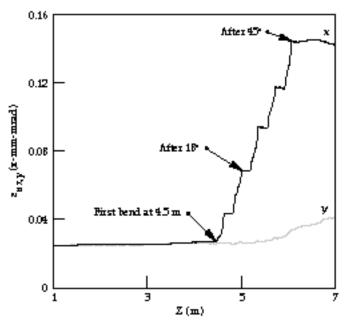


FIGURE 9. The WARP3d simulations show an emittance growth after 18° that should be experimentally detectable. (08-10-0896-1914pb01)

shows the difference in the phase space before and after 18° using grayscales to show the relative longitudinal velocities of the particles. The simulations show that there should be an experimentally detectable amount of emittance growth in an 18° bend, assuming a longitudinal thermal spread of 0.05% of the axial velocity.

#### **Sheet Beams**

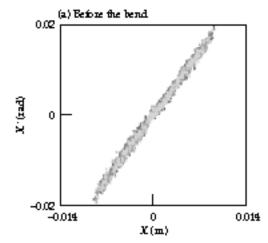
At the University of Wisconsin, WARP3d is being used in the examination of sheet electron beams formed by magnetic quadrupoles for use in high-power microwave sources. <sup>20,21</sup> The rapid axial variation of the beam profiles limits the use of the paraxial model and makes necessary the use of 3-D models. The 3-D envelope code TRACE-3D<sup>22</sup> is used for rapid iteration to design the system, but it does not model increases in emittance due to beam quality degradation. WARP3d simulations are used as a check of the envelope code design, to validate the envelope, and to examine the degradation of beam quality. An experiment is under construction and comparisons with simulation will be made.

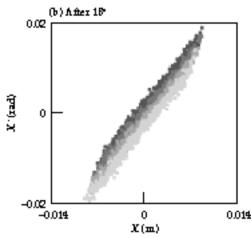
#### **Conclusions and Future Work**

WARP3d was developed to examine high-current, space-charge—dominated beams for heavy-ion fusion and has proven its value in a broad range of applications, playing a critical role in the design and analysis of a number of experiments. Many features and capabilities have been implemented to allow inclusion of much of the relevant physics and simulation of large-scale problems.

Considerable further code development is planned, taking advantage of modern programming techniques such as object-oriented programming, and making more use of tools such as computer-aided design systems for geometry input, mesh generators, and massively parallel processing machines. These developments are geared to allow quicker and more complete analysis of ongoing experiments, leading to complete simulation of full-scale drivers.

FIGURE 10. In the phase space, the transverse spreading of the beam due to axial thermal spread and a bend can be seen. The shading of the particles is proportional to axial velocity (lighter is faster). (08-10-0896-1915pb01)





#### **Notes and References**

- 1. R. O. Bangerter, Il Nuovo Cimento 106 A(11), 1445 (1993).
- A. Friedman, D. P. Grote, I. Haber, ICF Quarterly Report 1(4), 115, Lawrence Livermore National Laboratory, Livermore, CA, UCRL-LR-105821-91-4 (1991).
- 3. A. Friedman, D. P. Grote, and I. Haber, *Physics of Fluids B* 4(7), 2203 (July 1992).
- William H. Press et al., Numerical Recipes: The Art of Scientific Computing (Cambridge University Press, 1986) pp. 652–659.
- R. W. Hockney and J. W. Eastwood, Computer Simulations Using Particles (Adam–Hilger, Bristol, 1988) p. 215.
- TOSCA Reference Manual, Technical Paper VF-11-92-14, Vector Fields Limited, 24 Bankside, Kidlington, Oxford OX5 1JE, England.
- 7. W. B. Herrmannsfeldt, EGUN—An Electron Optics and Gun Design Program, Technical Report 331, SLAC, 1988.
- 8. K. R. Spangenburg, Fundamentals of Electron Devices (McGraw–Hill, New York, 1957).
- 9. A. Friedman and D. P. Grote, "Large-Timestep Techniques for Particle-in-Cell Simulation of Systems wth Applied Fields that Vary Rapidly in Space," *Proc.* 1996 Comput. Accel. Phys. Conf., Williamsburg, VA, Sept 24–Oct 7, 1996.
- A. Friedman, R. O. Bangerter, D. A. Callahan, D. P. Grote, et al., "A 3D Particle Simulation Code for Heavy Ion Fusion Accelerator Studies," in *Proc. of the 2nd European Particle Accelerator Conf.*, Nice, France (Editions Frontiers, Gif–sur–Yvette, France, 1990), p. 1699.
- I. Haber, D. A. Callahan, A. Friedman, D. P. Grote, and A. B. Langdon, "Transverse-Longitudinal Energy Equilibration in a Long Uniform Beam," *Proc. of the 1995 Particle Accelerator Conf.*, Dallas, TX, pp. 3283–4 (IEEE, 1996).
- 12. I. Haber, D. A. Callahan, A. Friedman, D. P. Grote, and A. B. Langdon, "Transverse-Longitudinal Temperature Equilibration in a Long Uniform Beam," to be published in Proc. of the International Symposium on Heavy Ion Fusion, Princeton, NJ, Sept 6–8, 1995, and in Journal of Fusion Engineering Design, 1996.

 I. Haber, D. A. Callahan, C. M. Celata, W. M. Fawley et al., "PIC Simulation of Short Scale-Length Phenomena," Space Charge Dominated Beams and Applications to High Brightness Beams, S. Y. Lee, Ed., AIP Conf. Proc. No. 377 (AIP, New York, 1996) p. 244.

TYZINI OD , ZI I IIKLE DIIVILIVOIDIVZE I IC CODE

- A. Giest et al., PVM3 User's Guide and Reference Manual, Technical Report ORNL/TM-12187.
- S. Yu, "Heavy Ion Fusion Injector Program," Proc. of the 1993 Particle Accelerator Conf., Washington, D.C., p. 703–705 (IEEE, 1993).
- J. J Barnard, F. Deadrick, A. Friedman, D. P. Grote et al., Physics of Fluids B, 5(7), 2698 (July 1993).
- A. Friedman et al., "Progress Toward a Prototype Recirculating Induction Accelerator for Heavy-Ion Fusion," *Proc. of the 1995* Particle Accelerator Conf., Dallas, TX, pp. 828–830 (IEEE, 1996).
- J. J. Barnard, H. D. Shay, S. S. Yu, A. Friedman, and D. P. Grote, "Emittance Growth in Heavy Ion Recirculators," 1992 Linear Accelerator Conf. Proc. (Ottawa, Canada, AECL-10728, 1992) p. 229.
- 19. J. C. Spall, "Multivariate Stochastic Approximation Using a Simultaneous Perturbation Gradient Approximation," *IEEE Transactions of Automatic Control*, **37**, 332–341 (1992).
- M. A. Basten, J. H. Booske, and J. Anderson, *IEEE Trans. Plasma Science* 22(5), 960–966 (1994).
- 21. M. A. Basten, J. H. Booske, and S. M. Lund, "Three Dimensional Analysis of Electron Sheet Beam Formation Using Magnetic Quadrupoles," Lawrence Livermore National Laboratory, Livermore, CA; submitted to Nucl. Instr. and Methods.
- TRACE-3D Documentation, Los Alamos Code Group, Los Alamos National Laboratory, Los Alamos, NM, Report LA-UR-90-4146 (1990).

# THREE-DIMENSIONAL NONLINEAR HYDRODYNAMICS CODE TO STUDY LASER-PLASMA INTERACTIONS

C. H. Still

R. L. Berger

A. B. Langdon

E. A. Williams

### Introduction

The development of a fully nonlinear, time-dependent hydrodynamic and heat transport code has allowed us to pursue several very interesting problems in laser beam self-focusing and filamentation for which the plasma density and flow velocities are strongly perturbed. Many treatments have used time-dependent linearized hydrodynamics in two and three dimensions (3-D) where the plasma motion is limited to directions transverse to the laser propagation direction. A truly nonlinear treatment uses particle-in-cell codes. Other nonlinear treatments have used a steady-state hydrodynamics response where the electron density is determined by equating the electron thermal and ponderomotive forces transverse to the laser propagation direction.

These approaches ignore some important physical processes. For example, time-dependent, nonlinear hydrodynamics is needed to address steepening of wave fronts, harmonic generation and decay instabilities, all of which play an important role in saturation of filamentation, stimulated Brillouin scattering (SBS), and stimulated Raman scattering (SRS). Filamentation has been studied using 1-D and 2-D nonlinear hydrodynamics codes in planar or cylindrical geometry. To our knowledge, the code we now describe is the only code with fully 3-D nonlinear hydrodynamics coupled to light wave propagation.

# The Hydrodynamics Equations

The hydrodynamic, heat transport equations in conservative form are the mass conservation equation

$$\frac{\partial}{\partial t} \rho + \nabla \cdot (\mathbf{v}\rho) = 0 \quad , \tag{1}$$

the momentum conservation equation for the  $j^{th}$  component of the momentum  ${\bf S}$ 

$$\frac{\partial}{\partial t} S_j + \nabla \cdot \left( \mathbf{v} S_j \right) + \nabla \cdot \mathbf{Q}_j + \frac{\partial}{\partial x_j} P + \frac{\partial}{\partial x_j} P_{\mathbf{e}} + \rho \frac{\partial}{\partial x_j} \phi = 0 \ , \eqno(2)$$

the ion energy conservation equation

$$\frac{3}{2} \left[ \frac{\partial}{\partial t} P + \nabla \cdot (\mathbf{v}P) \right] + P \nabla \cdot \mathbf{v} + \mathbf{Q} : \nabla \mathbf{v} = 0 \quad , \tag{3}$$

and the electron energy conservation equation

$$\frac{3}{2} \left[ \frac{\partial}{\partial t} P_{e} + \nabla \cdot (\mathbf{v} P_{e}) \right] + P_{e} \nabla \cdot \mathbf{v} = -\nabla \cdot \mathbf{q}_{e} + H_{e} \quad . \tag{4}$$

In these equations, P is the ion pressure,  $P_e$  is the electron pressure,  $\mathbf{Q}$  is the viscosity tensor (with  $j^{\text{th}}$  component  $\mathbf{Q}_j$ ),  $\mathbf{v}$  is the flow velocity,  $H_e$  is a source or sink, and  $\mathbf{q}_e$  is the heat flow. The momentum is related to the flow velocity by

$$\mathbf{S} = \rho \mathbf{v} \quad , \tag{5}$$

and the electron and ion temperature are related to the corresponding pressures by a perfect gas equation of state

$$P_{\rm e} = n_{\rm e} T_{\rm e} \tag{6}$$

$$P = n_{i}T_{i} \tag{7}$$

with  $\rho = m_i n_i$ . The ionization state is constant and, at present, quasi-neutrality is assumed, namely  $n_e = Z n_i$ . This last assumption will be relaxed in the near future.

The last term in the momentum equation [Eq. (2)] represents either a gravitation force, as used for

Rayleigh–Taylor instability calculations,<sup>6</sup> or a ponderomotive force, in which case

$$\phi = \frac{1}{2} \frac{m_{\rm i}}{Zm_{\rm e}} \left| \mathbf{v}_0 \right|^2 \quad . \tag{8}$$

Here,  $\mathbf{v}_0$  is the jitter velocity of the electron in the laser field  $\mathbf{E}_{0}$ ,

$$\mathbf{v}_0 = \frac{e\mathbf{E}_0}{m_e \omega_0} \quad . \tag{9}$$

In Eq. (3), we neglect the ion heat flow and real viscosity, which are usually very small. The artificial viscosity **Q** is used to handle shocks in the standard way as will be described shortly.

In Eq. (4),  $H_{\rm e}$  includes collisional heating (inverse bremsstrahlung). For problems of interest to date, the standard flux-limited heat flow

$$\mathbf{q}_{e} = -\kappa (T_{e}) \nabla T_{e} \tag{10}$$

where

$$\kappa(T_e) = \min\left(\kappa_{SH}, f n_e v_e T_e \frac{|\nabla T_e|}{T_e}\right)$$
(11)

is ineffective in limiting the heat flow because the gradients in  $T_{\alpha}$  are small over the scales of interest to filamentation. On the other hand, nonlocal transport<sup>7</sup> can be quite important. Unfortunately, a nonlinear, nonlocal 3-D treatment of electron transport is a research project in itself. Thus, we have taken the approach of linearizing Eq. (4) about a uniform  $T_{e0}$  to obtain  $\delta T_e = T_e - T_{e0}$ , which is calculated from nonlocal electron transport. The choice for  $T_{e0}$  has come either from experimental data or from LASNEX simulations. In most cases of interest, this approximation has been satisfactory. It becomes questionable when there are large excursions in density because of the concomitant large excursions in electron–ion and electron-electron scattering mean-free-paths. Fortunately, in most applications with such large excursions, selffocusing is ponderomotively driven rather than thermally driven. Electron-ion energy exchange terms have been dropped in Eqs. (3) and (4) because they are of interest only for nanosecond time scales; in general, filamentation time scales are much shorter.

For completeness, we include the equation for the light wave propagation given by the modified paraxial equation

$$\left(\frac{\partial}{\partial t} + v_g \frac{\partial}{\partial z} - \frac{ic^2}{2\omega_0} D_\perp^2 + v\right) E = -\frac{4\pi e^2 i}{2\omega_0 m_e} \delta n_e E$$
 (12)

for the complex light-wave envelope amplitude E oscillating at frequency  $\omega_0$  and wave vector

$$c^2 k_z^2 = \frac{4\pi e^2}{m_{\rm e}} \, \overline{n}_{\rm e} - \omega_0^2 \quad . \tag{13}$$

Here, we define

$$\bar{n}_{\mathrm{e}}(z) = \left\langle n_{\mathrm{e}}(x, y, z) \right\rangle_{xy} \quad , \tag{14}$$

$$\delta n_{\rm e} = n_{\rm e}(x, y, z) - \overline{n}_{\rm e}(z) \quad , \tag{15}$$

the light wave group velocity

$$v_{\rm g}(z) = \frac{c^2 k_0(z)}{\omega_0}$$
 , (16)

the inverse bremsstrahlung absorption rate v and the generalized diffraction operator<sup>8</sup>

$$D_{\perp}^{2} = \frac{2k_{0}\nabla_{\perp}^{2}}{k_{0} + \sqrt{k_{0}^{2} - \nabla_{\perp}^{2}}} \quad , \tag{17}$$

which extends validity of the paraxial equation to higher order in  $k_{\perp}$ . The numerical solution of Eq. (12) is described by Berger et al.<sup>2</sup>

# Numerical Solution of the Hydrodynamical Equations

We followed the procedure outlined by Bowers and Wilson<sup>9</sup> and implemented by Miller in 2-D for spherical or cylindrical geometry.<sup>10</sup> Our code, called NH3 if uncoupled to laser light, or F3D when coupled to laser light, is 3-D Cartesian to match the fast Fourier transform (FFT) solution techniques used for the light equation solver.

The advection steps in the continuity and energy equations [Eqs. (1) and (3)] are done similarly. The equation is split into three 1-D equations, which are solved successively,

$$\frac{\partial}{\partial t} \rho^{(+1/3)} = -\frac{\partial}{\partial x} \left( \rho^{(+0)} v_x \right) \tag{18}$$

$$\frac{\partial}{\partial t} \rho^{(+2/3)} = -\frac{\partial}{\partial y} \left( \rho^{(+1/3)} v_y \right) \tag{19}$$

$$\frac{\partial}{\partial t} \rho^{(+1)} = -\frac{\partial}{\partial z} \left( \rho^{(+2/3)} v_z \right) \tag{20}$$

where  $\rho^{(+0)}$  and  $\rho^{(+1)}$  denote the actual time-iterates, and the other two quantities are intermediate results. The advection is done by a 1-D scheme,

$$\rho_{i-1/2}^{(t+1)} = \rho_{i-1/2}^{(t)} + \left(F_i^{M_x} - F_{i+1}^{M_x}\right) / \Delta x \tag{21}$$

$$F_i^{M_x} = \hat{\rho}_i \bar{v}_i \Delta t \tag{22}$$

$$\overline{v}_i = \frac{1}{4} \left( v_{i,j,k} + v_{i,j+1,k} + v_{i,j,k+1} + v_{i,j+1,k+1} \right) \quad , \tag{23}$$

where the subscripts denote spatial position, using Van Leer's second-order upwind monotonic approximation for  $\hat{\rho}$ . <sup>9,11</sup> The Van Leer method defines

$$\rho_{\text{max}} = \max(\rho_{i-3/2}, \rho_{i-1/2}, \rho_{i+1/2})$$
 (24)

$$\rho_{\min} = \min(\rho_{i-3/2}, \rho_{i-1/2}, \rho_{i+1/2})$$
 (25)

$$\Delta \rho_1 = 2 \,\mathrm{mi} \, \left( \rho_{\mathrm{max}} - \rho_{i-1} / 2 \rho_{i-1} / 2 - \rho_{\mathrm{min}} \right) \tag{26}$$

$$\Delta \rho_2 = \frac{1}{2} \left( \rho_{i+1/2} - \rho_{i-3/2} \right) \tag{27}$$

$$\Delta \rho_3 = \max \left( \rho_{\text{max}} - \rho_{i-1/2}, -\rho_{i-1/2} - \rho_{\text{min}}, |\Delta \rho_2| \right)$$
 (28)

$$\delta_{i+1/2} = \operatorname{sign}(\Delta \rho_2) \min(\Delta \rho_1, \Delta \rho_3) / \Delta x \tag{29}$$

$$\hat{\rho}_{i} = \begin{cases} \rho_{i-1/2} + \frac{1}{2} \delta_{i-1/2} (\Delta x - v_{i} \Delta t), & \text{if } v_{i} > 0 \\ \rho_{i+1/2} - \frac{1}{2} \delta_{i+1/2} (\Delta x + v_{i} \Delta t), & \text{otherwise} \end{cases}$$
 (30)

This scheme guarantees a non-negative density.

Pressure changes due to mechanical work on a cell and artificial viscosity are handled separately. As with mass continuity, the energy equation is split into three 1-D equations to be solved successively, similar to Eqs. (17)–(20):

$$\frac{\partial}{\partial t} P^{(+1/3)} = -\frac{\partial}{\partial x} \left( P_{v_x}^{(+0)} \right) , \text{etc}$$
 (31)

Transport is done by a 1-D scheme similar to the mass equation:

$$P_i^{(t+1)} = P_i^{(t)} + \left(F_i^P - F_{i+1}^P\right) / \Delta x \tag{32}$$

$$F_i^P = \hat{P}_i \bar{v}_i \Delta t \tag{33}$$

$$\bar{v}_i = \frac{1}{4} \left( v_{i,j,k} + v_{i,j+1,k} + v_{i,j,k+1} + v_{i,j+1,k+1} \right) \tag{34}$$

where P is computed exactly the same way as  $\hat{\rho}$ . The  $P\nabla \cdot \mathbf{v}$  (PdV work) and artificial viscosity at  $t + \Delta t$  are

done given the momentum equation solution, which is at time level  $t + \frac{\Delta t}{2}$ .

Again, each component of momentum is advected

separately, e.g.,

$$\frac{\partial}{\partial t} S_x + \frac{\partial}{\partial x} (v_x S_x) + \frac{\partial}{\partial y} (v_y S_x) + \frac{\partial}{\partial z} (v_z S_x) = 0 \quad . \tag{35}$$

Artificial viscosity, pressure gradients, and ponderomotive force are each treated separately, and transport is done by an advection scheme:

$$\left(S_{x}^{t+1}\right)_{i,j,k} = \left[S_{x}^{(t)}\right]_{i,j,k} + \left[\left(F_{x}^{S_{x}}\right)_{i-1/2j,k} - \left(F_{x}^{S_{x}}\right)_{i+1/2j,k}\right] / \Delta x + \left[\left(F_{x}^{S_{y}}\right)_{i,j-1/2k} - \left(F_{x}^{S_{y}}\right)_{i,j+1/2k}\right] / \Delta y + \left[\left(F_{x}^{S_{z}}\right)_{i,j,k-1/2} - \left(F_{x}^{S_{z}}\right)_{i,j,k+1/2}\right] / \Delta z, \quad (36)$$

where

$$\left(F_{x}^{S_{x}}\right)_{i-1/2j,k} = \left(\hat{v}_{x}\right)_{i-1/2j,k} \overline{F}_{i+1/2j-1/2k-1/2}^{M_{x}}$$
(37)

(30) 
$$\left(F_x^{S_y}\right)_{i-1/2,i,k} = \left(\hat{v}_y\right)_{i-1/2,j,k} \overline{F}_{i+1/2,j-1/2,k-1/2}^{M_x}$$
 (38)

$$\left(F_x^{S_z}\right)_{i-1/2j,k} = (\hat{v}_z)_{i-1/2j,k} \, \overline{F}_{i+1/2j-1/2,k-1/2}^{M_x} \quad . \tag{39}$$

 $\overline{F}^{M_x}$  denotes the average mass-flux in the x-direction over the cell, and  $\hat{v}_x$ ,  $\hat{v}_y$ , and  $\hat{v}_z$  are computed using a slight modification of the Van Leer method defined in Eqs. (24)–(30) [the slope  $\Delta \rho_3$  is excluded from Eq. (29)]:

$$\delta_i = \operatorname{sign}(\Delta v_2) \min(\Delta v_1, |\Delta v_2|) / \Delta x \quad . \tag{40}$$

After the transport step is complete, the change in momentum from thermal pressure gradients

$$\frac{\partial}{\partial t} S_{x} = -\frac{\partial}{\partial x} P \tag{41}$$

$$(S_x)_{i,j,k}^{(t+1)} = (S_x)_{i,j,k}^{(t)} - \frac{\Delta t}{\Delta x} (\overline{P}_{i+1/2j,k} - \overline{P}_{i-1/2j,k})$$
 (42)

$$\overline{P}_{i+1/2j,k} = (P_{i+1/2,j-1/2k-1/2} + P_{i+1/2,j+1/2k-1/2} + P_{i+1/2,j-1/2k+1/2} + P_{i+1/2,j+1/2k+1/2}) / 4$$
(43)

and ponderomotive forces

$$\frac{\partial}{\partial t} S_{x} = -\rho \frac{\partial}{\partial x} \, \phi \tag{44}$$

$$(S_x)_{i,j,k}^{(t+1)} = (S_x)_{i,j,k}^{(t)} - \frac{\Delta t}{\Delta x} \,\overline{\mathsf{p}}_{i,j,k} \Big(\overline{\mathsf{q}}_{i+1/2j,k} - \overline{\mathsf{q}}_{i-1/2j,k}\Big)$$
 (45)

$$\bar{\phi}_{i+1/2j,k} = (\phi_{i+1/2,j-1/2,k-1/2} + \phi_{i+1/2j+1/2k-1/2} + \phi_{i+1/2j-1/2k+1/2} + \phi_{i+1/2j+1/2k+1/2}) / 4$$
(46)

is calculated, where  $\bar{\rho}$  is the average over the cell.

The artificial viscosity is handled similarly and has the form

$$(Q_{xx})_{i+1/2} = \begin{cases} C_{Q} \rho_{i+1/2} \left[ (\Delta v_{x})_{i+1/2} \right]^{2}, & \text{if } (\Delta v_{x})_{i+1/2} < 0 \\ 0, & \text{otherwise} \end{cases}$$

where

$$\left(\Delta v_{x}\right)_{i+1/2} = \left(\overline{v}_{x}\right)_{i+1} - \left(\overline{v}_{x}\right)_{i} \tag{48}$$

and  $\bar{v}_x$  is the average over the face

$$\left(\overline{v}_{x}\right)_{i} = \left[\left(v_{x}\right)_{i,j,k} + \left(v_{x}\right)_{i,j+1,k} + \left(v_{x}\right)_{i,j,k+1} + \left(v_{x}\right)_{i,j+1,k+1}\right] / 4 \quad (49)$$

Note that we only keep the diagonal elements from the artificial viscosity term in Eq. (2). Through numerical experimentation, we have determined that  $C_Q = 1$  is a reasonable choice, even in the presence of fairly steep shocks.

We have also included a time-step controller to allow a larger  $\Delta t$  when possible, but to ensure that the Courant condition is satisfied. In cases where plasma velocities grow an order of magnitude or more from their initial size, the time step is decreased so that the numerical scheme is stable. When coupled to F3D, the time step is never increased beyond the limit specified by the light propagation.

We have tested this hydrodynamics scheme on several different kinds of problems ranging from deflection of a laser beam in a flowing plasma 12 to plasma expansion into a vacuum. 13–14

# Simulation of the Self-Focusing of a High-Intensity Laser Beam

As an example of an interaction in which nonlinear hydrodynamics is important, we show the results of

propagating a 1.06- $\mu$ m laser beam with initial intensity of  $10^{16}$  W/cm² through a CH plasma whose initial electron density and temperature are uniform with values of  $n_{\rm e}=0.1n_{\rm c}$  and  $T_{\rm e}=1$  keV and thus  $v_{\rm 0}/v_{\rm e}=2$ . (These conditions are similar to those reported by Young et al.<sup>15</sup>) The laser electric field amplitude at z=0 is taken to be

$$E(x,y)_{z=0} = \begin{cases} E_0(t)\cos^2\left(\frac{\pi x}{L_x}\right)\cos^2\left(\frac{\pi y}{L_y}\right), & \text{if } |x| \le \frac{L_x}{2}, |y| \le \frac{L_y}{2} \\ 0, & \text{otherwise,} \end{cases}$$
 (50)

where  $L_x = L_y = 40~\mu\text{m}$ ,  $L_z = 100~\mu\text{m}$ ,  $-L_x \leq x \leq L_x$ ,  $-L_y \leq y \leq L_y$  and  $0 \leq z \leq L_z$ . The amplitude  $E_0(t)$  rises from 0 to a constant peak value over 100 ps. The field is periodic in the transverse directions, and outgoing at  $z = z_{\text{max}}$ .

In Fig. 1(a), isocontours of the laser intensity at 252 ps are shown. The contours are 2.5, 4.5,  $7.5 \times 10^{16}$  W/cm², with the darkest contour being least intense. After propagating about  $50~\mu m$ , the laser intensity reaches a strong focus with peak intensity  $I = 5 \times 10^{17}$  W/cm², after which it breaks apart into about four filaments. The initial laser power at z = 0 is 100 times the critical power for self-focusing.  $^{16}P_{\rm crit} = 9 \times 10^8$  W for these conditions, so we might expect the number of filaments  $N \approx P/P_{\rm crit} = 100$ . The evolution to this highly filamented state requires simulation of a much longer plasma because the distance to focus of a filament varies inversely with power. The distance to the first focus in steady state can be estimated from the steady-state spatial growth rate  $\kappa$  as  $L_f = \kappa^{-1} \cong 23~\lambda_0$  for this case. The steady-state focus actually is achieved at  $\sim 50~\lambda_0$ .

Isocontours of the electron density associated with this laser intensity distribution are shown in Fig. 1(b).

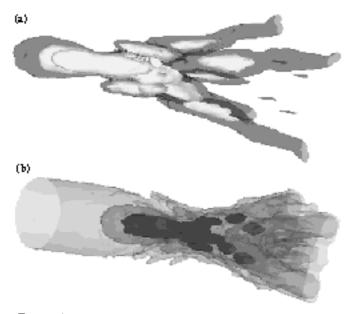


FIGURE 1. (a) Energy intensity contours; (b) density contours. Darkest contours are least intense (a) and least dense (b). (10-00-0896-1932pb01)

The density at the first focus, i.e. peak intensity, is essentially zero:  $5 \times 10^{-8} n_{\rm c}$ . The contours in Fig. 1(b) are  $10^{-2} n_{\rm c'}$ ,  $10^{-4} n_{\rm c'}$  and  $10^{-5} n_{\rm c'}$  lightest to darkest.

This configuration appears to be near the final state after a very dynamic epoch. The first focus of the laser moves backward at high velocity from  $z = 100 \, \mu \text{m}$  at 47 ps to  $z = 60 \, \mu \text{m}$  at 55 ps or a velocity of  $5 \times 10^8 \, \text{cm/s}$ .  $E_0(t)$  is still increasing during this period. The first focus stays around 55  $\mu \text{m}$  after 60 ps until the end of the simulation at 252 ps.

A number of filamentation codes, including the linearized hydrodynamic version of F3D, neglect the plasma motion along the laser propagation direction because the transverse scale length of the laser hot spot or speckle is much smaller than the axial scale; the ratio of lengths is 8*f* where *f* is the *f*-number of the focusing optic. In this simulation the axial flow is important. During the time the focus is moving from  $z = 100 \mu m$ to  $z = 60 \mu m$  at supersonic velocity, it accelerates the axial flow velocity of the fluid in front of best focus from near 0 to about  $-3 \times 10^8$  cm/s. The ponderomotive force also accelerates plasma supersonically in the positive axial direction at speeds up to  $3 \times 10^8$  cm/s and transversely at velocities  $\sim 6 \times 10^7$  cm/s. At the sides of the filaments, the plasma is compressed and heated. The energy in the supersonically moving plasma, when dissipated, results in local ion temperatures in excess of 10 keV. The initial ion temperature was 500 eV.

# **Summary**

As the self-focusing example of Fig. 1 illustrates, filamentation of intense laser beams produces a very nonlinear response in the plasma. The assumptions of a linearized treatment quickly break down. The nonlinear hydrocode described in this article has proven to be very robust and extends our ability to model experiments far beyond the limits of our earlier linear hydrodynamics treatment. Yet further improvements to the physical description are contemplated. The peak intensity achieved at best focus— $5 \times 10^{17}$  W/cm<sup>2</sup> at  $\lambda_0$ = 1.06  $\mu$ m—is weakly relativistic,  $v_0^2 / c^2 \approx 0.5$ , and suggests that relativistically correct expressions for the ponderomotive force be used. 18 The ions are accelerated to such a high velocity,  $\sim 5 \times 10^8$  cm/s, that interpenetration<sup>19</sup> rather than stagnation is anticipated at the edges of the evacuated regions associated with filaments. This happens because the ion-ion mean-freepath is estimated in some cases to be larger than the distance over which the flow decelerates. For similar reasons, ion heat conduction should be included in some cases. Inclusion of Poisson's equation might also prove necessary to model the ion-wave dynamics correctly.<sup>20</sup>

#### **Notes and References**

- 1. In addition, the density perturbation is limited in magnitude by replacing the linear response  $\delta N = (n n_0)/n_0$  by  $\ln (1 + \delta N)$  so the total density is never negative.
- R. L. Berger, B. F. Lasinski, T. B. Kaiser, E. A. Williams, et al., Phys. Fluids B 5 (7), 2243–2258 (1993); R. L. Berger, B. F. Lasinski, A. B. Langdon, T. B. Kaiser, et al., Phys. Rev. Lett. 75 (6), 1078–1081 (1995); S. Hüller et al., "Numerical Simulation of Filamentation and its Interplay with SBS in Underdense Plasmas," submitted to Physica Scripta (1996); A. J. Schmitt, Phys. Fluids 31 (10), 3079–3101 (1988); A. J. Schmitt, Phys. FluidsB 3 (1), 186–194 (1991).
- 3. A. B. Langdon and B. F. Lasinski, *Phys. Rev. Lett.* **34** (15), 934–937 (1975).
- M. A. Blain, G. Bonnaud, A. Chiron, and G. Riaguelo, Autofocalisation de Filamentation d'un Faisceau Laser dans le Cadre de l'Approximation Paraxiale et Stationnaire, CEA-R-5716; B. I. Cohen et al., Phys. Fluids B 3 (3), 766–775 (1991); V. E. Zakharov et al., Sov. Phys. JEPT 33 (1), 77–81 (1971).
- D. Havazelet et al., Phys. Fluids B 1 (4), 893–900 (1989);
   R. Rankin et al., Phys. Rev. Lett. 63 (15), 1597–1600 (1989);
   H. A. Rose, Phys. Plasmas 3 (5), 1709–1727 (1996).
- 6. S. H. Langer, Rayleigh-Taylor calculations.
- E. M. Epperlein, *Phys. Fluids B* 1 (11), 3082–3086 (1991);
   B. Kaiser, B. I. Cohen, R. L. Berger, B. F. Lasinski et al., *Phys. Plasmas* 1, 1287 (1994);
   J. R. Albritton, E. A. Williams,
   I. B. Bernstein, and K. P. Swartz, *Phys. Rev. Lett.* 57, 1887 (1986).
- 8. M. D. Feit and J. A. Fleck, Jr., J. Opt. Soc. Am. B 5 (3), 633–640 (1988).
- R. L. Bowers and J. R. Wilson, Numerical Modeling in Applied Physics and Astrophysics (Jones and Bartlett, Boston, MA, 1991), 199–347.
- 10. D. S. Miller, Convection in Type II Supernovae, Ph. D. Thesis (1993).
- 11. B. Van Leer, *J. Comp. Phys.* **23** (3), 276–299 (1977); B. Van Leer, *J. Comp Phys.* **32** (1), 101–136 (1979).
- D. Hinkel, E. A. Williams, and C. H. Still, Phys. Rev. Lett. 77 (7), 1298–1301 (1996).
- C. H. Still, R. L. Berger, A. B. Langdon, and D. S. Miller, "Nonlinear Eulerian Hydrodynamics in Three Dimensions," Anomalous Absorption Conference, Aspen, CO (1995).
- C. H. Still, R. L. Berger, A. B. Langdon, D. S. Miller, and E. A. Williams, "Nonlinear Eulerian Hydrodynamics in 3D," Bull. APS 40 (11), (1995).
- P. E. Young, G. Guethlein, S. C. Wilks, J. H. Hammer, et al., *Phys. Rev. Lett.* 76 (17), 3128–3131 (1996).
- 16. C. E. Max, Phys. Fluids 19 (1), 74-77 (1976).
- 17. B. I. Cohen et al., Phys. Fluids B 3 (3), 766–775 (1991).
- D. Bauer, P. Mulser, and W. H. Steeb, *Phys. Rev. Lett.* **75** (25), 4622–4625 (1996); G. Bonnaud, H. S. Brandi, C. Manus, G. Mainfray, et al., *Phys. Plasmas* **1** (4), 968–989 (1994); G. Sun et al., *Phys. Fluids* **30** (2), 526–532 (1987).
- 19. R. L. Berger et al., Phys. Fluids B 3 (1), 3–12 (1991).
- 20. B. I. Cohen et al., "Resonantly Excited Nonlinear Ion Waves," submitted to *Phys. Plasmas* (1996).

# THREE-DIMENSIONAL SIMULATIONS OF NATIONAL IGNITION FACILITY CAPSULE IMPLOSIONS WITH HYDRA

M. M. Marinak

S. W. Haan

R. E. Tipton

#### Introduction

Hydrodynamic instabilities are of critical importance in inertial confinement fusion (ICF) since they place fundamental limits on the design parameters required for capsule ignition. In capsule implosions in the National Ignition Facility (NIF), hydrodynamic instabilities are expected to evolve into the weakly nonlinear regime, so that nonlinear saturation of instability growth will control the amplitudes attained by perturbations in the shell. For perturbations with the same wave number, growth in the linear regime is the same in two and three dimensions. However, simulations of the Rayleigh-Taylor (RT) instability on classical interfaces<sup>1–5</sup>—as well as on foils driven by laser light<sup>6,7</sup> and x rays<sup>8</sup>—predict that symmetric three-dimensional (3-D) perturbations should grow largest in the nonlinear regime. An earlier potential flow model by Layzer<sup>9</sup> showed that round 3-D bubbles achieve the largest rise velocities. An increase in saturation amplitude with symmetry of the mode shape was seen in an extension of the potential flow model<sup>10</sup> and also with third-order perturbation theory.<sup>11</sup> Nova experiments done with planar foils driven by x rays exhibited this shape dependence, in quantitative agreement with simulations done with the HYDRA 3-D radiation hydrodynamics code. The larger, nonlinear saturation amplitudes attained by 3-D perturbations are a principal reason that simulations of surfaces with realistic 3-D perturbations are important to ICF research.

This article presents results from the first direct 3-D simulations of the NIF point-design (PT) capsule, which were performed with HYDRA. The effect of saturated hydrodynamic instability growth on NIF capsule implosions had been modeled previously using weakly nonlinear saturation analysis 12 and 2-D multimode simulations with LASNEX. 13–15 Direct 3-D numerical simulations most accurately treat saturation

effects and multimode coupling for capsules with realistic surface perturbations in the presence of multiple shocks, ablation, convergence, and finite shell thickness.

In this article, we begin by describing the HYDRA radiation hydrodynamics code, which performed these simulations. Descriptions of the NIF PT capsule and of the scope of these simulations follow. Finally, we discuss results from a number of multimode simulations of hydrodynamic instabilities.

#### **HYDRA**

HYDRA is a 3-D radiation hydrodynamics code based upon a block structured mesh, which has Arbitrary Lagrange Eulerian (ALE) capability. An operator splitting technique is used to treat each of the physical processes in HYDRA separately and to combine the results. The Lagrangian phase solves the compressible hydrodynamic equations using a monotonic form of artificial viscosity, 16 with predictor-corrector time stepping. A control volume technique is used to calculate surface areas and volumes of the hexahedral elements. This technique results in a consistent set of surfaces and volumes on distorted meshes while conserving momentum. The ALE capability allows the mesh to be remapped according to a specified grid motion algorithm, using Van Leer advection in these simulations. 17 Material interfaces are maintained with an Eulerian interface tracker, which is based upon the volume fraction method, 18 generalized to run on arbitrary hexahedrons. "Mixed" zones, which contain one or more material interfaces, are subdivided into separate components for each material.

Radiation transport is treated in a multigroup diffusion routine using tabular opacities. A thermonuclear burn package was installed that treats fusion reactions, including the production and depletion of isotope concentrations, with reaction cross sections obtained from

the Thermonuclear Data File (TDF) library. <sup>19</sup> Energetic charged particles are transported using an efficient multigroup algorithm.<sup>20</sup> It is an extension of diffusion, which retains the straight-line motion of particles undergoing collisions with electrons. Charged particles deposit momentum and energy into the fluid as they slow down, with the energy deposition divided among separate electron and ion channels. The user can specify independently the isotopes for which concentrations are to be followed and the energetic particle species which are to be transported. Since ICF capsules are thin to neutrons, an accurate treatment of neutron energy deposition is obtained with a model based upon an analytic solution to the neutron transport equations in the free-streaming limit. In the calculations presented here, the neutrons that interact with the capsule locally deposit the energy exchanged. Electron and ion conduction are treated, as well as electron-ion energy exchange, using coefficients from the model of Lee and More.<sup>21</sup>

By coupling several adjacent zones together, the user obtains greater freedom in zoning without the additional computational overhead and increased memory requirements associated with an unstructured mesh. Coupling the zones is essential to avoid the small Courant time step limits that would occur, for example, in narrow zones near the center or the pole of a mesh used in a 3-D capsule implosion simulation. This capability can be applied in the presence of mixed zones.

Several forms of the equations of state (EOS) are available, including the EOS4 tabular database and the inline quotidian EOS (QEOS). HYDRA runs on workstations and on vector supercomputers, and currently runs in parallel on the shared memory Cray J-90 SMP using multitasking.

Besides the planar foil simulations mentioned earlier,<sup>5</sup> HYDRA has been applied extensively to model Nova capsule implosions.<sup>22</sup>

# Point Design (PT) Capsule

The baseline capsule for the NIF, called the PT for "point design," has a 160- $\mu$ m-thick polystyrene ablator doped with bromine (Fig. 1). The ablator encloses an 80- $\mu$ m-thick layer of cryogenic DT ice. DT gas in equilibrium with the ice fills the capsule center at a density of 0.3 mg/cm³. The capsule is mounted in a gold cylindrical hohlraum 9.5 to 10.0 mm long by 5.5 mm in diameter.

The laser pulse is staged in order to implode the capsule on a low-entropy adiabat (Fig. 2). This pulse delivers 1.35 MJ of laser light, 150 kJ of which is absorbed by the capsule. This 1.35-MJ pulse, which is somewhat less than NIF's maximum (1.8 MJ), was chosen to leave an extra margin for errors in modeling. The light comes into each laser entrance hole in two cones. The relative power in these cones is dynamically varied to minimize the time-varying pole-to-waist asymmetry, which is described as a P<sub>2</sub> Legendre polynomial. Since the NIF

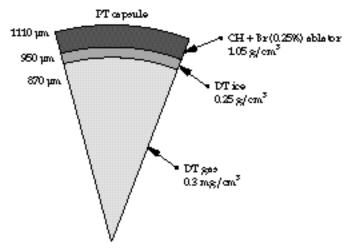


FIGURE 1. Schematic of the "point design" PT capsule shell. (50-05-0896-2031pb01)

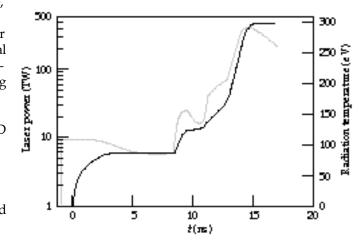


FIGURE 2. Laser power vs time to drive the PT target (gray curve, left scale), and temperature vs time optimal for the PT capsule (solid curve, right scale). (50-05-0896-2032pb01)

has 192 beams clustered in groups of four, there are effectively eight spots in each of the inner cones and 16 in the outer cones. In the absence of significant pointing and power balance errors, the intrinsic azimuthal variation in the hohlraum flux is small. With the standard cylindrical hohlraum, the drive asymmetries are designed to be nearly 2-D. The capsule surface roughness should be the primary source of 3-D asymmetries in the implosion.

The capsule-only simulations presented here model the hydrodynamic instabilities seeded by surface roughness. The average hohlraum flux obtained from an integrated LASNEX simulation<sup>3</sup> is imposed on the capsule. Hydrodynamic instabilities are simulated over a portion of the capsule solid angle, which extends equal amounts in the polar and azimuthal angles ( $\Delta\theta$ ,  $\Delta\phi$ ), with one of the boundaries coincident with the capsule equator. Multimode perturbations imposed are of the

form 
$$G(\theta, \phi) = \sum_{m} \sum_{n} a_{mn} \cos\left(\frac{m\pi\theta}{\Delta\theta}\right) \cos\left(\frac{n\pi\phi}{\Delta\phi}\right)$$
 where  $a_{mn}$ 

is the mode coefficient. Symmetry conditions exist at the transverse boundaries. These modes are the 3-D analog to the modes used in 2-D axisymmetric simulations performed over a portion of a quadrant.

Perturbations initialized on the outer ablator surface are based on traces from Nova capsules, while those on the inner DT surface are based on measurements of cryogenic ice. The data are Fourier analyzed to obtain a 1-D power spectrum. This spectrum may be shifted in mode number when applying the information to the PT capsule, which has a larger radius. The 1-D spectrum is converted to an estimated 3-D power spectrum<sup>23</sup> and

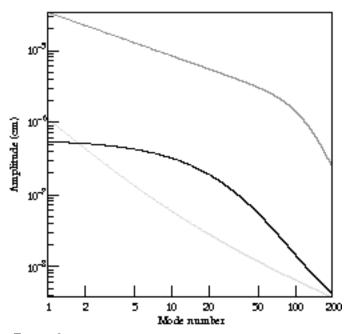


FIGURE 3. Surface perturbation spectra used in simulations of NIF PT capsules. The black curve is the early spectrum for the ablator surface obtained from measurements of a Nova capsule. The light gray curve is the spectrum from a more recent measurement of an optimized Nova capsule. The dark gray curve shows the spectrum of the ice surface. (50-05-0996-2212pb01)

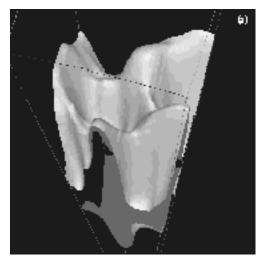
the power is distributed isotropically among the 3-D modes with equivalent wave number. Equivalent mode amplitudes from the spectra used in the simulations are shown in Fig. 3 as a function of the l mode number. Random phase factors are assigned to  $a_{mn}$  so that the topology of the surface does not have unusually large peaks and valleys due to excessive phase coherence.

### **Multimode Simulation Results**

We consider first a capsule with perturbation amplitudes, in the range of modes l = 10-1000, equal to 24 nm rms on the outer surface and 1 µm rms on the inner cryogenic DT surface. A domain extending 18° in each angle is used to simulate modes in the range l = 10-40. The grid used here measured  $32 \times 32 \times 169$  zones in the polar, azimuthal, and radial directions respectively, so that there are at least 16 transverse zones per wavelength for the least well resolved modes. As the laser pulse rises to peak power, it generates four staged shocks that compress the capsule shell, reducing the shell thickness to 20 µm early in the implosion phase. The grid motion algorithm employed follows this large change in shell aspect ratio and ensures that perturbation growth in the shell is resolved by zones with a fine spacing of 0.75 µm in the radial direction.

Perturbations that grow on the simulated ablator are seeded by initial ablator surface roughness and by the perturbed rarefaction wave that returns from the inner ice surface after the first inward-going shock arrives. During the implosion phase, the shell areal density  $A(\theta,\phi)=\int \rho(r,\theta,\phi)\,dr$  strongly resembles the initial outer surface perturbation, indicating that modes growing in the ablator are seeded predominantly by ablator surface perturbations. Valleys initially on the ablator surface develop into bubbles on the ablator, surrounded by interconnecting spike sheets and larger individual spikes, as shown by the iso-density contour plot Fig. 4(a).

Figure 4(b) shows bubble and spike ridge structures that are growing on the pusher–hot spot interface after



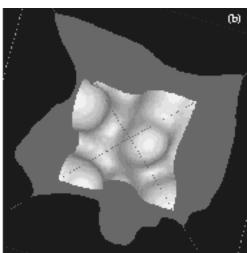


FIGURE 4. Two perspectives of the iso-density contours of  $60 \text{ g/cm}^3$  at 17.0 ns from a PT capsule simulation having 24-nm- and 1- $\mu$ m-rms perturbations initially on the outer ablator and inner ice surfaces, respectively. Multimode perturbations with l = 10-40 were initialized. (a) View of region just inside of the DT-ablator interface. (b) View of pusher-hot spot interface. (50-05-0896-2033pb01)

the rebounding shock has reached it. The locations of these bubbles correspond to the locations of equivalent structures in the ablator, which have fed through the shell. The resemblance to the imposed surface perturbation is characteristic of weakly nonlinear behavior. Some degree of roll-up is apparent, due to a Kelvin Helmholtz instability,<sup>7,9,10</sup> but it is much less than was observed on the classical fuel-pusher interface in Nova capsule simulations.<sup>20,22</sup> The structure of these perturbations has much power in modes  $l \leq 40$ . These growing structures remain visible until the capsule reaches peak compression and the hot spot achieves ignition conditions, with a column density of  $\rho r \sim 0.3 \text{ g/cm}^3$  and ion temperature of ~10 keV. As the capsule reaches peak compression and begins to ignite, the inner surface structure evolves toward lower mode numbers characterized by l = 10-15. This behavior appears to be strongly influenced by ablation driven by conduction from the hot spot and the effect of convergence, rather than by mode coupling, as was seen in planar geometry.<sup>7,24–27</sup> Since the shell has a peak convergence ratio of 37, there is a large decrease in the wavelength associated with a particular mode number during the implosion. At ignition the deposition of alpha particles is mostly responsible for "bootstrapping" the central temperature to over 60 keV. This burn propagates into the fuel layer, which has a peak density of  $> 1000 \text{ g/cm}^3$  at this time. Simulations are carried into the expansion phase for as long as the capsule continues to burn at a significant rate.

Figure 5 shows yields from simulations of several PT capsules that have different multimode surface perturbations with modes l=10–40. The capsule with the largest perturbation amplitudes failed to ignite because,

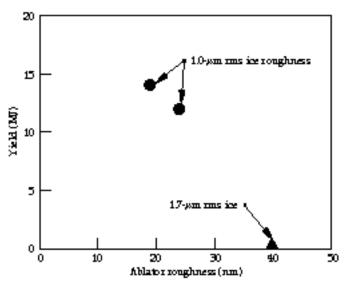


FIGURE 5. Yields for several PT capsule simulations having multimode perturbations with l=10–40 at both the ablator and inner DT-ice surfaces. Ice surface roughness was varied while the ablator roughness was fixed at 24 nm. (50-05-0896-2034pb01)

at the time of stagnation, spikes had penetrated 10 µm into the 30-um-radius hot spot, and bubbles were burning through the shell. Quench of ignition in the DT capsule by 10-µm spikes is consistent with results obtained with other modeling techniques.<sup>3</sup> The location of the yield cliff in Fig. 5 corresponds to a roughness on the outer surface which is ~40% smaller than that obtained with 2-D multimode simulations over this range of modes.<sup>3,4</sup> Higher nonlinear saturation amplitudes and nonlinear growth rates occur for the round, 3-D-bubble-spike features than for the 2-D bubble ridges, and these are responsible for the smaller allowable surface roughness. Differences in instability growth are illustrated by comparing results from one of these 3-D multimode simulations with an axisymmetric 2-D HYDRA simulation that also has surface perturbations consisting of modes l = 10–40. The initial rms value for roughness on the capsule surfaces is identical for these 2-D and 3-D simulations. The roughnesses correspond to surfaces with overall perturbations of 19.4 nm and 1.0 µm rms on the ablator and ice surfaces respectively. These amplitudes were chosen so that perturbations would evolve into the weakly nonlinear regime. Figure 6 compares filled contour plots of density on the domain boundaries at 17.0 ns for the 2-D and 3-D simulations with equivalent surface roughnesses. The larger saturated amplitudes attained by the 3-D perturbations are clearly apparent. Since the larger 3-D ablator bubbles are close to penetrating the shell, the bubble tips accelerate, 22 thereby increasing the apparent difference between the growth of 2-D and 3-D bubbles.

The nonlinear growth of the 3-D multimode perturbations is affected by mode coupling and perturbation shape effects. Broad bubbles and narrow

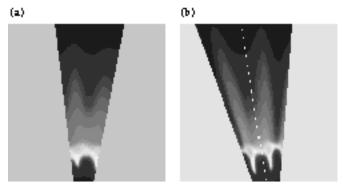


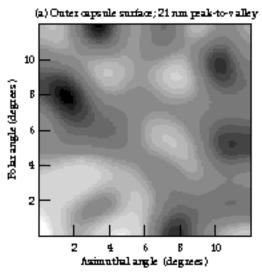
FIGURE 6. Filled contour plots of density at 17.0 ns for two capsules each having initial roughnesses equivalent to 19 nm rms and 1.0  $\mu$ m rms on the ablator and DT-ice surfaces, respectively. Contours are shown along the planar boundaries of the domains simulated with the radial direction extending upward. Both perturbations contain modes with l=10–40. Perturbation in (a) is 2-D axisymmetric while perturbation in (b) is 3-D, shown along two orthogonal boundary planes. The lightest color corresponds to peak density. (50-05-0896-2035pb01)

spike sheets begin to form early in the nonlinear regime, and for a time it can be described by second-order mode coupling theory. Nearby structures strongly influence the evolution of individual bubbles and spikes in the nonlinear phase. Previous attempts to estimate the effect of the higher 3-D saturation amplitudes within direct 2-D axisymmetric capsule simulations involved placing a single bubble or spike on the pole. This treatment is limited because it cannot reproduce the complex multimode coupling and interference effects that occur on a realistic 3-D surface.

The simulations we have discussed so far contain initial perturbations with modes l = 10-40. Modes 40 < l < 120, which are also RT unstable on the ablator, are much less capable of feeding through the shell and producing spikes during deceleration. The shorter length scales of their mode structures reduce their ability to feed through. But the shorter-wavelength modes can threaten the shell integrity during implosion, when the shell is thinnest. We now consider a simulation that includes modes spanning both of these ranges. Perturbations with modes l = 15-120 were simulated on both the inner ice and outer ablator surfaces on a 12° wedge. The grid measured  $64 \times 64 \times 169$  zones in the polar, azimuthal, and radial directions respectively. The outer surface perturbation corresponded to the best surface finish measured on a Nova capsule. Similar traces from Russian capsule shells, which have larger radii than Nova capsules, suggest that the long-wavelength surface roughness will not scale strongly to our disadvantage as we go to larger capsules. <sup>29</sup> Figure 7 shows contour plots of the initial perturbations simulated, which have amplitudes of 21 nm and 1.3 µm peak-to-valley on the outer ablator and inner DT ice surfaces, respectively.

Late in the implosion phase, the structure of the growing multimode perturbation has its peak amplitude at the classical interface between the polystyrene ablator and the DT fuel. Centered at this location, the perturbation will penetrate the shell when the amplitude is only a fraction of the shell thickness. The higher modes, which grow fastest on the classical ablator–DT interface, are of concern for the period before the peak implosion velocity is reached. After the implosion velocity peaks, convergence causes the capsule shell to thicken and the classical interface becomes RT stable. Although these perturbations continue to grow inertially, the rapid thickening of the shell separates the classical interface from the shell's inner surface fast enough that further growth of short wavelength modes is unimportant. The longer wavelength modes that feed through the shell, combined with perturbations on the inner capsule surface, assume principal importance once the rebounding shock begins to traverse the shell.

In the present simulation, the shell integrity was never threatened. Figure 8 shows the iso-density contours at 17.1 ns, when the capsule is close to igniting. The contour surface shown in Fig. 8(a) is located in the DT-fuel region of the shell, somewhat inside the polystyrene–DT interface, while the contour surface in Fig. 8(b) corresponds to the pusher–hot spot interface. The high modes apparent near the classical interface, typically near l = 90, have not fed through appreciably to the inner interface, which has features typically in the range l = 15-20. The yield (15.5 MJ) approaches that for an unperturbed capsule. Thus a PT capsule, with a surface finish equal to the best measured on a Nova capsule, easily ignites in the simulation. The margin of ignition in this simulation implies that substantially larger perturbation amplitudes can be tolerated on the outer surface, even with high-*l* modes present.



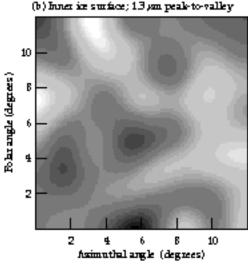
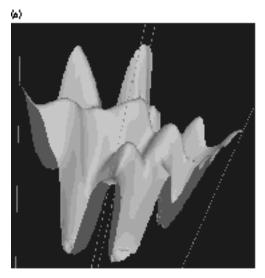
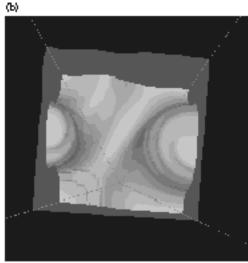


FIGURE 7. Contour plots of multimode perturbations initialized in simulation containing modes l=15–120. (a) Ablator surface perturbation with peakto-valley amplitude 21 nm. (b) Inner ice surface perturbation with peak-to-valley amplitude 1.3  $\mu$ m. (50-05-0896-2036pb01)

D SHVIGENTIONS OF THE CALSUE HVII EOSIONS VVIIII II I DIV

FIGURE 8. Iso-density contour surfaces near ignition time for a PT capsule simulation containing modes l = 15-120. (a)  $130 \text{ g/cm}^3$  surface just inside the DT-ablator interface. (b)  $650 \text{ g/cm}^3$  surface at pusher-hot spot interface. (50-05-0896-2037pb01)





## **Conclusions**

We presented results from the first 3-D simulations of the NIF PT capsule design. Realistic multimode perturbations seeded hydrodynamic instabilities that evolved into the weakly nonlinear regime. These perturbations were characterized by broad round bubbles surrounded by interconnecting spike sheets and larger individual spikes. Simulations showed that modes with l < 40 could threaten ignition by feeding through the shell and developing into spikes when the shell decelerates. Higher modes are much less capable of generating spikes that quench ignition, but they can threaten shell integrity during the implosion phase. The simulations showed that the PT capsule can tolerate spikes with amplitudes up to  $10~\mu m$  before ignition is quenched.

Three-dimensional multimode perturbations attained larger nonlinear amplitudes than 2-D multimode perturbations having the same initial rms roughness. This results in a constraint on the roughness of the ablator surface that is ~40% smaller than was obtained from 2-D multimode simulations over a similar range of modes. Even when modes spanning the range l=15–120 were included, however, a PT capsule with surface finishes equal to the best currently attainable easily ignited in the simulation. Future simulations of the PT will quantify the sensitivity of the capsule to surface roughnesses contained in different ranges of modes.

#### **Notes and References**

- G. Tryggvason and S. O. Unverdi, *Phys. Fluids A* 2 (5), 656–659 (1990).
- T. Yabe, H. Hoshino, and T. Tsuchiya, *Phys. Rev. A* 44 (4), 2756–2758 (1991).
- 3. J. Hecht, D. Ofer, U. Alon, D. Shvarts, S. A. Orszag, and R. L. McCrory, *Laser Part. Beams* 13 (3), 423–440 (1995); D. Ofer, J. Hecht, D. Shvarts, Z. Zinamon, S. A. Orszag, and R. L. McCrory, *Proceedings of the 4th International Workshop on the Physics of Compressible Turbulent Mixing*, edited by P. F. Linden, D. L. Youngs, and S. B. Dalziel (Cambridge University Press, Cambridge, 1993), pp. 119–128.
- 4. H. Sakagami and K. Nishihara, *Phys. Rev. Lett.* **65** (4), 432–435 (1990).
- 5. R. P. J. Town and A. R. Bell, *Phys. Rev. Lett.* **67** (14), 1863–1866 (1991)
- J. P. Dahlburg, J. H. Gardner, G. D. Doolen, and S. W. Haan, Phys. Fluids B 5 (2), 571–584 (1993).
- J. P. Dahlburg, D. E. Fyfe, J. H. Gardner, S. W. Haan, S. E. Bodner, and G. D. Doolen, *Phys. Plasmas* 2 (6) 2453–2459 (1995).
- 8. M. M. Marinak, B. A. Remington, S. V. Weber, R. E. Tipton, S. W. Haan, K. S. Budil, O. L. Landen, J. D. Kilkenny, and R. Wallace, *Phys. Rev. Lett.* **75** (20), 3677–3680 (1995).
- 9. D. Layzer, Astrophys. J. 122 (1), 1-12 (1955).
- 10. J. Hecht, U. Alon, D. Shvarts, Phys. Fluids 6 (12), 4019-30 (1994).
- 11. J. W. Jacobs and I Catton, J. Fluid Mech. 187, 329-352 (1988).
- 12. S. W. Haan, Phys. Rev. A 39 (11), 5812–5825 (1989).
- G. B. Zimmerman and R. M. More, J. Quant. Spectrosc. Radiat. Transfer 23 (5), 517–522 (1980); R. M. More, ibid. 27 (3), 345–357 (1982).
- S. W. Haan, S. M. Pollaine, J. D. Lindl, J. J. Suter, et al., *Phys. Plasmas* 2 (6), 2480–2487 (1995).

- W. J. Krauser, N. M. Hoffman, D. C. Wilson, B. H. Wilde, W. S. Varnum, D. B. Harris, F. J. Swenson, P. A. Bradley, S. W. Haan, S. M. Pollaine, A. S. Wan, J. C. Moreno, and P. A. Amendt, *Phys. Plasmas* 3 (5), 2084–2093 (1996).
- 16. D. J. Benson, Comp. Methods Appl. Mech. Eng. 93, 39–95 (1991).
- 17. B. Van Leer, J. Comput. Phys. 23 (3), 276–299 (1977).
- D. L. Youngs, in *Numerical Methods for Fluid Dynamics*, edited by K. W. Morton and M. J. Baines (Academic Press, New York, 1982) pp. 273–285.
- R. M. White, D. A. Resler, and S. I. Warshaw, in Proceedings of the International Conference on Nuclear Data for Science and Technology, 13–17 May 1991, Jülich, edited by S. M. Qaim (Springer-Verlag, Berlin, 1992) p. 834.
- 20. G. Zimmerman, private communication.
- 21. Y. T. Lee and R. M. More, Phys. Fluids 27 (5), 1273–1286 (1984).
- M. M. Marinak, R. E. Tipton, O. L. Landen, T. J. Murphy, P. Amendt, S. W. Haan, S. P. Hatchett, C. J. Keane, R. McEachern, and R. Wallace, *Phys. Plasmas* 3 (65), 2070–2076 (1996).

- 23. S. M. Pollaine, S. P. Hatchett, and S. H. Langer, *ICF Quarterly Report*, **4** (3), 87–89, Lawrence Livermore National Laboratory, Livermore, CA, UCRL LR105821-94-3 (1994).
- M. M. Marinak, R. E. Tipton, B. A. Remington, S. W. Haan, S. V. Weber, *ICF Quarterly Report*, 5 (3), 168–178, Lawrence Livermore National Laboratory, Livermore, CA, UCRL LR105821-95-3 (1995).
- 25. D. H. Sharp, Physica D 12 (1-3), 3-18 (1984).
- U. Alon, D. Shvarts, and D. Mukamel, *Phys. Rev. E* 48 (2), 1008–1014 (1993); *Phys. Rev. Lett.* 72 (18), 2867–2870 (1994).
- D. Shvarts, U. Alon, D. Ofer, R. L. McCrory, and C. P. Verdon, *Phys. Plasmas* 2 (6), 2465–2472 (1995).
- 28. S. W. Haan, Phys. Fluids B 3 (8), 2349-2355 (1991).
- 29. R. Cook, private communication.

# LASNEX—A 2-D PHYSICS CODE FOR MODELING ICF

J. A. Harte

W. E. Alley

D. S. Bailey

J. L. Eddleman

G. B. Zimmerman

#### Introduction

The LASNEX computer code was developed to study inertial confinement fusion (ICF), to design ICF experiments, and to analyze the results. The code has evolved over time and been greatly enhanced with improved physics and modern computer science tools. LASNEX was first referred to in the literature in 1972<sup>1</sup> and first documented in 1975.<sup>2</sup>

This article presents an overview of the code, describing the physics models, the code structure, the methods used to solve the equations, and the user interface, providing supplemental information and updates to the previous review article published in 1980.<sup>3</sup> Although the general structure of the physics in the code is very much the same, many improvements have been added since 1980. For instance, the user interface has been greatly enhanced by the addition of the Basis code development system.<sup>4</sup> In addition, the code has been improved in response to requests, suggestions, and feedback from its users, who often challenge its capabilities to a far greater degree than the code developers do. The success of LASNEX as an important scientific tool is due to the team effort of the code developers and its users.

LASNEX models in two dimensions by assuming axial symmetry. It represents the spatial variation of its many physical quantities, such as temperature, density or pressure, on a two-dimensional (2-D), axially symmetric mesh composed of arbitrarily shaped quadrilaterals. LASNEX evolves the hydrodynamics and follows the electron, ion, and radiation heat conduction, and the coupling among these energy fields. There are many possible sources and boundary conditions that can be imposed on a LASNEX simulation, which can vary both in time and space. The possible sources include fully three-dimensional (3-D) lasers or ion beams

using a ray tracing algorithm, temperature sources, frequency-dependent radiation sources, velocity sources, external electric circuits, and pressure sources. Thermonuclear reactions can be modeled by LASNEX, including the energy produced as well as the reaction products and their transport through the problem. We have several different atomic physics packages available which supply the coupling and transport coefficients and self-consistent thermodynamic quantities. LASNEX combines all these physical processes and evolves the system forward in time, rather than just solving for an equilibrium or steady-state configuration. This complexity and the large number of physical processes modeled present a challenge to us (as we try to describe the code) and to those using the code and interpreting the results. A computer simulation of an experiment calculates all the independent physical quantities at each time step to enable the system to evolve forward. Any quantity can be "measured" or monitored. Huge amounts of data are often the problem for computational physicists, rather than a lack of data (which can be a problem for experimentalists).

With LASNEX, a "typical" problem does not exist—its calculations can take many different forms. Because of this, in this paper we describe the code by presenting all its different parts and how they fit together, organized around the "circles and arrows" diagram shown in Fig. 1. Following the descriptions of the physics packages, we outline the computer science enhancements that have been added to increase LASNEX's power, versatility, and convenience. Finally, we present several LASNEX calculations that accurately model laboratory experiments. Ultimately, it is the agreement between the code calculation and experimental data that validates the code and gives us confidence that LASNEX can be used to predict and design future experiments (the National Ignition Facility, for example).

# Circles and Arrows Diagram

Figure 1 is a "circles and arrows" diagram that represents the LASNEX computer code: *circles* represent the fields in which energy resides and *arrows* represent the interactions among the various fields. There is also a circle labeled atomic physics that is connected to the arrows. This process supplies the physical data necessary for many of the other packages.

LASNEX solves a large set of coupled, nonlinear, partial differential equations that determine the temporal evolution of the many spatially dependent quantities as they are influenced by different physical processes. The solution of the equations for the different physical processes is "split," so that the code evolves one process after another forward in time by one timestep until they have all been done, feeding the results from one into the next. For each package, a maximum allowable or reasonable timestep is calculated for the next cycle. When all the processes have been solved for one step, the next step is taken using a value for the timestep that is the smallest of all the possible time steps.

One of the basic design philosophies of LASNEX is to allow the different physics packages to be turned on or off by the users based on their particular application. The actual processes that are used in any calculation are determined by the user, usually when the

calculation is initialized. Also, in a circle there can be several models for a given physical process. Once again, the physicists will choose which models to use based upon the problem parameters and the computer resources available. This choice of models can also affect the interactions among the different parts of the calculation represented by the arrows. The ability to choose at execute time between alternative modules for the same physical process has allowed us to develop and debug new physics packages while simultaneously maintaining a stable code for production use. Redundant physics models also allow a user to validate the correctness of each model and to trade computer time and problem size for accuracy, according to the needs of the particular situation.

### **Hydrodynamics**

The spatial variation of the physical quantities are described on a 2-D, axially symmetric mesh composed of arbitrarily shaped quadrilaterals. Typically, the hydrodynamics is Lagrangian<sup>5</sup> in which the mesh moves along with the material. LASNEX uses a staggered grid hydro algorithm adapted from the HEMP code of Wilkins.<sup>6</sup> On a regular mesh, it is second-order accurate in time and space. Several artificial viscosities are provided to treat shock waves of arbitrary strength, one of which approximates the dissipation given by a

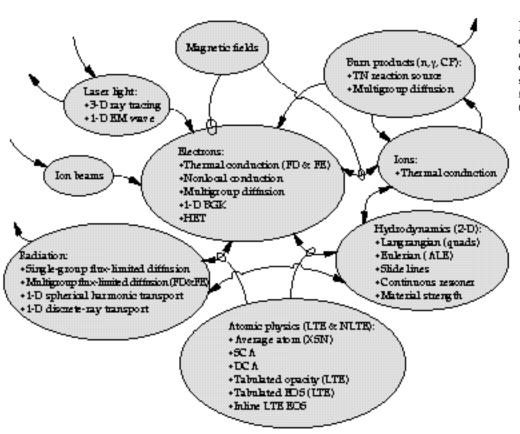


FIGURE 1. A schematic overview of LASNEX. The *circles* represent the fields in which energy resides; the *arrows* represent interactions among the different fields. (02-08-1292-3795pb02)

LABINEA 112 D 1 HI DICO CODE I OK INIODELINO IC

Riemann solution of the flow. There are also velocity filters used to damp spurious mesh oscillations, including anti-hourglass filters and artificial shear viscosities.

A material strength capability is available that generalizes the scalar pressure to a stress tensor appropriate for isotropic materials. It includes elastic and plastic flow regimes and a Von Mises yield criterion for the transition to plastic flow. There are provisions for user specification of the elastic constants and yield stress limits to allow very general constitutive models. There is a history-dependent fracture model that includes both compression and tensile failure modes, based on computing a strain damage integral from the plastic flow and using this damage to lower the yield strength in a prescribed way. The model allows effects such as spallation of brittle material to be treated. Its parameters are designed for great flexibility in treating material failure.

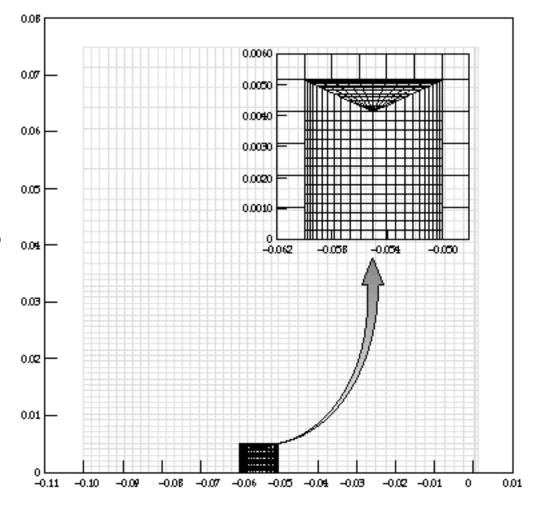
The hydrodynamics calculation usually takes a small fraction of the computer time required for a complete physics cycle, and often the Courant timestep (set by the requirement that a signal can travel only one zone width in one timestep) can be much smaller than all the other timesteps. In this case, LASNEX can "subcycle" the hydrodynamics, taking many

hydrodynamics cycles per major physics cycle to speed up the calculation.

When the LASNEX hydrodynamics method leads to severe mesh distortions or suboptimal resolution of the important physics, the user can request that the mesh be moved. There are two rezoners used in LASNEX—one for rezones at discrete times and another which operates continuously. The discrete time rezoner takes explicit user input to generate the new mesh coordinates. Discrete rezoning can be done interactively with graphical feedback or can be preprogrammed using Basis<sup>4</sup> interpreted user-defined functions to determine when and how to rezone the problem. (See the "User Interface" section for an example.) The continuous rezoner accepts user commands to define the desired mesh configuration and tries to satisfy these requirements through a relaxation process (one of which tends toward a mesh of equipotential lines). Rezoning every timestep can be equivalent to performing Eulerian or Arbitrary Lagrange Eulerian (ALE)<sup>7</sup> hydrodynamics. It requires that the remapping of all variables to the new mesh be done with high accuracy.

Both of the rezoners use a Van Leer slope limiting method in which spatial quantities are represented as

FIGURE 2. This mesh models a small, dense impurity in an otherwise homogeneous, lower density region. It is composed of two simply connected parts that are joined by slide lines. The slide lines allow part of the mesh to be much more finely resolved than the rest of the problem. Without slide lines, the fine zones would have extended all the way in both directions, increasing the problem size by over 50% and creating many small low-density zones with a much more restrictive Courant condition. (40-00-1196-2729pb01)



linear functions within each zone. This allows for second-order remap accuracy in smooth regions, while not generating extraneous maxima/minima at discontinuities. This is adequate for most quantities, but the material composition suffers some numerical diffusion. The addition of a material interface tracking algorithm would substantially reduce these errors.

The discrete rezoner allows an arbitrary overlap between the old and new mesh, but the continuous rezoner demands local overlap of the two meshes. The locality assumption permits an accurate momentum remap that also conserves kinetic energy, 8 while the more general case is treated by a less accurate interpolation method.

Ordinarily, the LASNEX mesh has a simple logical structure in which each interior quadrilateral zone has four nearest neighbors, a relationship that remains constant throughout the calculation. Optionally, one can specify slide lines, 9 logical line segments along which zones on one side are free to slide relative to the other side. This allows simulations with discontinuous velocities and also provides a means of zoning complicated initial geometries, such as shine shields or connecting regions of differing resolution. Figure 2 shows a LASNEX mesh with slide lines to connect regions of differing resolution. Every physics model that involves neighbor zones (hydrodynamics, diffusion, transport, laser ray trace, etc.) has had to be modified to include the special (time-dependent) slide line connectivities. These slide line modifications which connect logically disjoint zones have also been used to establish the periodic boundary conditions needed for multimode *z*-pinch calculations.

#### **Electrons**

To model the electrons, the user can choose thermal conduction, multigroup diffusion, one-dimensional (1-D) or 2-D nonlocal conduction, 1-D Bhatnagar, Gross, Krook (BGK) conduction, or a hybrid electron transport (HET) model that is currently under development. All the 1-D models allow either planar or spherical configurations.

Thermal electrons are assumed to be in a Maxwellian distribution. The electron thermal energy is transported using tensorial plasma conductivities in a magnetic field modified by applying a flux limiter (described later). The electrical conductivities in LASNEX go beyond the low-density, high-temperature formulae of Spitzer/Braginskii<sup>10</sup> by including dense plasma effects. They include the effects of electron degeneracy, Debye–Hückel screening, ion–ion coupling, and electron-neutral scattering (see refs. in Ref. 11). The treatment is based on a relaxation time (Krook<sup>12</sup>) model of the Boltzmann equation ignoring e–e collisions. LASNEX approximately includes e–e collisional effects by making Braginskii's correction to the

Lee/More coefficients. The cross sections used are analytic fits of a Coulomb cross-section form to numerical partial-wave expansions, with cut-off parameters to avoid unphysical answers. The effects of ion correlations in the liquid/solid regimes are treated by a modified Bloch–Grüneisen<sup>13</sup> formula. Finally, the various magnetic coefficients (which do satisfy the Onsager symmetry relations) are fits to the numerical integrals in the weak-field case and tabulated for the intermediate and strong-field case. Overall, the conductivities are believed accurate to a factor of 2 over a very wide range of densities (to  $100 \times \text{solid}$ ) and temperatures (eVs to 100 keV) and expressed in a computationally simple form.

Thermal electron conduction involves the solution of the diffusion equation on the arbitrary quadrilateral mesh. Since the mesh lines are not necessarily orthogonal, this requires a nine-point diffusion operator. The resulting matrix is solved by the Incomplete Cholesky–Conjugate Gradient (ICCG) method. <sup>14</sup> Both a finite difference and a finite element scheme are available to calculate the electron conduction. Finite difference schemes <sup>15</sup> are employed throughout the code to diffuse the zonal quantities, which are the basic unknowns. The finite element method <sup>16</sup> gives better solutions on nonorthogonal meshes. However, the finite element energy densities are point centered and must be integrated into the LASNEX architecture of zonally averaged quantities.

The diffusion equation is derived in the limit of near isotropy. Thus the mean free path should be considerably shorter than the characteristic length scale of the problem. Nevertheless, the diffusion equation can give meaningful results in other regimes if modified to insure that physical expectations will not be violated. The flux of energy should be bounded by the limit of all the energy flowing in one direction at the average velocity of the Maxwellian distribution. This is referred to as "flux limiting" and is achieved by modifying the diffusion coefficient so that when the gradients are very large the energy flux will be bounded by this criterion.

The thermal electron energy is coupled with the other fields in LASNEX as indicated by the arrows in Fig. 1. The energy of the electrons is shared with the ions through Coulomb collisions.<sup>17</sup> The electrons affect the material hydrodynamic motion by contributing to the plasma pressure.

Nonthermal, actually suprathermal, electron distributions can also be treated in LASNEX. This method was developed to study the hot electrons that are found in ICF applications. <sup>18</sup> In the code hot electrons are created by either a laser source or an ad hoc source defined by the user. They are transported and thermalized by a multigroup, flux limited diffusion method that is relativistically correct and allows for arbitrary isotropic distributions. <sup>19</sup> When suprathermal electrons

are being modeled, the thermal electrons are also present. Suprathermal electron transport is iterated, along with the determination of a self-consistent electrostatic potential, in a way that assures zero net current. Suprathermal electrons lose energy to the thermal electrons by Coulomb collisions, including the effect of the degree of ionization<sup>20</sup> and by doing Ohmic work through the electric field. The suprathermal electron bins can have arbitrary bin structure.<sup>21</sup> Suprathermal electron bremsstrahlung is modeled by a parametrized fit to the bremsstrahlung spectrum,<sup>22</sup> which accounts for partial ionization. The suprathermal electrons produce frequency-dependent bremsstrahlung photons that are transported in LASNEX's radiation package. The suprathermals also contribute to the plasma pressure.

The nonlocal electron conduction package in LASNEX solves the electron conduction equation with a nonlocal heat flux that vanishes at the boundaries. This nonlocal package models the features of fully kinetic Fokker–Planck calculations. These features are a reduced heat flux in the hotter region of the heat front, a preheat foot, and nonisothermal, low-density corona. The nonlocal electron transport option is available in both one and two dimensions. The 1-D model solves finite difference equations. (For all 1-D models, LASNEX allows either spherical or planar configurations.) The 2-D nonlocal conduction uses the finite element machinery.

Often in laser-produced plasmas, the range of the hot electrons is much larger than the temperature or density scale lengths, which give rise to free streaming and nonlinearities in the heat conduction. The 1-D BGK<sup>24</sup> electron thermal conduction model accounts for free streaming effects in steep temperature gradients by evaluating the electron distribution within the plasma via the BGK approximation to the Fokker–Planck equation. The resulting distribution is then used to evaluate the heat flux in the plasma.<sup>25</sup> A distribution function approach was developed because other models were unable to account reliably for the nonlocal electron heat transport.<sup>26</sup> The BGK approximation is used to improve the speed of the algorithm over a direct solve of the Fokker–Planck equation. Nevertheless, iteration of the algorithm is necessary to calculate the electric field, insuring charge neutrality and particle and energy conservation, neither of which is explicitly guaranteed by a blind application of the BGK approximation.

A package for hybrid electron transport (HET) is being developed to incorporate 2-D electromagnetic effects into electron transport. The model draws heavily on the ideas of Rodney Mason, associated with 2-D implicit plasma simulations.<sup>27</sup> The algorithm is designed to incorporate particle and/or fluid electrons—the particles would represent hot electrons generated by plasma processes, and the fluid electrons

would represent the background thermal electrons. Currently, only the field solver and the thermal electron parts of the package are implemented. The package accounts for electron transport via a generalized Ohm's law<sup>28</sup> which includes all of the Braginskii coefficients, <sup>29</sup> including the Hall and Nernst terms. For heat transport, the package also includes all of the Braginskii coefficients, including the Righi–Leduc term. Because the electric field is also important in transport, a field solver for Maxwell's equations, including the displacement current, was written that goes beyond the MHD approximation used in the present magnetic field package in LASNEX.<sup>30</sup> The MHD approximation assumes charge neutrality in the plasma which results in the displacement current being ignored. The HET package does not ignore the displacement current and therefore is not charge neutral. HET also does not ignore  $\partial j/\partial t$ . The fields are represented by continuous finite elements; the electric current is represented by discontinuous finite elements. The effects on transport using this model are already dramatic. In some situations the spontaneously generated magnetic field magnetizes the electrons with the result that thermal transport is inhibited. Improved results for laser-heated foil experiments have been noted.<sup>31</sup>

#### **Ions**

Thermal ions are assumed to be in a Maxwellian distribution. Flux limited diffusion methods are used to mix spatially different types of ions and to transport the ion thermal energy. Ion conduction uses the same ICCG method to solve the diffusion matrix as the electron conduction package. Real ion viscosity (momentum diffusion) is optionally included in the hydrodynamics equations, although it is typically small by comparison with the usual artificial viscosity.

The ions affect the material hydrodynamic motion by contributing to the pressure. Hydrodynamic work, including that done by the artificial viscosity, and the thermonuclear reactions heat the ions. The heat exchange with the electrons limits the ion temperature. The ion temperature is important for three practical reasons: (1) the thermonuclear fusion reaction rate is very sensitive to  $T_i$ ; (2)  $T_i$  controls the Coulomb logarithm used to calculate laser absorption by inverse bremsstrahlung and electron thermal and electrical conduction; and (3)  $T_i$  determines the Doppler contributions to the width of spectral lines, which can be important for x-ray laser designs.

#### Radiation

Radiative energy flow is one of the principal means of coupling laser energy into a target. Because of its importance in ICF, LASNEX has several methods

for calculating radiation transport: single group flux limited diffusion, multigroup flux limited diffusion using either finite difference or finite element solution scheme, 1-D spherical harmonic expansion of the transport equation, 1-D discrete-ray transport, and detailed radiation transport.

Single group flux limited diffusion assumes that the photons are in a Planck distribution characterized by a local radiation temperature. This method uses only Rosseland mean opacities and is valid if the system is thick to radiation.

Multigroup flux limited radiation diffusion assumes nearly isotropic photon distributions and allows for arbitrary frequency dependence. Frequency-dependent opacity data is required. The diffusion algorithm to model multigroup radiation diffusion can be treated by either the finite difference approximation or the finite element method,<sup>32</sup> similar to the electron diffusion. The ICCG linear system solver is employed in both schemes. By default, the finite difference and finite element models use an iterative scheme to couple the radiation energy to the matter.<sup>33</sup> A "partial temperature" coupling scheme which is often much faster (see Ref. 42) is also available for use, but it can give large swings of the intermediate values of the electron temperature during a single timestep, decreasing accuracy. Accuracy is controlled by reducing the timestep until the swings in the partial temperature are acceptable. However, this can result in very small timesteps. The recommended radiation electron coupling scheme is differenced implicitly in time; in steady state, it will relax to the correct answer in one step. This method, related to a scheme of Axelrod and Dubois, 34 may be thought of as a form of alternating-direction implicit iteration, in which one direction corresponds to photon energy and the other to spatial location. In certain circumstances, particularly when the timestep is large and the rates associated with transport and radiation-matter coupling are similar, the convergence can be quite slow. We have a convergence-acceleration scheme for use in these unusually stiff cases.<sup>35</sup> Shestakov et al.<sup>36</sup> describe test problems in radiative transfer and compare finite difference and finite element solutions to the radiation diffusion equations, illustrating the use of analytic solutions to validate the results of computer simulations.

Photon Compton scattering and its resulting energy exchange with electrons is also treated in LASNEX. To model relativistic Compton scattering, we evaluate the Compton scattering kernel by averaging the Klein–Nishina cross section over a relativistic Maxwellian distribution.<sup>37</sup> This scattering kernel is then integrated over all directions to obtain the transfer matrix used to solve the Boltzmann equation for isotropic photon distributions.<sup>38</sup> Finally, one can make the Fokker–Planck approximation which assumes that the photon frequency shift is small compared with the

photon frequency.<sup>39</sup> LASNEX can do Compton energy exchange by either the Boltzmann or Fokker–Planck methods. The Fokker–Planck method is finite differenced in a way that obtains exact steady-state results.<sup>40</sup> Since x-ray mean free paths are often comparable to the size of ICF targets, the diffusion approximation is not appropriate and we must solve the transport equation.

LASNEX has a 1-D (either spherical or slab)  $P_n$ radiation transport package in which the photon angular distribution is expanded in spherical harmonics where  $P_l$  is the coefficient of the *l*th Legendre polynomial.<sup>41</sup> The radiation transport equation is written as an infinite set of coupled equations for the  $P_1$ 's. Rather than terminating this infinite set at the *l*th moment by zeroing out  $P_{l+1}$ , Kershaw improved the results of the  $P_n$  calculation by setting  $P_{l+1}$  to a value within its bounds. Probability theory is used to calculate the upper and lower bounds. The 1-D  $P_n$  package uses the same relativistic Compton methods described earlier to evolve the 0th (isotropic) moment. Other moments only undergo Thompson scattering with no frequency shift. The  $P_n$  package couples the photon energy to matter using the "partial temperature scheme." <sup>42</sup> The 1-D  $P_n$  radiation transport has been useful both in actual design calculations and in testing the accuracy of various extensions to the diffusion theory.

Radiation transport in LASNEX is also modeled by a 1-D discrete-ray method. 43 It consists of solving the finite difference equations for the radiation intensity for a few selected directions. The total intensity at any point in space is the sum over the intensities of each of the discrete directions weighted in some consistent way, for example, by the fraction of the solid angle that each ray represents. We difference the radiation transport equation using upstream, implicit differencing, and we couple the radiation energy with matter by iteration using the multifrequency gray approximation.<sup>44</sup> A persistent problem with the Lund–Wilson scheme has been the accuracy in the thermal wave limit, when the zones are many mean free paths thick. LASNEX also has a 1-D, discontinuous finite element radiation transport package, bilinear in space and photon direction, which behaves correctly in the thermal wave limit.<sup>45</sup> The radiation transport equation has upwinded, discontinuous elements; the electron temperature equation has continuous elements. The resulting linear equations are solved by a modified splitting of the intensity and temperature parts. There is an optional Newton iteration for problems where the nonlinearity of the Planckian function is significant over a single timestep. In this, the Compton scattering is treated nonrelativistically, including scattering only in angle (Thomson scattering).

All radiation transport models deposit momentum when a photon is absorbed or scattered. In the Atomic Physics section, we describe the derivation of the

frequency-dependent radiative opacities used in the photon transport packages. Basically, we include bound-bound, bound-free, and free-free processes in either local thermodynamic equilibrium (LTE) or non-LTE. The frequency-dependent radiation intensity that escapes from a LASNEX mesh is often a very valuable problem diagnostic to compare with corresponding experimental spectra.

#### Lasers, Ion Beams, and Other Sources

A LASNEX calculation can be driven by several different types of sources and/or boundary conditions. Some sources, such as temperature, pressure, frequency-dependent radiation intensity, and velocity are imposed arbitrarily, while the beam deposition sources interact with the plasma in a more complete and physically consistent manner. Lasers and ion beams are calculated by tracking a number of rays through the spatial mesh. Power on the ray is decremented as deposition occurs. The temporal and spatial variations of all the possible sources can be specified by the users.

In 1983, a 3-D laser ray tracing package was added to LASNEX.  $^{46}$  Prior to this, all light rays were forced to travel in the (r,z) plane, which often created anomalously high intensities near the symmetry axis. The 3-D laser package computes the trajectories of an arbitrary set of laser rays through the mesh. The rays are bent according to the laws of refraction. Ray trajectories are computed using the gradient-index geometrical-optics equations. On the basis of computed ray path lengths, energy is deposited in each zone by inverse bremsstrahlung, including nonlinear corrections.  $^{47}$  The laser energy is also absorbed by a photoionization model based on the Saha equation.  $^{48}$ 

Noncollisional processes—plasma instabilities and resonance absorption—are modeled by angle-dependent absorption<sup>49</sup> or more simply by absorbing a given fraction of the energy that is left in each ray at its turning point. The ray intensity is correspondingly attenuated. When suprathermal electrons are present, absorption by the noncollisional process creates an electron distribution with a "hot" temperature derived from fits to plasma simulations.<sup>50</sup>

Typically, the LASNEX computational mesh is too course to resolve steep, inhomogeneous plasma-density structures that might arise from uneven illumination or hydrodynamic instabilities. Therefore, the code has a statistical model of the refractive scattering of laser light by random density fluctuations in the subcritical plasma. The scattering can occur along the entire ray path or only at the turning point. The hydrodynamic effect of the laser light is included with a ponderomotive force algorithm which has both scalar and tensor terms. 52

Since LASNEX tracks a finite number of rays through the mesh, we often see "ray effects," causing

the laser intensity to vary unphysically. A "fatray" package smoothes the laser energy deposition, using a finite element diffusion equation. This will not cause energy to be deposited past the critical surface because the smoothing takes place only for regions where the electron density is less than or equal to the critical electron density. Another option to decrease the ray effects (which we call "smearing") is to average the deposition over two zones each time it is applied, and it can be applied any number of times. The user has some directional control by choosing to apply the smearing along particular logical mesh lines.

Charged-particle beam deposition is calculated from stopping-power formulas that account for straggling and partial ionization.<sup>54</sup> We have made calculations from first principles of the dynamic charge state of a fast, heavy ion as it experiences various ionization and recombination processes while slowing down in a heated target material.<sup>55</sup> The important processes are collisional ionization balanced at equilibrium by radiative recombination.

Ion beams do not refract as light does. Therefore, we have a separate, simpler and faster ray trace package for ions. It assumes only straight ray paths in 3-D, which become hyperbolae when projected onto the (r, z) plane.<sup>56</sup> Momentum deposition from ion beams is implemented consistently.

For moderately intense, ultrashort pulse lasers, we have a subroutine which actually solves Maxwell's equations in 1-D, rather than using a ray trace approximation.<sup>57</sup> The algorithm takes advantage of the rapid oscillation and propagation of light waves compared with hydrodynamic motion. Thus, the steady-state 1-D solution to Maxwell's equations results in the Helmholtz equations. Both *s*- and *p*-polarized cases are accounted for by the package. Plasma waves are generated at the critical surface in the case of *p*-polarized light. To account for losses due to plasma waves without explicitly following the waves in the plasma, the total collision rate is modified in the resonance region to be the sum of: the electron–ion collision rate + the Landau damping rate at the critical point + the rate at which plasma waves leave the resonance region + the loss rate due to the wavebreaking of the plasma waves.<sup>57</sup> To maintain consistency, the algorithm automatically incorporates a WKB approximation in the low-density blow-off region when the low-density zone sizes approach the laser wavelength. The frequency-dependent conductivity has been improved to go beyond the Drude approximation and results in improved modeling of absorption in solids.

#### **Burn Products**

LASNEX calculates all significant thermonuclear reactions among isotopes of H, He, Li, Be, and B.<sup>58</sup>

Charged particles and neutrons produced are transported by multigroup diffusion methods that take into account nuclear scattering, in-flight reactions, and momentum deposition.<sup>59</sup> Gamma rays produced by inelastic nuclear interactions are also transported by multigroup diffusion, accounting for Compton scattering, photoionization, and pair production.<sup>60</sup> The neutron and gamma diffusion both use a multigroup extension of Levermore's diffusion method.<sup>61</sup> The charged particle transport is an extension of diffusion that retains particle inertia as it undergoes straight-line energy loss to electrons.<sup>62</sup> Charged particle energy loss rates include the effects of an arbitrary ratio of particle to electron thermal velocity, Fermi degenerate electrons, and bound electrons.<sup>63</sup> All burn products either escape from the problem, providing numerous diagnostic opportunities, or deposit their energy back into the thermal electron and ion fields.

### Magnetic Fields

Magnetic fields are generated automatically in 2-D problems or can be imposed by user-specified sources. The magnetic field package<sup>64</sup> in LASNEX includes J×B forces and the full Braginskii cross-field transport model. The Braginskii model has been extended with the Lee and More conductivities and includes the magnetic diffusion, Nernst, grad P, grad T, and Hall terms in Ohm's law, as well as the perpendicular and Righi–Leduc heat flows, j•E, and other terms in the heat equation. The user may optionally specify source terms that self-consistently couple the plasma to an external LRC circuit.

If requested, the magnetic package modifies the electrical conductivity to account for the anomalous resistivity due to lower-hybrid waves. Periodic boundary conditions are available for the study of multimode Rayleigh–Taylor (RT) perturbations. The energy conservation has been improved (order-of-magnitude improvement for 1-D, purely-Lagrangian calculations) and the magnetic flux is conserved during mesh rezoning. These enhancements, together with new, high-resolution rezoning schemes, programmed by the users with the Basis interface, have allowed the successful modeling of high-energy, radiating z-pinches. Features typically exhibited in these simulations are the strong nonlinear growth of magnetic RT modes, 65 and the formation of hot spots<sup>66</sup> near the axis due to unstable (m = 0) sausage modes.

Also, magnetic fields can be spontaneously generated in the presence of nonparallel temperature and density gradients which may occur in laser-produced plasmas. The resulting changes in the magnetic-field-dependent transport coefficients for all charged particles may significantly alter the plasma temperature and pressure profiles. This may be an important

effect in the design of some hohlraums or direct-drive targets which require a high degree of symmetry and efficient utilization of laser power.

#### **Atomic Physics**

The atomic physics models in LASNEX supply the equation-of-state (EOS) variables (e.g., pressure and energy as a function of temperature and density) used in the hydrodynamics, the degree of ionization used to establish various electron collisional rates, and the frequency-dependent opacities used by the radiation transport routines. In LTE, these quantities are functions only of the density and electron temperature and can be conveniently tabulated or evaluated by analytic expressions. LASNEX can access the internal Lawrence Livermore National Laboratory (LLNL) EOS data and the Los Alamos National Laboratory (LANL) Sesame data,<sup>67</sup> and it can use its own quotidian EOS (QEOS) package.

The QEOS<sup>68</sup> is an in-line EOS routine that is based on the Thomas–Fermi electron-gas approximation. The QEOS total energy is split up into three parts:

$$E_{\text{tot}}(\rho, T) = E_{\text{e}}(\rho, T) + E_{\text{b}}(\rho) + E_{\text{n}}(\rho, T) \tag{1}$$

where  $E_{\rm e}$  is the Thomas–Fermi (TF) energy,  $E_{\rm b}$  is an analytic (Cowan) bonding correction used to fit the experimentally known solid density and bulk modulus at standard temperature and pressure, and  $E_{\rm n}$  is the nuclear motion energy. It provides separate EOSs for electrons and ions. Since QEOS is based on a free energy, thermodynamic consistency is guaranteed, and the smooth TF term together with the analytic ion part generate continuous results from cold solid conditions through the liquid, vapor, and plasma states. The Z-scaling property of the TF model allows a single table to generate data for any element as well as provide the speed necessary for an in-line calculation.

LASNEX can also access LTE frequency-dependent opacity data in three different formats: it reads Cray binary files of opacity information in a format unique to LASNEX designed 20 years ago; it reads the LANL Paradise<sup>69</sup> opacity files; and it reads the LLNL machine independent opacity files,<sup>70</sup> using the portable data file (PDB) library of Stewart Brown.<sup>71</sup>

In non-LTE, the EOS, degree of ionization, and the opacity must be determined from the atomic populations which are found by solving rate equations and, in general, depend on the photon and suprathermal electron distribution functions. LASNEX has incorporated three major atomic physics packages, XSN, SCA, and DCA, which can be run in either LTE or non-LTE modes. All three provide LASNEX with pressure, energy, and frequency-dependent opacity and emissivity due to bound-bound, bound-free, and free-free processes.

XSN<sup>72</sup> is an average atom, atomic physics code that uses a simple Z-scaled, screened hydrogenic model to perform in-line calculations of arbitrary mixtures at all temperatures and densities. It is used to obtain material opacities for LTE and non-LTE, as well as EOS values under non-LTE conditions. It includes the effects of Fermi degeneracy, continuum lowering, and pressure ionization, 73 which are required to correctly model cold solids at high densities and is designed to closely match the Thomas–Fermi ionization values along the cold curve. The lack of *l*-splitting and the simple line-width formulae limit the accuracy of the opacities to average values. However, XSN's simplicity does provide the required speed and allows any mixture to be treated. Since the EOS is based on a free energy, it is automatically thermodynamically consistent. The lack of a bonding correction means that XSN's pressures at low temperature are too high, but in most cases, non-LTE effects are small under those conditions, and this package would rarely be run.

The average-atom atomic physics package Statistical Configuration Accounting (SCA)<sup>74</sup> produces more accurate opacity information than the default XSN package because its underlying atomic physics data is evaluated off line by a self-consistent, relativistic, Hartree–Slater program, called LIMBO.<sup>75</sup> Because the database which LIMBO produces is based on relativistic physics, the resulting opacity which SCA produces shows fine-structure splitting. Whereas, fine-structure splitting can be included into an XSN opacity only in an ad hoc fashion. As in XSN, the atomic physics is simplified by using the hydrogenic approximation, where the states of an ion are described by the quantum numbers of a single electron which is immersed in a spherically symmetric screened Coulomb potential.

The Detailed Configuration Accounting (DCA) atomic physics package<sup>76</sup> solves rate equations for the number of ions in each important excited state in each ionization state. This package is more expensive than XSN or SCA. It is used when accurate atomic physics is needed for line diagnostics or x-ray laser modeling. DCA can handle any number of states connected by radiative and collisional bound-bound, bound-free, and auto-ionization and dielectronic recombination processes. The states and transition rates are specified in data files generated by other codes. Optionally, a simple screened hydrogenic model can be produced at problem initialization. In addition, the DCA package calculates Voigt line shapes due to Doppler, Lorentz, and Stark broadening and, if requested, handles line transfer by a general purpose escape probability method that reduces to 1-D, static or Sobolev limits in planar or cylindrical geometry.<sup>77</sup> It includes effects of Fermi degeneracy and handles pressure ionization and continuum lowering in the Stuart/Pyatt approximation<sup>78</sup> by reducing the statistical weight smoothly to

zero as continuum lowering ionizes the weakest bound electron. To save computer time, the levels which are eliminated by continuum lowering or which are ionization states of low probability are removed from rate calculations and from the system of rate equations. The resulting reduced linearized system is then solved by banded or iterative matrix methods.

Another relatively new feature of the LASNEX atomic physics package is a multiphoton, dielectric breakdown package which models multiphotonionization seeding of avalanche breakdown. The model is based on the work of Feit et al.<sup>79</sup> in which a simple seeded exponential model was inferred from their Fokker–Planck studies. The seed rate is proportional to an integral power of the energy density of the laser light in the material. In this process, the electron density will build until a threshold level is reached. Above the threshold, the material breaks down by electron avalanche, which is modeled by an electron distribution that exponentially increases in time. The avalanche is quenched when a maximum of one electron per ion is reached, justified by assuming that the ionization potential for the next electron to be removed increases substantially.

#### **User Interface**

LASNEX has been a pioneer in interactive and steered computations. Even in its early days (more than twenty years ago), the users were able to investigate and modify their simulations while they were running. Graphical displays and numerical edits of the problem could be produced at any time, allowing the users to ascertain quickly whether the problem was running correctly and efficiently. With the inclusion of the Basis code development system, 80 a huge leap in interactivity was achieved at once. The programmable interface provided by Basis transformed LASNEX into "a whole new generation of design code."81 It gives LASNEX a complete, up-to-date, well maintained, and well documented computer science interface, allowing users to innovate without the intervention of the code developers. The code developers no longer have to get involved with specific user requests for diagnostics or special purpose models, freeing them from straightforward but time-consuming tasks.

Basis has a fully featured, FORTRAN-like interactive programming language interpreter which can access the variables and functions in the LASNEX compiled code. Basis supplies an interface to a complete graphics package that includes curves, markers, contours, text, frame control, and viewport control, as well as LASNEX-specific plotting commands, such as mesh plots and mesh-based contour commands. Basis also offers many mathematical packages, such as Bessel functions, fast-Fourier transforms, randomnumber generators, and polynomial fitting.

One of the most important components of Basis is a history package that allows the user periodically to execute specified commands and/or to collect any number of sets of values of arbitrary expressions. A variety of mechanisms can be used to select the frequency at which these generations are collected. Users may also specify logical conditions under which actions will occur, such as the occurrence of bowties, a zone reaching a certain temperature, etc. The history package employs the portable database system (PDB)<sup>71</sup> to store the collected data. The Portable-Filesfrom-Basis (PFB) package of Basis gives the users a convenient interface to the data files.

LASNEX users now accomplish many tasks using the tools of the Basis system. They have automated the tedious chore of generating sets of similar problems by writing Basis functions to do the work. Instead of a user issuing instructions from the terminal for a discrete problem rezone, they now can use the Basis interpreter and history functionality to sense when the mesh is in trouble, decide what should be done, and execute the rezone. In this way, LASNEX provides user-controlled, automatic mesh refinement facilities.

In many processes the users can add their own models to work with or to replace those of LASNEX. To accommodate the users' new programming power, we have introduced many "user defined arrays," in which they calculate their own values for various

TABLE 1. Example of automatic rezoning.

#### **Problem Description:**

Whenever any zone becomes folded over on itself ("bowtied"), return the mesh to a given "good" configuration, perform the rezone (mesh overlay and remapping of all the LASNEX variables), and proceed.

The user must define the function that tests the LASNEX mesh for troubles (here bowties) and corrects it, if necessary. In this example the mesh is simply set back to the original configuration defined when r\_good and z\_good were declared. The "h" card tells when (i.e., at every cycle from 1 to 10000) the function, "test\_n\_rezone," should be invoked.

Note: the "#" symbol indicates that the following text is a comment.

#### The Basis Coding:

endf

```
real8 r_good = rt, z_good = zt # Declare "good" coordinates and
                               # equate to LASNEX's rt and zt.
h 1:10000:1 test n rezone
                               # At every cycle call the function
                               # test_n_rezone.
function test_n_rezone
                               # Function definition.
                              # Test for bowties.
 if(nbowt(rt,zt,ireg).ne.0) then
   prezone
                               # Execute LASNEX command to
                               # prepare for rezoning.
                               # Reset the LASNEX mesh to the
   rt=r_good
   zt=z_good
                               #"good" ones.
                               # Mesh overlay and remap physical
   rezone
                               # quantities.
 endif
```

LASNEX quantities. For example, a user can supply the material EOS by calculating, at each timestep, the electron pressure and its derivatives with respect to density and temperature, the electron energy and its derivatives, and the corresponding ion components. Similarly, a user can define the thermal conductivities, zonal energy sources, zonal energy leak rates, or zonal electron thermal flux limit multipliers. We continue to add more user-defined variables to the code to take advantage of this capability.

Another application of the Basis interpreter is to create self-tuning simulations or a self-optimizing series of simulations. As a calculation is running, the Basis interpreter can decide how well the design is working based on certain criteria. Then, for example, the laser pulse shape or spatial profile can be changed to satisfy the criteria better.

Table 1 provides an automatic rezoning example to illustrate how Basis works within LASNEX to save the designers' time and to allow many jobs to run to completion without user intervention.

## **Example Calculations**

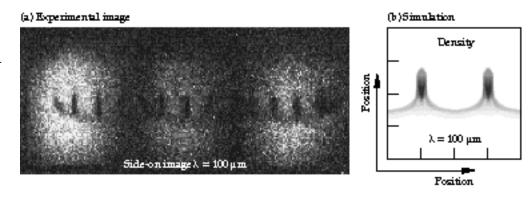
This section describes three ICF experiments simulated with LASNEX: a planar hydrodynamic instability experiment, a spherical hydrodynamic instability experiment, and a capsule implosion mix experiment. These examples illustrate that LASNEX can accurately model actual laboratory experiments.

## Planar Hydrodynamic Instability Experiment

A series of experiments was conducted with the Nova laser to measure hydrodynamic instabilities in planar foils accelerated by x-ray ablation.<sup>82</sup> We show results of a single-mode experiment and the corresponding LASNEX calculation. A low-density fluid pushing on a high-density fluid is RT<sup>83</sup> unstable, and perturbations on the surface between the fluids grow and take on a characteristic bubble and spike appearance. In these experiments, surface perturbations were imposed on one side of a foil that was mounted across a diagnostic hole in the wall of a cylindrical Au hohlraum. The foil was accelerated by the indirect x-ray drive generated by focusing eight pulse-shaped Nova beams into the hohlraum and was backlit with a large area spot of x-rays created by shining another Nova beam on discs of Mo, Rh, Sc, or Fe. Figure 3(a) shows the experimental image of a foil with 100-μm sinusoidal perturbations viewed side-on with a 2-D grated x-ray imager at 4.4 ns into the pulse. The foil has evolved into the classic bubble and spike shape characteristic of nonlinear RT instability. The LASNEX calculation Fig. 3(b) at 4.4 ns agrees with the experimental image. In fact, they are almost identical.

11 L D I III JICJ CODE I OK IVIODELING IC

FIGURE 3. (a) Results of perturbation growth experiment viewed side-on at a time of 4.4 ns. (b) Shaded density plot of the transmitted backlighter x-rays at 4.4 ns in the corresponding 2-D LASNEX simulation. (20-03-1293-4393pb02)



The 2-D LASNEX simulation used the time-dependent laser power that was measured in the experiment, tabular opacities created by a "first principles opacity" code, and tabular EOS data. The transmitted backlighter x-rays included the instrumental response.

## Spherical Hydrodynamic Instability Experiment

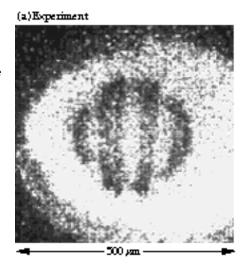
The next experiment was designed to study the physics of implosions with high RT growth factors. Using indirect drive, we imploded capsules with Germanium-doped ablators to minimize x-ray preheat and shell decompression and hence increased the inflight aspect ratios. X-ray backlit images of the capsule implosion were recorded at 4.7 keV with 55 ps and 15-µm resolution. Three parallel 3-µm-deep grooves were machined in the ablator to seed the instability. One groove encircled the center of the target; the other two were parallel and on opposite sides. Figure 4 showsthe backlit image of the capsule from the experiment and the LASNEX calculation at 2.22 ns to be virtually identical. <sup>84</sup> The grooves machined into the ablator for this experiment were not uniformly

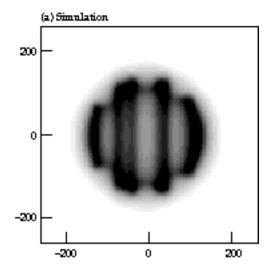
spaced—the one on the right was closer to the center; the effect of this is seen in both the experiment and code results. The groove on the left being farther from the center allowed a double ridge to be created as the perturbation amplitude grew from each groove. This did not occur on the right side, where the grooves were closer and the RT growth from the central and right-hand grooves merged into just one modulation. The LASNEX simulation was a standard 2-D calculation. It was able to accommodate many zones while still properly modeling the radiation by using a special method of weighting opacities that allows a faster convergence with a much smaller number (typically 5 or 6 compared with 50 to 100) of photon groups compared with the standard Rosseland weighted mean.<sup>85</sup>

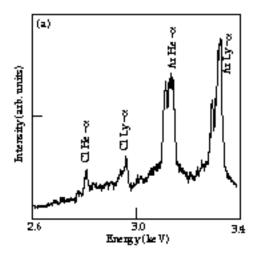
## Capsule Implosion Mix Experiment

This experiment addressed the issue of the hydrodynamic stability of the imploding fuel capsule. Experiments on Nova were performed to study how imperfections on the capsule surface grow by RT instability into large perturbations that cause pusher–fuel mix and degrade the capsule performance.<sup>86</sup> To diagnose

FIGURE 4. Backlit image of grooved Ge-doped imploded capsule at 2.2 ns into the pulse. Both the experimental data on the left and the LASNEX results on the right show the growth of the modulation. (40-00-1196-2730pb01)







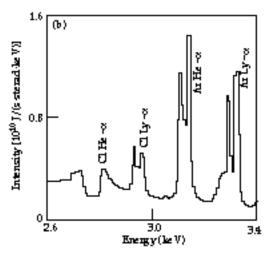


FIGURE 5. Spectra at peak x-ray emission in units of  $10^{10}$  J/s/sterad/keV from the implosion of a smooth surface capsule. (a) The experimental streaked crystal spectrometer data. (b) The 1-D DCA LASNEX simulation result. Relevant emission lines of Cl (the pusher dopant) and Ar (the fuel dopant) are labeled. (20-03-0795-1850pb02)

the enhanced mix, x-ray emission spectra of trace elements in the pusher (Cl) and fuel (Ar) were measured as the surface roughness increased. (Figure 5 shows example spectra.) The emission of the pusher dopant relative to the fuel dopant did increase with surface roughness as the cold pusher mixed more thoroughly with the hot fuel, due presumably to RT instabilities (see Fig. 6). Simulating the implosion of these capsules was a multistep process, employing both 1- and 2-D LASNEX calculations. The 2-D calculations were used to estimate linear growth for single-perturbation modes. The surface roughness and the linear

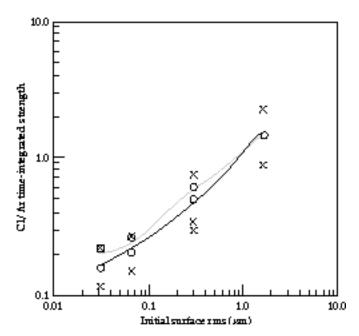


FIGURE 6. The ratio of the time-integrated Cl and Ar Lyman–alpha emission lines is plotted vs the initial surface roughness. An X (O) marks each experimental (simulation) point. The black (gray) lines connect the average values of the experimental (simulated) data at each distinct initial surface rms. (08-00-0996-2154pb01)

perturbation growth factors combined with Haan's<sup>87</sup> nonlinear saturation prescription were used to calculate the time-dependent width of the mix region. In 1-D implosion simulations with LASNEX, material was atomically mixed and thermal transport enhanced over a distance about the fuel–pusher interface, according to the width of the mix region.

Emission spectra were generated with the DCA atomic physics package. As seen in Fig. 6, the LASNEX results for the ratio of time-integrated Cl to Ar Lymanalpha emission agrees well with the experimental results. The trend of increased mix for rougher surfaces is very apparent. The experimental spectra and the spectra calculated by LASNEX also match as seen in Fig. 5.

## Acknowledgments

The extensive references in this article illustrate the number of scientists that have worked on LASNEX. In addition to George Zimmerman who originated LASNEX, we would like to acknowledge all those who have also contributed to it: Roberta Allsman, Harry Bruestle, Lee Busby, Paul Dubois, Art Edwards, Alex Friedman, Fred Fristch, David Kershaw, Jim Kohn, Zane Motteler, Dale Nielsen, Paul Nielsen, Jeff Painter, Manoj Prasad, Rich Sacks, Alek Shestakov, Al Springer, Lynd Stringer, Janet Takemoto, Susan Taylor, Sharon Wilson, and Brian Yang. The support and encouragement of John Nuckolls and Lowell Wood were instrumental in its early development and application. We also acknowledge the continuing support by division leaders from A, CP, and X-Divisions—from Peter Moulthrop and Bill Lokke through Dave Nowak, Dan Patterson, and Mordy Rosen. Feedback from the LASNEX users has also been invaluable, ranging from their encouragement and clever ideas to bug reports and complaints.

IJIVLA 112 D I III JICJ CODE I OK IVIODELINO IC.

#### **Notes and References**

- J. Nuckolls, L. Wood, A. Thiessen, and G. B. Zimmerman, Nature, 239, 5368, pp. 139–142 (1972).
- G. B. Zimmerman and W. L. Kruer, comments in *Plasma Physics and Controlled Fusion* 2, 51 (1975).
- G. B. Zimmerman, Laser Programs Annual Report, 3–71, Lawrence Livermore National Laboratory, Livermore, CA, UCRL-50021-80 (1980).
- P. F. Dubois, "Making Applications Programmable," Computers in Physics 8(1), Jan–Feb 1994.
- W. Schultz, Methods in Computational Physics (Academic Press New York, 1970), vol. 3, p. 1.
- 6. M. L. Wilkins, Meth. Comp. Physics 3, 211 (1964).
- 7. F. W. Harlow and A. A. Amsden, J. Comp. Phys. 16, 1 (1974).
- 8. D. S. Bailey, *Laser Programs Annual Report*, 3–57, Lawrence Livermore National Laboratory, Livermore, CA, UCRL-50021-84 (1984).
- M. L. Wilkins, "Calculation of Elastic-Plastic Flow" in Methods in Computational Physics, Bernie Alder, Sidney Fernbach, and Manuel Rotenberg, Eds. (Academic Press, New York, NY, 1964).
- S. I. Braginskii, "Transport Processes in a Plasma," in Reviews of Plasma Physics, M. A. Leontovich, Ed. (Consultants Bureau, N.Y. 1965), vol. 1, p. 205.
- Y. T. Lee and R. M. More, *Phys. Fluids* 27, 1273 (1984); Y. T. Lee, R. M. More, and G. B. Zimmerman, "A New Electron Transport Model for LASNEX," *Laser Programs Annual Report*, 3–61, Lawrence Livermore National Laboratory, Livermore, CA, UCRL-50021-81 (1981).
- N. A. Krall and A. W. Trivelpiece, Principles of Plasma Physics (McGraw–Hill, New York, 1973) p. 317.
- J. M. Ziman, Principle of Theory of Solids (Cambridge University Press, Cambridge, England, 1964).
- D. S. Kershaw, J. Comp. Phys. 26, (1978); Ibid., 38, 114 (1978); Idem, "Solution of Single Tridiagonal Linear Systems and Vectorization of the ICCG Algorithm on the Cray-1," in Parallel Computations, (Academic Press, New York, NY, 1982; Idem, Laser Programs Annual Report, 3–77, 3-79, Lawrence Livermore National Laboratory, Livermore, CA, UCRL-50021-79 (1979); Ibid., 3–67, UCRL-50021-81 (1981).
- G. J. Pert, J. Comp. Phys. 42, 20 (1981); D. S. Kershaw, Laser Programs Annual Report, 4–52, Lawrence Livermore National Laboratory, Livermore, CA, UCRL-50021-76 (1976); Idem, "Differencing of the Diffusion Equation in LASNEX," Lawrence Livermore National Laboratory, Livermore, CA, UCRL-82747 (1980); Idem, J. Comp. Phys. 39, 2, 375 (1981).
- A. I. Shestakov, J. A. Harte, and D. S. Kershaw, J. Comp. Phys. 76(2),385 (1988).
- This document describes the electron-ion coupling model in LASNEX: D. C. Eder, "Electron-Ion Coupling in LASNEX," Lawrence Livermore National Laboratory, Livermore, CA, UCID-21544 (1988).
- D. W. Forslund, J. M. Kindel, and K. Lee, *Phys. Rev. Lett.* 39, 284 (1977); K. Estabrook and W. L. Kruer, *Phys. Rev. Lett.* 40, 42 (1978) .
- D. S. Kershaw, "Interaction of Relativistic Electron Beams with High-Z Plasmas," UCRL-77047 (1975); *Idem, Laser Programs* Annual Report, 3–69, Lawrence Livermore National Laboratory, Livermore, CA, UCRL-50021-78 (1978); *Idem*, Lawrence Livermore National Laboratory, Livermore, CA, UCRL-83494 (1979); *Idem*, "Computer Simulation of Suprathermal Transport for Laser Fusion," *Laser Programs Annual Report*, 3–78, Lawrence Livermore National Laboratory, Livermore, CA, UCRL-50021-80 (1980).
- J. A. Harte and R. M. More, Laser Programs Annual Report, 3–66, Lawrence Livermore National Laboratory, Livermore, CA, UCRL-50021-82 (1982).

- 21. J. A. Harte and D. S. Kershaw, *Laser Programs Annual Report*, 3–63, Lawrence Livermore National Laboratory, Livermore, CA, UCRL-50021-81 (1981).
- 22. I. J. Feng and R. H. Pratt, "Parameterization of the Bremsstrahlung Spectrum," University of Pittsburgh, Internal Report, PITT–266 (1981); J. A. Harte and Y. T. Lee, Laser Programs Annual Report, 3–64, Lawrence Livermore National Laboratory, Livermore, CA, UCRL-50021-82 (1982).
- M. K. Prasad and D. S. Kershaw, Phys. Fluids B 1, 2430 (1989); Ibid., 3, 3087 (1991).
- P. L. Bhatnagar, E. P. Gross, and M. Krook, *Phys. Rev.* 94, 511 (1954); M. Krook, *J. Fluid Mech.* 6, 523 (1959).
- G. Ecker, Theory of Fully Ionized Plasmas (Academic Press, New York, NY, 1972); I. P. Shkarofsky, T. W. Johnston, and M. P. Bachynski, The Particle Kinetic of Plasmas, (Addison–Wesley, Reading, Massachusettes, 1966).
- J. F. Luciani, P. Mora, and R. Pellat, *Phys. Fluids* 28, 835 (1985); J. R. Albritton, E. A. Williams, I. B. Bernstein, and K. P. Swartz, *Phys. Rev. Lett.* 57, 1887 (1986); M. Prasad, and D. Kershaw, *Phys. Fluids B* 1, 2430 (1989).
- R. J. Mason, J. Comp. Phys. 71, 429 (1987); R. J. Mason, "Hybrid and Collisional Implicit Plasma Simulation Models," in Multiple Time Scales, J. U. Brackbill and B. I. Cohen, Eds. (Academic Press, Reading, MA, 1985).
- 28. T. J. M. Boyd and J. J. Sanderson, *Plasma Dynamics* (Barnes & Noble, Inc., New York, NY, 1969).
- S. I. Braginskii, "Transport Processes in a Plasma," in *Reviews of Plasma Physics*, M. A. Leontovich, Ed. (Consultants Bureau, New York, NY, 1965), vol. 1, p. 205.
- 30. P. D. Nielsen and G. B. Zimmerman, "Treatment of Theta–Directed Magnetic Fields in LASNEX," Lawrence Livermore National Laboratory, Livermore, CA, UCRL-53123 (1981).
- 31. J. H. Hammer, Lawrence Livermore National Laboratory, Livermore, CA, private communication (1996).
- A. I. Shestakov, J. A. Harte, D. S. Kershaw, J. Comp. Phys., 76, 2, 385 (1988); A. I. Shestakov, "Radiation Diffusion with the Finite-Element Method," Laser Programs Annual Report, Lawrence Livermore National Laboratory, Livermore, Ca, UCRL-50021-85 (1985); Idem, Laser Programs Annual Report, 2–94, Lawrence Livermore National Laboratory, Livermore, CA, UCRL-50021-86 (1986).
- A. Friedman and D. S. Kershaw, Laser Programs Annual Report, 3–68, Lawrence Livermore National Laboratory, Livermore, CA, UCRL-50021-82 (1982).
- T. S. Axelrod, P. F. Dubois, and C. E. Rhoades, Jr., J. Comp. Phys. 54, 204 (1984).
- A. Friedman, Laser Programs Annual Report, 3–62, Lawrence Livermore National Laboratory, Livermore, CA, UCRL-50021-83 (1983).
- 36. A. I. Shestakov, D. S. Kershaw, and G. B. Zimmerman, *Nuclear Science and Engineering* **105**, 88 (1990).
- D. S. Kershaw and M. K. Prasad, Laser Programs Annual Report, 2–73, Lawrence Livermore National Laboratory, Livermore, Ca, UCRL-50021-85 (1985).
- D. S. Kershaw, Laser Programs Annual Report, 2–96, Lawrence Livermore National Laboratory, Livermore, CA, UCRL-50021-86 (1986); A. I. Shestakov, D. S. Kershaw, M. K. Prasad, and G. B. Zimmerman, Ibid., 2–89 (1987); A. I. Shestakov, D. S. Kershaw, and M. K. Prasad, J. Quant. Spectrosc. Radiat. Transfer 40(5), 577 (1988).
- 39. M. K. Prasad, A. I. Shestakov, D. S. Kershaw, and G. B. Zimmerman, J. Quant, Spectrosc. Radiat. Transfer 40(1), 29 (1988).
- 40. C. D. Levermore, Discretization Methods for Fokker–Planck Operators, UCRL-91396 (August 1984).

- D. S. Kershaw, "Flux Limiting on Nature's Own Way," Lawrence Livermore National Laboratory, Livermore, CA, UCRL-78378 (1976); *Idem, Laser Programs Annual Report*, 4–56, Lawrence Livermore National Laboratory, Livermore, CA, UCRL-50021-76 (1976).
- A. I. Shestakov, J. A. Harte, and D. S. Kershaw, "Solution of the Diffusion Equation by Finite Elements in Lagrangian Hydrodynamic Codes," 2, Lawrence Livermore National Laboratory, Livermore, CA, UCRL-95066 (1986).
- B. G. Carlson, "The Numerical Theory of Neutron Transport," in Methods in Computational Physics (Academic Press, New York, 1963) vol. 1.
- C. M. Lund and J. R. Wilson, "Some Numerical Methods for Time-Dependent Multifrequency Radiation Transport Calculations in One Dimension," Lawrence Livermore National Laboratory, Livermore, CA, UCRL-84678 (1980).
- D. S. Kershaw, Laser Programs Annual Report, 2–78, Lawrence Livermore National Laboratory, Livermore, CA, UCRL-50021-85 (1985); J. F. Painter, "Finite Element Radiation Transport in One Dimension," Lawrence Livermore National Laboratory, Livermore, CA, UCRL-MI-119254 (1994).
- A. Friedman, Laser Programs Annual Report, 3–51, Lawrence Livermore National Laboratory, Livermore, CA, UCRL-50021-83 (1983); Idem, "Calculation of Laser Light Transport on a Lagrangian R–Z Mesh," Lawrence Livermore National Laboratory, Livermore, CA, UCRL-93644 (1985).
- A. B. Langdon, *Phys. Rev. Lett.* 44, 575 (1980); V. P. Silin, *Sov. Phys.*–ETP 20, 1510 (1965).
- Ya. B. Zel'dovich and Yu. P. Raizer, Physics of Shock Waves and High Temperature Hydrodynamic Phenomena (Academic Press, New York, NY, 1966) vol. I, chp. V, p. 265; D. Eder, Lawrence Livermore National Laboratory, private communication (1995).
- D. S. Bailey, Laser Programs Annual Report, 2–91, Lawrence Livermore National Laboratory, Livermore, CA, UCRL-50021-75 (1975).
- K. Estabrook, J. Harte, and D. Bailey, Laser Programs Annual Report, 3–31, Lawrence Livermore National Laboratory, Livermore, CA, UCRL-50021-78 (1978).
- A. Friedman and E. A. Williams, Laser Programs Annual Report, 3–61, Lawrence Livermore National Laboratory, Livermore, CA, UCRL-50021-84 (1984).
- J. Harte, Laser Programs Annual Report, 4–31, Lawrence Livermore National Laboratory, Livermore, CA, UCRL-50021-77 (1977); J. Harte and G. Zimmerman, "Ponderomotive Force in a Hydrodynamic Simulation Code," Lawrence Livermore National Laboratory, Livermore, CA, UCRL-79860 (1977).
- M. K. Prasad, Lawrence Livermore National Laboratory, Livermore, CA, private communication.
- R. M. More and D. S. Bailey, Laser Programs Annual Report, 2–72, Lawrence Livermore National Laboratory, Livermore, CA, UCRL-50021-79 (1979).
- D. S. Bailey, Y. T. Lee, and R. M. More, Laser Programs Annual Report, 3–64, Lawrence Livermore National Laboratory, Livermore, CA, UCRL-50021-81 (1981).
- A. I. Shestakov, Lawrence Livermore National Laboratory, Livermore, CA, private communication.
- W. E. Alley, *ICF Quarterly Report* 2(4), 160–165, Lawrence Livermore National Laboratory, Livermore, CA, UCRL-LR-105821-92-4 (1993).
- R. M. White, D. A. Resler, and S. I. Warshaw, "Evaluation of Charged-Particle Reactions for Fusion Applications," Proc. of the Int'l. Conf. Nuclear Data for Science and Technology, S. M. Qaim, Ed. (Julich, Germany, 1991) p. 834; M. J. Harris, W. A. Fowler, G. R. Caughlan, and B. A. Zimmerman, Ann. Rev. Astron. Astrophys. 21, 165 (1983); G. B. Zimmerman, Laser Programs Annual Report, 3–64, Lawrence Livermore National Laboratory, Livermore, CA, UCRL-50021-83 (1983).

 R. J. Howerton, R. E. Dye, and S. T. Perkins, "Evaluated Nuclear Data Library," Lawrence Livermore National Laboratory, Livermore, CA, UCRL-50400, vol. 4, Rev. 1 (1981) .

11 2 D I III OICO CODE I OK IVIODELING ICI

- 60. D. E. Cullen, M. H. Chen, J. H. Hubbell, S. T. Perkins, E. F. Plechaty, J. A. Rathkopf, and J. H. Scofield, "Tables and Graphs of Photon-Interaction Cross Sections from 10 eV to 100 GeV Derived from the LLNL Evaluated Photon Data Library (EPDL)," Lawrence Livermore National Laboratory, Livermore, CA, UCRL-50400, vol. 6, Rev. 4 (1989).
- 61. C. D. Levermore and G. C. Pomraning, *The Astrophysical Journal* **248**, 321 (1981).
- G. B. Zimmerman, Laser Programs Annual Report, 3–76, Lawrence Livermore National Laboratory, Livermore, CA, UCRL-50021-79 (1979); E. G. Corman, W. E. Loewe, G. E. Cooper, and A. M. M. Winslow, Nuclear Fusion 15, 377 (1975).
- G. B. Zimmerman, "Recent Developments in Monte Carlo Techniques," 6–7, Lawrence Livermore National Laboratory, Livermore, CA, UCRL-JC-105616 (1990).
- 64. P. D. Nielsen and G. B. Zimmerman, "Treatment of Theta-Directed Magnetic Fields in LASNEX," Lawrence Livermore National Laboratory, Livermore, CA, UCRL-53123 (1981); P. D. Nielsen, "A Computational Investigation of the Limits to Pease–Braginskii Collapse of a Z-Pinch," Lawrence Livermore National Laboratory, Livermore, CA, UCRL-53166 ( (Ph.D. Thesis, 1981).
- J. H. Hammer, J. L. Eddleman, P. T. Springer, M. Tabak, A. Toor, K. L. Wong, G. B. Zimmerman, C. Deeney, R. Humphreys, T. J. Nash, T. W. L. Sanford, R. B. Spielman, and J. S. De Groot, *Phys. Plasmas* 3, 2063 (1996).
- S. Maxon, J. H. Hammer, J. L. Eddleman, M. Tabak, G. B. Zimmerman, W. E. Alley, K. G. Estabrook, J. A. Harte, T. J. Nash, T. W. L. Sanford, and J. S. De Groot, *Phys. Plasmas* 3, 1737 (1996).
- "Sesame: The LANL EOS Database," S. P. Lyon and J. D. Johnson, Eds., LANL, Los Alamos, NM, LA-UR-92-3407 (1992)
- R. M. More and G. B. Zimmerman, Laser Programs Annual Report, 3–55, Lawrence Livermore National Laboratory, Livermore, CA, UCRL-50021-83 (1983); R. M. More, K. H. Warren, D. A. Young, and G. B. Zimmerman, Phys. Fluids 31, 3059 (1988); D. A. Young and E. Corey, J. Appl. Physics 78, 3748 (1995).
- J. Abdallah and B. E. H. Clark, Los Alamos National Laboratory, Los Alamos, NM, private communication (1994).
- C. Iglesias, B. Wilson, and J. Harte, Lawrence Livermore National Laboratory, Livermore, CA, private communication (1996)
- S. A. Brown and D. Braddy, "PACT Users' Guide," Lawrence Livermore National Laboratory, Livermore, CA, UCRL-MA-112087 (1995).
- W. A. Lokke and W. Grasberger, "XSNQ-U: A Non-LTE Emission and Absorption Coefficient Subroutine," Lawrence Livermore National Laboratory, Livermore, CA, UCRL-52276 (1977); G. Pollak, "Detailed Physics of XSN-U Opacity Package," LANL, Los Alamos, NM, LA-UR-90-2423 (1990).
- 73. G. B. Zimmerman and R. M. More, J. Quant. Spectrosc. Radiat. Transfer 23, 517 (1979).
- 74. W. E. Alley, Lawrence Livermore National Laboratory, Livermore, CA, private communication (1995).
- D. A. Liberman, J. R. Albritton, B. G. Wilson, and W. E. Alley, *Phys. Rev. A* 50, 171 (1994).
- Y. T. Lee, G. B. Zimmerman, D. S. Bailey, D. Dickson, and D. Kim, "A Time-Dependent Ionization Balance Model for Non-LTE Plasma," Lawrence Livermore National Laboratory, Livermore, CA, UCRL-95149; Y. T. Lee, J. Quant. Spectrosc. Radiat. Transfer 38, 131 (1987).
- 77. Y. T. Lee, R. A. London, and G. B. Zimmerman, *Phys. Fluids B* 2, 2731 (1990); A. I. Shestakov and D. C. Eder, *J. Quant. Spectrosc. Radiat. Transfer* 42, 483 (1989).

EMBINEA 112 D I III BICS CODE I OK INIODELLING ICI

- 78. J. C. Stewart and K. D. Pyatt, Ap. J. 144, 1204 (1966).
- B. C. Stuart, M. D. Feit, A. M. Rubenchik, B. W. Shore, and M. D. Perry, *Phys. Rev. Lett.* **74**, 2248 (1995).
- 80. P. F. Dubois, *Computers in Physics* **8** (1), Jan./Feb. 1994; L. Busby, P. F. Dubois, S. Wilson, *ICF Quarterly Report* **3**(1), 50 Lawrence Livermore National Laboratory, Livermore, CA, UCRL-LR-105521-93-1(1993).
- 81. L. Suter, Lawrence Livermore National Laboratory, Livermore, CA, veteran LASNEX user, private communication (1996).
- 82. B. A. Remington, S. V. Weber, S. W. Haan, J. D. Kilkenny, S. G. Glendinning, R. J. Wallace, W. H. Goldstein, B. G. Wilson, and J. K. Nash, *Phys. Fluids B* 5, 2589 (1993).
- 83. S. Chandarsekhar, *Hydrodynamic and Hydromagnetic Stability* (Oxford University Press, London, 1968), Ch. 10.
- 84. S. W. Haan, Lawrence Livermore National Laboratory, Livermore, CA, private communication (1996).
- 85. M. M. Marinak, Lawrence Livermore National Laboratory, Livermore, CA, private communication (1996).
- 86. T. R. Dittrich, B. A. Hammel, C. J. Keane, R. McEachern, R. E. Turner, S. W. Haan, and L. J. Suter, *Phy. Rev. Lett.* **74**, 2324 (1994).
- 87. S. W. Haan, Phys. Rev. A 39, 5812 (1989).

## THE ICF3D CODE

A. I. Shestakov M. K. Prasad J. L. Milovich

N. A. Gentile J. F. Painter G. Furnish

Z. Motteler T.-Y. B. Yang P. F. Dubois

#### Introduction

ICF3D is a three-dimensional radiation hydrodynamics simulation computer code being developed for ICF applications. It has a number of distinguishing features:

- Portable; works on uniprocessors and massively parallel processors (MPP).
- Written in the object-oriented programming (OOP) language C++.
- Based on unstructured grids.
- Discretized using finite elements; the hydrodynamics is modeled using discontinuous functions.

We believe these features are important for a variety of reasons.

These design codes must be portable, if they are to run on future computers. Computers are evolving at such a rapid pace that today's supercomputer will be obsolete in two to three years. However, software development is a painfully slow and labor-intensive task. Thus, it is important that codes developed now can run efficiently on tomorrow's computers. Today's supercomputer is a parallel machine, a collection of individual "boxes" each with its own memory and with one or more processing elements (PEs). ICF3D is written to take advantage of this architecture. It parallelizes by decomposing physical space into nearly disjoint subdomains and relies on explicit calls to system message-passing routines. This approach allows us to scale the computation. If more boxes are available, bigger problems can be run.

In order to have reusable code, software should be robust and modular. This is facilitated by an OOP approach. In a modular code, if something needs to be rewritten or modified, one can retain the trusted components. Functions or modules often need to protect their internal variables from inadvertent corruption by other routines; such protection leads to "data hiding." For better organization, one may wish to use "classes,"

or to define new entities, each with their individual methods, e.g., a cell and a means of calculating its volume. These requirements are easily accommodated by OOP languages such as C++. Traditionally, scientific software has used FORTRAN. ICF3D is embracing C++. This approach is not without risks. Although OOP in general, and C++ in particular, is now widely used, it rarely appears in computational physics. In the past, C++ compilers were notoriously slow in optimizing code, and for scientists, speed is nearly as important as accuracy. This state of affairs is changing, and the pessimistic results previously reported by Haney<sup>2</sup> are no longer true.<sup>3</sup>

Codes based on unstructured grids can easily model real experiments with complicated geometries. For example, in an indirectly driven ICF experiment, a spherical capsule is embedded in a nearly vacuous cylindrical hohlraum with partially opened ends. Some experiments may have additional shields inside the hohlraum to protect the capsule. During the experiment, the walls and capsule undergo significant displacement. In modeling, a traditional, fully structured mesh will have difficulty simulating and resolving the initial configuration and its subsequent motion. An unstructured grid is useful as it allows different cell types to be connected. The extra overhead in allowing complicated cells is offset by the flexibility afforded when the original domain is discretized and/or the problem regridded.

Simulation codes of this type benefit by being discretized using finite elements. Unstructured grids and complicated geometries naturally lead to finite element (FE) methods. ICF3D's grid consists of a collection of hexahedra, prisms, pyramids, and/or tetrahedra. Processes such as diffusion are modeled by nodal FE methods in which the variables are given a continuous representation throughout the domain. The hydrodynamics is simulated by a novel scheme<sup>4</sup> based on the discontinuous FE method. This allows a natural representation of inherently discontinuous phenomena, such as shocks.

In this article, the first section provides an overview of ICF3D's modules, discusses how the physics packages are coupled, and describes the individual packages in more detail. The next section presents some results. In the conclusion, we describe our future plans.

We have a couple of clarifications to make about our word usage. In internal discussions, the name "ICF3D" sometimes denotes both the "stand-alone" physics code as well as the environment used to initialize problems, execute them, control the execution, and analyze the results. To avoid confusion, in this article ICF3D refers only to the stand-alone code. In addition, throughout the article, we use "module" and "package" interchangeably to denote a set of routines that perform a specific task.

#### **ICF3D Modules**

ICF3D runs on a variety of machines. Its I/O is in a special format, which is described in this article in "ICF3D Initialization" (see p. 168). Once the input files are prepared, ICF3D may be run like any other C++ program. ICF3D also has an interactive controlling environment. The interpretive language Python<sup>5</sup> controls the execution.

In the following subsections, we discuss the ICF3D modules. The modules consist of one or more C++ functions. When properly designed, modules should be easy to check, and if the need arises, easy to replace with better modules. The modules' execution is controlled by user-set parameters. Most modules can be run separately. This code has separate modules for Initialization, Hydrodynamics, Heat Conduction, Radiation Diffusion, Equation of State (EOS), and Parallel Processing.

One important issue is how to couple the physics packages. The problem is complicated since the packages may have different representations of the variables, e.g., cell or node centered. This difference is exemplified by the hydro and radiation diffusion packages. The former evolves equations for the density  $\rho$ , the momentum density  $\rho \mathbf{v}$ , and the total energy density  $\rho E$ . The radiation diffusion package couples the temperature *T* to the spectral radiation energy density u, where v is the photon frequency. The coupling difficulty arises because hydro variables have a discontinuous FE representation, whereas any quantity undergoing diffusion (a second-order differential operator) must have a continuous representation, if the diffusion is modeled by FE. A straightforward coupling of a nodal u, to a zonal T may create anomalous diffusion.<sup>6</sup> Hence, the radiation-to-matter coupling should be done with functions having similar (nodal and continuous) representations.

The equations of interest are the conservation laws for mass, momentum, and total matter energy, respectively:

$$\partial_t \mathbf{p} + \nabla \cdot \mathbf{F}_{\mathbf{p}} = 0 \quad , \tag{1}$$

$$\partial_t(\rho \mathbf{v}) + \nabla \cdot \mathbf{F}_{\rho \mathbf{v}} = \rho \mathbf{g} \quad , \tag{2}$$

and

$$\partial_t(\rho E) + \nabla \cdot \mathbf{F}_{\rho E} = \rho \mathbf{g} \cdot \mathbf{v} + H_{\varepsilon} + S_{\varepsilon} + \int K_{v\varepsilon} dv \quad . \tag{3}$$

Equation (3) is coupled to the transport (diffusion) equation of the radiation field

$$du_{v} / dt = \nabla \cdot (D_{v} \nabla u_{v}) - K_{v \varepsilon} . \tag{4}$$

In Eqs. (1) to (3),  $\mathbf{F}_i$  denotes the flux of i, i.e.,  $\mathbf{F}_\rho v_x = \rho v_x \mathbf{v} + p$ , and  $\mathbf{F}_{\rho E} = (\rho E + p) \mathbf{v}$ , where  $v_x$  is the x velocity component and p is the pressure. In Eqs. (2) to (4),  $\rho \mathbf{g}$  is an external force density,  $\epsilon$  is the internal energy,  $H_\epsilon$  is the heat conduction term,  $S_\epsilon$  is a source of energy (e.g., due to laser deposition),  $K_{v\epsilon}$  describes the radiation-to-matter coupling, d/dt is the Lagrangian derivative, and  $D_v$  is the diffusion coefficient of the radiation field. In the future, when  $\epsilon$  is split into separate electron and ion components,  $K_{v\epsilon}$  will denote the radiation-to-electron coupling, and  $S_{\epsilon'}$  if due to a laser, will be an electron source.

Equation (3) is solved by operator splitting. At the start of the time cycle, we compute all the coefficients we need, such as conductivity. Then, we do a hydro step; Eqs. (1) to (3) are advanced together except that in Eq. (3) the *H*, *S*, and *K* terms are ignored.

The hydro module allows for the passive advection of an arbitrary number of other variables. Presently, this feature is only used for the "mass fractions." In the future, Eq. (4) would also be solved by operator splitting. The convective part would be done by the hydro, while the transport and radiation-to-matter coupling would be done at the end of the cycle.

The hydro module produces an intermediate total energy  $E^{(1)}$ . We now introduce the subscript d to denote variables whose numerical representation is discontinuous. If the grid consists of only regular hexahedra, there are eight cells adjacent to each node. Hence,  $f_d$  denotes a function with eight values per node. At the conclusion of the hydro step, we compute an intermediate internal energy

$$\varepsilon_d^{(1)} = E_d^{(1)} - v_d^2 / 2 \quad . \tag{5}$$

This step is potentially dangerous since Eq. (5) implicitly assumes that  $v_d^2/2$  is a valid representation for the kinetic energy  $e_k$ . Unfortunately,  $e_k$  is not computed directly but is only derived by squaring the velocity. The difficulty is illustrated by considering an ideal gas for which we require  $\varepsilon \ge 0$ . Since the code evolves  $\rho$ ,  $\rho \mathbf{v}$ , and  $\rho E$ , there are no explicit assurances that  $E \ge v_d^2/2$ .

The variables  $\rho_d$  and  $\epsilon_d^{(1)}$ , and the EOS yield the pressure  $p_d^{(1)}$  and the temperature  $T_d^{(1)}$ . The other physics packages compute changes to the internal energy  $\Delta \epsilon_d$ . The cycle concludes by computing the final energies

$$\varepsilon_d = \varepsilon_d^{(1)} + \Delta \varepsilon_d$$
 and  $E_d = E_d^{(1)} + \Delta \varepsilon_d$  . (6)

The change  $\Delta \varepsilon_d$  consists of the H, S, and K terms that were ignored by the hydro step. At the end of the time cycle, we have both a continuous nodal T and a discontinuous  $\varepsilon_d$ . The two variables may not be consistent. If necessary, we use the EOS to get a self-consistent pressure  $p_d$  and a temperature  $T_d$  from  $\rho_d$  and  $\varepsilon_d$ . Since  $T_d$  has a discontinuous FE representation, it may not agree with the continuous FE (nodal) value obtained by coupling to the radiation. To be more precise, after multiplying through by the time step, we write

$$\rho \Delta \varepsilon = H_{\varepsilon} + S_{\varepsilon} + \int K_{v\varepsilon} dv \quad . \tag{7}$$

The energy difference is expressed as a temperature difference

$$\Delta \varepsilon = c_v \left( T - T^{(1)} \right) \quad , \tag{8}$$

where

$$c_v = \frac{\partial \varepsilon}{\partial T} \Big|_{\rho^{(0)}, T^{(0)}} \tag{9}$$

is the specific heat computed at the start of the time cycle.

We now specify how the variables of Eqs. (7) to (9) are defined. The continuous FE representation of the temperature at the end of the hydro at the  $j^{th}$  grid point is

$$T_j^{(1)} = \frac{\int_{\Omega} dV \, \phi_j \, \rho_d \, c_{v,d} \, T_d^{(1)}}{\int_{\Omega} dV \, \phi_j \, \rho_d \, c_{v,d}} \quad , \tag{10}$$

where  $\Omega$  denotes the entire domain and  $\phi_j$  is the FE basis function centered at the  $j^{\text{th}}$  grid point. The integrals in Eq. (10) are sums over all the cells that support  $\phi_j$ . Furthermore, the integrals are lumped, i.e., for any

$$\int_{\Omega} dV \, \phi_j \, f = \sum_{cell} \left( \int_{\Omega \cap cellj} dV \, \phi_j \right) f_{d,j} \quad , \tag{11}$$

where  $cell_j$  is a cell with  $x_j$  as one of its vertices and  $f_{d,j}$  is the discontinuous value in  $cell_j$  at  $x=x_j$ . In the FE discretization of the heat conduction and radiation-to-matter coupling equations, we lump all but the transport term. Each equation is discretized by multiplying by  $\Delta t \phi_i$  and integrating over  $\Omega$ .

Once  $T^{(1)}$  is known, we use operator splitting and FE to first do the heat conduction and the energy deposition

$$\rho c_{v} \left( T^{(2)} - T^{(1)} \right) = \nabla \cdot \kappa^{(0)} \nabla T^{(2)} + S(\rho, T^{(1)}) \quad . \tag{12}$$

In Eq. (12), the heat transport is implicit in  $\Delta T^{(2)}$ , but the conductivity is computed using values at the start of the cycle. The source S is explicit. If it is due to a laser, and its deposition depends on both  $\rho$  and T, we use the latest values, the ones obtained after the hydro step. For laser deposition, we need continuous representations of  $\rho$  and T in order to compute their gradients. A continuous (nodal) density is given by its nodal values

$$\rho_{j} = \frac{\int_{\Omega} dV \, \phi_{j} \, \rho_{d}}{\int_{\Omega} dV \, \phi_{j}} \quad , \tag{13}$$

where the integral in the numerator is lumped, as in Eq. (11). Using the nodal values,  $\nabla$   $\rho$  is easily obtained from the analytic, continuous representation

(8) 
$$\rho(x,y,z) = \sum_{j} \phi_{j}(x,y,z) \rho_{j}$$
 (14)

The gradient is continuous within cells and discontinuous across cell faces.

Equation (12) is followed by the radiation-to-matter coupling. Equation (4) is coupled to

$$\rho c_v \left( T^{(3)} - T^{(2)} \right) = \int K_{v\varepsilon}^{(3)} dv \quad , \tag{15}$$

where K is implicit in the final, continuous temperature. Equations (4) and (15) are solved by standard FE techniques; everything except the transport term in Eq. (4) is lumped. The result is a continuous representation for both the final radiation energy density  $u_{\rm v}$  and matter temperature  $T^{(3)}$ .

To summarize, T is a derived quantity and  $\varepsilon$  is fundamental. During the heat conduction and radiation-to-matter coupling, we keep track of the energy changes in each cell. If the changes are small, then the  $\varepsilon$  after the hydro is not modified much. Hence, any sharp features are not smeared out. In particular, if there are no matter energy sources, very small heat-transport coefficients, and insignificant radiation-to-matter coupling, then the hydro should work as if it is the only package running. Similarly, if we have only hydro and a zonal matter energy source running, and the source is distributed according to Eq. (11), then the results should still stay sharp.

#### **ICF3D** Initialization

The grid consists of three types of objects: cells, faces, and nodes. A node is characterized by its sequence number and its coordinates. Cells and faces use the object-oriented concept of inheritance. Faces may be quadrilateral or triangular, whereas four types of cells are allowed: tetrahedra, pyramids, prisms, and/or hexahedra. The cell, face, and node objects are related. For example, a hexahedron has 6 faces and 8 nodes. Each interior face has two cells on either side. The cells need not be regular; the quadrilateral faces need not be coplanar. However, the cells cannot be so distorted to preclude an isoparametric mapping to regular elements, e.g., quadrilaterals to a unit cube. For Lagrangian node motion, this implies that if the grid becomes sufficiently distorted, the problem must be regridded. We do not yet have a means of regridding.

We have not yet written a general, unstructured mesh generator. In order to run test problems, we have instead written a simple, separate mesh generator that outputs mesh description files for subsequent reading by ICF3D. However, we stress that ICF3D is written to run on completely unstructured meshes. Our generator is described in "Problem Generation" (see p. 172); it writes ICF3D input files that describe the mesh in the Advanced Visual Systems (AVS) Unstructured Cell Data (UCD) format. (AVS is a commercial software visualization product.) This format, which consists of two lists, is a terse description of the grid. The first is a node list; each node is described by its unique sequence number (an integer) and by the values of its coordinates (three real numbers). The second is a cell list; each cell is described by its type—e.g., a pyramid—and by a list of integer sequence numbers that comprise the cell's vertices. The cell's vertices must be given in a prescribed way, e.g., a pyramid's apex is listed first.

We have used the UCD because it is commercially available, but it is not adequate for use in generating an unstructured mesh. For example, the format does not explicitly list which cells share given a node. Also the format never mentions faces. To define the mesh, ICF3D requires that the different objects (cells, faces, and nodes) have a set of interconnecting pointers to describe which cells lie on either side of a face, which nodes make up the face, etc.

The discontinuous hydrodynamic scheme imposes even more requirements on the mesh description. The dependent variables are cell–node based. For example, each cell's density is described by its value on the vertices. Since the hydrodynamic variables are allowed to be discontinuous, a neighboring cell has different nodal values. Thus, such variables are considered "doubly indexed": once over cells, then again over the cell's nodes. When the hydrodynamic face fluxes are computed, the routine loops over each face, follows the

pointer to each of the adjoining cells, and goes to the appropriate node to pick up the value. This requires the mesh to provide an additional set of pointers: face—cell—node.

Some physics packages are more efficient if additional connectivity information is supplied. For the hydrodynamics, the limiting routine, which deletes unphysical extrema, requires that each cell point to all other cells that share its nodes. The continuous, piecewise-linear, nodal FE scheme that discretizes the second-order elliptic operator imposes a similar requirement. Each node, which by construction is a vertex of one or more cells, needs a list of the other vertices. On a regular hexahedral grid, the nodal neighbor list gives rise to a 27-point stencil.

All this information is computed at the start of the run and saved. Presently, since we do not have a regridding routine, the topological description of the grid does not change during the course of a run—even in a Lagrangian calculation.

#### **EOS Package**

In the discontinuous finite element method, density, pressure, and velocity are linear functions. These variables are used to calculate the hydrodynamic fluxes. The Roe solver (which computes the fluxes) needs various derivatives of thermodynamic quantities. This requires that the EOS module compute some variables as functions of different combinations of other quantities. In particular, we need

$$\varepsilon(\rho, p)$$
,  $p(\rho, \varepsilon)$ ,  $\frac{\partial \varepsilon(\rho, p)}{\partial p}$ ,  $\frac{\partial \varepsilon(\rho, p)}{\partial \rho}$ , and  $\frac{\partial \varepsilon(\rho, T)}{\partial T}$ .

Such functions are part of our C++ EOS class. Compartmentalizing these functions into a class allows for better management of data common to all functions for a specific material. For example, in the case of tabulated equations of state, the functions are calculated from the same database. The ICF3D EOS class uses the C++ concepts of inheritance and virtual function overloading to allow new equations of state to be easily implemented.

Currently, three different types of equations of state are supported by the EOS class: ideal gases, ASCII versions of EOS tables for various materials, and a version of the SESAME equation-of-state tables from the Los Alamos National Laboratory. Tabular data are fitted by bicubic splines. The EOS class "constructor," called after the problem initializes, computes spline coefficients. The coefficients are saved and used to evaluate the functions. This makes for faster calls, at the cost of storing a larger amount of data. We intend to add a class that uses the TABLib library. This will

allow ICF3D to use tabular equations of state stored as PDB files.

If a cell has more than one material, ICF3D calculates and advects mass fractions. In this case, the cell's thermodynamic quantities are specified by a total  $\rho$ , total energy density (or total p, or total T), and a set of mass fractions for the different materials.

#### **Hydrodynamics**

The ICF3D hydrodynamic scheme is described in Ref. 4. The algorithm advances two scalar hyperbolic equations for the density  $\rho$  and the total energy density  $\rho E$ , and the vector equation for the momentum density  $\rho \mathbf{v}$ . The scheme is compact and is easily parallelized since it gets all of its accuracy locally; it does not reach out to more than one neighboring cell to approximate the dependent variables.

The two essential features of the hydro scheme are its ability to do fully Arbitrary Lagrangian Eulerian (ALE) calculations and its ability to run in different coordinate systems. ALE combines the best features of Eulerian and Lagrangian codes. The "arbitrary" aspect allows the user to specify the mesh's motion to resolve a feature that would not be possible to resolve with either a purely Eulerian or a purely Lagrangian code. The hydro module is implemented in 3-D Cartesian, cylindrical, and spherical geometries. We are continuing to develop the ALE features to ensure code robustness. In particular, we have focused attention on two areas. The first involves the Lagrangian limit of the ALE code where the mesh follows the fluid motion. This is a nontrivial problem since discontinuous functions represent the velocity fields, whereas the mesh is required to be continuous. We have developed a scheme to move the grid points that ensures a vanishing average mass flux across a face.

Secondly, the shock stabilization algorithm has been adapted to combine the pure Runge-Kutta solution, the 3-D generalized Van Leer stabilized solution (the limiting procedure), and the first-order Godunov limit solution. This "adaptive" combination assures the greatest possible accuracy as we go from very smooth regions to extremely strong shocks. However, in 2- and 3-D problems, this stabilization is insufficient to stabilize extremely strong shocks. We have implemented a Lapidus-type artificial viscosity<sup>9</sup> to stabilize the remaining "transverse" oscillations near such shocks.

We have successfully run the code on two test problems of particular interest to ICF: the 3-D Rayleigh—Taylor (RT) instability growth problem and the 2-D Richtmyer—Meshkov (RM) shocked perturbation problem. The ressults are described in the "Hydrodynamic Problems" section of this article (see p. 175).

#### **Heat Conduction**

Currently, ICF3D uses only a single matter temperature T. The change of the internal energy  $\epsilon$  due to temperature is expressed as

$$\rho c_{\nu} \partial_t T = \nabla \cdot \kappa \ \nabla T + S_{\varepsilon} \quad , \tag{16}$$

where  $S_{\epsilon}$  is an external source term,  $\kappa$  is the conductivity, and  $c_{\rm v}=\partial_{\epsilon}/\partial T$  is the specific heat. In the future, sources such as laser energy deposition will be incorporated into  $S_{\epsilon}$ . <sup>10</sup>

Equation (16) is discretized by a standard nodal FE scheme in which T is given a continuous "piecewise linear" representation. The dependent variable is the nodal temperature value. For testing purposes, we provide three conductivity models:  $\kappa$  = constant, a power law, and one given by the Spitzer–Härm formula.<sup>11</sup>

The heat conduction package gathers the various coefficients ( $c_v$ ,  $\kappa$ , etc.) of Eq. (16) and calls the mathematical diffusion solver package described in "FE Diffusion Package" (see p. 170).

#### **Radiation Transport**

Radiation transport is modeled with the diffusion approximation. The coupling to matter is governed by the opacity  $\kappa_v$ . The relevant equations are

$$\partial_t u_{\mathbf{v}} = \nabla \cdot D_{\mathbf{v}} \nabla u_{\mathbf{v}} + c \rho \kappa_{\mathbf{v}} \left[ B_{\mathbf{v}}(T) - u_{\mathbf{v}} \right]$$
 (17)

and

$$\rho c_{\nu} \partial_{t} T = -\int dv c \rho \kappa_{\nu} \left[ B_{\nu}(T) - u_{\nu} \right] \quad , \tag{18}$$

where  $B_{\nu}(T)$  is the Planck function. In the above equations the unknowns are the radiation energy densities  $u_{\nu}$  and the matter temperature T.

The same FE scheme used for heat conduction discretizes Eq. (17). In addition,  $u_{v}$  is discretized with respect to frequency: for each range, or frequency "group,"  $u_{v}$  is its average radiation energy density.

To solve the two equations, we use the "fully implicit" scheme described in Ref. 12. First, the source term is linearized about the temperature at the start of the time cycle

$$B_{\mathbf{v}}(T) = B_{\mathbf{v}} \Big|_{T_o} + dB_{\mathbf{v}} / dT \Big|_{T_o} (T - T_o) \quad . \tag{19}$$

The discretization leads to a large system of linear equations, which is solved by a matrix-splitting iteration. We write the system as  $A\mathbf{x} = S$ , where  $\mathbf{x} = (u_{v}, T)$  denotes the vector of unknown energy densities and temperature. As described below, we split A in two

ways: first, as  $A = A_d + A_{c'}$  then, as  $A = A_l + A_{nl}$ . For the first splitting, we solve

$$A_d \mathbf{x}_1 = S - A_c \mathbf{x}_0 \quad .$$

For the second, we solve

$$A_1 \mathbf{x}_2 = S - A_{nl} \mathbf{x}_1 \quad .$$

The two splittings constitute one iteration. The iterations are repeated until  $u_v$  and T converge.

In the first splitting,  $A_d$  is the part of the matrix that arises from the diffusion operator in Eq. (17).  $A_c$  is the remaining part of A and includes the radiation–matter coupling. The first splitting is equivalent to solving for  $u_v$  while keeping T fixed. Since the groups are only coupled through T, the individual group densities may be solved independently of each other. This results in repeated calls to the diffusion solver.

In the second splitting,  $A_l$  is the "local" part of the matrix, formed from A by ignoring all spatial coupling.  $A_l$  is a block diagonal matrix, with each block corresponding to a single mesh point. The blocks are of order  $N_v + 1$ . By ordering  $u_v$  first, it follows that each block consists of an order  $N_v$  diagonal matrix in the upper left corner and completely filled last row and column. Hence, the blocks are quickly solved with Gaussian elimination.

We plan to experiment with other linear solution methods and to choose the ones that offer the best combinations of speed and accuracy. One such method is the "partial temperature" scheme.<sup>6</sup> This method has the advantage of not requiring any iterations. For the price of advancing a single diffusion equation once, one gets  $u_v$  and T implicitly coupled.

We also plan to add the advection of  $u_v$ . The above method is physically correct only when the code runs in the Lagrangian mode. For Eulerian or other modes in which the mesh does not move with the fluid, we need to consider that the radiation is also carried by the fluid.

Lastly, we need to incorporate a routine to calculate realistic opacities  $\kappa_{\rm v}$ . Presently, ICF3D has only three types of opacities: a user-specified constant, a simple formula  $\kappa_{\rm v} = (T/{\rm v}^3)(1-\alpha e^{-{\rm v}/T})$ , and tabulated "cold" opacities.

## **FE Diffusion Package**

The heat conduction and radiation diffusion modules both call the diffusion package, a routine that solves the generic equation

$$g\partial_t f = \nabla \cdot D\nabla f + S - \alpha f \quad . \tag{20}$$

The diffusion package transforms Eq. (20) into a linear system and calls the solver. Equation (20) is discretized

by FE methods. The unknown function f is represented in terms of basis functions

$$f = \sum \phi_j(x) f_j \quad ,$$

where  $\phi_j$  is the usual piecewise linear function  $\phi_j$   $(x_i) = \delta_{ij}$ . The main difference between the diffusion basis functions and those used for the hydrodynamic module is that for diffusion, support  $(\phi_j)$  extends over all cells with  $x_i$  as a vertex.

The time derivative in Eq. (20) is discretized using fully implicit differencing. With one exception, all coefficients are assumed to be known and constant within a cell. The exception is the radiative source, Eq. (19), in which T and  $T_0$  have nodal representations.

After discretizing the temporal derivative, Eq. (20) is multiplied by  $\phi_i \Delta t$  and integrated over the entire domain. This leads to a sparse linear system for the coefficients  $f_i$ .

$$(g + \alpha - \nabla \cdot D\nabla)f = g \quad f_0 + S \quad . \tag{21}$$

Integration by parts turns the transport term into a surface integral and a volume integral of the type

$$\int_{\Omega} dV \ D \ \nabla \phi_i \cdot \nabla \phi_j \quad . \tag{22}$$

If  $x_i$  is not a boundary node, or if one prescribes a boundary symmetry condition for the flux  $(-D\partial f/\partial n = 0)$ , then the surface integral does not appear. All terms except the transport term are lumped. This implies that only the flux contributes to the off-diagonal coefficients of the matrix. Because of the symmetry in Eq. (22), the matrix is symmetric. It is easy to show that the matrix is also positive definite.

Unfortunately, we may not get an M matrix since some off-diagonal coefficients may be positive. The M-matrix property—only non-negative coefficients for the matrix inverse—is desirable since the diffusion module advances positive quantities such as *T*. The right-hand side of Eq. (21) is itself positive since it is a sum of the source and the old energy. To show the loss of the M-matrix property, recall that the transport term is discretized by Eq. (22). The diagonal contribution with i = j is clearly positive. For the off-diagonal terms, consider the contribution to Eq. (22) from just one element, K. By construction, D is constant and positive over the element. Hence, let D = 1. In 2-D triangles, it is easy to show that  $\nabla \phi_i \cdot \nabla \phi_i \leq 0$ , if none of the interior angles are obtuse. In 2-D quadrilaterals, the result is more restrictive, since the sign depends on the aspect ratio of the sides. The issue is exacerbated in 3-D. Consider the hexagon

$$K = \{(x, y, z) : |x| \le 1, |y| \le Y, |z| \le Z\}$$

and the functions

$$\phi \pm = (1 \pm x)(Y + y)(Z + z)/8YZ$$
.

A direct integration yields

$$\int_{\kappa} dV \nabla \phi_{+} \cdot \nabla \phi_{-} = \left( Y^{2} + Z^{2} - 2Y^{2}Z^{2} \right) / 9 YZ \quad . \tag{23}$$

Again, the sign depends on the aspect ratio. If Y = Z and Y < 1, we get the undesired positive sign.

It remains to be seen whether the lack of the M-matrix property proves harmful. It does make the system harder to solve (see the section below, "Solution of Linear Systems.") We are aware that for the case:  $S = \alpha = 0$  and g = 1, the linear system of Eq. (21) has the form

$$(M + \Delta t S)f = Mf_0 \quad , \tag{24}$$

where M is the lumped (diagonal) mass matrix and S, the stress matrix, is the discretization of the diffusion operator. For negligibly small  $\Delta t$ ,  $(M + \Delta t \, S)^{-1} \approx M - \Delta t S$ . Hence, if S has positive off-diagonal terms, then for a properly chosen and still positive  $f_0$ , we may obtain an f with some components negative.

Once the diffusion module has initialized the linear system, it calls the linear solver.

### Solution of Linear Systems

ICF3D generates two types of linear systems. One kind arises when the hydrodynamic module inverts mass matrices to compute the fundamental variables. The order of those systems equals the number of degrees of freedom in a cell, e.g., eight in a hexahedron. To solve these systems, we have written a set of general routines that perform Gaussian elimination with partial pivoting. <sup>13</sup>

The second type of systems is created by the diffusion module. For such problems, the matrix *A* is large, sparse, symmetric, and positive definite (SPD). Because of the unstructured grid, the matrix sparsity pattern is random. SPD systems are best solved by the preconditioned conjugate gradient (PCG) method. Three preconditioners are available: Incomplete Cholesky (IC), one-step Jacobi (diagonal scaling), and multistep Jacobi. In this section, we only discuss the uniprocessor version of the solver. "Parallel Solution of Linear Systems" (see p. 175) describes the MPP modifications.

The PCG algorithm is well documented in the literature. <sup>13</sup> We shall not rederive it here, but instead describe our implementation. Unless the grid topology is changed, the sparsity pattern remains the same. Hence, if the discretization couples node  $x_i$  to node  $x_j$ , then the ith row of the matrix has a nonzero entry in

the  $j^{\text{th}}$  column. Since the matrix is symmetric, row j has the same entry in the  $i^{\text{th}}$  column. Thus, the following data structure suffices to describe the sparsity pattern. For each row i, we define an integer array  $C_i$  of dimension  $C_{i,dim}$  where the integer  $C_{i,dim}$  is the number of nonzero entries in row i to the left of the diagonal. For some rows, for example the first,  $C_{i,dim} = 0$ . The array  $C_i$  contains the column numbers of the nonzero matrix entries. For example, if the seventh unknown is only coupled to the third and fifth,  $C_{7,dim} = 2$  and  $C_7 = (3,5)$ .

This description is computed only once, at the start of the run. The pattern is computed from the nodal neighbor construct described in "ICF3D Initialization" (see p. 168). Of course, if the problem were to be regridded (and the mesh topology changed), the sparsity pattern would be recomputed. Although the above discussion focuses on a sparsity pattern due to an FE discretization of a nodal quantity, the procedure can be generalized. For example, if we need to discretize a zonal quantity, we first determine the zone's neighbors for this application and then follow the same procedure. The linear solver need not distinguish how the linear system was derived. All we supply is a description of the system, i.e., the matrix order and sparsity pattern, the matrix elements, the maximum number of iterations allowed, the preconditioner desired, etc.

To use the IC preconditioner, we do more preliminary work. For uniprocessors, the IC variant factors the matrix into the product

$$A = LDL^{T}$$

where D is diagonal, L is lower triangular with unit diagonal and a sparsity pattern that matches that of A, i.e., no fill-in. It can be shown<sup>14</sup> that computing an entry in the lower triangle of L, e.g., row i and column j, involves a dot product of the previously computed entries of row i and row j. For efficiency, we do not compute products of a nonzero entry in one row by a zero entry in another. Avoiding such unnecessary multiplications requires extra preliminary work and additional storage in order to describe which entries contribute to the product. As a result, the evaluation of L proceeds faster, but with the penalty of indirect addressing of the necessary elements.

We have only tested our solver on small problems. First of all, we have confirmed that for sparsity patterns in which all nonzero matrix entries are bunched about the diagonal, IC returns the exact decomposition and PCG converges in one step. Secondly, we obtain the results in Table 1 for Laplace's equation on the unit cube with Dirichlet boundary conditions. Using a uniform grid with L = 1/(n+1) and n = 15, we obtain a system of order  $n^3$ .

Note that even though two-step Jacobi took nearly 50% more iterations than IC, the time spent was almost

TABLE 1. Results for Laplace's equation on the unit cube with Dirichlet boundary conditions L = 1/(n+1) and n = 15. Time is in arbitrary units.

Preconditioner	Iterations	Time
One-step Jacobi	30	_
Two-step Jacobi	18	56.15
Incomplete Cholesky	13	56.13

identical. The nearly twofold decrease in the iteration count between one- and two-step Jacobi agrees with the results of Ref. 15. However, this problem is characterized by uniform and equal  $\Delta_{x'}$ ,  $\Delta_{y'}$  and  $\Delta_{z'}$ , which implies that we obtain an M matrix. Hence, the first-order Jacobi iterative method converges, <sup>16</sup> and one can apply the results of Ref. 15 to make the two-step Jacobi method an efficient preconditioner.

However, for nonuniform meshes, Eq. (23) implies a loss of the M-matrix property. Furthermore, it is easily shown that the matrix need not be strictly diagonally dominant. Hence, the Jacobi method need not converge and the two-step preconditioner may even delay convergence. To illustrate, we consider the same problem as above except we set  $X_{\rm max} = 1$  and  $Y_{\rm max} = Z_{\rm max} = 0.1$ . We again use n+1 uniformly spaced points in each direction. The results appear in Table 2.

TABLE 2. Same problem as for Table 1, with  $X_{\text{max}} = 1$ , and  $Y_{\text{max}} = Z_{\text{max}} = 0.1$ .

n	Preconditioner	Iterations
11	None	40
11	One-step Jacobi	37
11	Two-step Jacobi	40
11	Incomplete Cholesky	10
21	None	58
21	One-step Jacobi	56
21	Two-step Jacobi	441

For n = 11, two-step Jacobi is slightly worse than one-step and no better than the conjugate gradient method without a preconditioner, while IC took four times fewer iterations. However, for n = 21, two-step Jacobi actually did considerably more harm than good.

Lastly, in the above problem, we confirmed that the numerical solution equals the exact solution, (1-x)(1-y)(1-z). On a hexagonal mesh, the exact solution belongs to the domain spanned by the test functions.

#### **Problem Generation**

The task of generating truly unstructured meshes, even those limited to hexagonal, prismatic, pyramidal, and/or tetrahedral cells, is a formidable job and is, in itself, the subject of ongoing research of other groups and companies. For our test problems, we improvised by writing a separate code, the generator, that creates only logically hexagonal grids.

To each point, the generator assigns an integer three-tuple (k, l, m), where the indices are positive and bounded by  $(k_{\text{max}}, l_{\text{max}}, m_{\text{max}})$ . The generator also specifies the initial and (currently, time independent) boundary conditions, the material(s) of choice via EOS tables, and discretizes the frequency spectrum. To facilitate the generation, we have enveloped this process under a controller or script language parser. The system was originally developed under Basis,  $^{17}$  but we have adopted Python,  $^{5}$  a new, portable language that is easily extended. Using a technique similar to that for LASNEX, a set of generator functions describe the problem in an ASCII file written in Python. After the generator reads the file, it writes the ICF3D input files in the UCD format.

The generator has been extended to specify meshes that are not logically hexagonal. We allow for voids within the domain, e.g., to represent solid bodies. The generator also allows the user to describe the grid in one coordinate system and write the input file in another. Thus, we may discretize the sphere in  $(r, \theta, \phi)$  and compute in Cartesian coordinates. This presents a special challenge, because the individual elements are not symmetric in the expected directions. The generator also decomposes the domain for MPPs. The user chooses along which of the k, l, and/or m directions to parallelize. For example, one could divide a  $k_{\rm max}$ ,  $l_{\rm max}$ ,  $m_{\rm max}$  = (31, 51, 81) domain amongst 2 × 2 × 4 = 16 PEs, where each PE owns 15 × 25 × 20 cells.

Python can interact with and "steer" the execution. Steering permits the user to directly interact with the various code modules, thereby allowing real-time analysis of the computed results. Unfortunately, this mode of operation requires that the controller/interpreter be portable to the machine of choice. This requirement may not be simple to fulfill, particularly on MPPs. Consequently, we provide two modes of operation. In one, which is still under development, the computing core (ICF3D) and the controller (Python) are tightly coupled. We use this mode on uniprocessors. The second mode gives us the flexibility of running ICF3D on a variety of platforms with no concern of the steering engine's portability. This mode evokes the distributed computing model; the stand-alone ICF3D is controlled by a Python session executing at a local workstation.

ICF3D is run in this second, distributed mode, on a variety of computers, uniprocessors and MPPs. This

allows us to use the parallel machines exclusively for computations and relegates the generation and postprocessing chores to the desktop. The user directs where to execute ICF3D, and the generator takes care of the details: reading the user's deck, preparing the input files, shipping them to the computer of choice, initializing the run, etc. While this is not as flexible as a truly steerable code where parser and code are intimately connected in a single executable, it has given us an invaluable means to develop and debug ICF3D and has provided an easy interface to the MPP of choice. The system supports continuation runs via restart files as well as a link to the debugger on the remote machine. Our only requirements on the remote machine are a correct C++ environment with standard remote-shell execution capabilities. Since the interface is the same regardless of the computing engine—MPP or uniprocessor—the parallelization is completely transparent to the user. The decomposition of the domain and subsequent recombination of the results from the individual PEs are done by the generator. In a typical run, after ICF3D finishes, the data is automatically transmitted to the workstation to be saved for later postprocessing or examined immediately. For subsequent processing with the AVS visualization software, ICF3D also writes files in the AVS UCD data format.

### **Parallel Processing**

We target distributed memory processors (DMPs) and rely on explicit calls to message passing functions. This is the optimal strategy for computers such as the CRAY T3D and the IBM SP2, as well as networks of workstations (if the network is provided with the appropriate message-passing library). The strategy also works on shared memory computers (SMPs). ICF3D has successfully run on uniprocessor workstations and DMPs such as the T3D, as well as on SMPs like the 12-node SGI Power Challenge.

We divide the physical domain into nearly disjoint subdomains, one per PE, and "leave" the subdomains distributed on the PEs. Each PE receives a description of only its subdomain plus a layer of adjacent ghost cells. In Fig. 1, we display the entire subdomain (including ghost cells) sent to one PE. The subdomain consists of 96 owned cells and 236 ghosts. (This example has a bad surface-to-volume ratio.) There are 108 hexahedra, 96 prisms, 96 pyramids, and 32 tetrahedra. Only 48 hexahedra, 16 prisms, 24 pyramids, and 8 tetrahedra are owned cells. The peculiar cones and innermost sphere primarily consist of ghost cells. They appear since the domain decomposition requires that each owned cell know about all cells that share one of its vertices.

The subdomains are described in the input files, which are written in the modified AVS UCD format.

The modification consists of assigning global as well as local sequence numbers to both cells and nodes, and tagging the cells with the number of the PE that owns it. The input files are written by the generator; and only it has access to the entire domain. The generator initializes the problem, decomposes the domain, and determines which PE owns which cell. The assignment of nodes to specific PEs is done by ICF3D itself. Thus, since cells do not migrate across the PEs, the task of load balancing the PEs is assigned to the generator.

We use a "coarse grained" parallelization strategy; the code is not replete with parallelization commands. Crucial code segments have been identified as requiring information that resides on another PE. At such segments we insert statements of the type

#### if (Number PEs >1) call fooMPP();

Such branching statements appear at a high level in the code.

For parallelization purposes, the physics modules may be roughly divided into three kinds: embarrassingly parallel, clearly parallelizable, and hard to parallelize efficiently. The first type consists of modules such as the EOS; nothing special is done since each PE works only on the cells it owns. Explicit time-differencing methods such as the hydrodynamic step are clearly parallelizable. Such methods have an easily identifiable, compact domain of dependence. For example, a cell's hydro variables at one time step depend on only

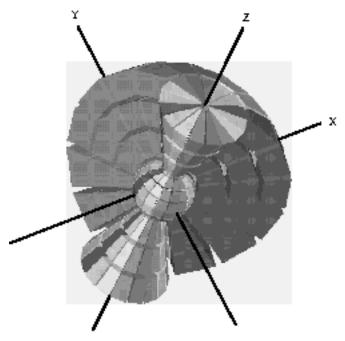


FIGURE 1. Entire subdomain given to a PE when decomposing a sphere and running in Cartesian coordinates. Figure includes both owned and ghost cells. (50-06-1296-2785pb01)

old values of that cell and its neighbors. If the neighbor cells are owned by the same PE, no extra work is required. If some of the surrounding cells belong to another PE, a copy of that cell is a ghost cell of this PE. It is the responsibility of the message-passing routines to get the required information. The third, hard-to-parallelize-efficiently are those modules that require global communication, e.g., the initialization and solution of linear systems. That subject is discussed in "Parallel Solution of Linear Systems" (see p. 175).

When running in parallel, we use one of two libraries in one of two modes. In one mode, for portability, we call routines from the industry standard MPI message-passing library. On the Cray T3D, we also provide the option of using the native SHMEM library, since efficient implementation of MPI is site-dependent. In the early stages of our parallelization work, the LLNL MPI library was extremely slow. Now, the SHMEM and MPI performances are nearly equivalent. Nevertheless, having a choice of libraries has proved invaluable; when one breaks, we switch to the other. In the other mode, we have an additional object-oriented layer, C4,<sup>18</sup> which is itself written in C++ and thus allows better use of that language. For example, MPI routines require that we explicitly state the data type of the arguments. In C++, such type-description is unnecessary since, unlike in FORTRAN, the argument carries information about its type. C4 has also been generalized so that it either calls SHMEM or MPI.

The interface to the MPI, SHMEM, or C4 functions is through special message-passing objects (MPOs), which are constructed at the start of the run. These objects store the information required to effect the message passing. For example, assume that at each time step,  $PE_0$  sends to  $PE_0$  nodal data corresponding to nodes with global sequence numbers 500 and 1,000,001. These nodes will have different local sequence numbers, e.g., 10, 11 on  $PE_0$ , and 50, 70 on  $PE_9$ . The MPO stores the number of the other PE, the length of the message, and the local sequence numbers on this PE. Thus, on  $PE_0$  the MPO knows it is to receive two numbers from  $PE_0$  which are to be stored in locations 50, 70.

Whenever we enter a module that requires communication, such as the hydro package, we allocate buffers of the proper size to store the messages. The buffers are deallocated when that module is exited. In the future, to avoid repeated calls to memory allocation routines, we will allocate a permanent block of memory during the initialization step and have the MPO reuse this block.

### **Parallel Hydrodynamics**

The hydrodynamic module is fully parallelized. We use three kinds of MPOs. (Only two are needed for Eulerian calculations.) One communicates facial infor-

mation, the other nodal. The former is used to compute fluxes (on cell faces) on inter-PE boundaries. The latter is used in the limiting process, which deletes unphysical extrema in the solution. For Lagrangian runs, additional MPOs pass the required information to compute the velocity of nodes lying on inter-PE boundaries. We have verified that, to round-off precision, the results are independent of the partitioning of the domain amongst the PEs.

The hydro scheme, being explicit, lends itself nicely to parallelization, with results scaling with the number of PEs used. In Table 3, we display timings from a test problem. The problem is run in Cartesian coordinates, but the mesh is generated with cylindrical coordinates. In the results, we fix the number of cells and increase the number of PEs. Let  $N_{PE}$  denote the total number of PEs, PE config the PE configuration in the  $(R, \theta, Z)$  directions, cell config the number of owned cells in  $(R, \theta, Z)$ , cell the ratio of owned to ghost cells, Time the execution time, Speedup the ratio of Time to Time for the 32-PE run, and  $E = Speedup/(N_{PE}/32)$  the efficiency. The efficiency results reflect the fact that as  $N_{PE}$  increases, cell corrected a greater message passing overhead.

TABLE 3. Timing results (in s) obtained from a test problem run in Cartesian coordinates and with mesh generated with cylindrical coordinates.

$N_{ m PE}$	PE <sub>config</sub>	Cell <sub>config</sub>	Cell <sub>ratio</sub>	Time	Speedup	E
32	(8, 1, 4)	(8, 16, 8)	1.32	959.7	_	_
64	(8, 1, 8)	(8, 16, 4)	0.90	501.0	1.92	0.96
128	(16, 1, 8)	(4, 16, 4)	0.74	264.6	3.63	0.91
256	(16, 1, 16)	(4, 16, 2)	0.42	149.9	6.40	0.80

## Parallel Solution of Linear Systems

At the time of writing this article, we are still developing parallel solutions to linear systems. What follows here is a general discussion of the topic; timings and scalings will be presented at a later date.

The linear systems generated by ICF3D are large, sparse, symmetric, and positive definite, and therefore ideally suited for PCG. For uniprocessors, we offer three kinds of preconditioners: IC, one-step, and multistep Jacobi. Their parallel implementation is described below.

The CG iterations consist of vector sums, inner products, matrix vector multiplications, and the solution of the preconditioning system. These operations are easy to implement if the nodes are assigned to the PEs. This is done in parallel at the start of the run. Nodes on or inside inter-PE boundaries are assigned without any

need for message passing. Ownership of nodes on the "outside" of the ghost cells requires point-to-point communication. After this initialization, every node on every PE has been tagged with the PE that "owns it."

Once the nodes have been assigned, the vector sums are trivial to implement. Each PE only updates the nodes it owns. For the inner products, each PE computes a preliminary accumulation of its owned nodes and then calls a global "reduction" routine provided by the message-passing library. These calls are potential bottlenecks since they require an all-to-all PE communication.

The matrix is distributed amongst the PEs as follows. We use a row-wise assignment of the matrix coefficients. Each PE eventually gets all the matrix coefficients for the rows corresponding to nodes that it owns. The coefficients come from integrations over cells, e.g., Eq. (22). If  $x_i$  is owned by the PE but lies on an inter-PE boundary, the contribution from a particular cell is done by the PE that owns the cell. With the FE scheme, each PE computes the matrix coefficients just as in the uniprocessor case, i.e., it integrates only over owned cells. Then, special MPOs determine which contributions need to be exchanged with other PEs. As for the hydro MPOs, the matrix MPOs are constructed during the initialization phase.

Once the matrix is distributed, the matrix vector multiplications are relatively straightforward. If

$$y_i = \sum_j A_{i,j} x_j \tag{25}$$

is one of the owned elements of the PE, the product is easily done if the PE has the latest  $x_j$  values. For some  $y_i$ , the requisite  $x_j$  are owned by other PEs. Those values are delivered to the PE by other MPOs.

Lastly, we discuss the preconditioners. For one-step Jacobi, message passing is not required. Multistep Jacobi, which is one example of a polynomial preconditioner, <sup>13</sup> requires a matrix vector multiplication. Each step is preceded by a send/receive. For IC, our plan is to perform the usual ICCG(0) algorithm but ignore coupling across the PEs. In this way, we avoid the fundamental bottleneck of ICCG, namely, how to parallelize the solutions of the triangular systems. If the domain decomposition has a low surface-to-volume ratio, this approach is efficient. Effectively, the decomposition is even more incomplete than on a uniprocessor. At the very least, this parallelizes, does not require any message passing, and should outperform one-step Jacobi because the latter is the limiting case of a decomposition so incomplete that it ignores all coupling.

#### **Numerical Results**

In this section we present results of test problems in order to display some of ICF3D's capabilities and check the algorithms. The section is divided into three

parts. "Hydrodynamic Problems" (see below) discusses two hydrodynamic problems—the Rayleigh–Taylor and Richtmyer–Meshkov instabilities—which use only the hydro physics module and ideal gases, i.e.,

$$(\gamma - 1)c_v T = (\gamma - 1)\varepsilon = p / \rho ,$$

where  $\gamma$  and  $c_v$  are user-specified constants. In "Non-linear Diffusion Problem" (see p. 177), we turn our attention to the heat conduction module and simulate nonlinear diffusion. The calculation is done in 3-D Cartesian coordinates, but by construction, the problem should be spherically symmetric. Finally, in "Coupled Physics Problem" (see p. 178), we discuss a contrived test problem that exercises all of the available physics modules, a realistic material, hydro, heat conduction, and radiation, and compare our results to LASNEX.

#### **Hydrodynamic Problems**

We consider a class of instabilities where two fluids of different densities are subjected to an acceleration **g**. Theoretical work on the growth of a perturbed interface in which a light fluid supports a heavy fluid was originally presented by Taylor<sup>19</sup> who studied perturbations of the type

$$\delta z = a \cos kx \quad , \tag{26}$$

where  $z_0 = \text{const.}$ ,  $ka \ll 1$ , and the wave number  $k = 2 \pi/\lambda$ . Taylor showed that the amplitude a satisfies

$$\frac{d^2a}{dt^2} = kg(t)a(t)A \quad , \tag{27}$$

where  $A = (\rho_2 - \rho_1)/(\rho_2 + \rho_1)$  is the Atwood number, defined in terms of the densities on either side of  $z_0$ , and where  $\mathbf{g} = -g \hat{\mathbf{z}}$ .

We simulate two cases: (1) the Rayleigh–Taylor instability in which g = const. and (2) the Richtmyer–Meshkov instability in the acceleration is impulsive, e.g., caused by a shock.

#### Rayleigh-Taylor Instability

We consider the nearly incompressible case suggested by Tabak;<sup>20</sup> we set  $\gamma = 10$  in both gases. The computational domain consists of a box with axial extent,  $0 \le z \le 2\lambda$ . The initial equilibrium density distribution is

$$\rho = \begin{cases} 10(z/l)^{1/9} & 0 \le z \le \lambda \\ 100(z/l)^{1/9} & \lambda \le z \le 2\lambda \end{cases}$$
 (28)

where  $l = 1.1\lambda$ . We run this problem in the Lagrangian mode. At t = 0, we initialize the grid with a sinusoidal

perturbation at  $z = \lambda$  with amplitude  $a = 2.25 \times 10^{-4} \Delta z$  **Richtmyer–Meshkov Instability** 

perturbation at  $z=\lambda$  with amplitude  $a=2.25\times 10^{-4}$   $\Delta z$  where  $\Delta z=2\lambda/N_z$  is the unperturbed grid spacing. The perturbation is feathered into the z direction three zones deep on either side of the interface. We consider three problems. In each one, we initialize one-half wavelength in the transverse direction. In all cases we use 40 cells in the z direction. The problems are

- A 2-D case with 20 cells in the x direction. The perturbation is given by Eq. (26) with  $z_0 = \lambda$ .
- A 3-D case with 20 cells in both *x* and *y* directions. The perturbation is given by

$$\delta z = z_0 = a\cos(k_x x)\cos(k_y y)$$
 , and  $k_x = k_y$ .

• A 3-D case with 20 cells in both x and y directions. The perturbation is as above except  $k_x = 3k_y$ . The wavelengths are chosen so that all cases have the same total wave number  $k = \sqrt{k_x^2 + k_y^2}$ .

For constant g, Eq. (27) implies that the perturbation grows exponentially with growth rate  $\Gamma = \sqrt{Agk}$ . Hence, all three cases should grow at the same rate. With  $k = 2\pi/0.001$  and g = 0.33671717, we obtain  $\Gamma = 41.6$ . Figure 2 displays  $\log_{10}(a)$  vs t for  $t \le 0.25$  and  $t \ge 0.05$ , after the system has settled into an eigenmode. After 0.25, the mode reaches an amplitude of approximately 0.1  $\lambda$  and saturates. The numerical  $\Gamma$  is within 1% of the theoretical value. This test problem shows the ability of ICF3D to model the linear regime thereby demonstrating the accuracy of the method. In Fig. 3, we display the interface at t = 0.14 for the  $k_x = k_y$  case.

In this problem, analyzed by Richtmyer,<sup>21</sup> a perturbed interface interacts with an incident planar shock. Before the shock's arrival, the interface is in equilibrium since the two gases have equal pressures. From 1-D theory (no perturbation), a shock-on-contact interaction results in a displacement of the interface and two waves, one transmitted, another reflected. The transmitted wave is always a shock. The type of reflected wave depends on the unshocked density of the gas on the side from which the shock is traveling. If this side is of higher (lower) density than the other gas, the transmitted wave is a rarefaction (shock). If the "shock-incident" side is of higher density, the amplitude of the perturbation changes sign. In either case, after the interaction, the amplitude is abruptly diminished, but later grows linearly in time.

For the simulation, we run in the Eulerian mode to avoid tangling the mesh and to follow the growth into the nonlinear regime. In the results, z is the horizontal direction and x the vertical. We use the specifications relayed by Dimonte.<sup>22</sup> The domain consists of  $(0,0) \le (z,x) \le (0.04,0.005)$ . We simulate only half a wavelength along x and apply symmetry conditions at transverse boundaries. For z, we apply symmetry at z=0, and inflow at z=0.04. The initial perturbation is given by Eq. (26) with  $a=10^{-3}$ , k=200  $\pi$ , and  $z_0=0.03$ . The initial conditions are characterized by three regions: the left  $z < z_0$ , the right unshocked  $z_0 \le z < z_s$ , and the right shocked  $z_s \le z$ , where  $z_s=0.32$  is the position of the incident, planar shock. The conditions are described in cgs units in Table 4.

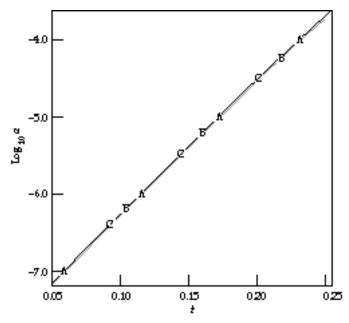


FIGURE 2. Rayleigh–Taylor problem showing common logarithm of mode amplitude vs time. Labels A, B, and C correspond to 2-D, 3-D square, and 3-D asymmetric cases, respectively. (50-06-1296-2786pb01)

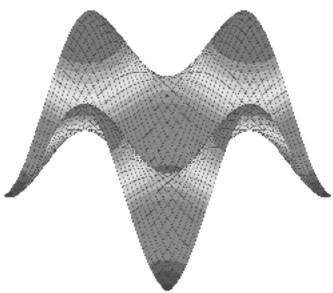


FIGURE 3. Rayleigh–Taylor problem showing perturbed interface at t = 0.14 ns. (50-06-1296-2787pb01)

TABLE 4. Conditions (cgs units) used in the Richtmyer–Meshkov instability problem.

Region	Density	Velocity	Pressure	γ
$z < z_0$	0.12	0	$4.92048 \ 10^{10}$	1.45
$z_0 \le z < z_s$	1.7	0	$4.92048 \ 10^{10}$	1.8
$z < z_0$	3.6617120	$-2.453647 \ 10^5$	$2.4\ 10^{11}$	1.8

With these conditions, we expect a reversal of the interface, followed by a growth of the amplitude and an eventual nonlinear stage setting in. In Fig. 4, we present a time sequence of p. Fig. 4(a) shows the initial condition. In Fig. 4(b), t = 7 ns, the shock has already hit the interface, producing a transmitted shock and a reflected rarefaction. Note the reversal of the interface. The results in Figs. 4(c) and 4(d), at t = 22 ns and 37 ns respectively, show the onset of the nonlinear stage. In Fig. 4(e), t = 53 ns, the interface is beginning to form spikes. By this time, the shock has reflected off the left boundary but has not yet interacted with the interface. By the end of the simulation, t = 77.5 ns Fig. 4(f), the reflected shock has passed through the interface. The interface is now severely deformed. At this time the shock is at z = 0.014 and has itself developed a slight deformation. These results are in qualitative agreement with the ones published by Cloutman et al.<sup>23</sup>

#### Nonlinear Diffusion Problem

We now consider the spherically symmetric, nonlinear diffusion equation

$$\frac{\partial T}{\partial t} = \frac{a}{r^2} \frac{\partial}{\partial r} \left( r^2 T^n \frac{\partial T}{\partial r} \right) , \qquad (29)$$

where a and n are constants. If the initial condition is a delta function and the domain extends to infinity, the analytic solution is given in Ref. 24. By conservation of energy (heat), the solution satisfies

$$\int_0^\infty 4\pi r^2 T dr = Q \quad .$$

The analytic solution is given in terms of the radial position of the front  $r_f$  and the temperature at the center  $T_c$  in

$$T = T_{\rm c} \left( 1 - r^2 / r_{\rm f}^2 \right)^{1/n}, r \le r_{\rm f} \quad , \tag{30}$$

$$r_{\rm f} = \xi \left(aQ^n t\right)^{1/(3n+2)}$$
 , (31)

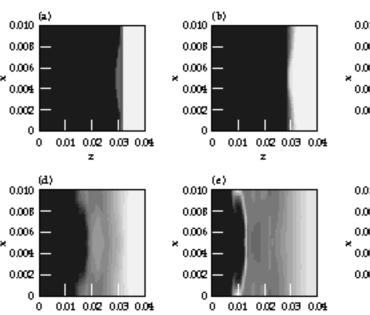
and

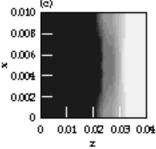
$$T_{\rm c} = \left[\frac{n\xi^2}{2(3n+2)}\right]^{1/n} \left[\frac{Q^2}{(at)^3}\right]^{1(3n+2)} . \tag{32}$$

The constant  $\xi$  depends only on the conductivity exponent n. For our test, we use n = 3 and obtain

$$\xi|_{n=3} = 0.8979$$

For the numerical test, we set a = Q = 1 and discretize 1/8 of a sphere:  $0 \le r \le 1$  and  $0 \le \theta$ ,  $\phi \le \pi/2$ ,





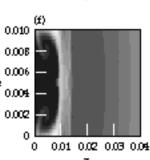


FIGURE 4. Richtmyer–Meshkov problem showing density  $(g/cm^3)$  at various times. (a) is at t=0 ns; (b) at t=7.0 ns, (c) at t=22.2 ns, (d) at t=36.8 ns, (e) at t=53.3 ns, and (f) at t=77.5 ns. (50-06-1296-2788pb01)

where  $\theta$  denotes the polar angle. We impose symmetry conditions along  $\phi = 0$  and  $\theta = \phi = \pi/2$ . Along r = 1 we also impose symmetry, but this condition is unnecessary since we halt the calculation when  $r_f \approx 0.8$ .

We generate the grid in spherical coordinates by constructing a logical (k, l, m) grid, where  $(1, 1, 1) \le (k, l, m) \le (k_{\max}, l_{\max}, m_{\max})$ , set  $(k_{\max}, l_{\max}, m_{\max}) = (21, 9, 9)$ , and use uniform grid spacing. There are  $(k_{\max} - 1) (l_{\max} - 1) (m_{\max} - 1) = 1280$  cells. Before running, we convert the grid into Cartesian coordinates. This creates cells of all admissible types since the spherical to Cartesian coordinate transformation results in degenerate nodes. There are  $(m_{\max} - 1) (k_{\max} - 2)$  prisms along the z axis. At the origin there are  $m_{\max} - 1$  tetrahedra and  $(m_{\max} - 1) (l_{\max} - 1)$  pyramids. The remaining cells are hexahedra.

In Fig. 5 we present the numerical solution at t = 0.2821 ns along each Cartesian coordinate axis. The analytic solution given by Eqs. (30) through (32) is also displayed as curve D. The numerical solutions on the three axes are nearly indistinguishable. Examination of the data shows that the central temperature, 0.0671, is within 1% of the analytic value, 0.0676.

#### **Coupled Physics Problem**

The final test problem was constructed to test the interaction of all the physics packages presently available in ICF3D: a real gas EOS, hydro motion, Spitzer-Härm heat conduction, and radiation diffusion. The problem models a shock tube filled with beryllium (SESAME table no. 2020); the numbers used in the simulation are not meant to model any experiment.

We run this in a 1-D mode, i.e., only one cell in each of the x and y directions. The initial conditions vary only with z. The initial density  $\rho$  is 1.0 gm/cc everywhere. We initialize with a higher (1 keV) temperature on the left, and on the right, we set T=0.1 keV. The initial velocity is set to zero. For the radiation, we use only one group and set the opacity to a constant 1 cm<sup>2</sup>/gm. We impose symmetry conditions on the left and right boundaries and run in the Lagrangian mode, using 203 zones in the calculation. Initially, the grid is uniform.

In Fig. 6 we display the pressure at t = 0.1 ns when ICF3D computes the joint effect of hydrodynamics, radiation transport, and heat conduction. Since there are no analytic solutions for this problem, we compare the ICF3D calculation to one done with LASNEX. The

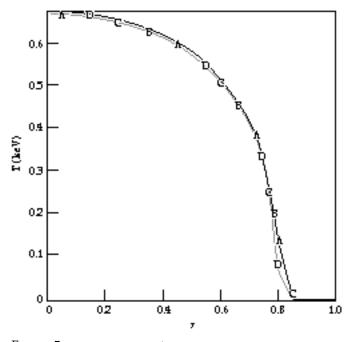


FIGURE 5. Diffusion problem showing temperature profile vs radius along coordinate axes x, y, and z (curves A, B, and C) at t = 0.2821 ns. Curve D is the analytic solution. (50-06-1296-2789pb01)

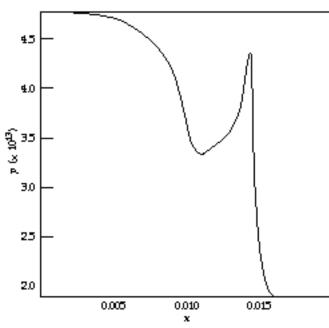


FIGURE 6. Shock tube problem results from ICF3D showing p vs z. All physics running. (50-06-1296-2790pb01)

LASNEX result (Fig. 7) agrees with ours: similarly shaped curves with the same pressures at the boundaries, the same shock location, and so forth. The main differences are that ICF3D gives a slightly sharper shock front and a sharper pressure peak behind the shock.

#### Conclusion

At the moment, ICF3D is an experimental code. We have made many advances, but much more needs to be done before ICF3D may be called a real design tool. Nevertheless, it is useful to list our accomplishments to date and our plans for the future.

After running numerous test problems, we are convinced of the viability of the hydrodynamic scheme. It may require some revision and modification, but it is fundamentally sound and is well suited for ICF design calculations. As opposed to higher order schemes like PPM,<sup>25</sup> ICF3D's scheme is very compact. Hence, it parallelizes easily.

The other physics modules are straightforward 3-D extensions of standard FE methods. Our previous experience with FE in LASNEX (see accompanying article on p. 150) shows that piecewise linear functions suffice for diffusive transport. Our other primary

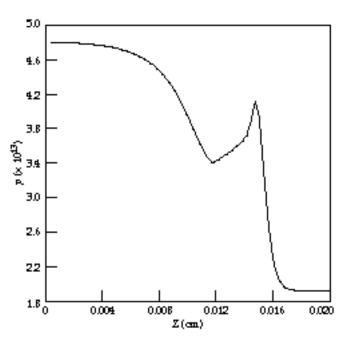


FIGURE 7. Shock tube problem results from LASNEX showing p vs z. (50-06-1296-2791pb01)

concern is whether or not the inherently nodal representation of diffusion type problems clashes with the fundamentally cellular representation of the hydro variables. Again, experience in LASNEX as well as the encouraging results from the "Coupled Physics Problem" section (see p. 178) alleviates this concern. Hence, we should be able to reap all of the benefits from FE methods.

So far, the parallelization efforts are a resounding success. In the past year, most of the hydro development effort has been done on the LLNL CRAY T3D because we obtain results that much faster when running on 32 PEs. We are now finishing parallelizing the linear solver and look forward to running coupled problems in parallel.

We have found the C++ programming language to be a helpful tool in organizing a physics code of the complexity of ICF3D. Our experience has given us new ideas on how to organize even larger codes for ease of maintenance and how to program them for maximum speed. We plan to implement these ideas so that ICF3D can grow into the best possible full-scale production code. The full-scale code will also benefit from our research in such areas as numerical hydrodynamics and the use of parallel processors to solve linear equations for diffusion problems.

#### **Notes and References**

- 1. Furthermore, the time to develop codes does not scale linearly. For example, LASNEX represents a nearly 100 man-year effort; yet 200 developers would not be able to reproduce LASNEX from scratch in six months.
- 2. S. W. Haney, Computers in Physics 8 (6), 690-694 (1994).
- S. W. Haney, Lawrence Livermore National Laboratory, CA, private lecture series (1996).
- D. S. Kershaw, M. K. Prasad, and M. J. Shaw, "3D Unstructured Mesh ALE Hydrodynamics with the Upwind Discontinuous Finite Element Method," Lawrence Livermore National Laboratory, Livermore, CA, UCRL-JC-122104 Rev.1 (1996).
- P. F. Dubois, K. Hinsen, and J. Hugunin, Computers in Physics 10

   (3), 262-267 (1996). Python Documentation [online]. Available: www.python.org.
- A. I. Shestakov, J. A. Harte, and D. S. Kershaw, J. Comp. Physics, 76 (2), 385–413 (1988).
- 7. "SESAME: The Los Alamos National Laboratory Equation of State Database," Eds. S. P. Lyon and J. D. Johnson, Los Alamos National Laboratory Report LA-UR-92-3407. Also: "T-1 Handbook of Material Properties Data Bases," K. S. Holian, Ed., Los Alamos National Laboratory Report LA-10160-MS November 1984.

ME 10102 COBE

- 8. S. A. Brown, "TABLib User's Manual," Lawrence Livermore National Laboratory internal report (1995).
- 9. A. Lapidus, J. Comp. Phys. 2, 154-177 (1967).
- T. B. Kaiser and J. A. Byers, Bull. Am. Phys. Soc. 41 (7), 1555 (1996).
- 11. L. Spitzer, Jr., and R. Härm, Phys. Rev. 89 (5), 977-981 (1953).
- 12. A. Friedman and D. S. Kershaw, 1982 Laser Program Annual Report, pp. 3–68, Lawrence Livermore National Laboratory, Livermore, CA, UCRL-50021-82 (1982).
- 13. G. H. Golub and C. F. Van Loan, *Matrix Computations*, Second Edition (John Hopkins Univ. Press, Baltimore, 1989).
- A. I. Shestakov and D. S. Kershaw, "ICCG on Unstructured Grids," Lawrence Livermore National Laboratory informal report, April 30, 1996. Contact by email: shestakov@llnl.gov.
- P. F. Dubois, A. Greenbaum, and G. H. Rodrigue, Computing 22 (3) 257–268 (1979).
- R. S. Varga, Matrix Iterative Analysis (Prentice Hall, Inc., Englewood Cliffs, N.J., 1962) p. 84.

- 17. P. F. Dubois, Computers in Physics 8 (1), 70–73 (1994).
- 18. G. Furnish, Gyrokinetic Simulation of Tokamak Turbulence and Transport in Realistic Geometry, Ph.D. thesis, Appendix C, Univ. of Texas, Austin, 1996, Institute of Fusion Studies doc. IFSR-740. [Also available online at http://dino.ph.utexas.edu/furnish/c4.]
- 19. G. Taylor, Proc. R. Soc. London Ser. A. 201 (1095), 192–196 (1950).
- M. Tabak, D. H. Munro, and J. D. Lindl, *Phys. Fluids B* 2 (5), 1007–1014 (1990).
- R. D. Richtmyer, Commun. Pure Appl. Math. 13 (2), 297–319 (1960).
- 22. G. Dimonte and B. Remington, *Phys. Rev. Lett.* **70** (12), 1806–1809 (1993).
- L. D. Cloutman and M. F. Wehner, *Phys. Fluids A* 4 (8), 1821–1830 (1992).
- 24. Ya. B. Zel'dovich and Yu. P. Raizer, *Physics of Shock Waves and High-Temperature Hydrodynamic Phenomena*, Vol. II, Ch. X, Sec. 6 (Academic Press, New York and London, 1967) pp. 668–672.
- P. Colella and P. W. Woodward, J. Comp. Phys. 54 (1), 174–201 (1984).

## NIF DESIGN OPTIMIZATION

W. Williams
C. Orth
R. Sacks
J. Auerbach
J. Lawson
M. Henesian
K. Jancaitis
P. Renard

## Introduction

There are many potential designs for the proposed National Ignition Facility (NIF) that would be expected to meet the machine's functional requirements, but at widely varying costs. Given the size of this project, an effort has been made to assure that we are, indeed, designing the least expensive option possible.

During the previous three years of NIF design, we have considerably refined computer codes used for such optimization analysis. During the conceptual design phase of NIF, we used a simplified code, culminating in the configuration presented in the *Conceptual Design Report* (CDR)<sup>1</sup> published in May 1994. For the NIF Advanced Conceptual Design (ACD), we used a grouping of several codes that allowed design optimization coupled with more sophisticated propagation models. In this article, we review some of the assumptions and modeling procedures used in both sets of computer codes. We also summarize our results from the ACD optimization activity that resulted in the current (Title I) NIF design.

# Computer Codes Used in NIF Optimization

Two computer codes were primarily used in NIF optimization: CHAINOP and PROPSUITE. The multiplatform code CHAINOP is the original optimization tool used during the CDR design process for NIF. CHAINOP's goal is to combine models of laser chain layout, cost, and performance in a way amenable to speedy analysis of several thousand potential system designs, identifying those least expensive configurations that fulfill functional requirements. (A laser "chain" refers to the sequence and spacing of optical components in one beam of a large laser system; there are 192 laser chains in NIF.) CHAINOP permits certain kinds of constraints, such as

damage fluence limits, B-integral limits, and irradiance modulation limits, that guide the optimization into safe laser designs via simple, often heuristic models. With a ray-trace model for tracking beam size changes and single-value loss and saturating gain models for energetics, CHAINOP reveals little specific detail of spatial and temporal characteristics of pulse propagation. These apparent simplifications are somewhat deceptive, however. Many of the heuristic models contained in CHAINOP are the result of detailed studies of physical processes, and allow the code to predict reliably laser designs that are consistent with the more robust modeling tools that were subsequently developed.

As our confidence grew in the modeling efforts for individual processes like diffraction propagation, frequency conversion, amplifier pumping, and optics damage, we were able to assemble individual computer codes into a more sophisticated optimization package called PROPSUITE. The backbone of PROPSUITE is a beam propagation code called PROP92 that uses Fourier methods to follow temporal and spatial details of a laser pulse as it traverses an optical chain. Among other things, this code includes effects of paraxial, nonlinear beam diffraction, beam movement for vignetting purposes, energy clipping at pinholes, and clipping of the beam on a hard aperture. It also allows for inclusion of detailed phase representations of optics surfaces. For a detailed discussion of PROP92, see p. 207 of this *Quarterly*. During optimizations, the laser was modeled along the direction of beam propagation, and in one transverse dimension—in this case, along the horizontal axis. The spatial resolution considered was up to ~32,000 points over a 50-cm aperture, sufficient to resolve the fine spatial features of the optics surfaces. Simulations involving both transverse dimensions are too slow to put in an optimization loop; however, designs from the one-dimensionsal (1-D) optimizations have been further analyzed and confirmed in two-dimensional (2-D) simulations.

The PROPSUITE collection also includes frequencyconversion computer codes with either plane-wave models or a 1-D spatio-temporal model of conversion (THGFT02 and THGXTZ002). Specifics of amplifier flashlamp pumping are modeled by a 2-D optical raytrace computer code. The thermo-mechanical effects that cause pump-induced distortions are handled with public-domain software TOPAZ and NIKE3D. PROPSUITE also used the SUPERCODE shell, exercised extensively for tokamak systems studies, to perform multivariable optimizations. Additional codes were developed to do system layout calculations, based on rules in CHAINOP, and to tie the codes together. For optimizations, calculations of several thousand possible designs were done on a cluster of 28 workstations using parallel processing with the public domain software PVM.

In the following sections we discuss some of the basic modeling concepts contained in both CHAINOP and PROPSUITE.

#### **Chain Layout**

Both CHAINOP and PROPSUITE were designed around the NIF multipass architecture of a relayed, mirrored cavity containing one or two amplifiers, a spatial filter, and a Pockels cell switch/polarizer. The cavity is followed by a booster amplifier, transport spatial filter, transport mirrors, frequency converter, final focusing lens, kinoform diffractive optic plate, and debris shield. A schematic of the layout is shown in Fig. 1. Other architectures were considered for NIF over the years, including Nova-like Master Oscillator–Power Amplifiers (MOPAs), two-pass systems, and others. CHAINOP and PROPSUITE have

also been employed to look at the French Reverser/Uturn architecture.

For most NIF optimizations, this basic architecture was fixed, with the thickness of laser slabs and the number of slabs in each amplifier being the only layout parameters varied.

#### Laser Beam Size

CHAINOP and PROPSUITE use the same approach for determining the size of the laser beam that can be fit within a chain, starting with the hard (metal) aperture of the laser. This aperture can be square or rectangular, the current NIF design being 40 cm square. Determination of the size of beam that can fit within this aperture is dependent on the component spacings in the layout and necessary alignment tolerances. Component spacings determine the slight angle of the beam with respect to the chain axis necessary to pass through different pinholes on each pass in the spatial filters. As this angle increases, the size of beam that can fit within the hard aperture is reduced. This reduction in fill factor is known as vignetting. Separate pinholes for each pass are necessary primarily because ablated plasma on the edge of a pinhole can potentially block that pinhole to any subsequent passes of the beam. Pinhole separations are set by the more restrictive of either machining constraints in pinhole fabrication or sizes of optics that sit near the pinhole plane. These pinholeplane optics include a mirror to inject the beam on the first pass in the transport spatial filter and a beam dump to catch that small fraction of the beam in the cavity not ejected by the Pockels switch on switch-out. The cavity filter pinhole spacings in NIF are set by machining constraints.

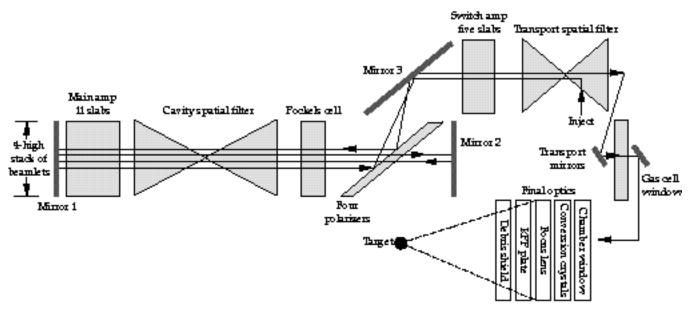


FIGURE 1. Schematic of NIF layout (not to scale). (70-00-1296-2745pb01)

An alignment tolerance of ~0.5 cm is included around the injected beam inside the hard aperture. This allows for beam or optics misalignment in the chain.

The beam intensity is nominally flat-topped, spatially, and tapers to zero at the edges. This taper is modeled with an error function, a shape somewhat more robust against diffraction ripples than some other shapes. Steeper edges increase the beam fill factor but simultaneously cause intensity spikes from edge diffraction and beam clipping at the pinholes. The taper distance of ~3 cm in the baseline design was determined as part of our optimization process.

The variables studied during NIF optimization affecting the beam size were hard aperture, number of laser slabs (which affects vignetting loss), and apodization tolerance.

## Amplifier Gain and Pump-Induced Distortions

Gain of an amplifier slab depends on the stored energy density in the slab. This in turn depends on the pumping from flashlamps, Nd<sup>3+</sup> concentration, slab thickness, and depumping due to Amplified Spontaneous Emission (ASE). The pumping term from flashlamps depends on the number of lamps per slab, their diameter, and electrical power pumped into the lamps. Both CHAINOP and PROPSUITE used a representation of the emission spectrum of flashlamps as a function of pumping power, absorption spectrum of laser glass, ASE depumping rate, and lamp-to-slab coupling efficiency. Coupling efficiency was based on 2-D ray-trace calculations, validated by measurements on Beamlet (a prototype of one NIF beamline in operation at LLNL), and is a function of reflector geometries, component spacings, slab thicknesses, and other parameters. Ray tracing was not included in the optimization directly. Rather, both codes used information from previous runs that covered the parameter space of interest.

Because PROPSUITE considers propagation effects on the beam spatial profile, we included pump-induced distortions in modeling. This distortion is the local steering imposed on the beam caused by the nonuniform heating of laser slabs and their subsequent deformation. Predicting this distortion requires three-dimensional (3-D) thermo-mechanical modeling of laser slabs under pumping conditions, giving time-dependent slab motion. These are lengthy computations, so prior to doing optimizations, a large number of cases were run covering ranges of the variables of interest. These results were stored in a database in which the code could interpolate to find distortions for any given combination of variable values.

Laser slab gain in both CHAINOP and PROPSUITE was modeled using the Frantz–Nodvick equations,

which describe both the exponential growth of the beam fluence and the decay of the population inversion.<sup>2</sup> These equations are based on assumptions that (1) pumping to the upper laser level is negligible during the time the laser pulse extracts energy; (2) gain reduction due to spontaneous emission is negligible compared to stimulated emission during extraction; and (3) the cavity geometry is such that the laser pulse does not overlap on itself in space at any given time. With these approximations, extraction is only a function of fluence, and information regarding the detailed temporal shape of the pulse is not necessary. This allows us to reduce calculation time significantly by approximating a temporally shaped pulse with a temporally square pulse, while still accurately calculating the energetics of extraction and saturation. This is described in more detail below in the section entitled Temporal Pulse Shape.

The variables studied during NIF optimization affecting the gain and pump-induced distortion were thickness of the laser slabs, Nd<sup>3+</sup> concentration in the laser glass, duration of the flashlamp pumping pulse, and number-per-slab and diameter of flashlamps.

#### **Optics Losses and Aberrations**

Optics losses in CHAINOP are simply subunity multipliers on beam energy and power. They include representations of laser glass surface scatter and bulk transmission, transmission of antireflection (AR) coated optics at  $1\omega$  and  $3\omega$ , bulk absorption of KDP/KD\*P at  $1\omega$  and  $3\omega$ , and reflectivity of high-reflectivity (HR) coated mirrors. Bulk absorption of the fused silica is negligible for thicknesses of optics considered in NIF. Transmissivity and reflectivity of the polarizer were used to represent several effects, including coating reflectivity, BK7 substrate absorption, switching efficiency of the Pockels cell, and depolarization fraction of the beam due to stressed optics. Losses were not temporally dependent.

Losses were similarly included in PROPSUITE. In addition, by using a propagation code, it became possible to include spatially dependent representations of the surface finishes and bulk homogeneity properties of optics in the chain. This information was taken from a variety of measured parts chosen to reflect projected NIF manufacturing and finishing techniques. Because considerably fewer parts had been measured than were needed to represent an entire laser chain, it became necessary to synthesize the 100-plus necessary files. We did this by assuming that, for example, amplifier slabs will have the same finish as the measured parts, as quantified by the Power Spectral Density (PSD) curve.<sup>3</sup> We assumed, however, that phases of the Fourier components of the surface representations are randomized from one slab to another, resulting in less constructive addition of phase noise from slab to

slab. These aberration files are the dominant source for beam intensity and phase modulation in simulations.

During NIF optimization, losses and aberration files were not varied from a baseline set of assumptions.

#### Temporal Pulse Shape

NIF will use temporally shaped pulses for many experiments, including ICF ignition. To reduce calculational requirements, these pulses were represented in CHAINOP by an equivalent square pulse, having a power the same as the required peak power for a shaped pulse, and having the same total energy. This is a reasonable approximation because the Frantz–Nodvick equations depend only on beam energy (fluence), not the time history of power over the nanosecond durations of interest for NIF. Consequently, temporally square pulses of a given energy see the same overall gain as temporally shaped pulses of the same energy.

In CHAINOP, a square pulse is divided into two pieces: the main body and the tail end. Because gain in a laser slab is dependent on fluence history through the slab previous to that point in time, as the amplifier saturates, the tail end of the pulse sees a significantly lower gain than the front. A pulse that will be temporally flat at the end of the chain must, therefore, be temporally increasing at injection. Beam filamentation —catastrophic self-focusing due to the effects of a nonlinear refractive index—depends on the instantaneous beam irradiance. Consequently, monitoring the power of the pulse's tail in CHAINOP allows us to track and limit the tendency of the beam to filament.

In contrast, PROPSUITE is capable of tracking the beam shape at an arbitrary number of times. We used eight time steps to represent the temporally shaped indirect-drive ICF ignition pulse (See Fig. 2). For this pulse, the maximum effect from the nonlinear index of refraction of the optics occurs somewhat before the end of the pulse and at a time that varies with position in the chain, justifying this more detailed modeling.

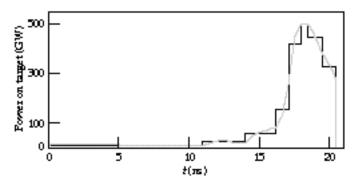


FIGURE 2. Temporally shaped pulse used for optimizations. The gray line is the actual pulse shape needed on target. The black line is the eight-step approximation to this shape used in modeling. (70-00-1296-2748pb01)

#### **Frequency Conversion**

The frequency conversion efficiency ( $3\omega$  irradiance/ $1\omega$  irradiance) can be a function of space and time given temporal or spatial variations of the beam. Since neither temporal nor spatial modulation is calculated in CHAINOP, both peak-power conversion efficiency (averaged across the beam aperture) and energy conversion efficiency for temporally shaped pulses needed for NIF are code inputs. Power conversion efficiency is used to determine the filamentation threat to the  $3\omega$  optics and peak power on target. Energy conversion efficiency is used to determine energy on target and damage threat calculations.

In PROPSUITE both temporal and spatial intensity information are available. Consequently, we use three codes to calculate conversion efficiency directly. A plane-wave/temporally varying field code is used to predict the  $1\omega$  temporal shape that would give the required  $3\omega$  pulse on target for any given converter design. The spatially and temporally resolved  $1\omega$  pulse at the converter with this temporal shape is then generated with PROP92. The conversion of this beam is then calculated with a full spatio-temporal code that includes the capability of having converter-crystal surface-finish noise added to the beam phase. See the article "Frequency-Conversion Modeling" on p. 199 of this <code>Quarterly</code> for a discussion of these frequency conversion codes.

For NIF optimizations, thicknesses of the type I doubler (KDP) and type II tripler (KD\*P) and the detuning angle of the doubler crystal were varied independently. To allow for difficulties in aligning crystals with respect to the beam, and for other problems, conversion calculations for the  $1\omega$  beam were actually done at three detuning angles of the doubler, a variable center angle and  $\pm 30~\mu rad$  around that. A weighted average of the three was then used to determine energy on target.

#### **Beam Modulation**

Since CHAINOP is zero-dimensional, the spatial intensity/fluence modulation of the beam cannot be directly calculated. This information, however, is necessary for evaluating damage to optics from high fluences. Accordingly, a semi-empirical rule was implemented that the peak-to-mean modulation in fluence  $(\phi)$  is given by

$$\phi_{\text{peak}} = \phi_{\text{avg}} (1.3 + 0.1 e^{\Delta B})$$
 (1)

 $\Delta B$  is the B integral accumulated by the beam between pinhole passes (using approximately the mean spatial intensity). The B integral, in general, is defined as

$$B(z) = \frac{2\pi}{\lambda} \gamma_{\rm nl} \int_0^z I(z') dz' = \frac{80\pi^2 n_2}{\lambda cn} \int_0^z I(z') dz' \quad , \tag{2}$$

and is the nonlinear phase retardation (in radians) experienced by a beam of intensity I ( $W/m^2$ ) and wavelength  $\lambda$  (m) in traversing a medium of thickness z (m) with refractive index  $n_0$  and nonlinear index  $n_2$  (from  $n = n_0 + n_2 | E|^2$ ). (The nonlinear index may also be a function of z in nonisotropic materials.) Bespalov–Talanov theory predicts<sup>4</sup> that small-scale spatial ripples in the beam will grow nonlinearly, with the most unstable perturbations growing as  $e^{\Delta B}$ . This, combined with the fact that beam modulation past a scatterer in the absence of nonlinear effects is no more than 1.4:1, and that in large laser systems it has been experimentally observed that beam modulation is ~2:1 after a  $\Delta B$  of 2 radians, leads to Eq. (1).

In PROPSUITE, beam modulation is calculated directly, including diffraction and nonlinear effects.

## Optics Damage Thresholds from High Fluence

High laser fluences on optics over nanosecond-pulse durations of interest for NIF can cause surface or bulk damage sites. This damage is seen as pits in the surface or coating of an optic, or damage spots in bulk. The fluence threshold when this damage occurs is experimentally found to be a function of the pulse duration. For temporally Gaussian pulses, the experimental database is well matched by the functional form fluence damage threshold  $(J/cm^2) = a\tau^b$ , where a and b are experimentally determined and material-dependent constants and  $\tau$  (ns) is the full-width-half-maximum of the pulse.

NIF pulses will typically range in temporal shape, and may be significantly non-Gaussian. To account for the effect of arbitrarily shaped pulses on damage threshold, we used a damage diffusion model<sup>5</sup> to determine the damage thresholds. Because the ICF indirect-drive ignition pulse shape used for optimizations is more square than Gaussian, the result is a 5 to 20% reduction in damage thresholds from those for a Gaussian pulse for various materials and coatings. This diffusion model adjustment of damage threshold has not yet been experimentally tested.

The  $3\omega$  optics (tripler, final focus lens, kinoform phase plate, and debris shield) are exposed to 1, 2, and  $3\omega$  light simultaneously. In general, damage fluence limits at the longer wavelengths are significantly higher than at shorter wavelengths, but we have found no additional information regarding multiwavelength interactions. Accordingly, we have based our damage limits on the  $3\omega$  fluence only, with a damage threshold decreased by 10% from its value under monochromatic illumination. This assumption remains an area of uncertainty in our modeling, since we predict system performance to be limited by  $3\omega$  damage in the tripler.

Both CHAINOP and PROPSUITE used the same damage thresholds.

#### **Filamentation Risk**

Filamentation damage (or "angel hair" damage) is seen when the nonlinear index of refraction of an optical material causes self-focusing of small sections of a high-intensity beam. These sections may start out as small-intensity (a few percent above average) ripples or bumps of a few millimeters in size on the beam. As they self-focus, they decrease in size to hundreds of micrometers in diameter or smaller, and increase to very high irradiances (>100 GW/cm²). At some point the irradiance is high enough to damage the material and leave a visible track.

This filamentation growth is a complex function of the beam irradiance, nonlinear index of the material, and size and shape of the irradiance perturbation that self-focuses. It is also an inherently three-dimensional problem, making modeling calculationally intensive, although possible with present tools. However, it is in fact not necessary to model growth of a filamenting bump to the point of damage in order to design NIF because we desire to be far from this limit. Consequently, a more heuristic approach was used in the optimizations, based on the experimental observation that *if small-scale beam noise is present*, large lasers tend to begin to break up into filaments after the beam has experienced a B integral of ~2 radians. This deserves a little more explanation.

The presence of small-scale beam noise is important because bumps of small size (a few millimeters) grow significantly faster than large-scale modulations. This difference in growth rate has been understood for many years.<sup>4</sup>

Elimination of these small-scale noise ripples is one of the purposes of spatial filters in large laser systems. Each laser chain in NIF will have two such spatial filters, one in the cavity, and one for transport to the target, as shown in Fig. 1. At the focal plane of each filter there is a pinhole through which the beam passes. The pinhole size, however, is such that only spatial frequencies present in the beam (in either phase or intensity) of less than a certain value can pass through the pinhole. Power at frequencies higher than this cut-off value is dumped on the surface around the hole. For NIF this cut-off half-angle is 100 µrad, corresponding to spatial ripple wavelengths of 1 cm. The net effect of this spatial filtering is that perturbations with transverse wavelengths less than 1 cm are clipped off at the pinholes. Consequently they cannot grow for more than the B integral they experience between pinhole passes.

In the chain design, then, we can limit B integral seen by the laser between pinholes to a certain value as a surrogate for calculating the beginnings of filament growth. For NIF optimizations, the between-pinhole B integral limit (also known as  $\Delta B$ ) was set to 2.2 rad. This constraint was used in both CHAINOP and PROPSUITE.

## Optimization Variables and Constraints

Techniques used in laser system optimizations are discussed in the article "Laser Optimization Techniques" on p. 192 of this *Quarterly*. Our codes were implemented with simplex, parabolic interpolation, and gradient-search routines. The figure of merit that the optimizer attempted to minimize by changing variables, and, at the same time, honoring several constraints, was system cost divided by energy on target. These variables included hard aperture, injection fluence, number of laser slabs in each amplifier, laser slab thickness, Nd<sup>3+</sup> concentration in laser slabs, flashlamp packing fraction, and apodization edge width. In using a gradient-search optimization technique, we took care in code development that there were no discontinuities in value or 1st derivative of figure of merit or constraints, as a function of these variables. Constraints that the optimizer used included energy on target, fluence damage to components, and  $\Delta B$  limits.

#### **Cost Algorithms**

We have used different levels of cost modeling during development of the NIF design. Those used in later calculations included cost scaling rules, as a function of the optimization variables, for ~30 nonoptical subsystems of NIF, and ~140 optical cost categories. These rules were built on a cost database in the NIF *Conceptual Design Report*, and were provided by the NIF engineering team.

## **NIF Optimizations**

Optimization studies with CHAINOP resulted in the CDR design. Similar studies with PROPSUITE resulted in the Advanced Conceptual Design (ACD) layout. The current NIF design (Title I, or preliminary design) has changed little overall since the ACD, so, for purposes of this discussion, the two will be considered equivalent. In this section, we describe the ACD optimization process and compare those results to the conceptual design.

During the ACD, we used three optimization approaches. In two approaches, optimization routines were used to find the least expensive design that meets functional requirements. These methods yielded a high-quality answer, but gave limited insight into tradeoffs in design options. The third method was to evaluate a large number of separate configurations manually, covering some range of parameter space on a uniform grid, and to graphically sort data according to design criteria. This approach enables greater understanding of the design space, but does not offer assurance that the best possible design has been included on the grid. The combination of this and the

optimization approaches gives confidence that available design space has been explored thoroughly.

Results from these methods are discussed below.

### **Studies Using Optimizing Software**

By decision of the NIF project, some parameters were not varied during the final ACD optimization. Specifically, after some preliminary results, the optical clear aperture of the laser was fixed at 40 cm, laser slab thickness at 4.1 cm, and transport spatial filter length at ≥60 m. The optical clear aperture and slab thickness values were both larger than those found by the unbiased application of our optimization process. They were chosen to increase the 1ω performance margin (larger stored energy) and to decrease the risk of beam filamentation (lower between-pinhole B integral). The minimum transport spatial filter length was set primarily from concerns about pinhole blowoff in the last beam pass through the filter. (A shorter filter would proportionately decrease the pinhole size necessary to filter features of given scale. This would both increase the irradiance on the pinhole edge and decrease the closure distance.) The detailed physics of pinhole closure is currently poorly understood, making a more conservative choice advisable. Other values for these parameters would have saved additional money, but at the cost of decreased experimental flexibility and increased technical risk.

Given these constraints, we performed an optimization to determine the least expensive design overall, and also the least expensive design with no amplifier adjacent to the Pockels cell switch (the current design). These results are shown in Table 1. They are compared to the design arrived at during the CDR using CHAINOP (with small changes to allow better comparison between cases). The expected reduction in NIF cost by moving from the CDR design to the other two designs, as determined from the cost algorithms, is also included.

It can be seen in this table that the least expensive design (with the above constraints) is a 9/5/3 layout (the layouts are referred to by the number of slabs in each of the three amplifiers); the 9/5/3 layout is approximately \$10M less expensive than the CDR design, but has a somewhat higher peak  $\Delta B$ . The optimal design without a switch amp is the 11/0/7 design, with a cost approximately \$4M less than that in the CDR. The \$4M difference between the CDR and Title I designs is a small fraction of the total cost ( $\sim 0.5\%$ ). The fact that CHAINOP, used for the CDR optimization, would suggest a design so close in cost (fractionally) to the Title I design, developed by PROPSUITE, gives confidence that CHAINOP provides accurate answers in spite of its relative simplicity.

Although we predict that both the 9/5/3 and 11/0/7 designs will meet the performance criteria that were set, there are a number of operational reasons to

TABLE 1. Comparison of the CDR design (9/5/5) and ACD optimized cases (9/5/3) and (9/5/3).

Parameter	Modified* CDR with new converter	Least expensive, constrained,** optimized	11/0/7, constrained,** optimized
Hard aperture (cm)	40	40	40
Main amp # slabs	9	9	11
Switch amp # slabs	5	5	0
Boost amp # slabs	5	3	7
Slab thickness (cm)	3.36	4.1	4.1
Injection energy (J) ***	3.2	1.2	2.2
Doubler thickness (cm)	1.35	1.36	1.36
Tripler thickness (cm)	1	1	1
Doubler detuning angle (µrad)	200	200	200
Flashlamp pump pulse length (µsec)	360	390	360
$Nd^{3+}$ concentration ( $10^{20}/cm^3$ )	4.18	3.87	3.59
Transport spatial filter length (m)	65	60	60
Last two $\Delta B'$ s (radian) (at beam center)	1.3/2.05	1.7/2.2	1.7/1.8
Conversion efficiency (energy/peak power) (%)****	60/80	60/79	60/79
Capacitor bank (MJ)	373	347	353
Total length (M1 to L4) (m)	135	128	123
Energy (MJ)/peak power (TW) in 600 μm LEH ***	2.2/612	2.2/608	2.2/607
Cost relative to CDR (M\$)	0	-10	-4

<sup>\*</sup> Changes from CDR: 1 × 1-cm pinhole spacing in cavity, new gain/loss assumptions, 4 × 2 amplifiers, 3.5-cm spatial filter lenses, and addition of target chamber window. These assumptions were common to the other two designs.

prefer the 11/0/7 layout. Most apparently, from Table 1, it has a noticeably lower maximum  $\Delta B$ , yielding some additional safety against nonlinear effects. Equally compelling, the similarity to the 11/0/5 design for Beamlet (the operational prototype NIF beamline) makes operational experience gained on that machine more relevant and will likely decrease prototyping costs and/or risks. The absence of a switch amplifier also both obviates concerns about the effects of magnetic fields on the operation of the plasma electrode Pockels cell and greatly simplifies the alignment procedure. There are also some design cost savings in not having a switch amplifier included in the analysis. For all of these reasons, the NIF project chose the 11/0/7 design as its baseline for the ACD.

The shift to the current NIF 11/0/5 design was done as part of the Title I preliminary design activities. It entailed slightly different assumptions than used here, with somewhat increased risk, in order to realize a lower cost.

## **Studies Using Parameter Scan Optimization**

In addition to optimizations, we used PROPSUITE to perform parameter scans of the cost and performance of

a large number of designs ( $\sim$ 50,000) in the vicinity of the optimized NIF design. Parameters varied for this study were slab thickness, number of slabs in each amplifier, Nd<sup>3+</sup> concentration, and flashlamp pump pulse length. This was done for 26 different combinations of the slab counts in the three amplifiers (X/Y/Z).

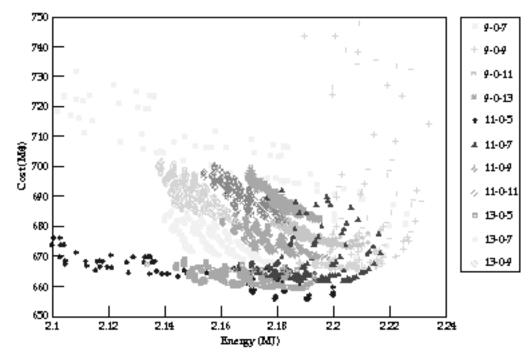
Figure 3 shows the results for cases with no switch amp (Y = 0). Cost is plotted vs output energy, with the several points for each slab combination being different combinations of Nd<sup>3+</sup> concentration, slab thickness, and pump pulse length. The temporally shaped ICF indirect-drive pulse from Fig. 2 was used in each case. All other parameters were the same between designs (including a 40-cm hard aperture). It can be seen that there is some grouping of the various designs, with the least expensive designs being 11/0/7, 11/0/5, and 13/0/5. Some designs with tighter grouping show a greater robustness to parameter changes than others (e.g., 11/0/7 vs 9/0/7). This is desirable in a system. The designs at higher cost are typically characterized by thin slabs and large injection energies. For instance, the large number of thin slabs incurs a higher slab finishing cost and larger capacitor bank. Too few slabs in the boost amplifier, which is only double-passed, requires a larger injection energy and a more expensive front end.

<sup>\*\*</sup> Constraints: 192 beamlets, 40-cm hard aperture, 60-m transport spatial filter, 4.1-cm thick slabs.

<sup>\*\*\*</sup> Before spatial preshaping for gain roll-off across the aperture.

<sup>\*\*\*\*</sup> Averaged over ±30-µrad doubler detuning angle.

FIGURE 3. Full parameter scan results for cases with no switch amp (*X*-0-*Z*). (70-00-1296-2779pb01)



All the designs in Fig. 3 produce slightly different energies and peak powers on target. In order to simplify comparisons, it is possible to normalize all the designs to have 2.2 MJ/600 TW on target by projecting small changes in hard aperture and by scaling cost accordingly. This scaling of the aperture leaves the B integral unchanged for each design by increasing/decreasing the beam area. For example, if a design produced 2.15 MJ and 580 TW, it would be scaled to a 40.7-cm hard aperture, giving 600 TW and 2.22 MJ. The cost was scaled as (hard aperture)<sup>0.8046</sup>, based on studies done previously with CHAINOP.

With this normalization, we plotted the various cases against maximum  $\Delta B$  in the system (Fig. 4). In this display it can be seen that the 11/0/7, 11/0/5, and 13/0/5 designs are still least expensive, but that they have substantial differences in maximum  $\Delta B$ , with the 11/0/7 design displaying the lowest  $\Delta B$ .

In Figs. 5 through 7, successive filters are applied to the data in Fig. 4. A large injection energy requirement typically indicates a design where the modeled pulse is close to the extraction limit of the system. This leaves system performance very vulnerable to small uncertainties in losses or gains. Designs with injection energies of a few joules or less are safer; Fig. 5 shows cases that have injection energies  $\leq$ 5 J. The most attractive designs are still the 11/0/7, 11/0/5, and 13/0/5, although many of the 11/0/5 designs with thinner slabs were eliminated.

Designs with overly large capacitor banks (and correspondingly small injection energies) are simply

uneconomical, as more energy is stored than necessary. These can also be thought of as designs with too many slabs. Figure 6 shows cases filtered for capacitor bank size  $\leq$ 400 MJ. The 11/0/7, 11/0/5, and 13/0/5 designs are still most attractive. Note that the optimum number of slabs is 16 to 18.

Results of a final filtering requiring laser slab thicknesses  $\leq$ 4.2 cm are shown in Fig. 7, reflecting fabrication uncertainties with thick slabs. This filter removes all the remaining 11/0/5 designs, leaving the 11/0/7 and the 13/0/5 designs as having comparable minimum costs. The 11/0/7 designs, however, have lower B integral. Clearly, given these criteria, the best design with no switch amplifier is the 11/0/7.

We can compare these results to cases with a switch amplifier. In Fig. 8, a subset of cases is shown having slab counts of X/0/Z, X/3/Z, and X/5/Z, with all the aforementioned filters applied. It is first useful to note that there are a large number of cases with approximately the same cost (\$660–\$670M), but some difference in B integral. Given that, however, it can be seen that the 9/5/3 design is the least expensive design, with the 9/3/5 and 11/0/7 close behind. These results agree with those cases found by the optimizer, and shown in Table 1: the 9/5/3 design is the least expensive, but has a somewhat higher B integral than the 11/0/7 (2.1 to 2.2 vs 1.7 to 1.8 rad). The design chosen by the project is circled on Figs. 7 and 8. The 11/0/7 designs that have slightly lower cost and B integral than the one selected have thinner slabs than the prescribed 4.1 cm.

IVII DESIGN OF TRANSPORT

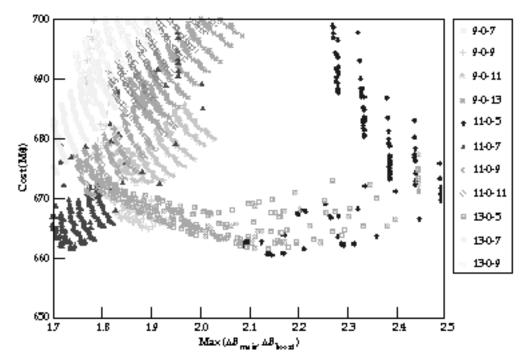


FIGURE 4. Data from Fig. 3 (*X*-0-*Z* parameter scan), aperture-scaled to 2.2MJ, and compared on the basis of maximum B integral. (70-00-1296-2780pb01)

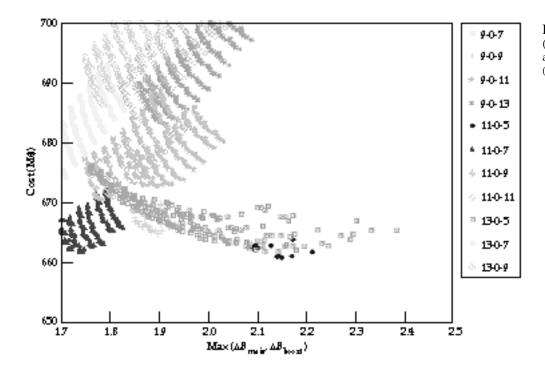


FIGURE 5. Data from Fig. 4 (X-0-Z parameter scan), clipped at injection energy  $\leq$ 5 J. (70-00-1296-2781pb01)

INI DESIGN OF THE LATION

FIGURE 6. Data from Fig. 5 (X-0-Z parameter scan), clipped at injection energy  $\leq$ 5 J and capacitor bank size  $\leq$ 400 MJ. (70-00-1296-2782pb01)

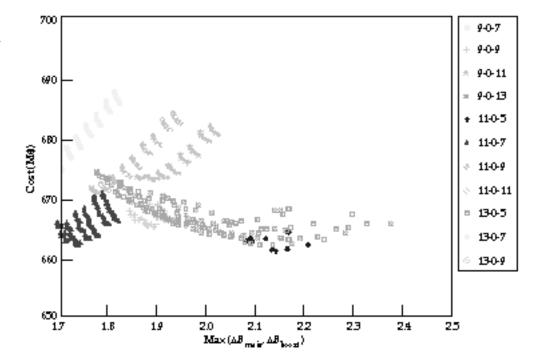
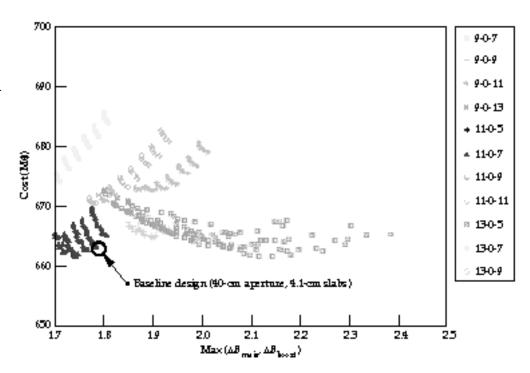


FIGURE 7. Data from Fig. 6 (X-0-Z parameter scan), clipped at injection energy  $\leq$ 5 J, capacitor bank size  $\leq$ 400 MJ, and laser slab thickness  $\leq$ 4.2 cm. (70-00-1296-2783pb01)



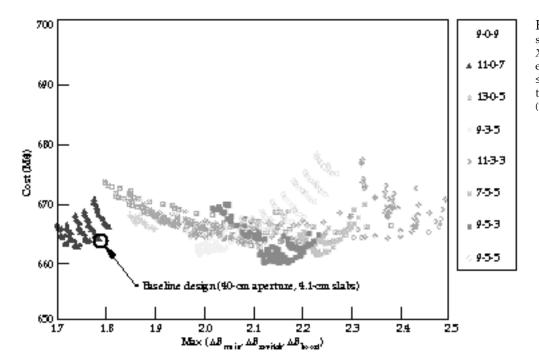


FIGURE 8. Comparison of subset of parameter scans for X-0-Z and X-Y-Z with injection energy  $\leq$ 5 J, capacitor bank size  $\leq$ 400 MJ, and laser slab thickness  $\leq$ 4.2 cm. (70-00-1296-2784pb01)

## Summary

The NIF design is based on cost/performance optimization studies. These studies were done in two phases, and with two codes: a zero-dimensional performance model (CHAINOP) for the *Conceptual Design Report*, and a one-dimensional propagation model (PROPSUITE) for the Advanced Conceptual Design (ACD). These ACD results using PROPSUITE led to 11/0/7 design of Table I. The current Title I 11/0/5 design activity was a result of further cost and risk studies. These efforts give us confidence that we are designing the (approximately) least expensive system meeting the functional requirements.

## Acknowledgments

The authors would like to thank Mark Rotter (LLNL) for assistance in setting up and running the NIKE3D and TOPAZ codes used in thermo-mechanical modeling of laser slabs.

#### **Notes and References**

- National Ignition Facility Conceptual Design Report, UCRL-PROP-117093, Lawrence Livermore National Laboratory, Livermore, CA, 94550 (1994).
- 2. L. M. Frantz and J. S. Nodvik, J. Appl. Phys., 34(8), 2346 (1963).
- 3. J. Lawson, Proc. Conf. on Optical Manufacturing and Testing SPIE Vol. 2536, pg.38 (July 1995).
- 4. J. Trenholme, LLNL Laser Program Annual Report, UCRL-50021-74, pg. 179 (1974).
- 5. J. Trenholme, personal communication.
- W. Williams, K. Manes, J. Hunt, P. Renard, et al., *ICF Quarterly Report*, 6(1), 7, Lawrence Livermore National Laboratory, Livermore, CA UCRL-LR-105821-96-1 (1995).

## LASER OPTIMIZATION TECHNIQUES

C. D. Orth

S. W. Haney

W. H. Williams

#### Introduction

One of the challenges in designing a large laser system like the proposed National Ignition Facility (NIF) is determining which configuration of components meets the mission needs at the lowest construction cost with the largest margin in performance without any optical damage. Such an endeavor could credibly require evaluation of a million different designs because we must consider a range of values for each of many parameters: different numbers of beamlets, different aperture sizes, different numbers of laser slabs, different thicknesses of slabs, etc. The evaluation of so many designs with even a minimum of detail is impractical with current computing ability. There is hence a premium on the development of techniques to determine the best design without evaluating all of the practical configurations.

## What Is an Optimization?

Optimization is the process of finding the best set of values for a system's identified design parameters. There are three steps to optimization. First, we identify exactly what aspects or measures of the system would define a better system if they were enhanced, such as improved output, lowered cost, improved reliability, or a combination of measures with appropriate weighting factors. This is often the most difficult step, because it requires that we truly understand what constitutes a better system. Second, we define a mathematical function known as a figure of merit (FOM) that incorporates these measures and has both of the following characteristics: (1) the value of the FOM increases or decreases according to our selected measure of goodness, and (2) the FOM is dependent on all of the design parameters under study, such that the value of the

FOM varies if the value of any parameter is varied. Third, we search the parameter space to find the design that maximizes or minimizes the FOM, depending on how the FOM is defined.

To optimize a large laser system, we must consider more than just an FOM. Much of the physics of light propagation is nonlinear, in the sense that a change in each of the many parameters does not produce a proportional change in the laser output. This means that we cannot use any of the linear optimization methods that are known. There are also many equality and inequality constraints to consider, such as not exceeding a certain construction cost, not exceeding a certain input energy, not damaging any of the optical elements, and outputting at least a certain 3ω laser energy. Optimization of a laser system is thus not only nonlinear, but also constrained, and is hence called nonlinear constrained optimization. In addition, because a graph of the FOM plotted as a function of all of the variable parameters is often a multiple-peaked surface, with several peaks of different heights, there are local maxima (peaks) in the FOM that can easily fool a computer into incorrectly "thinking" it has found the optimum. What we need, therefore, is a method that can quickly and correctly find the highest peak in the FOM space, the so-called global optimum. Moreover, the FOM space is sometimes noisy in one or more of the parameters, with additional peaks and valleys superimposed on top of the otherwise smooth topology. We thus need a technique that can smooth out the noise. A mathematical statement of such a nonlinear constrained optimization problem is to maximize (or minimize) a suitably smoothed (or averaged) FOM function  $f(\mathbf{x})$  subject to equality constraints  $c_i(\mathbf{x}) =$ 0, i = 1, ..., k, and inequality constraints  $c_i(\mathbf{x}) \ge 0, i = k+1$ , ..., m, where parameter vector  $\mathbf{x} = (x_1, x_2, ..., x_n)$  represents *n* variables.

# Selecting an Optimization Technique

Many different techniques exist for nonlinear constrained optimization. These techniques differ in the way in which the computer navigates the FOM space in search of the tallest peak or deepest valley. The most common methods sample the topology in some region to determine the slope of the terrain in various directions, and hence the direction that leads to the optimum. These methods, which are all iterative, differ in the following ways in which the local terrain is sampled:

- 1. The downhill simplex method<sup>1</sup> uses only function evaluations (i.e., evaluations of the FOM), not derivatives, to move in the direction of the optimum using manipulations of the geometrical figure (simplex) formed by the original point and *n* somewhat arbitrary displacements in the *n* directions corresponding to the *n* parameters considered. This method is robust, but typically slow to converge.
- 2. Simple derivative (gradient) methods sample the space for two (or more) values of each parameter to determine a local slope in the FOM, and then step off a fixed step in the direction of maximum slope. One serious problem with this method is that, once the best direction in which to go for the next calculation is identified, we don't really know how far to go in that direction. Consequently, this method can be slow to converge.
- 3. Quadratic methods, in essence, calculate the FOM for three values of each parameter, fit the resulting FOM values to a quadratic function such as a parabola, and calculate exactly how far to go for the next estimate of where the FOM peak might lie. This method is much "smarter" than the above methods because it knows how far to step out for the next iteration. Two common methods of this type are Brent's method and Powell's method. Brent's method uses parabolic interpolation. Powell's method finds the solution that zeros the gradient of a Lagrange function formed as a sum of the FOM function and a linear combination of the constraint functions. It approximates the full nonlinear problem by a quadratic problem to find the direction to go in the FOM space, then determines how far to go in that direction by doing a one-dimensional optimization in that direction. While Brent's method uses only three function evaluations for each parameter, Powell's method uses one function evaluation, one derivative evaluation, one estimate for the second derivative, plus other function evaluations for each subsequent line search. These methods are powerful and fast, and are the methods used in the codes that we employ.

- 4. Simulated annealing methods<sup>2</sup> randomly sample points over a large portion of the parameter space and then slowly decrease the size of the sampling space around any optimum so found, according to mathematics analogous to Boltzmann thermodynamic cooling. This method is good for selecting the best global ordering of a large combination of discrete elements of some kind when many local optima exist, but it converges too slowly and is thus not practical for our problem.
- 5. Genetic methods<sup>3</sup> form a pool of design candidates, "mate" the ones having the highest FOMs (the parents) by combining attributes in some way to produce other candidates (the offspring), and then remove the unlikely candidates (extinction). This method can also be effective in finding a global optimum among many local optima, but it also converges too slowly.

The first three methods listed above can be confused if the FOM (or constraint) surface is noisy, unless additional smoothing algorithms are included. Simulated annealing and genetic methods are inherently more able to navigate successfully along noisy surfaces, but are expected to converge too slowly to be effective for the optimization of a large laser system. We therefore chose to use quadratic optimization methods to speed up the computational time. As a result, however, we had to deal with discontinuities in the FOM as one form of noise.

## Dealing with Discontinuities in the FOM

There are several sources of fluctuations in the FOM that affect an optimizer evaluating various designs of a large laser system. Although stochastic (statistical) noise can sometimes be a problem when methods employ random numbers, a more typical problem arises from the discontinuous FOM jumps that correspond to integer steps. Integers are encountered in such parameters as the numbers of laser slabs in the amplifiers, the number of flashlamps for each slab, and the number of beamlets in the laser. If the FOM (or a constraint) moves abruptly as the optimizer searches from one integer to the next, as it usually does, the optimizer can be confused by the local optima thereby introduced. This is especially true for gradient-search techniques, which are based on real numbers. We can overcome such fluctuations by incorporating either some type of smoothing technique or by substituting real numbers for the integer quantities so that the optimizer can consider noninteger (i.e., nonphysical) values of the parameters.

A second source of discontinuities arises in optimizations involving spatial-filter pinholes because

of the integer-like effect of the transverse spatial representation of the beam by a fixed number of grid points (e.g., 512 points over a horizontal width of 50 cm). To explain these discontinuities, we must first explain the purpose and function of pinholes.

All of the large laser chains at LLNL involve the use of spatial filters that focus the beam and force it to go through a 100- to 200- $\mu$ m-diam pinhole in a metal plate. The purpose of such a pinhole is to cut off the highangle noise present in the beam, thereby smoothing the transverse spatial intensity profile. Such smoothing occurs because, in the focal plane of a lens, the spatial intensity profile corresponds to the power in the various angular components in the beam. Thus, if the intensity profile is decomposed into its Fourier components, the relative powers in the low-frequency components correspond to the intensities seen near the centerline of the focal plane. Higher-frequency components focus at increasingly farther distances from the centerline because they are propagating at larger angles. These various frequency components grow in magnitude at different rates due to, among other things, the nonlinear indices of refraction of the optical materials in the laser, as described by the Bespalov– Talanov theory. The high-frequency components tend to grow faster, so it becomes desirable to clip off the power in these frequencies periodically in the laser chain to keep the beam as spatially flat as possible. For a beam with a reasonably smooth spatial profile, the power in the high-frequency components is low enough to permit a pinhole to do this clipping without ablating away too much of the pinhole structure and thereby disrupting the last temporal portions of the laser pulse.

In propagation simulations employing a finite number of grid points, the power in the Fourier components is summed into the same number of bins as there are grid points. Consequently, as the diameter of the pinhole changes with changing pinhole acceptance angle, there are discrete jumps in clipped-beam power as the edge of the pinhole moves from one frequency bin (grid point) to the next. These jumps result in abrupt changes in the spatial intensity profile of the beam after it leaves the filter. If the optimizer is monitoring, for example, the peak fluence as a constraint against optical damage, it can be confused by the local optima that such discontinuities generate. The solution we have used to overcome this confusion is to average the FOM over several adjacent function evaluations.

## Optimizing the NIF Design

Optimization of the NIF design is one example of how we can use our optimization techniques. As described in more detail in the article "NIF Design Optimization" on p. 181 of this *Quarterly*, the conceptual design<sup>5</sup> for the NIF configuration arose through

use of a code called CHAINOP,<sup>6</sup> which was capable of using either a simplex optimization routine or a gradient-search routine. We accessed this gradient-search routine as part of a large systems analysis programming shell called SuperCode.<sup>7</sup> SuperCode uses the quadratic version of Powell's method, as written in an Argonne National Laboratory implementation of a variable metric method labeled VMCON.<sup>8</sup> Because VMCON evaluates gradients, care was taken to minimize discontinuities in the FOM and constraints by using noninteger laser slab and flashlamp counts, as well as smoothed cost functions.

In the second optimization effort, for the Advanced Conceptual Design (ACD) phase of the NIF, we implemented three separate approaches. In one approach, we used SuperCode to evaluate ~100,000 specific designs distributed around the conceptual design point in the major parameters, and we applied various cuts to constrain dynamical and engineering quantities such as cost and nonlinear growth of spatial noise. For a second approach, we used SUPERCODE to do an optimization. As with CHAINOP, we used fractional slabs and noninteger flashlamp counts, but optimization over pinhole acceptance angle could not be performed. A third approach, coded as OPTIMA1, is based on a modified version of Brent's method (parabolic interpolation). A similar approach had been used in the diodepumped solid-state laser (DPSSL) design studies for inertial fusion energy. 9 OPTIMA1 can use either of two different methods to smooth the FOM space and can treat integer parameters directly. This code therefore allowed the consideration of noisy parameters, including integer slab and flashlamp counts, and pinhole acceptance angles.

There were several reasons we chose multiple approaches in optimizing the NIF laser for the ACD. First, when we started, we knew that there were complexities such as noisy parameters, and we were not sure that any one approach would prove successful in the end. Second, the performance of optimizers is usually dependent on the problem considered, so the length of time needed for any one optimizer to converge to a solution was unknown for the NIF problem. In general, performance is better if the optimization algorithm is tailored to the problem in some way. On the other hand, the use of a well tested fast algorithm like VMCON can often prove very effective. Third, we wanted multiple opinions from independent approaches to improve the reliability of the results.

All three approaches used parallel processing through Parallel Virtual Machine (PVM) software. This software allows one master computer to send tasks to many different slave computers and retrieve the results. In our case, we had one HP 715/80 UNIX master workstation tasking 28 similar slave workstations that each evaluated the performance of one NIF design (SUPERCODE) or performed the suboptimization for one

parameter (OPTIMA1). The total computing power was 20–30 megaflops for each of 28 computers, or about 0.75 gigaflops. The use of this workstation cluster enabled the codes to search through a space representing a million candidate designs at a rate over 20 times faster than it would have taken with only one computer. This facility proved valuable because it reduced the total calculation time from the 46 days it would have taken for 10<sup>6</sup> assessments at about two minutes per assessment of each candidate design on one computer to about one or two days using the workstation cluster.

#### Features of SuperCode

SUPERCODE<sup>7</sup> couples a toolbox of systems analysis tools to a powerful user interface. The systems analysis tools currently consist of the following:

- A constrained nonlinear optimization package based on VMCON.<sup>8</sup>
- A nonlinear optimization package based on a genetic algorithm.<sup>3</sup>
- A nonlinear equation solver.
- A Monte Carlo sampling package for performing uncertainty analyses.
- Parameter scans.
- Uncertainty analyses.
- Facilities for exploiting PVM software to speed up optimizations.

These tools are controlled by a programmable shell that understands a large subset of the C++ computer language, including arithmetic expressions, loops, decision structures, functions, classes, and objects. Users can interactively manipulate the set of equations to be passed to the systems analysis tools, monitor progress of a calculation, postprocess results, and plot them using an interactive graphics package. SuperCode was the main code used in setting the NIF baseline design, and has been used to design tokamak reactors and experiments, hybrid electric vehicles, rail guns, and neutron sources. SuperCode is available on UNIX, MacOS, and Windows platforms.

#### The OPTIMA1 Code

OPTIMA1 is based on the particular parabolic-interpolation method that proved successful for the DPSSL inertial fusion energy study. This method increases the independence of the parameters, often permitting the full optimization to be accomplished by independent one-parameter optimizations. The key to this method is to incorporate an inner loop that maximizes the laser's injection energy subject to all constraints. An outer loop then deals with all of the other parameters designated as active optimization variables. Both loops advance by making one function evaluation and using that together with the last two calculations near-

est the current best value to determine a next guess. Penalty functions reduce the value of the FOM by exponentially degrading the FOM as any active variable violates a constraint. The current list of features includes the following:

- Easy addition of parameters.
- Treatment of both discrete (integer, even-integer, or odd-integer) and analog (real) parameters.
- Two types of smoothing for noisy parameters (random-number smoothing and perturbation smoothing).
- Ability to restart runs from a dump file.
- Operation on either a single or multiple (parallel-processing) platforms (using PVM software).
- Table-like scans over a single parameter.
- Input-file selection of the optimization FOM from among any product or quotient of the parameters or calculated quantities.
- Performance of a sensitivity study around the final parameter vector.

OPTIMA1 is very flexible and robust. It usually takes more time to converge to a solution for small ( $<10^{-3}$ ) precisions, however, because the penalty functions create a "cliff" in the FOM space that requires special treatment in the parabolic interpolator. In addition to helping choose the NIF design parameters, OPTIMA1 has been useful in performing sensitivity studies on the parameters (e.g., the maximum allowable doubler detuning angle) and in determining optical specifications through studies varying the aberrations placed on the optical components. OPTIMA1 is written in UNIX HP FORTRAN.

# Overcoming Specific Modeling Difficulties

After selecting a set of optimization techniques, we had to deal with many problems that were specific to the optimization of a large laser. First, we found many designs having the same value of energy delivered to the laser entrance hole (LEH) of the target, but with differing construction costs, so we had to include cost in the FOM or cost as a constraint. Two solutions that proved effective were (1) minimizing cost subject to performance constraints and (2) maximizing the ratio of energy delivered to the LEH and total cost, subject to the other constraints.

The second problem was finding a way to include realistic aberration sources for every optic that would account for surface roughness and bulk phase retardations. The challenge was to develop techniques to use measurements taken over varying aperture sizes and on a limited number of parts while preserving the spatial distributions of wavefront roughness in such a form that realistic aberration sources could be simulated for every optic. This was done by devising a technique using a

power spectral density (PSD) function defined as the square of the discrete Fourier transform of the measured phase retardations, multiplied by the length of the 1–D measurement (or multiplied by the length and width in 2D). We combined the measurements from three spatial-frequency ranges

(0 to 0.1 mm<sup>-1</sup>, 0.1 to 1 mm<sup>-1</sup>, and 1 to 10 mm<sup>-1</sup>) while mitigating the effects of finite sampling apertures by using a windowing filter function (a Hanning filter). This filter broadened (or blurred) the resulting width of the spatial frequency structures and eliminated frequencies generated by the discontinuities at the edges of the samples. The PSDs thereby obtained did not possess any relative phase information in the Fourier domain, but were merely the spectral distributions of the wavefront errors. We then used the PSD for a given type of optic to determine the magnitude of the Fourier coefficient and added a random phase in the Fourier domain. Using inverse Fourier transformation, we obtained a unique wavefront distortion for every optic needing a simulated phase-front aberration.

The third modeling difficulty was that laser gain and pump-induced distortions depend on the choice of pumping parameters (pump pulse duration, Nd doping concentration, flashlamp explosion fraction, flashlamp diameter, and flashlamp packing fraction). Pump-induced distortion is phase noise added to the beam because the nonuniform distribution of flashlamp light absorbed by the laser slabs causes nonuniform heating, which distorts the slabs. Because determining the proper pump-induced distortions is calculationally intensive (involving ray tracing and 3-D thermomechanical modeling), we ran the 3-D codes for a range of each of the pumping parameters and incorporated the results in the optimizations using a table look-up procedure.

The fourth problem was that the use of spatial-filter pinholes with abrupt edges in calculations with a finite number of transverse spatial grid points causes ringing (aliasing), which introduces artificial modulation of the downstream beam intensity profile. We therefore used high-resolution runs with many points to define problem areas and incorporated smoothing algorithms developed at LLNL.

The fifth problem was damage to the optical components that can arise from either high fluence or filamentation, which both depend on the noise on the beam. (Filamentation is the process by which the intensity of a narrow beamlet increases as the beamlet is focused by nonlinear propagation through solid materials.) A proper treatment of these effects therefore requires very high spatial resolution to define the peaks in the transverse intensity profiles. Such resolution would make the iteration cycle time prohibitively slow if many points had to be used in two transverse

dimensions. Consequently, we performed most of our calculations using 1-D codes with 512 spatial points, which is insufficient to determine filamentation, and evaluated the likelihood of filament formation and the resultant optical damage using a phenomenological model<sup>11</sup> developed at LLNL based on measured Beamlet data. For ordinary (nonfilamentation) optical damage assessment, we used measured peak fluence limits as constraints for every component.

The sixth modeling difficulty was that the desired NIF laser pulse at the LEH is a  $3\omega$  pulse consisting of a long low-power foot followed by a main pulse roughly 3.5 ns wide. Because the laser input is at  $1\omega$ , and because the harmonic conversion from  $1\omega$  to  $3\omega$  is intensity-dependent, we had to incorporate precise algorithms for this conversion process (see the article entitled "Frequency Conversion Modeling" on p. 199 of this *Quarterly*); we also had to iterate to make sure that the  $1\omega$  pulse shape produced the desired output  $3\omega$  pulse shape.

# **Optimization Flow**

Each optimization iteration included a number of steps involving other codes, as outlined in Fig.1 for the particular case of OPTIMA1 using the Ethernet connections to the cluster of 28 workstations. As directed by the master, a slave machine would suboptimize one parameter by first running two codes to help establish the temporal shape of the input beam: a plane-wave frequency conversion code (thgft02) to assess the converter performance with the given parameter values and an inverse harmonic-conversion code (invconv3) to calculate the 1ω input temporal shape that would give the desired 3ω output temporal shape with that converter. Following the formation of the apodized transverse spatial shape of the input beam, the optimizer would generate the input file for PROP92 and run PROP92 to propagate the input signal down the chain of optical components from the input of the laser to the harmonic converter. This step included phase aberration sources to simulate the experimental surface finishes and bulk properties for each optic, as well as the amplifier gain files generated from 2.5-D amplifier modeling and the pump-induced distortion files generated from 3-D thermomechanical modeling (see the companion article entitled "The PROP92 Fourier Beam Propagation Code" for a complete description of the physics in PROP92). After running a code to analyze the PROP92 output file, the optimizer would run a frequency conversion code (thgxtz001) to convert the  $1\omega$  light to  $3\omega$  light. Thereafter, the optimizer would formulate an input file for PROP92, this time for the 3ω light, and run PROP92 to propagate the beam down the rest of the laser chain to obtain the laser pulse entering the target LEH. After

LABER OF THYHEATTON TECHNIQUES

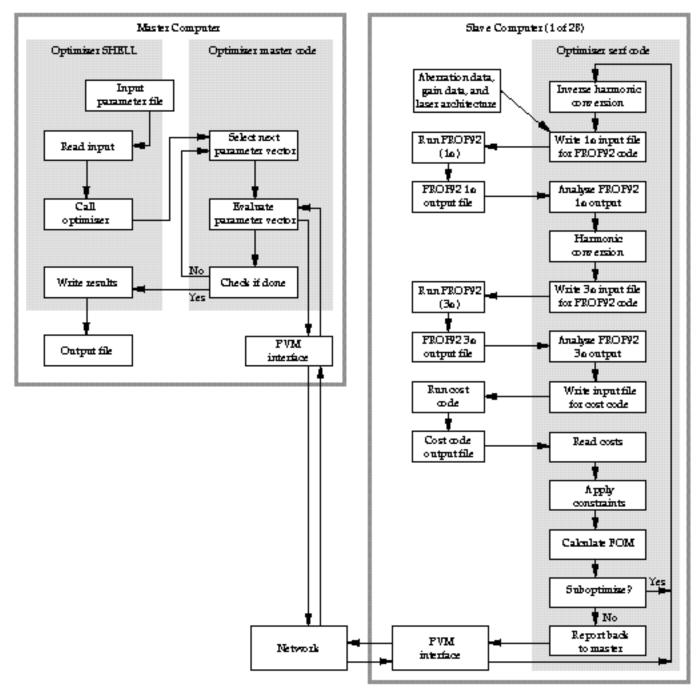


FIGURE 1. NIF optimization flow chart for OPTIMA1. (40-00-1296-2752pb01)

running a code to analyze the PROP92  $3\omega$  output file, the optimizer would run a routine to generate an input file for the cost code, run the cost code to calculate the resulting cost of the NIF facility, and run a routine to apply the constraints. The optimizer would then calculate the FOM as the LEH energy, or the ratio of that energy to the cost, or simply as the cost constrained to obtain the desired

energy and power at the LEH—all as penalized by the constraints that failed. After several suboptimizations, the slave reports the results for that parameter back to the master, which decides how to form the full parameter vector for the next set of suboptimizations. When the changes in all parameters are less than specified precisions, the process stops.

## Summary

Nonlinear constrained optimization of the design of a large laser such as the NIF is the process of finding the set of values for the laser's identified design parameters that optimizes the figure of merit (FOM). Among the different optimization techniques available, we selected quadratic methods based on Brent's method and Powell's method, as modified to treat the discontinuities imposed by integer parameter values. An established code (SUPERCODE) and a new code (OPTIMA1) were configured with realistic aberration sources for every optic, a cost model of the whole laser system, methods to incorporate the effects of different values of the pumping parameters, models for optical damage as well as filamentation, and full harmonic conversion of the desired 3ω pulse shape. We also incorporated parallel processing through use of Parallel Virtual Machine (PVM) software operating on a group of 28 workstations. The resulting techniques allow optimization of the NIF laser and other laser systems based on realistic components and realistic laser light propagation.

#### **Notes and References**

- 1. J. A. Nelder and R. Mead, Computer Journal 7, 308–313 (1965).
- S. Kirkpatrick, C. D. Gelatt, and M. P. Vecchi, Science 220, 671–680 (1983); S. Kirkpatrick, Journal of Statistical Physics 34, 975–986 (1984).
- 3. E.g., E. Betensky, Opt. Eng. 32, 1750 (1993).
- J. Trenholme, Laser Program Annual Report, Lawrence Livermore National Laboratory, Livermore, CA, UCRL-50021-74, p. 177 (1975).
- National Ignition Facility Conceptual Design Report, Lawrence Livermore National Laboratory, Livermore, CA, UCRL-PROP-117093 Vol. 2, NIF-LLNL-94-113 (1994).
- J. Trenholme, "CHAINOP: Laser Chain Optimization Code," Lawrence Livermore National Laboratory, Livermore, CA, internal report (Oct. 1992); also see accompanying article on p. 181 in this *Quarterly*.
- 7. S. W. Haney, W. L. Barr, J. A. Crotinger, L. J. Perkins, et al., Fusion Technology 21, 1749 (1992).
- 8. R. L. Crane, K. E. Hillstrom, and M. Minkoff, "Solution of the General Nonlinear Programming Problem with Subroutine VMCON," Report ANL-80-64, Argonne National Laboratory (1980).
- C. D. Orth, S. A. Payne, and W. F. Krupke, Nuclear Fusion 36(1), 75 (1996).
- J. K. Lawson, D. M. Aikens, R. E. English, Jr., C. R. Wolfe, "Specification, Production, and Testing of Optical Components and Systems," SPEIE Proceedings, 13–16 May 1996, Glasgow, Scotland, UK, vol. 2775, p. 345 (1996).
- 11. Mark A. Henesian, "Simulations of  $3\omega$  Beam Filamentation in the Beamlet Focus Lens and General Comments on Filamentation Theory," Lawrence Livermore National Laboratory, Livermore, CA, internal memo LS&T-LMO 96-001 (May 1996); and "Simulations of  $1\omega$  Beam Filamentation in the Beamlet Laser, Filamentation Theory in Glass Slabs, and PROP92's Filamentation Code," Lawrence Livermore National Laboratory, Livermore, CA, internal memo, LS&T-LMO 96-003 (May 1996).

# Frequency-Conversion Modeling

J. M. Auerbach D. Milam

C. E. Barker P. W. Milonni\*

D. Eimerl J. B. Trenholme

K. R. Manes B. Van Wonterghem

#### Introduction

With respect to the rest of the Nd:glass laser system, the frequency converter is quite small in terms of weight and size. However, it is a critical component because laser fusion targets require irradiation by ultraviolet laser light to operate successfully. The frequency converter produces ultraviolet light ( $\lambda=0.351~\mu m$ ) from the infrared light ( $\lambda=1.053~\mu m$ ) generated in the neodymium-doped glass section of the laser.

As shown in Fig. 1, the basic frequency converter for tripling consists of two crystals (advanced designs have more than two crystals). The first crystal, known as the second harmonic generator (SHG), frequency doubles a predetermined amount of incident infrared (1 $\omega$ ) light. The frequency-doubled (2 $\omega$ ) light has a wavelength of 0.526  $\mu$ m. The 2 $\omega$  and 1 $\omega$  light are then mixed in the second crystal, known as the third harmonic generator (THG) or mixer, to form ultraviolet (3 $\omega$ ) light at a wavelength of 0.351  $\mu$ m. The output of the THG is 1 $\omega$ , 2 $\omega$ , and 3 $\omega$  light. The proportions of light at the three wavelengths depend on the operating configuration and the intensity and phase of the input laser pulse to the converter.

The goal of frequency-conversion modeling is to produce a converter design that results in the best performance for a required output laser pulse and that is the least sensitive to operational tolerances (such as alignment) and crystal manufacturing faults (such as surface roughness).

A frequency converter requires precise tolerances. Crystals must be tilted to an accuracy of microradians, and crystal thicknesses must be accurate to millimeters to achieve desired performance. Crystal surfaces must also be finished to a smoothness of hundredths of a

micron so that the energy of a 3ω laser pulse will almost completely pass through the laser entrance hole of the hohlraum.

Frequency conversion is one example of the process of three-wave mixing. The crystals used in frequency converters are anisotropic, thus, frequency-conversion modeling must take account of the directions of the principal axes of the crystals with respect to the polarizations of electric fields in three-wave mixing. Frequency conversion is optimal at a phase-matched condition. Phase matching involves placing the principal axis of each crystal of the converter at a certain angular separation from the propagation direction. This angular separation, which must be accurate to within microradians, is called the phase-matching angle. The codes used for frequency-conversion modeling calculate phase-matching angles and the variation of converter performance for departures from the phase-matched condition. In mathematical terms, phase matching means that the difference between the wave number of the output harmonic field and the wave numbers of the input harmonic fields equals

We can define the phase mismatch factor  $\Delta k$  as follows:

$$\Delta k = 2\pi/\lambda_{\rm h} - 2\pi/\lambda_{\rm f} - 2\pi/\lambda_{\rm g} , \qquad (1)$$

where  $\lambda$  is the wavelength in the media, h denotes the output harmonic field, and f and g denote the input harmonic fields. Here,  $\lambda = \lambda_0/n$ , where n is the index of refraction, and  $\lambda_0$  is the wavelength in vacuum. The value of n depends on the type of crystal material, the polarization of the field, crystal orientation, the local propagation angle of the electric field, the instantaneous wavelength if it is time-varying due to phase modulation, and temperature. Modeling codes must

<sup>\*</sup>Los Alamos National Laboratory, Los Alamos, New Mexico.

I REQUERCE CONVERSION INDODELING

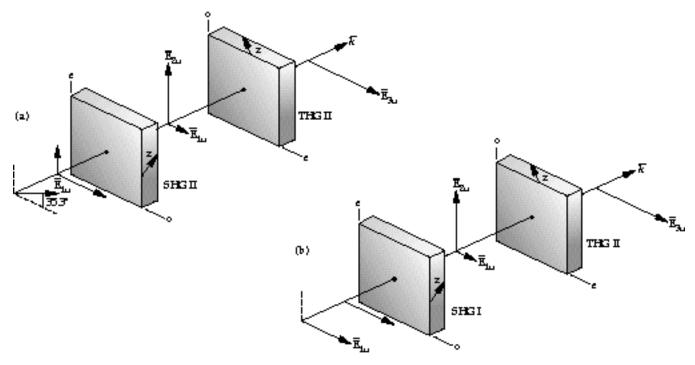


FIGURE 1. Schematic of two-crystal frequency triplers. (a) Type II/Type II crystal scheme and polarization directions for tripling. (b) Type I/Type II crystal scheme and polarization directions for tripling. 40-00-1296-2736pb01

take into account all these dependencies. Whereas  $\Delta k = 0$  for phase matching, as we will show later,  $\Delta k$  is sometimes deliberately made nonzero in the SHG to obtain a certain amount of red and green light for the THG.

We have developed a class of frequency-conversion codes such that each code is differentiated from the others by the level of detail in the specification of the input electric field **E** to the converter. In the most general case:

$$\mathbf{E} = \mathbf{E}(x, y, z, t, \lambda_c) , \qquad (2)$$

where, x and y are the transverse spatial coordinates, z is the coordinate in the direction of propagation, t is time, and  $\lambda_c$  is the center wavelength.

The different codes and electric field specifications are as follows:

1. For plane-wave steady-state fields:

$$\mathbf{E} = \mathbf{E}(z, \lambda_c) \quad . \tag{3}$$

2. For plane-wave time-varying fields:

$$\mathbf{E} = \mathbf{E}(z, t, \lambda_c) \quad . \tag{4}$$

3. For spatially varying steady-state fields (in three dimensions):

$$\mathbf{E} = \mathbf{E}(x, y, z, \lambda_c) \quad . \tag{5}$$

4. For spatially varying and time-varying fields:

$$\mathbf{E} = \mathbf{E}(x, z, t, \lambda_c) \tag{6a}$$

for one transverse spatial dimension, and

$$\mathbf{E} = \mathbf{E}(x, y, z, t, \lambda_{c}) \tag{6b}$$

for two transverse spatial dimensions.

# Types of Frequency Converters

The two types of crystal material used in the frequency converters for Nova, Beamlet, and the National Ignition Facility (NIF) are potassium dihydrogen phosphate (KDP) and deuterated potassium dihydrogen phosphate (KD\*P). The crystals are of the negative uniaxial type.<sup>1</sup>

As shown in Fig. 1, each crystal can be operated in a Type I or Type II configuration. In a Type I configuration, incoming electric fields are all in one polarization direction, and the output harmonic field polarization is orthogonal to the input field's polarization. In a Type II configuration, incoming electric fields are orthogonal. The crystal axes along which the incoming electric fields are aligned are called the ordinary (o) and the extraordinary (e) axis. In the plane defined by the propagation direction and ordinary axis, there is no dependence of the index of refraction on crystal tilt angle  $\theta$ . In the plane defined by the propagation direction and the extraordinary axis, the index of refraction varies with crystal tilt angle. This feature is used to adjust the phase mismatch

 $\Delta k$  by a process called angular detuning.

In the following discussion, we denote the electric fields involved in the three-wave mixing process by f, g, and h. A scalar representation can be used because each field is in one polarization, which is parallel to either the ordinary or extraordinary axis of each crystal. In a SHG crystal, f and g represent the  $1\omega$  fields, and g represents the g field. In a THG crystal, g represents the g field. In a Type I SHG, g and g are parallel to the ordinary axis, and g is parallel to the extraordinary axis. In a Type II THG, g and g are parallel to the extraordinary axis, and g is parallel to the ordinary axis. From these configurations and field conventions, we can formulate equations governing the evolution of fields in the converter crystals.

# **Equations of Frequency Conversion**

The evolution of the f, g, and h fields in a crystal for the most general case, with f = f(x,y,z,t), g = g(x,y,z,t), and h = h(x,y,z,t), is determined by solving the following set of coupled, nonlinear differential equations:

$$\begin{split} \partial f/\partial z + 1/v_{g1}\partial f/\partial t &= iC(\theta)hg^*e^{i\Delta kz} - 0.5\alpha_1 f + k_0[\gamma_{11}|f|^2 \\ &+ 2\gamma_{12}|g|^2 + 2\gamma_{13}|h|^2]f - i/2k_f(\nabla^2 f) - \rho f\partial_f/\partial r_e \end{split} , \tag{7}$$

$$\begin{split} & \partial g / \partial z + 1 / v_{g2} \partial g / \partial t = i C(\theta) f h^* e^{i \Delta k z} - 0.5 \alpha_2 g \\ & + i \lambda_1 / \lambda_2 k_0 [2 \gamma_{21} \, \big| \, f \big|^2 + \gamma_{22} \, \big| \, g \, \big|^2 + 2 \gamma_{23} \, \big| \, h \, \big|^2 \big] g \\ & - i / 2 k_g (\nabla^2 g) - \rho_g \partial g / \partial r_{\rm e} \ , \end{split} \tag{8}$$

and

$$\frac{\partial h}{\partial z} + \frac{1}{v_{g3}} \frac{\partial h}{\partial t} = iC(\theta) f g e^{-i\Delta k z} - 0.5 \alpha_3 h$$

$$+ i\lambda_1 / \lambda_3 k_0 [2\gamma_{31} | f|^2 + 2\gamma_{32} | g|^2 + \gamma_{33} | h|^2] h$$

$$- i/2k_h(\nabla^2 h) - \rho_h \frac{\partial h}{\partial r_e}, \qquad (9)$$

where  $\nabla^2$  is the Laplacian operator, which for Cartesian coordinates is:

$$\nabla^2 = \frac{\partial^2}{\partial x^2} + \frac{\partial^2}{\partial y^2} \ . \tag{10}$$

We derived Eqs. (7–9) by starting with Maxwell's equations for a nonlinear medium. The first term on the left side of Eqs. (7–9) is the derivative in the propagation direction to be integrated. We want to calculate the evolution of the three fields as a function of z, the propagation direction.

The second term on the left side of Eqs. (7–9) is used

only in the conversion codes that model time-varying electric fields. Here,  $v_{gn}$  is the group velocity, where n = 1, 2, 3. The group velocity is defined by the equation

$$v_{\rm g} = \partial \omega / \partial k$$
 , (11)

where  $\omega = \omega(k)$  is the dispersion relationship for a converter crystal material. The use of only  $v_{\rm g}$  indicates that we are using only a first-order approximation to the dispersion relation. For the bandwidths in our modeling, this is an excellent approximation.

The first term on the right side of Eqs. (7–9) is the three-wave mixing or frequency-conversion term. (This term is included in all the types of our conversion codes.) Here, C is the coupling coefficient, which is a function of angle  $\theta$  between the z axis and the principal axis of the converter crystal. The phase mismatch factor  $\Delta k$  is in the complex exponential. A nonzero value of  $\Delta k$  degrades the conversion.

The second term on the right side of Eqs. (7–9) corresponds to bulk absorption, where  $\alpha_n$  denotes the absorption coefficients.

The third term on the right side corresponds to phase retardation arising from the nonlinear index of refraction. Note that the phase retardation for each field not only depends on its own intensity but also on the intensities of the other two fields. The quantities  $\gamma_{mn}$  are the nonlinear index coefficients. This term is included in all codes with temporal-field variations and/or spatial-field variations in at least one transverse dimension. It is not needed in plane-wave, steady-state codes because the uniform phase produced would have no effect.

The fourth term on the right side corresponds to paraxial diffraction. This term is included in codes where the fields vary in one or two transverse dimensions.

The fifth term on the right side is the "walk-off" factor, which is nonzero only if the field vector is in the extraordinary direction. Thus, we use the notation  $r_{\rm e}$  for the coordinate in the extraordinary direction, which can be x or y, depending on the crystal configuration. The term  $\rho$  is the walk-off factor, which gives the variation of refractive index with angle  $\theta$ . Walk-off accounts for the fact that, as a field propagates in a direction different from the phase-matching direction, it will no longer move with the other fields but will "walk off" from them because the index of refraction varies with direction.

#### Method of Solution

Equations (7–9) are solved by a split-step method to give the fields as a function of x, y, z, and t (or a subset of these variables, depending on the type of code). In this method, the derivative of each field

with respect to z is split into two components with different terms from the right hand sides of Eqs. (7–9). The integration for one component is carried out in the space–time domain, and the integration for the other component is carried out in the frequency/spatial-frequency domain. The terms in the equations are divided in the space–time domain according to:

- Frequency conversion (three-wave mixing).
- · Passive loss.
- Nonlinear index phase retardation.

This part of the derivative of each field with respect to *z* is integrated using a fourth-order Runge–Kutta method.

The second component, which includes the time derivative of each field and the diffraction and walk-off terms, is integrated by first Fourier transforming the terms into the frequency/spatial-frequency (for x, y) domain. After the equations are transformed, they become ordinary differential equations in z instead of partial differential equations in x, y, z, t. The equations are then integrated with respect to z and inverse Fourier transformed to give the second component of the updated fields.

Thus, in Eqs. (12–14) below, we denote the angular frequency as  $\omega$  and the wave numbers in the x,y, and extraordinary axes directions with  $\kappa_{x'}$ ,  $\kappa_{y'}$  and  $\kappa_{e'}$  respectively. After Fourier transforming the time-derivative, diffraction, and walk-off terms, the second part of the split-step solution involves integrating:

$$dF/dz = -i\omega/v_{g1}F + i(\kappa_x^2 + \kappa_y^2)/2k_fF + i\rho_f\kappa_eF , \qquad (12)$$

$$dG/dz = -i\omega/v_{g2}G + i(\kappa_x^2 + \kappa_y^2)/2k_2G + i\rho_g\kappa_eG \ , \eqno(13)$$

and

$$dH/dz = -i\omega/v_{\rm g3}H + i(\kappa_x^2 + \kappa_y^2)/2k_3H + i\rho_h\kappa_{\rm e}H \ , \eqno(14)$$

where F, G, and H denote the Fourier transforms of the second part of the split-step solution of f, g, and h. Here,  $\kappa_{\rm e}$  can be either  $\kappa_x$  or  $\kappa_y$  depending on the orientation (x or y) of the crystal extraordinary axis. After Eqs. (12–14) are integrated with respect to z, the results are inverse Fourier transformed to give the second component of the updated fields. The two components of the fields are then added to give the total updated field after a z increment,  $\Delta z$ .

# **Outputs of the Codes**

Our codes have various tabular and graphics outputs, which are illustrated below. In addition, the spatial and space–time codes can produce a file containing output harmonic and residual harmonic field distributions, which are compatible with the PROP92 propagation code. With this capability, we can propagate a converted beam through a set of optics using PROP92, as well as a  $1\omega$  beam created by PROP92 as the input  $1\omega$ 

field distribution for a conversion calculation.

# Applications of the Frequency-Conversion Codes

## Sensitivity Study of Doubler Detuning Angle by Plane-Wave Codes

As previously mentioned, the frequency-conversion crystals must be tilted with an accuracy of microradians for proper operation. This is especially true for a Type I SHG, where angular detuning is used to control the mix of  $1\omega$  and  $2\omega$  light into the THG. For design of the converter mounting and alignment equipment, it is important to know the alignment accuracy required for conversion efficiency within specifications. The variation of conversion efficiency with doubler detuning angle can be easily determined for a wide set of converter designs using the plane-wave frequency-conversion codes.

Figure 2 shows the output from a plane-wave frequency-conversion code. The plot shows  $3\omega$  conversion efficiency vs initial  $1\omega$  intensity for several values of SHG detuning angle. The latter quantity is the identifying parameter for each curve. The modeled converter configuration consisted of a 13-mm-thick KDP Type I

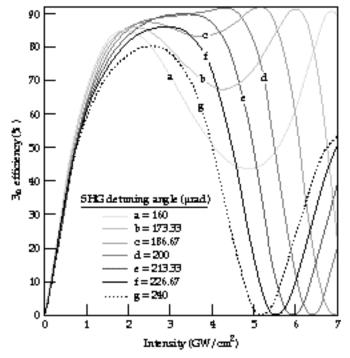


Figure 2. Output of plane-wave, steady, frequency-conversion code showing  $3\omega$  conversion efficiency as a function of input  $1\omega$  intensity for various doubler crystal detuning angles. 40-00-1296-2737pb01

SHG and a 11-mm-thick KD\*P THG with a fixed detuning angle of 30 µrad. Notice that the sensitivity of converter performance increases with initial  $1\omega$  intensity. Thus, in considering the effect of SHG detuning angle alignment on converter performance for temporally shaped pulses, one must analyze the converter performance at the peak intensity of the shaped pulse. It is also important to note that conversion efficiency can drop off drastically as  $1\omega$  intensity increases. Decreased efficiency results from the incorrect ratio of  $1\omega$  and  $2\omega$  light into the THG. This behavior is important in the design of the dynamic range of the converter.

# **Effects of Applied Temporal Phase Modulation on Conversion**

When phase modulation is applied to a field,  $\mathbf{E}_0(z,t)$ , the resulting field for a single modulation frequency f and depth of modulation  $\sigma$  is given by:

$$\mathbf{E}_{\mathrm{pm}}(z,t) = \mathbf{E}_{0}(z,t)\mathrm{e}^{i\sigma\sin 2\pi ft} \ . \tag{15}$$

The bandwidth *bw* over which the phase modulation sweeps is given by:

$$bw = 2\sigma f . (16)$$

As the frequency sweeps from one limit to the other, the effective wavelength of each field also changes, which affects, in turn, the phase mismatch factor [Eq. (1)]. As the phase mismatch  $\Delta k$  varies, the conversion efficiency varies. It is this process that turns a periodic phase modulation into an amplitude modulation.

There are two current uses for applied phase modulation on laser pulses. First, bandwidth is used to suppress Stimulated Brillouin Scattering (SBS) in large optics. The bandwidth used in this application is 30 GHz. Our conversion codes show that this bandwidth causes a small degradation in conversion

efficiency, which needs to be considered along with other degrading factors.

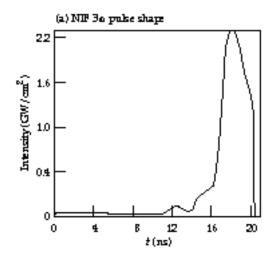
The second application is for beam smoothing by spectral dispersion. Plans are for  $1\omega$  bandwidths in the range of 90 to 150 GHz. Our frequency-conversion codes have shown that planned converter designs suffer significant degradation in performance at such large bandwidths.

In the following examples, we show how the temporal codes model conversion of laser pulses having complex time dependencies. We show the effects of applying a 150-GHz-bandwidth phase modulation on a laser pulse having a temporal shape like that proposed for NIF indirect drive. The converter design we used consists of a 12.7-mm-thick KDP Type I SHG and a 9-mm-thick KD\*P Type II THG.

Figure 3(a) shows the  $3\omega$  intensity temporal pulse shape, and Figure 3(b) shows the  $1\omega$  intensity pulse used to generate the  $3\omega$  pulse for the case with no bandwidth. The two graphs were produced by one of the temporal frequency-conversion codes. The peak  $1\omega$  intensity is  $2.75~\text{GW/cm}^2$ . The energy conversion efficiency was calculated to be 56.5%.

The code was then run a second time starting with the  $1\omega$  pulse of Fig. 3(b); however, a phase modulation with a bandwidth of 150 GHz was impressed on the  $1\omega$  pulse. Figure 4 shows the temporal profile of intensity of the resulting  $3\omega$  pulse. The calculated energy conversion efficiency is 43.4%. Thus, the energy conversion efficiency relative to that of the pulse of Fig. 3(a) decreases by about 13%. In addition, the pulse has severe intensity modulation at twice the phase modulation frequency. The lowest intensity values correspond to times when  $\Delta k$  is largest in magnitude, and the peak values correspond to the times when  $\Delta k = 0$ . These simulations show the need for alternate converter designs for large-bandwidth operation of NIF.

One of the alternate designs is a converter with one



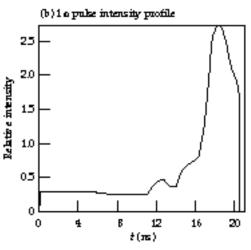


FIGURE 3. Sample output from the temporal frequency-conversion codes. (a) Temporal profile of intensity of a  $3\omega$  laser pulse with a NIF-like shape. (b) Temporal profile of intensity of the  $1\omega$  pulse derived from the pulse shape of (a) for a converter consisting of a 1.27-cm-thick KDP doubling crystal and a 0.9-cm-thick KD\*P tripling crystal. 40-00-1296-2738pb01

REQUERCE CONVERSION INDOCESING

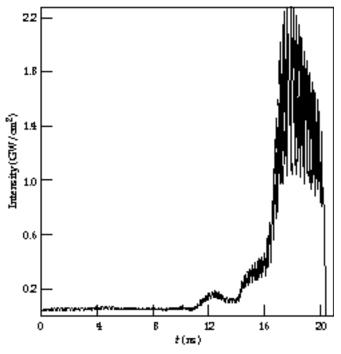


Figure 4. Temporal profile of intensity of the  $3\omega$  pulse produced when the  $1\omega$  pulse of Fig. 3(b) with 150 GHz of applied phase modulation is propagated through the two-crystal 1.27/0.9 converter. 40-00-1296-2740pb01

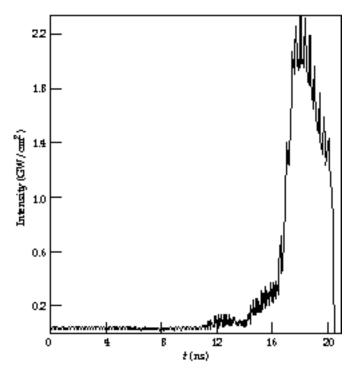
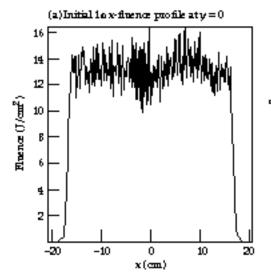


FIGURE 5. Temporal profile of intensity of the  $3\omega$  pulse produced when the  $1\omega$  pulse of Fig. 3(b) with 150 GHz of applied phase modulation is propagated through a three-crystal converter. The KDP doubler is 1.2 cm thick with a detuning angle of 210  $\mu$ rad. The first KD\*P tripler crystal is 0.7 cm thick with a detuning angle of 950  $\mu$ rad. The second KD\*P tripler crystal is 0.9 cm thick with a detuning angle of  $-350~\mu$ rad. 40-00-1296-2741pb01



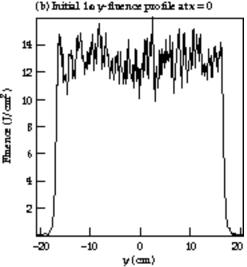


FIGURE 6. Profiles of fluence of the initial  $1\omega$  field distribution. (a) Center (y = 0) x profile of fluence. (b) Center (x = 0) y profile of fluence. 40-00-1296-2742pb01

SHG and two THG crystals. The temporal frequency-conversion code shows that this design produces a much smoother  $3\omega$  pulse, as shown in Fig. 5. In addition, the calculated conversion efficiency is 53.3%, which corresponds to a drop of only 3% relative to that of the pulse of Fig. 3(a). For higher peak intensities in the NIF-like pulse, the difference in conversion

# Simulations of Field Distributions with Temporal and Transverse Spatial Variations (x, y, z, t) Using PROP92

The PROP92 code models the propagation of laser beams with spatial variations in one or two transverse dimensions and a temporal variation represented in a

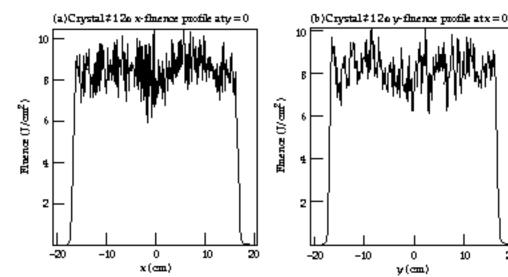


FIGURE 7. Profiles of fluence of the 2ω field distribution at the output of the doubler crystal. (a) Center (y = 0) x profile of fluence. (b) Center (x = 0) y profile of fluence. 40-00-1296-2744pb01

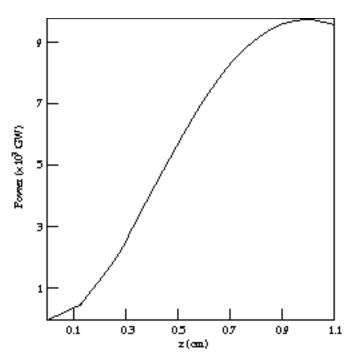


FIGURE 8.  $2\omega$  energy as a function of distance into the doubler crystal. 40-00-1296-2746pb01

discrete set of time slices. With this temporal representation, it is difficult to model conversion of fields with applied bandwidth, but it is easy to model beams with intensity envelopes of arbitrary temporal shape and no bandwidth. However, for small bandwidths and the converter designs of interest for NIF, the effects of bandwidth are small, and results from PROP92 are quite accurate. Following is an example of the use of the frequency-conversion code for which the fields are functions of x, y, z, and  $\Delta t_{n}$ , where  $\Delta t_{n}$  denotes the time slice array.

The  $1\omega$  field distribution used in this example corresponds to simulation of a shot on the Beamlet laser

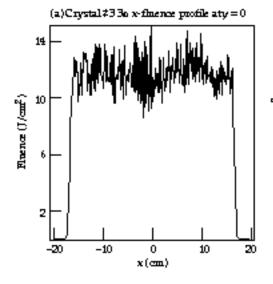
system in which the  $1\omega$  output fluence is  $13 \text{ J/cm}^2$  in a 3-ns temporally flat pulse. The pulse is represented by three time slices. The first slice corresponds to the first 0.01 ns of the pulse; the second slice to the next 2.98 ns of the pulse; and the last slice to the last 0.01 ns of the pulse. Each slice is a field distribution defined on an x–y grid. Figures 6(a) and 6(b) show the center x and y profiles, respectively, of the initial  $1\omega$ fluence. The converter used in this example consists of an 11-mm-thick KDP SHG detuned at 240 µrad and a 9-mm-thick KD\*P THG. The 1ω field distributions are propagated through the SHG. Modeled physical processes include frequency conversion, nonlinear index phase retardation, paraxial diffraction, and walk-off.

10

Figures 7(a) and 7(b) show the center x and y profiles, respectively, of the  $2\omega$  fluence distribution. The SHG energy conversion efficiency was calculated to 63.37%. This value is determined by the internal detuning angle, which is set as close as possible to produce equal intensities of  $1\omega$  and  $2\omega$  light into the SHG. Because the fields are spatially varying, only a few grid points of the beams will meet the equalintensity condition for a specified detuning angle. Note that the 2ω fluence modulation is almost identical in shape to the  $1\omega$  fluence modulation, indicating that intensity dominates the conversion process. This result is expected because the phase profiles from the PROP92 calculation indicate only small transverse gradients. However, with large, local transverse phase gradients (which do not apply in the present example), the walk-off term can become large and affect frequency conversion.

Figure 8 shows the  $2\omega$  energy in the doubler crystal as a function of distance *z* into the crystal. Note the slight rollover in the curve at the end of the crystal, which indicates that the detuning angle was not quite at the value for optimum conversion.

LQUEINCT CONVERSION INIODELINO



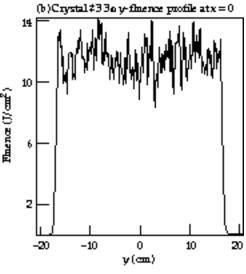


FIGURE 9. Profiles of fluence of the  $3\omega$  field distribution at the output of the tripler crystal. (a) Center (y = 0) x profile of fluence. (b) Center (x = 0) y profile of fluence. 40-00-1296-2747pb01

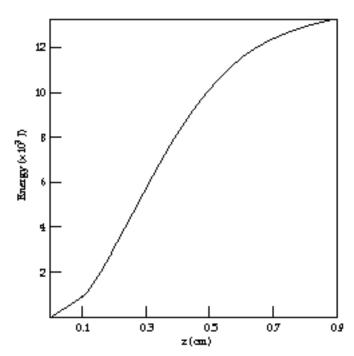


Figure 10. 3  $\!\omega$  energy as a function of distance into the tripler crystal. 40-00-1296-2749pb01

Figures 9(a) and 9(b) show the center x and y profiles, respectively, of  $3\omega$  fluence. Once again, the modulation is almost identical to that of the  $1\omega$  fluence profiles, indicating that conversion is determined mainly by the intensity distributions of the fields and not by their phase distributions. Calculated  $3\omega$  energy conversion efficiency is 88.38%. Figure 10 shows the  $3\omega$  energy as a function of distance into the tripler crystal. The  $3\omega$  field distributions calculated by this code can be used as input to PROP92 to model propagation of the  $3\omega$  beam in the output section of Beamlet and NIF. The output section extends from the output of the frequency converter to the output of the final focusing lens.

# Summary

Frequency conversion is a complex nonlinear process requiring precise tolerances for optimum results. The newly developed frequency-conversion codes have aided the designers of Beamlet and NIF in specifying the correct converter designs needed for a variety of operating scenarios.

#### References

1. J. F. Nye, *Physical Properties of Crystals* (Oxford University Press, 1986) pp. 237–238.

# THE PROP92 FOURIER BEAM PROPAGATION CODE

R. A. Sacks

M. A. Henesian

S. W. Haney

J. B. Trenholme

### Introduction

Numerical simulations of the laser beam propagation<sup>1</sup> have been used in designing and optimizing all of LLNL's high-power lasers for inertial confinement fusion (ICF). The architecture and design of the laser for the National Ignition Facility (NIF) were determined and optimized using a suite of new codes including CHAINOP, BTGAIN, and PROP92.

CHAINOP<sup>2</sup> is a very fast lumped-element energetics code with an extensive cost database, a choice of optimization algorithms, and a set of heuristic rules for diffraction and nonlinear effects and for operational constraints.

BTGAIN<sup>3</sup> is a far-field model based on the Bespalov–Talanov theory<sup>4</sup> for the linearized growth of decoupled single-mode beam perturbations in a nonlinear medium. Itincludes Frantz–Nodvik saturated gain, the facility to input beam perturbations of arbitrary spectral content at each component, and a postprocessor that can construct near-field beam statistics.

PROP92 was originally written and released by R. G. Nelson<sup>5</sup> in 1992, with advice and assistance from J.B. Trenholme. It is a full-featured optics propagation and laser simulation code. Internal models are included for most of the components in the optical amplifier and transport system. A Fourier technique is used to solve the nonlinear Schrödinger (NLS) equation, yielding a representation of the (single-polarization) complex electric field in two transverse directions plus time (2D) as the beamtransports through andisaffected by the optical elements. Alternatively, PROP92 can also operate in 1-D planar or 1-D circularly symmetric modes. In the latter case, Hankel/Besseltransforms are used insteadof Fourier transforms. Average wavefront curvature is explicitly removed in the Talanov transformation. Both

gain and nonlinear index effects are calculated in the near field with a split-step approach. Propagation is done in the far field.

In this article, we describe the algorithms and structure of the PROP92 code. We discuss 2-D operation, since the restriction to either 1-D planar or 1-D circular is straightforward.

# Vacuum Propagation Algorithm

PROP92 describes the laser beam in terms of a complex electric field,  $\mathbf{E}(x,y,z,t)$ . The dominant plane-wave portion of the beam and its center-point position, tilt, and curvature are all explicitly removed to define a wave function u for numerical evaluation

$$\mathbf{E}(x,y,z,t) = \mathbf{e}e^{i(k_0z - \omega_0t)}e^{i[\bar{\kappa}_x(x - x_0) + \bar{\kappa}_y(y - y_0)]}e^{-ik_0(x - x_0)^2 / 2R(z)} \times e^{-ik_0(y - y_0)^2 / 2R(z)}u(x,y,z,t) .$$
 (1)

In Eq. (1), the laser's optical frequency is  $\omega_0$ , and the wave number is  $k_0 = n_0 \omega_0/c$ , where  $n_0$  is the index of refraction of the medium through which the beam is propagating, and c is the vacuum speed of light. The average tilt on the wavefront is described by the quantities and , and the central position  $(x_0, y_0)$  satisfies

$$x_0(z + \delta z) = x_0(z) + \overline{\kappa}_x \, \delta z / k_0$$
  

$$y_0(z + \delta z) = y_0(z) + \overline{\kappa}_y \, \delta z / k_0 \quad . \tag{2}$$

*R* is the average wavefrontcurvature, with the convention that positive *R* corresponds to a focusing wave. It satisfies

$$R(z + \delta z) = R(z) - \delta z . (3)$$

The complex wave function *u* is represented on a regular rectangular grid

$$u_{j,k} = u(x_j + x_0, y_k + y_0, z, t) , \qquad (4)$$

where j and k are integers in the range  $-N_x/2 \le j < N_x/2$ ,  $-N_y/2 \le k < N_y/2$ ,  $x_j = jL_x / N_x$ ,  $y_k = kL_y / N_y$ ,  $L_x$  and  $L_y$  are the physical dimensions of the calculational grid, and  $N_x$  and  $N_y$  are the number of grid points.

In a linear medium (no gain, no nonlinear index effects), the electric field obeys the wave equation

$$\nabla^2 \mathbf{E} - \frac{n_0^2}{c^2} \frac{\partial^2}{\partial t^2} \mathbf{E} = 0 \quad . \tag{5}$$

Using Eq. (1) and applying the slowly varying  $(\partial u/\partial t << \omega_0 u)$  and paraxial  $(\partial^2 u/\partial z^2 << k_0 \partial u/\partial z)$  approximations, we find that u translates as

$$u(\mathbf{r}, z + \delta z) = \frac{R_0}{R} \int \frac{d^2 \kappa}{(2\pi)^2} e^{i\frac{R_0}{R} \kappa \cdot \mathbf{r}} e^{-\frac{iR_0}{2k_0 R} \kappa^2 \delta z}$$

$$\times \int d^2 \mathbf{r}' e^{-i\kappa \cdot \mathbf{r}'} u(\mathbf{r}', z, t)$$
(6)

where  $R_0 = R(z)$ , and  $R = R(z+\delta z)$ . In Eq. (6), we can see the familiar Fourier propagation algorithm: (a) Fourier transform, (b) multiply each Fourier mode by a phase that is linear in propagation distance and quadratic in angle, and (c) inverse transform. Because u is represented on a discrete mesh, the continuous transform in Eq. (6) is replaced by a discrete fast Fourier transform (FFT). This means that the field is actually represented by a function that is periodic in both near-field and far-field coordinates. The effective grid dilatation apparent in the inverse transform is actually carried out in PROP92 by changing the values of  $L_x$  and  $L_y$  at the new observation point  $z + \delta z$ . Scaling the computational grid tends to maintain resolution for focusing beams (which would otherwise occupy progressively less of the grid) and avoids aliasing of defocusing beams (which would otherwise try to outgrow the grid and thus "wrap" information around the edges). The prefactor,  $R_0/R$ , may be thought of as scaling the intensity to conserve energy as the transverse extent of the beam changes.

# **Nonlinear Self-Focusing**

In centro-symmetric (invariant under inversion through the origin) and isotropic materials, the singlefrequency wave equation may generally be written as

$$\left(\nabla^2 + \frac{n^2(E)\omega^2}{c^2}\right)\mathbf{E} = 0 \quad , \tag{7}$$

where the field-dependent refractive index is

$$n(E) = n_0 + \frac{1}{2}n_2E^2 + \dots$$
(8)

Applying the slowly varying wave and paraxial approximations yields the NLS equation

$$\left[\frac{\partial}{\partial z} - \frac{i}{2k_0} \nabla_T^2 - \frac{2\pi i}{\lambda_{\text{vac}}} \gamma I\right] u = 0 , \qquad (9)$$

where  $\gamma = n_2/(n_0c\varepsilon_0)$ ,  $\lambda_{\rm vac}$  is the vacuum wavelength, and  $I = n_0c\varepsilon_0 \mid u \mid^2/2$  is the local irradiance. The parameter  $\gamma$  is a material property that measures the field phase advance per unit of intensity and per unit of length. Because  $n_2$  and  $\gamma$  are positive for materials of interest, local high-intensity perturbations create their own focusing phase perturbations, thereby amplifying the perturbation, and ultimately leading to catastrophic filament collapse. Equation (9) is written with the intensity explicitly introduced because in PROP92, the electric field is normalized such that  $|u|^2 = I$ . As presented, Eqs. (5), (6), and (9) are not affected by this normalization choice.

In PROP92, nonlinear propagation effects are computed by a split-step algorithm. The propagation through the nonlinear medium is divided into a number of steps of length  $\delta z$ . Vacuum propagation steps [Eq. (6)] are alternated by thin-optic transformations,

$$u(x,y,z) \leftarrow u(x,y,z)e^{i\Delta B(x,y,z)}$$
,

where

$$\Delta B(x, y, z) = \frac{2\pi\gamma}{\lambda_{\text{vac}}} \left| u(x, y, z) \right|^2 \delta z \quad . \tag{10}$$

For higher-order accuracy, the process is "leapfrogged," with a diffraction step of length  $\delta z/2$  at the beginning and end of the nonlinear optic.

Research shows that PROP92's split-step algorithm agrees with experimental results both at  $1\omega$  and at  $3\omega^{6,7}$  when sufficient resolution is included in the calculation. There are, however, two difficulties with simply relying on the propagation algorithm for computing all self-focusing threats:

1. Catastrophic self-focusing cannot occur in 1D,<sup>8</sup> but time and resource constraints require that we use PROP92's 1-D planar mode for much of our design optimization.<sup>9,10</sup>

2. Even in 2D, it is often not feasible to adequately resolve beam features at the sizes that are most prone to self-focusing amplification.

Given these difficulties, we have recently added<sup>11</sup> a number of features to the code to warn users about filamentation danger.

Sulem et al. have shown<sup>12</sup> that intensity perturbations of the most unstable size and shape will collapse, during propagation through a uniform nonlinear medium, in a distance such that  $\Delta B_0 = \gamma I_0 \Delta z = 2.3$ , where  $I_0$  is the maximum intensity at the peak of the initial perturbation. By detecting and reporting the maximum over the transverse position of the  $\Delta B$  through the thickness of any given optic, PROP92 tracks the safety margin with respect to collapse in that optic. To allow for optical gain (also calculated by a split-step algorithm), the maximum  $\Delta B(x,y)$  is recalculated from the current z-position to the exit face of the optic at each z-step.

Before the NLS becomes singular, the collapse process is limited by nonlinear processes, such as optical breakdown (not included in the model). These breakdown processes led to the "angel hair" tracks in the Nova and Beamlet high-power optics. PROP92 has a test for breakdown-induced tracking, based on an extrapolation of the peak irradiance in the beam. Trenholme<sup>13</sup> has numerically verified that during the filamentation process, all perturbations evolve to a shape resembling the "ground state" (which collapses most rapidly) and that late in the collapse the intensity scales as  $(z_c - z)^{-4/3}$ , where  $z_c$ is the position of the singular collapse point. At each z-step through the slab, the maximum calculated intensity is scaled by  $[z_c/(z_c-z_{exit})]^{4/3}$  to project a maximum anticipated self-focused intensity in the slab. A warning message is printed if this projected intensity exceeds a user-entered breakdown intensity.

Finally, PROP92 includes a check on the adequacy of the grid spacing to resolve the most important structure. This check is based on the Bespalov–Talanov (BT) theory of the linearized growth of independent Fourier modes.<sup>3,4</sup> If we expand u as

$$u(x,y,z) = u_0 \left[ 1 + \sum_{\alpha_{-\kappa}^{\kappa}} \alpha_{\kappa}(z) e^{i\kappa \cdot \mathbf{r}} \right], \qquad (11)$$

$$\begin{pmatrix}
\alpha_{\kappa}(z) \\
\alpha_{-\kappa}^{*}(z)
\end{pmatrix} = \begin{bmatrix}
\cosh S\Theta - i\frac{\Theta - B}{S\Theta}\sinh S\Theta & i\frac{B}{S\Theta}\sinh S\Theta \\
-i\frac{B}{S\Theta}\sinh S\Theta & \cosh S\Theta + i\frac{\Theta - B}{S\Theta}\sinh S\Theta
\end{bmatrix} \begin{pmatrix}
\alpha_{\kappa}(0) \\
\alpha_{-\kappa}^{*}(0)
\end{pmatrix}, (12)$$

substitute u into Eq. (9), and drop terms of order  $\alpha^2$ , we find that  $\alpha_{\kappa}$  and are coupled, and they grow such that where

$$\Theta = \kappa^2 z / 2k_0$$

$$B = \gamma u_0^2 z$$

$$S = \sqrt{1 - \mathcal{B}/\Theta} . \tag{13}$$

Defining the mode amplitude as  $|\alpha_{\kappa}|^2 + |\alpha_{-\kappa}|^2$ , maximum gain at given  $\kappa$  occurs when

$$\alpha_{-\kappa}^* = e^{-i\phi} \alpha_{\kappa}$$

$$\phi = \frac{\pi}{2} + \tan^{-1} \left[ \frac{\Theta - B}{S\Theta} \tanh S\Theta \right] . \tag{14}$$

This maximum modal gain is

$$G = 1 + \frac{2B^2}{(S\Theta)^2} \sinh^2 S\Theta$$

$$+ \frac{2B}{S\Theta} \sinh S\Theta \sqrt{1 + \frac{B^2}{(S\Theta)^2} \sinh^2 S\Theta} . \tag{15}$$

Maximizing G with respect to  $\Theta$ , we find that the mode with maximum growth according to BT is

$$\Theta_{\text{max}} = B \tag{16}$$

PROP92 issues a warning if the spatial frequency of this mode is greater than the Nyquist frequency  $\kappa_{\rm Ny}=2\pi \min(N_x/L_{x'},N_y/L_y)$ .

# **Optical Damage**

Besides tracking caused by nonlinear self-focusing, which leads to superhigh intensity and plasma formation, large optical *fluence* can lead to optical damage ranging from color-center formation to material fracture. So far, there is no adequate explanation of what causes the formation of these damage sites. However, Campbell et al. have compiled <sup>14</sup> an extensive experimental database of damage fluences for various materials during

their exposure to nearly Gaussian pulses of various pulse lengths. When the pulse length is between about 10 ps  $\Phi_D = C \tau^{\beta}$  (17)

where  $\Phi_D$  is the fluence at which damage sites first appear,  $\tau$  is the Gaussian pulse width, and C and  $\beta$  are material-dependent constants. In particular,  $\beta$  ranges between about 0.3 and 0.5 for the various materials of interest and is independent of  $\tau$ , for a given material, over 4 to 5 decades of pulse duration.

For many applications, such as driving ICF targets on NIF, it is necessary to subject optical materials to high fluence with a temporal pulse history that does not resemble Gaussian. To assess the danger of optical damage from such pulses, we have implemented a phenomenological diffusion-like model, for damage from arbitrarily shaped pulses.

The model assumes that damage is related to the accumulation of some quantity D whose source is proportional to the local laser irradiance, and which accumulates with a diffusive kernel. Damage is presumed to occur instantly if D exceeds some material-dependent critical value  $D_{\rm D}$ . Trenholme demonstrated that no true diffusion model in 1, 2, or 3 dimensions can match the observed data. Rather, he was led to posit a form,

$$D(t) = A \int_0^\infty \frac{I(t-s)}{s^{d/2}} ds , \qquad (18)$$

where d is an effective dimensionality, I is the local irradiance, and A is a constant. Although Eq. (18) is formally singular when  $d \ge 2$ , this is not important because all existing damage data correspond to  $d \le 1$ . Equation (18) is related to the measured data by substituting for I, a Gaussian with peak value  $I_D$  and full width at half maximum  $\tau$ . Evaluating the maximum over t of the resulting damage integral gives

$$D_D = I_D A \tau^{1-d/2} \max_{\xi} \int_0^\infty \frac{\exp[-4\ln 2(\xi - s)^2]}{s^{d/2}} ds , \quad (19)$$

where, for given d, the maximum of the integral is simply a number that can be evaluated once numerically, and the scaling with  $\tau$  is explicit. Evaluating the fluence,  $\Phi_D$ , for the same Gaussian pulse and setting it equal to  $C\tau^\beta$  identifies d as  $2\beta$  and yields

$$D_{\rm D} = \frac{AC}{\sqrt{\pi}} (4 \ln 2 )^2 \max_{\xi} \int_0^\infty \frac{e^{-(\xi - s)^2}}{s^{\beta}} ds .$$
 (20)

For each optic for which damage calculations are

desired, the experimental scaling values C and  $\beta$  are input to PROP92. Equation (20) is then evaluated, and the limit value of the damage integral is stored. Each time that the beam passes that point in the laser chain, the damage integral [Eq. (18)] is evaluated for each spatial grid point on the calculational mesh. The maximum of the ratio  $D/D_D$  is reported. If that maximum is greater than one, a warning is issued and the damaged area fraction is reported. Note that the constant A drops out of this calculation.

# **Laser Component Models**

PROP92 is a general-purpose computational tool for simulating the operation of laser chains and for optimizing their performance. To enable this process, it contains a library of models of the components that make up the chain and a sequencer that controls the order in which the beam encounters each of these modules. In 2D, the beam is stored as an  $N_x \times N_y \times N_t$  array of complex numbers. We have already described how the propagation between components is modeled as an inverse FFT of a phase times an FFT of this array. We have also described how the array is diagnosed to assess the danger of filamentation or optical damage. In this section, we describe the transformations we use to model some of the more important optical components that comprise typical laser chains.

#### Slabs

In PROP92, a slab is a region of space, of length  $\Delta z$ , filled with a uniform medium of given  $n_0$  and  $\gamma$ , with given small-signal gain G (at small input fluence,  $\Phi_{\rm in}$ ), the output fluence is G  $\Phi_{\rm in}$ ), saturation fluence  $\Phi_{\rm sat}$  and transmissivity T. If the gain is not unity, then gain typically depends on the transverse coordinates and evolves as part of the propagation algorithm.

Propagation through slabs is modeled by a splitstep process, with the step size  $\delta z$  ( $\Delta z/\delta z=$  integer) specified by the user. A propagation step with length  $\delta z/2$  is followed by the application of nonlinear phase  $B(x,y,\delta z)$  and a gain calculation (described below) that also correspond to length  $\delta z$ . After that, propagation steps of length  $\delta z$  are alternated with near-field effects corresponding to  $\delta z$ . A final propagation of length  $\delta z/2$  completes the slab. Transmissivity is applied as a field multiplier at the slab entrance and exit.

The gain calculation is a simple Frantz–Nodvik<sup>16</sup> transformation. The initial slab gain G(x,y) is divided equally among the z-slices—each has gain  $g(x,y,z) = G(x,y) \delta z/\Delta z$ . This array of real numbers is stored on disk and read into memory successively as needed. At each spatial point, the temporal dependence of the field is thought of as a sequence of piecewise-constant

values, so afluence  $\Phi_j = |E(x,y,t_j)|^2 \delta t_j$  can be associated witheach time slice. As the  $j^{th}$  time slice at x,y passes through the gain slice at x,y,z, the Frantz–Nodvick model for a two-level, homogeneously broadened laser line is

$$\Phi_{\text{out}} = \Phi_{\text{sat}} \ln \left[ 1 + g \left( e^{\Phi_{\text{in}} / \Phi_{\text{sat}}} - 1 \right) \right]$$

$$g_{\text{out}} = \frac{g_{\text{in}}}{g_{\text{in}} - e^{-\Phi_{\text{in}} / \Phi_{\text{sat}}} (g_{\text{in}} - 1)} . \tag{21}$$

The field for this time slice is scaled to the new fluence, and the gain distribution for this *z*-slice is overwritten by the new values so that the slab is cumulatively saturated.

#### **Aberrations**

PROP92 is capable of imposing a variety of phase aberrations on the field. Included are the low-order Seidel aberrations tilt, focus, astigmatism, spherical, and coma. Also, phase ripples,

$$E \leftarrow Ee^{2\pi i a \cos(\mathbf{q} \cdot \mathbf{r} + \chi)}$$
, (22)

can be applied at arbitrary amplitude, scale length, transverse direction, and phase. Another possibility is random phase noise with specified peak-to-valley amplitude and correlation length. Finally, an arbitrary phase-shift distribution can be specified numerically.

#### Lenses

A lens is treated as a combination of a slab (with unity gain but with some thickness and given linear and nonlinear indices) and a thin lens transformation,

$$R \leftarrow \frac{Rf}{R+f} \quad . \tag{23}$$

Lens aberrations must be specified as separate "aberration" components.

# **Spatial Filters**

A spatial filter consists of two focusing lenses of focal lengths  $f_1$  and  $f_2$ , separated by a distance  $f_1 + f_2$ , and a pinhole at the common focal plane. In a laser chain, spatial filters fulfill three important functions. First, since the field at the lens focal plane is a dimensional-scale and an intensity-scale of the incoming field's Fourier transform, the pinhole strips off the high-spatial-frequency portions of the beam.

Otherwise the beam would be more prone to self-focusing. Second, in passing through the filter, the beam's transverse dimensions are magnified by the factor  $m = f_2/f_1$ , with a corresponding change in irradiance. Third, since an object at distance d before the filter is imaged at a distance  $m(f_1 + f_2 - md)$  after the filter, the evolution of long-scale-length phase noise into amplitude modulation is inhibited by proper placement of filters in the system.

Spatial filters can be treated as a sum of their constituent parts: a lens transformation, followed by a propagation of length  $f_1$ , clipping at the pinhole, propagation by  $f_2$ , and another lens. As long as the beam entering the filter is not focusing or defocusing, it is rigorously correct to use the lumped-element transformation implemented in PROP92 instead. The lumped-element transformation consists of clipping the Fourier transform of the field array, propagating through a negative distance  $-(f_1 + f_2)/m$ , magnifying the beam by m, and spatially inverting the beam in the transverse plane  $E(x,y) \leftarrow E(-x,-y)$ . PROP92 offers a variety of options for pinhole sizes, shapes, orientations, and transverse offsets (including the option to describe the filter function numerically). The pinhole edge is smoothed over several transverse grid steps to avoid aphysical numerical ringing.

#### **Mirrors**

Mirror components reverse the logical direction that the beam sequencer traverses chain components, enabling us to model multipass architectures. Tilts on the mirrors are permitted, affecting and in Eq. (1), and thereby affecting the beam's average transverse position as it samples aberration and gain fields. Recently, Henesian has added a model for phase-conjugating mirrors, including an intensity-thresholding effect.

#### Masks and Obscurations

Both masks and obscurations modify the beam by applying a near-field intensity filter that varies with transverse position. Both offer a number of built-in shapes and orientations. They offer control over the degree of edge smoothing, and both offer the option for numerical description of the filter function. A mask represents a filter that passes the center of the beam and removes the edge (such as would occur because of the finite physical aperture of chain components). An obscuration removes some small portion of the center of the beam (such as would occur if the beam struck a small obscuration). Obscurations also offer the option of applying a specified phase to a portion of the beam, to repre-

sent, for example, regions of surface irregularity or of bulk index variation.

### **Adaptive Optics**

Adaptive optics are used in laser systems to correct for long-scale-length aberrations induced on the beam. At some point in the chain, the beam reflects from a deformable mirror. The mirror's surface can be distorted by as much as several wavelengths by displacing an array of mechanical actuators. At another point, a phase sensor is located. Operation of the adaptive optic consists of adjusting the displacement of the mirror actuators to minimize the transverse variation of the phase at the sensor.

On NIF, the deformable mirror is one of the end mirrors in the multipass cavity. Phase is detected by a Hartmann sensor, which consists of a lenslet array (on NIF it will be triangular) and a light sensor capable of detecting the centroid of the focal spot from each lenslet. The operational algorithm attempts to minimize the sum of the squares of the focal spot displacements. A transfer matrix is measured by observing the spot movements resulting from small travel of each of the actuators. A matrix inversion then predicts the actuator displacements necessary to best cancel a measured set of spot displacements. By placing this correction procedure into a feedback loop, continuous correction for time-varying effects (such as air-path turbulence and decaying thermal sources) has been accomplished.<sup>17</sup>

Modeling the correction procedure has two parts: (1) determining the beam phase modification accompanying a given set of actuator displacements and (2) finding the best set of displacements to use. For the first part, we have implemented a model where the mirror surface (hence the applied phase field) is assumed to be a sum of Gaussians,

$$\phi(x, y) = \sum_{j} a_{j} e^{-\left|\mathbf{r} - \mathbf{r}_{j}\right|^{2} / \sigma^{2}} \quad . \tag{24}$$

In Eq. (24), the sum is over the set of actuators,  $\mathbf{r}_j$  are the set of centersof influence (nearlythe sameasthe physical actuator positions),  $\sigma$  is the influence width, and the source strengths  $a_j$  are related to the actual actuator displacements. Typically, the  $\mathbf{r}_j$  are located on a regular triangular or rectangular array with some outward displacement for the sources on the array boundary caused by their nonhomogenous environment. The values of  $\mathbf{r}_j$  and  $\sigma$  are inputs to PROP92's adaptive-optic model. In one of its modes of operation, the  $a_j$  are also input parameters, in which case the component is modeled as a determined phase

modification. This form of operation allows optimization of the best set of source strengths to meet some external objective, for example maximizing the energy into a hohlraum laser entrance hole.

In another mode of operation, PROP92 can adjust the  $a_j$  to apply a best local phase correction in minimizing the fluence-weighted mean square deviation from flat phase. "Adapt" components that are multipassed retain the shape that is determined the first time they are encountered. This method, since the phase correction is local and simply determined, is useful for obtaining a quick and reasonably accurate approximation of the performance enhancement that might be expected.

Although it is not strictly part of PROP92, Henesian has built up a realistic model of the adaptive optic operation as it will be implemented on Beamlet and NIF. At the end of a PROP92 simulation of a chain, the field array is dumped to disk. This file is read by a postprocessor routine that simulates the action of the Hartmann sensor. Portions of the array are masked off and brought to focus, and the centroid of each focal spot is calculated. If there are  $N_{\rm a}$  actuators, then  $N_{\rm a}$  separate PROP92 runs are required to determine the transfer matrix, which is easily inverted (or SV decomposed if, as typically, it is nonsquare). For a given set of component aberrations, two more PROP92 runs suffice to measure the corrections required and to predict the performance with those corrections.

#### **Plots**

Considerable attention has been given to the graphical presentation of PROP92 results. At any point in the chain simulation, the user can display plots of near-field intensity, fluence, or phase—or of intensity or fluence either in the far field or in a partial focus region. These can be displayed as surface plots, contour plots, or cuts, either through specified position or through the maximum intensity point. The vertical scale can be linear or logarithmic. PROP92 has the capability to window the plots, which add resolution to a region of interest. As mentioned, PROP92 is capable of dumping the field array to disk, which enables us to use the graphical power of packages such as IDL for postprocessing.

# **Summary**

PROP92 is a full-featured Fourier optics laser modeling, design, and optimization tool. It includes integrated models for a comprehensive set of optical elements and effects, as well as sophisticated algorithms for assessing the risk of optical damage and filamentation. As detailed elsewhere in this *Quarterly*, PROP92 predictions have been validated by compari-

son with Nova, OSL, and Beamlet experiments. Given reliable data on material properties and optical quality, we have confidence in PROP92's predictions of NIF performance.

#### **Notes and References**

- 1. W. W. Simmons, J. T. Hunt, and W. E. Warren, *IEEE J. Quantum Electron.*, **OE-17**, 1727–1743 (1981).
- W. Williams, J. Trenholme, C. Orth, S. Haney, R. Sacks, et al., ICF Quarterly Report 6(4), Lawrence Livermore National Laboratory, Livermore, CA, UCRL-LR-105821-96-4 (1996).
- 3. J. B. Trenholme, 1975 Laser Program Annual Report, Lawrence Livermore National Laboratory, Livermore, CA, UCRL-50021-75 (1975), pp. 236–245.
- 4. V. I. Bespalov and V. I. Talanov, JETP Letters 3, 307-312 (1966).
- R. G. Nelson, "PROP92, A Family of Laser Beam Propagation Codes," Lawrence Livermore National Laboratory, Livermore, CA, internal memo (unnumbered), August 1992.
- W. H. Williams, K. R. Manes, J. T. Hunt, P. A. Renard et al., *ICF Quarterly Report* 6(1), 7–14, Lawrence Livermore National Laboratory, Livermore, CA, UCRL-LR-105821-96-1 (1996).
- D. Milam et al., "Beam Breakup and Filamentation at the Third Harmonic Wavelength," Proceedings of the Second Annual International Conference on Solid State Lasers for Application to Inertial Confinement Fusion, Paris, France, October 20–25, 1996.
- 8. H. C. Yuen and W. E. Ferguson, Jr., *Phys.Fluids* **21**(8), 1275–1278 (1978); E. Fermi, J. Pasta, and S. Ulam, *Collected Papers of Enrico Fermi*, edited by E. Segré (University of Chicago, Chicago, 1965), vol. 2, p. 978.
- 9. W. Williams, S. Haney, R. Sacks, C. Orth, et al., "The 11-0-7 NIF

- Laser Design: Description and Background," Lawrence Livermore National Laboratory, Livermore, CA, memo NIF-LLNL-96-283 (1996).
- S. W. Haney, W. H. Williams, R. A. Sacks, J. M. Auerbach, and C. C. Widemeyer, "Report on Work Package #1: NIF Energetics Under Reduced Slab Count/Reduced PAM Size Operation," Lawrence Livermore National Laboratory, Livermore, CA, memo NIF-0000582 (1996).
- M. A. Henesian, "Simulations of 3ω Beam Filamentation in the Beamlet Focus Lens and General Comments on Filamentation Theory," Lawrence Livermore National Laboratory, Livermore, CA, memo LS&T-LMO-96-001 (1996).
- P. L. Sulem, C. Sulem, and A. Patera, "Numerical Simulations of Singular Solutions to the Two-Dimensional Cubic Schrödinger Equation," Communications on Pure and Applied Mathematics, (John Wiley and Sons, New York), vol. XXXVII, pp. 755–778.
- J. B. Trenholme, "Overview of Basic Filamentation Concepts," Laser Modeling and Optimization talk, August 17, 1995; see also J. T. Hunt, "A Comparison of Nova and Beamlet's Design Margin Against Filamentation," Lawrence Livermore National Laboratory, Livermore, CA, memo NIF-LLNL-95-498, L-20374-01 (1995).
- J. H. Campbell and F. Rainer, "Optical Glasses for High-Peak-Power Laser Applications," Lawrence Livermore National Laboratory, Livermore, CA, UCRL-JC-109255 (1992); Proceedings of the 1992 SPIE Conference, San Diego, CA, July 19–24, 1992.
- J. B. Trenholme, "Damage from Pulses with Arbitrary Temporal Shapes," Lawrence Livermore National Laboratory, Livermore, CA, memo LST-LMO-94-001 (Ver. 2) L-18179-2 (1995).
- L. M. Frantz and J. N. Nodvik, J. Appl. Phys. 34(8), 2346–2349 (1963).
- 17. M. W. Kartz, W. C. Behrendt, R. G. Hartley, A. F. Hinz, et al., "Wavefront Correction for Static and Dynamic Aberrations to Within 1 Second of the System Shot in the NIF Demonstration Facility," Second Annual International Conference on Solid State Lasers for Application to Inertial Confinement Fusion, Paris, France, October 22–25, 1996.
- 18. M. A. Henesian, S. W. Haney, M. Thomas, and J. B. Trenholme, "Modeling for Deformable Mirrors and the Adaptive Optics

# NOVA/BEAMLET/NIF UPDATES JULY-SEPTEMBER 1996

G. Hermes

R. Speck

A. Clobes

# **Nova Operations**

During this quarter, Nova Operations fired a total of 314 system shots resulting in 320 experiments. These experiments were distributed among ICF experiments, Defense Sciences experiments, X-Ray Laser experiments, Laser Sciences, and facility maintenance shots.

This is the final report for FY 1996. During the past year, Nova fired a total of 1192 system shots resulting in a total of 1263 experiments. There were 981 target experiments done in the 10-beam chamber and 86 experiments done in the 2-beam chamber. There were 110 experiments conducted in support of laser science work, including precision pointing, Petawatt system activation, and miscellaneous beam propagation experiments. We fired 85 calibration shots in support of routine and precision operations.

We have started implementing smoothing by spectral dispersion (SSD) on all 10 beamlines of Nova. Hardware for the preamplifier grading table and relay lens assemblies was installed this quarter. Experiments using 10-beam SSD are planned for FY 1997.

A conceptual design for a  $4\omega$  probe beam for the 10-beam chamber has been completed. This beamline will be created by a "pick-off" mirror installed into the center obscuration of beamline 8 in the switchyard. This subaperture,  $1\omega$  beam will be propagated to the 10-beam chamber, where it will be converted to  $4\omega$  and used as a target diagnostic probe beam. Actual installation of hardware will begin next quarter.

In continuing support of the Petawatt Project, the design of the Petawatt minichamber was completed and fabrication has started. This minichamber will be used during the initial Petawatt demonstration to measure system performance and beam focusability. Installation of the minichamber is planned for January 1997. The design of the parabolic mirror system that will be used for the Petawatt beam on the 10-beam chamber has been completed. The vacuum housing and mirror

gimbals for the parabola are being fabricated. The vacuum system for the Petawatt compressor chamber was also installed and activated.

The Gated X-Ray Imager #5 (GXI 5), modified to use a charge-coupled device (CCD) readout, is continuing to be used as a secondary diagnostic to provide opportunities for shakedown and activation. The GXI is also being characterized off-line to evaluate its performance using the CCD readout as compared to film. The use of a CCD camera allows immediate viewing of data following a system shot.

#### **Beamlet**

During the fourth quarter of FY 1996, experiments done on Beamlet addressed the following issues:

- Correcting the wavefront for thermally driven gas turbulence in the amplifiers and the beam tubes.
- Measuring the  $3\omega$  conversion efficiency of the 34-cm output beam, the modulation of the  $3\omega$  near-field beam at the focus lens, and the  $3\omega$  focal-spot energy distribution.
- Conducting large-area damage tests of KDP at 3ω.
- Determining the performance of Beamlet with 20-ns pulses shaped like those required for indirect-drive ignition on NIF.
- Measuring the contrast ratio and beam modulation of the near-field beam input into the main amplifier.

The Beamlet control system was modified to allow the adaptive optics system to correct the beam wavefront up to one second before shot time (T-1s) to provide a capability to correct for gas turbulence effects in the beam path. To test this system, we fired shots to compare the  $1\omega$  spot size and beam brightness with and without the T-1s system. We observed that beam quality was improved with the T-1s system but that the improvement was smaller than expected. Because Beamlet has no active cooling system, we saw a more

dominant effect from the accumulation of thermal distortion with repeated shots. Spot size and small-angle scatter increased substantially when repeated shots separated by 2-h intervals were fired. After the fourth shot, up to 15% of the energy was scattered outside of 33  $\mu$ rad. The T-1s system has been used continuously since it was installed in early July.

We fired 53 shots in the  $3\omega$  campaign, 13 to activate and calibrate new diagnostics and 40 to obtain data on 3ω conversion efficiency, near-field beam modulation at the focus lens, and the  $3\omega$  focal-spot energy distribution. The new diagnostics included a 3ω dark-field imaging capability that allowed direct comparison of the scattered power fraction outside 33 μrad with corresponding 1ω measurements. The data shots were with short pulses of nominally 200-ps duration. In one series, the booster amplifier was unpumped to simulate the end of a NIF ignition pulse. In this series, we obtained 3ω power up to 2.3 TW with delta B in the booster amplifier up to 1.7 and with 200-μrad pinholes in both the cavity and transport spatial filters. We obtained up to 3.1 TW (delta B up to 2.0) with smaller 130-μrad cavity and 100-μrad transport filter pinholes. In a second series to reach powers similar to NIF SBSS performance requirements (3.5 TW of 3ω power in 1-ns pulses), we pumped the full 11-5 amplifier set. We achieved 3ω power up to 3.65 TW (corresponding to 4.6 TW for a NIF-sized beam) with 200-μrad pinholes in both the cavity and transport spatial filters at a  $1\omega$ drive power of 5.7 TW. Attempts to use smaller pinholes  $(130/100 \,\mu\text{rad})$  with the pumped booster resulted in back reflections from the transport spatial filter that damaged the injection optics. This problem was not observed with the larger pinholes.

The large-aperture damage tests of KDP were the second series to test KDP. The samples were tested with 3-ns FWHM Gaussian pulses. During the series, Beamlet provided 3 $\omega$  energies very close to those requested by the experimenters. Three samples were tested: a previously conditioned crystal, a new crystal, and a fast-growth crystal. All three samples were damaged below the expected fluence. In previous Beamlet campaigns, however, our 32-cm and 37-cm KDP/KD\*P frequency-conversion crystals generated NIF output fluences on several shots without damage.

In the long-pulse campaign, we evaluated Beamlet's performance with typical pulse shapes proposed for indirect-drive ignition on NIF. The shots did not include frequency conversion but used absorbing glass as a beam dump in the frequency-conversion enclosure. We modified the pulse generation system to generate 20-ns shaped pulses. The modification in the master oscillator room (MOR) used a slow pulser to generate a long foot and used the prototype Arbitrary Wavefront Generator to provide a shaped main pulse. A cavity extension in the regenerative amplifier extended

the gain window to 23 ns without affecting the stability and performance. We began the series with standard 200- $\mu$ rad carbon pinholes in the transport spatial filter. We started at low energy and slowly increased the output energy up to slightly in excess of 13 kJ when evidence of pinhole closure was apparent. We changed the transport filter pinhole to a 200-µrad stainless steel conical pinhole designed to alleviate closure problems and repeated the energy ramp-up. With this design we reached in excess of 15 kJ, with no evidence of closure. Unfortunately, because of a failure in the bandwidth generation system, stimulated Brillouin scattering (SBS) generated in lens L3 caused the lens to fail and implode into the transport spatial filter, and the series had to be terminated. Rebuilding the spatial filter with new square lenses is expected to take 3 to 4 weeks.

In an attempt to resolve a discrepancy between the measured and calculated near-field profiles of the Beamlet output beam, we recorded near-field images at various planes in the preamplifier and injection optics. From these data we determined the spatial modulation at the input to the main amplifier (the calculations had assumed zero modulation at the input). Preliminary analysis now indicates that nearly all of the spatial intensity modulation is already present on the beam before input to the main amplifiers. When this is taken into account, the discrepancy between measured and calculated profiles at the output should be resolved.

#### **NIF**

This quarter, the engineering effort focused on narrowing the design options, further developing the specific designs, and updating the *Conceptual Design Report* (CDR) cost estimate based on extensive vendor quotations. The Conventional Facilities Title I Design, including the cost estimate, is now complete, and the Special Equipment Design and cost estimate 95% complete. The comprehensive Title I Design Review will begin early next quarter (October 8).

The Title I Design Reviews were delayed from the Title I Plan by one month following delay in the release of the *Programmatic Environmental Impact Statement for Stockpile Stewardship and Management* (PEIS) beyond the planned mid-September date. This time was used for value engineering of the designs and cost optimization to ensure that NIF is consistent with the minimum platform to achieve the Primary Criteria and Functional Requirements and the DOE Baseline Change Control Board Level 1 directions. The revised schedule completes the Title I Design in ten months, which is two months faster than the CDR schedule.

Planning for the Title I Design Review was completed, including completing the *Title I Design Review Plan*, which was released to Project personnel and used in detailed planning of the remaining Title I work. The

U-2 UCRL-LR-105821-96-4

plan includes the overall objectives, organization, and schedule, as well as an outline of the agenda for the review meetings and the contents of the Design Basis books. The overall Chairman of the Review Committee was selected, as well as committee members consisting of external and internal reviewers with significant expertise in their areas of review.

In parallel with the design effort, Title I cost and schedule estimates were developed. The cost estimate establishes the project cost baseline, is used as the basis for final design and construction estimation, and provides a high degree of confidence that the Project can be completed within the established baseline. The estimate provides budget outlay (BO) and budget authority (BA) profiles, a time-phased resource requirements plan, and a commitment profile. "Bottoms-up" estimates were generated by the lead/responsible engineers based on extensive vendor quotations. These estimates will be inputted to the NIF Planning system, which is an extension of the Business Planning system developed by LLNL and has been in use for over 10 years.

Following data input and verification, a Title I cost estimate contingency analysis based on a Monte Carlo simulation built from individual system risk assessment was developed. This analysis resulted in an overall contingency allocation for the Project. Planning for the DOE Independent Cost Estimate (ICE) Review has been completed and a kickoff meeting scheduled for the first week in October; ICE Review team members have been invited to the Title I Design Review.

In Manufacturing Engineering, manufacturing assessments were provided to the Special Equipment and lead engineers in support of the Title I design and costing effort. Over 270 detailed cost estimate validations were generated. A manufacturability report was drafted for the Title I Design Reviews.

In support of completion of Title I Design, and in preparation of Title II Design, upgrade and modification of the engineering support systems, including computer-aided design and drafting (CADD) and the Sherpa Product Data Management (PDM) systems, continued. An updated version of the PDM software was implemented and tested on a selected basis. This version, which is user-friendly and contains expanded help functions, reduces or eliminates the need for training. Conversion of the entire system to the updated version was delayed to ensure noninterference with completion of Title I Design. Classes on use of the NIF PDM system continue, and administrative support personnel are providing assistance to new and less experienced users.

PDM release procedures have been updated, and training on use of the PDM system continue to reflect the modifications to documents and design drawings control. The number of documents in the PDM system

increases by about 50 per week, and by the end of the quarter there were over 600 documents in the system. Also, configuration management implementation continues. Training and implementation continue on drawing release, drawing revisions, and Engineering Change Request preparation.

The engineering effort focused this quarter on continuing design iterations to simplify the systems, reduce cost, and ensure a minimum platform system that meets the Primary Criteria and Functional Requirements and the Level 1 DOE Baseline Change Control Board actions. Extensive vendor quotes and refined cost estimates were collected, reviewed, and incorporated into the Title I cost estimate.

Specific Title I Design and supporting activities this past quarter include the following:

- Value Engineering of the LTAB and OAB was completed by Sverdrup to augment the continuing value engineering efforts. The study was completed and the results reviewed and incorporated into the design.
- Parsons was awarded the Project Labor Agreement Development and Oversight contract. The process for negotiating a Conventional Facilities Project Labor Agreement has been defined to reduce the schedule risks and cost impacts due to labor disputes during the Conventional Facilities construction.
- In cooperation with Conventional Facilities, issues associated with co-occupancy of special equipment installers and building constructors in the laser bay to expedite the schedule were resolved. An integrated plan for installing switchyard structures into the building erection sequence was established. Safety planning with the NIF Construction Manager for job site operations was begun.
- A combined target chamber/building construction schedule has been finalized. The schedule interfaces suggest that the chamber be built on the pedestal rather than constructed outside the target building and moved onto the pedestal.
- The Statement of Work for the target chamber fabrication was completed. Comments have been received and incorporated by NIF procurement, selection criteria were refined, and a Request for Proposal is scheduled for release early in FY 1997. Meetings with two potential target chamber fabricators were held, and both vendors confirmed the estimated fabrication time as well as choice of material.
- Changes to the target chamber diagnostic port locations were made based on input received from the Joint Committee for Target Diagnostics, consisting of members from the participating Laboratories. A port location interface control document (ICD) was completed and approved to document the information and assure that future changes are adequately reviewed and approved.

- Design iterations in the Final Optics Assembly continue. Individual 1 × 1 Integrated Optics Modules (IOMs) were selected to simplify the system and for ease of maintenance. Work was performed on a plan for the manufacturing of final optics cells by various methods, and visits to selected vendors for building a prototype final optics cell were prepared.
- Potential effects of distributed heat sources on the thermal stability of the optical systems were addressed by the NIF Thermal Working Group. This effort is closely coupled with the Parsons team performing the computational fluid dynamics analyses and members of the LLNL Thermal/Fluids Group.
- The Optical Configuration Layout drawing set, describing optical component position, orientation, and sizes, was completed. These drawings are an important source of interface information to the Special Equipment areas.
- To enable the initiation of long-lead optics procurement, several key drawings relating to fused silica material, lens finishing, and flat finishing have progressed to a near-final design state. Several significant analyses were documented. Among these were the clear-aperture budget and component damagethreshold requirements.
- All vendor optical cost studies were received, and NIF costs updated with the most current information available. Procurement strategy for optics has been completely defined, and the final version will be released with the Title I Design Basis Book.
- Significant cost savings were realized by production engineering of the amplifier demonstration AMPLAB components for use in NIF under a TRW Master Task Agreement work order. Concepts for amplifier cooling, support, and assembly hardware that meet NIF clean assembly requirements were completed.
- Several key amplifier power conditioning drawings were completed as part of Title I design, including the modified module layout and updated capacitor bay general arrangement. Life testing began at LLNL, in collaboration with the ICF Core Science and Technology Program, on prototype capacitors from two vendors and on the prototype module at Sandia National Laboratories-Albuquerque as part of the development program. Cost estimates were completed for key components, such as capacitors, and incorporated into the Title I cost rollup.
- The Software Requirement Specifications are essentially complete. Quality Level assessments for the Integrated Computer Control System were completed and approved. Remaining ICDs were completed, except for some minor revisions.

- Precision optical diagnostics design was improved with a simplified trombone and provisions for transport mirror maintenance. The midchain sensor design was completed, and requirements were completed for the target chamber diagnostic instrument manipulator.
- In Beam Transport, numerous design improvements that simplified the system and reduced costs were incorporated. They include simplified spatial filter beam tubes and reduced thickness of switchyard structure floor gratings, saving dead weight and increasing optical stability. Additional design optimization on the periscope structure reduced its weight, and use of component commonality reduced the part count in the switchyard and target bay mirror mounts.
- Utility layouts in the target bay and diagnostic building were completed. Revised cost estimates were generated and incorporated into the Title I estimate.
- Samples are arriving to validate parts of the NIF finishing process from Zygo and Tinsley. The first Phase 1 lens was received from Tinsley and is currently under evaluation.
- The draft Startup Plan and a preliminary startup schedule were completed. The second draft of the operations engineering schedule was completed for project inclusion and integration. The Title I Operations modeling effort has been completed and a report drafted.
- The NIF Preliminary Safety Analysis Report has been completed, and related DOE and institutional comments have been resolved. Institutional approval of the report by the Associate Directors for Laser Programs and Plant Operations has been received. DOE has concurred and will provide the Safety Evaluation Report, which gives final concurrence in early October.
- The PEIS has delayed the Notice of Availability to late October 1996 at the earliest. An analysis of delay impacts was prepared for DOE. The NIF *Technical Analysis* document, which includes justification and site comparisons, has been completed and is ready for publication.
- The environmental permit strategy was reviewed with DOE/OAK and DOE/HQ. All DOE comments to support the *Safety Evaluation Report* have been resolved.
- The *Quality Assurance Program Plan* (QAPP) was revised for Title II design, equipment procurement, and construction. Laboratory Project and DOE approval have been received. Eight Project procedures to implement the QAPP update were revised or prepared.

U-4 UCRL-LR-105821-96-4

The Title I Design Reviews will be done time-phased, starting with the schedule critical path Conventional Facilities (including the Laser and Target Area Building, Optics Assembly Building, and site preparation) followed by three Special Equipment review segments. DOE actions, including determination by DP-1, with EH-1 concurrence, to proceed with limited Title II design concurrent with completion of the final PEIS and Record of Decision (ROD), will minimize the near-term adverse impact to the Project.

To maintain progress and keep the Project on schedule requires an ROD by mid-December 1996. Other activities that will be completed next quarter, leading to beginning of site preparation in mid-March 1997, include completing the ICE Review and preparing packages for the DOE Level 1 Baseline Change Control Board meeting in mid-December.

# **PUBLICATIONS**

#### A

Afeyan, B. B., and Chou, A. E., Theory and Simulation of Parametric Instabilities in Turbulent Plasmas Illuminated by Lasers with Spatial Structure, Lawrence Livermore National Laboratory, Livermore, CA, UCRL-JC-124670 ABS. Prepared for 38th Annual Mtg of the American Physical Society Div of Plasma Physics, Denver, CO, Nov 11–15, 1996.

Afeyan, B. B., Chou, A. E., and Luhmann, N. C., Externally Launched Narrow-Wavepacket Approach to Fluctuation Reflectometry, Lawrence Livermore National Laboratory, Livermore, CA, UCRL-JC-124668 ABS. Prepared for 38th Annual Mtg of the American Physical Society Div of Plasma Physics, Denver, CO, Nov 11–15, 1996.

Amendt, P., Glendinning, S. G., Hammel, B. A., Hatchett, S., Landen, O., Murphy, T. J., Rosen, M. D., Suter, L. J., Desenne, D., Jadaud, J. P., and Lafitte, S., New Methods for Controlling and Diagnosing Hohlraum Drive Symmetry, Lawrence Livermore National Laboratory, Livermore, CA, UCRL-JC-124658 ABS. Prepared for 38th Annual Mtg of the American Physical Society Div of Plasma Physics, Denver, CO, Nov 11–15, 1996.

Anderson, A. T., *X-Ray Ablation Measurements and Modeling for ICF Applications*, Lawrence Livermore National Laboratory, Livermore, CA, UCRL-LR-125352. Submitted to *Experimental Heat Transfer*.

#### В

Back, C. A., Glenzer, S. H., Estabrook, K., Kauffman, R. L., Landen, O. L., MacGowan, B. J., Powers, L. V., Shepard, T. D., and Stone, G. F., *Characterization of Electron Temperature in Hohlraum Targets by X-Ray Spectroscopy*, Lawrence Livermore National Laboratory, Livermore, CA, UCRL-JC-124655 ABS. Prepared for *38th Annual Mtg of the American Physical Society Div of Plasma Physics*, Denver, CO, Nov 11–15, 1996.

Back, C. A., Woolsey, N. C., Asfaw, A., Glenzer, S. H., Hammel, B. A., Keane, C. J., Lee, R. W., Liedahl, D., Moreno, J. C., Nash, J. K., Osterheld, A. L., Calisti, A., Stamm, R., Talin, B., Godbert, L., Mosse, C., Ferri, S., and Klein, L., *Experiments on Hot and Dense Laser-Produced Plasmas*, Lawrence Livermore National Laboratory, Livermore, CA, UCRL-JC-123592. Prepared for 13th Intl Conf on Spectral Line Shapes, Florence, Italy, Jun 17–21, 1996.

Barker, C. E., Auerbach, J. M., Adams, C. H., Bumpas, S. E., Hibbard, R. L., Lee, C. L., Roberts, D. H., Campbell, J. H., Wegner, P. J., Van Wonterghem, B. M., and Caird, J. A., *National Ignition Facility Frequency Converter Development*, Lawrence Livermore National Laboratory, Livermore, CA, UCRL-JC-124856 ABS. Prepared for 2nd Annual Intl Conf on Solid-State Lasers for Application to Inertial Confinement Fusion, Paris, France, Oct 22–25, 1996.

Barnard, J. J., and Lund, S. M., *Theory of Longitudinal Beam Halo in High Current Ion RF Linacs*, Lawrence Livermore National Laboratory, Livermore, CA, UCRL-JC-124883 ABS. Prepared for *38th Annual Mtg of the American Physical Society Div of Plasma Physics*, Denver, CO, Nov 11–15, 1996.

Beach, R., Bibeau, C., and Honea, E., Scaling Diode End-Pumped Solid-State Lasers to High Average Power, Lawrence Livermore National Laboratory, Livermore, CA, UCRL-JC-124929 ABS. Prepared for High-Power Lasers and Applications, San Jose, CA, Feb 8–14, 1997.

Bel'kov, S. A., Dolgopolov, Yu. V., Kochemasov, G. G., Kulikov, S. M., Solov'eva, M. N., Sukharev, S. A., and Voronich, I. N., *Measurement of SBS Physics Parameters*, Lawrence Livermore National Laboratory, Livermore, CA, UCRL-CR-122700.

Berger, R. L., Still, C. H., Hinkel, D. E., Langdon, A. B., Munro, D. H., Williams, E. A., Kirkwood, R. K., MacGowan, B. J., Montgomery, D. S., and Moody, J. D., *Multi-Dimensional Evolution of Stimulated Scattering and Filamentation*, Lawrence Livermore National Laboratory, Livermore, CA, UCRL-JC-124465 ABS Rev. 1. Prepared for 38th Annual Mtg of the American Physical Society Div of Plasma Physics, Denver, CO, Nov 11–15, 1996.

Bernat, T., Limits to the Smoothness of Solid Hydrogen-Isotope Surfaces, Lawrence Livermore National Laboratory, Livermore, CA, UCRL-JC-125138 ABS. Prepared for 11th Target Fabrication Specialists' Mtg, Orcas Island, WA, Sept 8–12, 1996.

Berning, M., Rubenchi, A., and Wood-Vasey, M., Weakly Nonlinear Evolution of Interface Instabilities, Lawrence Livermore National Laboratory, Livermore, CA, UCRL-JC-124673 ABS. Prepared for 38th Annual Mtg of the American Physical Society Div of Plasma Physics, Denver, CO, Nov 11–15, 1996.

Boley, C. D., and Rhodes, M. A., Model of the Influence of Magnetic Fields on a Plasma Electrode Pockels Cell, Lawrence Livermore National Laboratory, Livermore, CA, UCRL-JC-124539 ABS. Prepared for 2nd Annual Intl Conf on Solid-State Lasers for Application to Inertial Confinement Fusion, Paris, France, Oct 22–25, 1996.

Brusasco, R., Cook, R., Wilemski, G., Saculla, M., and Gaines, D., Beryllium Doped Plasma Polymer Coatings Using Cyclopentadienyl Beryllium Methyl as a Precursor, Lawrence Livermore National Laboratory, Livermore, CA, UCRL-JC-125143 ABS. Prepared for 11th Target Fabrication Specialists' Mtg, Orcas Island, WA, Sept 8–12, 1996.

Buckley, S., Letts, S. A., Wilemski, G. J., Fearon, E., Vu, D., Cook, R. C., and Schroen-Carey, D., *Processing and Properties of NIF Scale Targets Using Interfacial Polycondensation*, Lawrence Livermore National Laboratory, Livermore, CA, UCRL-JC-125123 ABS. Prepared for 11th Target Fabrication Specialists' Mtg, Orcas Island, WA, Sept 8–12, 1996.

Budil, K. S., Cauble, R. C., Celliers, P. M., Collins, G. W., Da Silva, L. B., Hammel, B. A., Chiu, G., and Ng, A., Characterization of Preheat in Laser-Driven Target Using Interferometry, Lawrence Livermore National Laboratory, Livermore, CA, UCRL-JC-124880 ABS. Prepared for 38th Annual Mtg of the American Physical Society Div of Plasma Physics, Denver, CO, Nov 11–15, 1996.

Budil, K. S., Remington, B. A., Rubenchik, A. M., Berning, M., Wood-Vasey, W. M., Peyser, T. A., Mikaelian, K. O., and Perry, T. S., Investigation of the Multimode Classical Rayleigh—Taylor Instability, Lawrence Livermore National Laboratory, Livermore, CA, UCRL-JC-124548 ABS. Prepared for 38th Annual Mtg of the American Physical Society Div of Plasma Physics, Denver, CO, Nov 11–15, 1996.

Burkhart, S. C., Wilcox, R., Penko, F., and Browning, D., Amplitude and Phase Modulation with Waveguide Optics, Lawrence Livermore National Laboratory, Livermore, CA, UCRL-JC-124531 ABS. Prepared for 2nd Annual Intl Conf on Solid-State Lasers for Application to Inertial Confinement Fusion, Paris, France, Oct 22–25, 1996.

Burnham, A. K., Tobin, M. T., and Anderson, A. T., Evaluation of First Wall Materials for the National Ignition Facility Target Chamber, Lawrence Livermore National Laboratory, Livermore, CA, UCRL-JC-124510 ABS. Prepared for 2nd Annual Intl Conf on Solid-State Lasers for Application to Inertial Confinement Fusion, Paris, France, Oct 22–25, 1996.

Burnham, A., Alford, C., Dittrich, T., Makowiecki, D., Wallace, R., Honea, E., King, C., and Steinman, D., *Evaluation of B*<sub>4</sub>*C as an Ablator Material for NIF Capsules*, Lawrence Livermore National Laboratory, Livermore, CA, UCRL-JC-125144 ABS. Prepared for  $11th\ Target\ Fabrication\ Specialists'\ Mtg$ , Orcas Island, WA, Sept 8–12, 1996.

P-2 UCRL-LR-105821-96-4

#### $\mathbf{C}$

Cable, M. D., Barbee, T. W., Lerche, R. A., Nelson, M. B., Moran, M. J., Ress, D. B., Sangster, T. C., Trebes, J. E., Turner, R. E., Phillips, T. W., Hicks, D., Li, C. K., Petrasso, R. D., and Seguin, F., *Diagnostics for High Density Implosions at the National Ignition Facility*, Lawrence Livermore National Laboratory, Livermore, CA, UCRL-JC-124239. Prepared for *Intl Atomic Energy Agency (IAEA) 16th Fusion Energy Conf*, Montreal, Canada, Oct 7–11, 1996.

Caird, J. A., Patton, H. G., Seppala, L. G., Thompson, C. E., and Wegner, P. J., Beamlet Focal Plane Diagnostic, Lawrence Livermore National Laboratory, Livermore, CA, UCRL-JC-124872 ABS. Prepared for 2nd Annual Intl Conf on Solid-State Lasers for Application to Inertial Confinement Fusion, Paris, France, Oct 22–25, 1996.

Campbell, E. M., Eimerl, D., Kruer, W. L., Weber, S., and Verdon, C. P., *The 0.53-µm Laser Option for Inertial Fusion*, Lawrence Livermore National Laboratory, Livermore, CA, UCRL-JC-125112. Submitted to *Comments on Plasma Physics and Controlled Fusion*.

Campbell, E. M., Holmes, N. C., Libby, S. B., Remington, B. A., and Teller, E., *The Evolution of High Energy-Density Physics: from Nuclear Testing to the Superlasers*, Lawrence Livermore National Laboratory, Livermore, CA, UCRL-JC-124258 Rev. 1. Submitted to *Laser and Particle Beams*.

Campbell, J. H., Hurst, P., Heggins, D., Steele, W., and Bumpas, S., *Laser Induced Damage and Fracture in Fused Silica Vacuum Windows*, Lawrence Livermore National Laboratory, Livermore, CA, UCRL-JC-124876 ABS. Prepared for *28th Annual Symp on Optical Materials for High Power Lasers*, Boulder, CO, Oct 7–9, 1996.

Celliers, P. M., Estabrook, K., Wallace, R. J., Murray, J. E., Da Silva, L. B., MacGowan, B. J., Van Wonterghem, B. M., and Hunt, J. T., Novel Spatial Filter Pinhole for High Energy Pulsed Lasers, Lawrence Livermore National Laboratory, Livermore, CA, UCRL-JC-124029 ABS. Prepared for 24th European Conf on Laser Interaction with Matter, Madrid, Spain, Jun 3–7, 1996.

Chang, J. J., Arnold, P. A., and Warner, B. E., Improvement of High-Current Large-Volume Discharge with Profiled Hollow-Cathode Electrodes, Lawrence Livermore National Laboratory, Livermore, CA, UCRL-JC-125247. Submitted to IEEE Transaction of Plasma Science. Chou, A. E., Afeyan, B. B., and Luhmann, N. C., *Two Dimensional Simulations of Fluctuation Reflectometry*, Lawrence Livermore National Laboratory, Livermore, CA, UCRL-JC-124669 ABS. Prepared for *38th Annual Mtg of the American Physical Society Div of Plasma Physics*, Denver, CO, Nov 11–15, 1996.

Cohen, B. I., Lasinski, B. F., Langdon, A. B., and Williams, E. A., *Resonantly Excited Nonlinear Ion Waves*, Lawrence Livermore National Laboratory, Livermore, CA, UCRL-JC-124922. Submitted to *Physics of Plasmas*.

Collins, G. W., Bittner, D., Monsler, E., Letts, S., Tiszauer, D., Feit, M., Mapoles, E., and Bernat, T., Forming and Smoothing  $D_2$  and HD Layers for ICF by Infrared Heating, Lawrence Livermore National Laboratory, Livermore, CA, UCRL-JC-124255 ABS. Prepared for 11th Target Fabrication Specialists' Mtg, Orcas Island, WA, Sept 8–12, 1996.

Collins, G. W., Budil, K. S., Cauble, R., Celliers, P., Da Silva, L. B., Holmes, N., Wallace, R., Dixit, S., Hammel, B. A., Kilkenny, J. D., and Ng, A., *Temperature Measurements of Shock Compressed Liquid D*<sub>2</sub>, Lawrence Livermore National Laboratory, Livermore, CA, UCRL-JC-124885 ABS. Prepared for 38th Annual Mtg of the American Physical Society Div of Plasma Physics, Denver, CO, Nov 11–15, 1996.

Collins, G. W., Kozioziemski, B. J., Bernat, T. P., Mapoles, E. R., and Unites, W., *Crystal Growth and Roughening of Solid D*<sub>2</sub>, Lawrence Livermore National Laboratory, Livermore, CA, UCRL-JC-125121 ABS. Prepared for *11th Target Fabrication Specialists' Mtg*, Orcas Island, WA, Sept 8–12, 1996.

Collins, G. W., Mapoles, E. R., Sanchez, J. J., Bernat, T., Sater, J. D., Bittner, D., Sheliak, J. D., and Hoffer, J. K., Reducing DT Surface Roughness for Cryogenic Ignition Targets, Lawrence Livermore National Laboratory, Livermore, CA, UCRL-JC-124884 ABS. Prepared for 38th Annual Mtg of the American Physical Society Div of Plasma Physics, Denver, CO, Nov 11–15, 1996.

Colston Jr., B., Everett, M., Nathel, H., and Otis, L., *Optical Coherence Tomography for Dental Applications*, Lawrence Livermore National Laboratory, Livermore, CA, UCRL-JC-125241-ABS. Prepared for *Optical Society of America*, Rochester, NY, Oct 20, 1996.

Correll, D. L., and Vergino, E., *NIFTY*, Lawrence Livermore National Laboratory, Livermore, CA, UCRL-JC-124868 ABS. Prepared for 38th Annual Mtg of the American Physical Society Div of Plasma Physics, Denver, CO, Nov 11–15, 1996.

Crane, J., Martinez, M., Moran, B., Laumann, C., Davin, J., Beach, R., Golick, B., Jones, R., Wing, R., Braucht, J., Perry, M., and Mitchell, S., Description and Performance of the Preamplifier for the National Ignition Facility (NIF) Laser System, Lawrence Livermore National Laboratory, Livermore, CA, UCRL-JC-124517 ABS. Prepared for 2nd Annual Intl Conf on Solid-State Lasers for Application to Inertial Confinement Fusion, Paris, France, Oct 22–25, 1996.

#### D

Da Silva, L. B., Barbee Jr., T. W., Cauble, R., Celliers, P., Decker, C. D., Kalantar, D. H., Key, M. H., London, R. A., Moreno, J. C., Trebes, J. E., Wan, A. S., and Weber, F., *Application of Soft X-Ray Lasers for Probing High Density Plasmas*, Lawrence Livermore National Laboratory, Livermore, CA, UCRL-JC-125218. Prepared for *5th Intl Conf on X-ray Lasers*, Lund, Sweden, Jun 10–14, 1996.

Da Silva, L. B., Budil, K. S., Cauble, R. C., Celliers, P. M., Collins, G. W., Hammel, B. A., Holmes, N. C., Wallace, R. J., Dixit, S. N., Kilkenny, J. D., and Ng, A., Density Measurements of Shock Compressed Liquid D<sub>2</sub>, Lawrence Livermore National Laboratory, Livermore, CA, UCRL-JC-124921 ABS. Prepared for 38th Annual Mtg of the American Physical Society Div of Plasma Physics, Denver, CO, Nov 11–15, 1996.

Davin, J., Braucht, J., Skulina, K., Deadrick, F., Laumann, C., Martinez, M., Bartlow, M., and Hawkins, S., Design of the Preamplifier Integration Testbed for the National Ignition Facility (NIF), Lawrence Livermore National Laboratory, Livermore, CA, UCRL-JC-124382 ABS. Prepared for 2nd Annual Intl Conf on Solid-State Lasers for Application to Inertial Confinement Fusion (ICF), Paris, France, Oct 22–25, 1996.

De Groot, J. S., Denney, C., Eddleman, J. L., Estabrook, K. G., Hammer, J. H., Sanford, T. W. L., Speilman, R. B., and Toor, A., Non-LTE Effects in Imploding Z-Pinches, Lawrence Livermore National Laboratory, Livermore, CA, UCRL-JC-124687 ABS. Prepared for 38th Annual Mtg of the American Physical Society Div of Plasma Physics, Denver, CO, Nov 11–15, 1996.

De Groot, J. S., Matte, J. P., Estabrook, K., and Kruer, W. L., *Heat Transport in High Temperature Hohlraums*, Lawrence Livermore National Laboratory, Livermore, CA, UCRL-JC-125108 ABS. Prepared for *26th Anomalous Absorption Conf*, Fairbanks, AK, Aug 26–30, 1996.

Decker, C. D., Turner, R. E., Landen, O. L., Kornblum H. N., Amendt, P., Suter, L. J., Murphy, T. J., Wallace, J., Hauer, A. A., Knauer, J., Marshall, F. J., Bradley, D., McCrory, R. L., Seka, W., and Soures, J. M., Modeling Radiation Drive in Recent Hohlraum Experiments on Omega, Lawrence Livermore National Laboratory, Livermore, CA, UCRL-JC-124671 ABS. Prepared for 38th Annual Mtg of the American Physical Society Div of Plasma Physics, Denver, CO, Nov 11–15, 1996.

Demiris, A., Metal-Plastic Composite Targets for Instability Studies on Nova, Lawrence Livermore National Laboratory, Livermore, CA, UCRL-JC-125129 ABS. Prepared for 11th Target Fabrication Specialists' Mtg, Orcas Island, WA, Sept 8–12, 1996.

Dittrich, T. R., Haan, S. W., and Strobel, G. L., *NIF Capsule Design Candidates*, Lawrence Livermore National Laboratory, Livermore, CA, UCRL-JC-124667 ABS. Prepared for *38th Annual Mtg of the American Physical Society Div of Plasma Physics*, Denver, CO, Nov 11–15, 1996.

Dittrich, T. R., Haan, S. W., Pollaine, S., Burnham, A. K., and Strobel, G. L., *NIF Capsule Design Update*, Lawrence Livermore National Laboratory, Livermore, CA, UCRL-JC-124913 ABS. Prepared for *11th Target Fabrication Specialists' Mtg*, Orcas Island, WA, Sept 8–12, 1996.

Dittrich, T., Haan, S., Pollaine, S., Burnham, A., and Strobel, G., *NIF Capsule Design Update*, Lawrence Livermore National Laboratory, Livermore, CA, UCRL-JC-124913 ABS Rev. 1. Prepared for *11th Target Fabrication Specialists' Mtg*, Orcas Island, WA, Sept 8–12, 1996.

Dixit, S. N., Rushford, M. R., Thomas, I. M., Herman, S. M., Britten, J. A., Shore, B. W., and Perry, M. D., Color Separation Gratings for Diverting the Unconverted Light Away from the NIF Target, Lawrence Livermore National Laboratory, Livermore, CA, UCRL-JC-124512 ABS. Prepared for 2nd Annual Intl Conf on Solid-State Lasers for Application to Inertial Confinement Fusion, Paris, France, Oct 22–25, 1996.

#### $\mathbf{E}$

Eder, D. C., Bardsley, J. N., Boley, C. D., Feit, M. D., Koniges, A. E., Kozlowski, M. R., London, R. A., Penetrante, B. M., Rubenchik, S., Wurz, H., and Kappler, F., Low Temperature Plasma Ablation, Lawrence Livermore National Laboratory, Livermore, CA, UCRL-JC-124666 ABS. Prepared for 38th Annual Mtg of the American Physical Society Div of Plasma Physics, Denver, CO, Nov 11–15, 1996.

P-4 UCRL-LR-105821-96-4

Eder, D. C., Maitland, D. J., London, R. A., Small, W., Heredia, N. J., and Soltz, B. A., 2D Simulations of Laser Assisted Tissue Welding, Lawrence Livermore National Laboratory, Livermore, CA, UCRL-JC-124936 ABS. Prepared for Society of Photo-Optical Instrumentation Engineers BiOS '97 Mtg, San Jose, CA, Feb 8–14, 1997.

Ehrlich, R. B., Amendt, P. A., Dixit, S. N., Hammel, B. A., Kalantar, D. H., Pennington, D. M., and Weiland, T. L., *Developing Beam Phasing on the Nova Laser*, Lawrence Livermore National Laboratory, Livermore, CA, UCRL-JC-124513 ABS. Prepared for 2nd Annual Intl Conf on Solid-State Lasers for Application to Inertial Confinement Fusion, Paris, France, Oct 22–25, 1996.

Emanuel, M. A., Skidmore, J. A., and Carlson, N. W., *High-Power Laser Diodes at 808*, 941 and 1800 nm, Lawrence Livermore National Laboratory, Livermore, CA, UCRL-JC-124909 ABS. Prepared for *Society of Photo-Optical Instrumentation Engineers Optoelectronics* '97, San Jose, CA, Feb 8–19, 1997.

Erlandson, A. C., Zapata, L. E., Pedrotti, L., Jancaitis, K. S., Saks, R. W., Rotter, M. D., Seznec, S. E., LeTouze, G., Carbourdin, O., and Fornerod, J. C., The Effect of Amplifier Component Maintenance on Laser System Availability and Operating Costs for the U.S. National Ignition Facility and the French Laser Megajoule, Lawrence Livermore National Laboratory, Livermore, CA, UCRL-JC-124911 ABS. Prepared for 2nd Annual Intl Conf on Solid-State Lasers for Application to Inertial Confinement Fusion, Paris, France, Oct 22–25, 1996.

Eroshenko, V. A., Bondarenko, S. V., and Kochemasov, G. G., *Multidimensional Theoretical/Computational Modeling of Non-Coaxial SBS*, Lawrence Livermore National Laboratory, Livermore, CA, UCRL-CR-122699.

Estabrook, K. G., De Groot, J. S., Kruer, W. L., and Matte, J. P., *Heat Transport in High Z Plasmas at High Laser Powers*, Lawrence Livermore National Laboratory, Livermore, CA, UCRL-JC-124689 ABS. Prepared for *38th Annual Mtg of the American Physical Society Div of Plasma Physics*, Denver, CO, Nov 11–15, 1996.

Estabrook, K. G., De Groot, J. S., Kruer, W. L., and Matte, J. P., *Heat Transport in High Z Plasmas at High Laser Powers*, Lawrence Livermore National Laboratory, Livermore, CA, UCRL-JC-124852 ABS. Prepared for *38th Annual Mtg of the American Physical Society Div of Plasma Physics*, Denver, CO, Nov 11–15, 1996.

Estabrook, K., Celliers, P., Murray, J., Wallace, R., Stone, G., Van Wonterghem, B., MacGowan, B., Da Silva, L., Hunt, J., and Manes, K., *An Improved Pinhole Spatial Filter*, Lawrence Livermore National Laboratory, Livermore, CA, UCRL-JC-124475. Prepared for *26th Annual Anomalous Absorption Conf*, Fairbanks, AK, Aug 26–30, 1996.

#### F

Fearon, E., Letts, S., Allison, L., and Cook, R., *Attempts to Fabricate Special ICF Targets Using the Decomposable Mandrel Technique*, Lawrence Livermore National Laboratory, Livermore, CA, UCRL-JC-125130 ABS. Prepared for *11th Target Fabrication Specialists' Mtg*, Orcas Island, WA, Sept 8–12, 1996.

Feit, M. D., and Rubenchik, A. M., Laser Intensity Modulation by Nonabsorbing Defects, Lawrence Livermore National Laboratory, Livermore, CA, UCRL-JC-124536 ABS Rev. 1. Prepared for 28th Annual Symp on Optical Materials for High Power Lasers, Boulder, CO, Oct 7–9, 1996.

Feit, M. D., and Rubenchik, A. M., Laser Intensity Modulation by Nonabsorbing Defects, Lawrence Livermore National Laboratory, Livermore, CA, UCRL-JC-124536 ABS. Prepared for 2nd Annual Intl Conf on Solid-State Lasers for Application to Inertial Confinement Fusion, Paris, France, Oct 22–25, 1996.

Feit, M. D., Rubenchik, A. M., Faux, D. R., Riddle, R. A., Eder, D. C., Penetrante, B. M., Milam, D., Genin, F. Y., and Kozlowski, M. R., Modeling of Laser Damage Initiated by Surface Contamination, Lawrence Livermore National Laboratory, Livermore, CA, UCRL-JC-124538 ABS Rev. 1. Prepared for 28th Annual Symp on Optical Materials for High Power Lasers, Boulder, CO, Oct 7–9, 1996.

Feit, M. D., Rubenchik, A. M., Faux, D. R., Riddle, R. A., Eder, D. C., Penetrante, B. M., Milam, D., Genin, F. Y., and Kozlowski, M. R., *Modeling of Laser Damage Initiated by Surface Contamination*, Lawrence Livermore National Laboratory, Livermore, CA, UCRL-JC-124538 ABS. Prepared for 2nd Annual Intl Conf on Solid-State Lasers for Application to Inertial Confinement Fusion, Paris, France, Oct 22–25, 1996.

Fochs, S. N., Garcia, M., Rhodes, M., and Boley, C., *B-Field Interactions and Electrode Optimization in the Plasma Electrode Pockels Cell*, Lawrence Livermore National Laboratory, Livermore, CA, UCRL-JC-124532 ABS. Prepared for 2nd Annual Intl Conf on Solid-State Lasers for Application to Inertial Confinement Fusion, Paris, France, Oct 22–25, 1996.

Furnish, G. M., Miller, D. S., Painter, J. F., Gentile, N. A., and Eme, W. G., HED: an Inertial Confinement Fusion Modelling Code for High Energy Density Simulations, Lawrence Livermore National Laboratory, Livermore, CA, UCRL-JC-124685 ABS. Prepared for 38th Annual Mtg of the American Physical Society Div of Plasma Physics, Denver, CO, Nov 11–15, 1996.

Furnish, G. M., Nystrom, W. D., and Lebrun, M. J., Continuing Development of the Generalized Tokamak Simulator, Lawrence Livermore National Laboratory, Livermore, CA, UCRL-JC-124678 ABS. Prepared for 38th Annual Mtg of the American Physical Society Div of Plasma Physics, Denver, CO, Nov 11–15, 1996.

#### G

Genin, F. Y., and Stolz, C. J., Morphologies of Laser-Induced Damage in Hafnia-Silica Multilayer Mirror and Polarizer Coatings, Lawrence Livermore National Laboratory, Livermore, CA, UCRL-JC-124879 ABS & VG. Prepared for Society of Photo-Optical Instrumentation Engineers 3rd Intl Workshop on Laser Beam and Optics Characterization, Quebec, Canada, Jul 8–10, 1996.

Genin, F. Y., and Stolz, C. J., Morphologies of Laser-Induced Damage in Hafnia-Silica Multilayer Mirror and Polarizer Coatings, Lawrence Livermore National Laboratory, Livermore, CA, UCRL-JC-124879 VG. Prepared for Society of Photo-Optical Instrumentation Engineers 3rd Intl Workshop on Laser Beam and Optics Characterization, Quebec, Canada, Jul 8–10, 1996.

Genin, F. Y., and Stolz, C. J., Morphologies of Laser-Induced Damage in Hafnia-Silica Multilayer Mirror and Polarizer Coatings, Lawrence Livermore National Laboratory, Livermore, CA, UCRL-JC-124879. Prepared for Society of Photo-Optical Instrumentation Engineers 3rd Intl Workshop on Laser Beam and Optics Characterization, Quebec, Canada, Jul 8–10, 1996.

Genin, F. Y., Furr, J., Kozlowski, M. R., and Brusasco, R. M., Massive Laser Damage of Fused Silica at 355 and 1064 nm Initiated by Surface Contamination, Lawrence Livermore National Laboratory, Livermore, CA, UCRL-JC-124537 ABS. Prepared for 2nd Annual Intl Conf on Solid-State Lasers for Application to Inertial Confinement Fusion, Paris, France, Oct 22–25, 1996.

Genin, F. Y., Furr, J., Michlitsch, K., Kozlowski, M. R., and Krulevitch, P., Laser-Induced Damage of Fused Silica at 355 and 1064 nm Initiated at Aluminum Contamination Particles on the Surface, Lawrence Livermore National Laboratory, Livermore, CA, UCRL-JC-124878 ABS.

Prepared for 28th Annual Symp on Optical Materials for High Power Lasers, Boulder, CO, Oct 7–9, 1996.

Genin, F. Y., Stolz, C. J., and Kozlowski, M. R., *Growth of Laser-Induced Damage During Repetitive Illumination of HfO*<sub>2</sub>-SiO<sub>2</sub> *Multilayer Mirror and Polarizer Coatings,* Lawrence Livermore National Laboratory, Livermore, CA, UCRL-JC-124877 ABS. Prepared for 28th Annual Symp on Optical Materials for High Power Lasers, Boulder, CO, Oct 7–9, 1996.

Genin, F. Y., Stolz, C. J., Kozlowski, M. R., Atherton, L. J., and Hue, J., Functional Damage Threshold of NIF and LMJ Mirrors and Polarizers at 1064 nm, Lawrence Livermore National Laboratory, Livermore, CA, UCRL-JC-124533 ABS. Prepared for 2nd Annual Intl Conf on Solid-State Lasers for Application to Inertial Confinement Fusion, Paris, France, Oct 22–25, 1996.

Genin, F. Y., Stolz, C. J., Reitter, T., Bevis, R., and Von Gunten, M., Effect of Electric Field Distribution on the Morphologies of Laser-Induced Damage in Hafnia-Silica Multilayer Polarizers, Lawrence Livermore National Laboratory, Livermore, CA, UCRL-JC-124873 ABS. Prepared for 28th Annual Symp on Optical Materials for High Power Lasers, Boulder, CO, Oct 7–9, 1996.

Glendinning, S. G., Dixit, S. N., Hammel, B. A., Kalantar, D. H., Key, M. H., Kilkenny, J. D., Knauer, J. P., Pennington, D. M., Remington, B. A., Wallace, R. J., and Weber, S. V., Measurements of Linear Regime Rayleigh—Taylor Growth Rates in Laser-Driven Planar Targets, Lawrence Livermore National Laboratory, Livermore, CA, UCRL-JC-124653 ABS. Prepared for 38th Annual Mtg of the American Physical Society Div of Plasma Physics, Denver, CO, Nov 11–15, 1996.

Glendinning, S. G., Dixit, S. N., Hammel, B. A., Kalantar, D. H., Key, M. H., Kilkenny, J. D., Knauer, J. P., Pennington, D. M., Remington, B. A., Wallace, R. J., and Weber, S. V., Measurements of Linear Regime Rayleigh—Taylor Growth Rates in Laser-Driven Planar Targets, Lawrence Livermore National Laboratory, Livermore, CA, UCRL-JC-124653 Rev. 1. Submitted to Phys. Rev. Lett.

Glendinning, S. G., Dixit, S. N., Hammel, B. A., Kalantar, D. H., Key, M. H., Kilkenny, J. D., Knauer, J. P., Pennington, D. M., Remington, B. A., Wallace, R. J., and Weber, S. V., Measurements of Linear Regime Rayleigh—Taylor Growth Rates in Laser-Driven Planar Targets, Lawrence Livermore National Laboratory, Livermore, CA, UCRL-JC-124653. Submitted to Phys. Rev. Lett.

P-6 UCRL-LR-105821-96-4

Glendinning, S. G., Hsing, W., Galmiche, D., Remington, B. A., Kalantar, D. H., Haan, S. W., Wallace, R. J., and Marinak, M. M., Measurements of Rayleigh—Taylor Growth in Ablatively Driven Converging Hemispherical Targets at Nova, Lawrence Livermore National Laboratory, Livermore, CA, UCRL-JC-124674 ABS. Prepared for 38th Annual Mtg of the American Physical Society Div of Plasma Physics, Denver, CO, Nov 11–15, 1996.

Glenzer, S. H., Back, C. A., Estabrook, K. G., Kirkwood, R. K., Wallace, R., MacGowan, B. J., Hammel, B. A., Cid, R. E., and De Groot, J. S., *Thomson Scattering from Two-Species Laser-Produced Plasmas*, Lawrence Livermore National Laboratory, Livermore, CA, UCRL-JC-123752. Submitted to *Rev. Sci. Instrum*.

Glenzer, S. H., Back, C. A., Estabrook, K. G., MacGowan, B. J., Montgomery, D. S., Kirkwood, R. K., Moody, J. D., Munro, D. H., and Stone, G. F., *Electron Temperature and Density Measurements in Laser-Produced Large Scale-Length Gasbag Plasmas by X-Ray Spectroscopy*, Lawrence Livermore National Laboratory, Livermore, CA, UCRL-JC-124948. Submitted to *Phys. Rev. Lett. E.* 

Glenzer, S. H., Wrubel, Th., and Kunze, H.-J., *Investigation of a Short-Wavelength Laser Plasma of a Gas-Liner Pinch Discharge*, Lawrence Livermore National Laboratory, Livermore, CA, UCRL-JC-124886. Submitted to *Phys. Rev. Lett. E.* 

#### Η

Haan, W. S., Dittrich, T. R., and Strobel, G., Modeling of Hydrodynamic Instabilities on Indirect Drive Ignition Targets, Lawrence Livermore National Laboratory, Livermore, CA, UCRL-JC-124545 ABS. Prepared for 38th Annual Mtg of the American Physical Society Div of Plasma Physics, Denver, CO, Nov 11–15, 1996.

Hammer, J. H., Eddleman, J. L., Estabrook, K. G., Foord, M., Maxon, S., Springer, P., Tabak, M., Toor, A., Wong, K., Zimmerman, G. B., and De Groot, J. S., 2D Radiation MHD Simulations of Neon-Argon SATURN Z-Pinches, Lawrence Livermore National Laboratory, Livermore, CA, UCRL-JC-124855 ABS. Prepared for 38th Annual Mtg of the American Physical Society Div of Plasma Physics, Denver, CO, Nov 11–15, 1996.

Haney, S. W., *Beating the Abstraction Penalty in C++ Using Expression Templates*, Lawrence Livermore National Laboratory, Livermore, CA, UCRL-JC-125237. Submitted to *Comput. & Phys.* 

Herman, S. M., Britten, J. A., Body, R. D., Shore, B. W., Agayan, R. R., and Perry, M. D., Further Development of Shallow-Relief Gratings for Beam Diagnostics Applications on NIF, Lawrence Livermore National Laboratory, Livermore, CA, UCRL-JC-124505 ABS. Prepared for 2nd Annual Intl Conf on Solid-State Lasers for Application to Inertial Confinement Fusion, Paris, France, Oct 22–25, 1996.

Hinkel, D. E., Still, C. H., Berger, R. L., Langdon, A. B., and Williams, E. A., *Backscatter, Filamentation and Laser Light Smoothing in Flowing Plasmas*, Lawrence Livermore National Laboratory, Livermore, CA, UCRL-JC-124684 ABS. Prepared for 38th Annual Mtg of the American Physical Society Div of Plasma Physics, Denver, CO, Nov 11–15, 1996.

Ho, D. D.-M., "Laser Cooling for Heavy-Ion Fusion," Lawrence Livermore National Laboratory, Livermore, CA, UCRL-JC-124289 ABS. Prepared for 26th Annual Absorption Conf., Fairbanks, AK, Aug 26–30, 1996.

Ho, D. D.-M., and Brandon, S. T., "Autoneutralization of Space-Charge-Dominated Beams for Heavy-Ion Fusion," Lawrence Livermore National Laboratory, Livermore, CA, UCRL-JC-120830. Submitted to *Nuclear Fusion*.

Horvath, J., Rodriguez, S., Fornerod, J., Bosch, P., Alger, T., Lee, T., Swort, D., Seznec, S., and Erlandson, A., NIF/LMJ Prototype Amplifier Mechanical Design, Lawrence Livermore National Laboratory, Livermore, CA, UCRL-JC-124520 ABS. Prepared for 2nd Annual Intl Conf on Solid-State Lasers for Application to Inertial Confinement Fusion, Paris, France, Oct 22–25, 1996.

Hsieh, E. J., Landen, O. L., and Wallace, R. J., Be Tamping of Diagnostic Holes for NIF Scaled Experiments, Lawrence Livermore National Laboratory, Livermore, CA, UCRL-JC-124893 ABS. Prepared for 11th Target Fabrication Specialists' Meeting, Orcas Island, WA, Sept 8–12, 1996.

Hue, J., Genin, F., Maricle, S., and Kozlowski, M., *Towards Predicting the Threshold of the Large Area: Threshold Mapping*, Lawrence Livermore National Laboratory, Livermore, CA, UCRL-JC-124874 ABS. Prepared for 28th Annual Symp on Optical Materials for High Power Lasers, Boulder, CO, Oct 7–9, 1996.

#### J

Jin, H., Peterson, P. F., Turner, R. E., and Anderson, A. T., Experiment and Analysis of Ablation and Condensation in NIF First Wall Materials, Lawrence Livermore National Laboratory, Livermore, CA, UCRL-JC-124540. Prepared for American Nuclear Society 12th Topical Mtg on the Technology of Fusion Energy, Reno, NV, Jun 16–20, 1996.

#### K

Kalantar, D. H., Measurements of Direct Drive Laser Imprint in Thin Foils by XUV Radiography Using an X-Ray Laser Backlighter, Lawrence Livermore National Laboratory, Livermore, CA, UCRL-JC-124654 ABS. Prepared for 38th Annual Mtg of the American Physical Society Div of Plasma Physics, Denver, CO, Nov 11–15, 1996.

Kalantar, D. H., Bell, P. M., Costa, R., Landen, O. L., and Orzechowski, T. J., *Characterization of X-Ray Streak Cameras for Use on Nova*, Lawrence Livermore National Laboratory, Livermore, CA, UCRL-JC-123776. Prepared for 22nd Intl Congress on High Speed *Photography and Photonics, Santa Fe*, NM, Oct 27–Nov 1, 1996.

Kalantar, D. H., Haan, S. W., Hammel, B. A., Landen, O. L., Keane, C. J., and Munro, D. H., *X-Ray Backlit Imaging of Indirect Drive Implosions to Measure In-Flight Capsule Aspect Ratio and Convergent Hydrodynamics*, Lawrence Livermore National Laboratory, Livermore, CA, UCRL-JC-124652 ABS. Prepared for 38th Annual Mtg of the American Physical Society Div of Plasma Physics, Denver, CO, Nov 11–15, 1996.

Kalantar, D., Bell, P. M., Costa, R., Landen, O. L., and Orzechowski, T. J., *Characterization of X-Ray Streak Cameras for Use on Nova*, Lawrence Livermore National Laboratory, Livermore, CA, UCRL-JC-123776 ABS Rev. 1. Prepared for 22nd Intl Congress on High Speed *Photography and Photonics, Santa Fe*, NM, Oct 27–Nov 1, 1996.

Kane, J., Glendinning, S. G., Wood-Vassey, M., Remington, B. A., Arnett, D., Rubenchik, A., Liang, E. P., London, R., and Castor, J., Modeling of Supernova-Relevant Hydrodynamic Instability Experiments on the Nova Laser, Lawrence Livermore National Laboratory, Livermore, CA, UCRL-JC-124550 ABS. Prepared for 38th Annual Mtg of the American Physical Society Div of Plasma Physics, Denver, CO, Nov 11–15, 1996.

Kauffman, R. L., Powers, L. V., Glendinning, S. G., Orzechowski, T., Suter, L. J., Berger, R. L., Dixit, S., Hammel, B. A., Hinkel, D. E., Kirkwood, R. K., Kornblum, H. N., Landen, O. L., MacGowan, B. J., Pennington, D., Shepard, T. D., Williams, E. A., Juraszek, D., Richard, A. L., and Blain, M. A., Effects of Beam Conditioning on Gas-Filled Hohlraum Performance, Lawrence Livermore National Laboratory, Livermore, CA, UCRL-JC-124682 ABS. Prepared for 38th Annual Mtg of the American Physical Society Div of Plasma Physics, Denver, CO, Nov 11–15, 1996.

Kershaw, D. S., Milovich, J. L., Prasad, M., Shaw, M. J., and Shestakov, A. I., *ICF3D-Hydro: 3D Parallel Unstructured Mesh Hydrodynamics Code*, Lawrence Livermore National Laboratory, Livermore, CA, UCRL-JC-124683 ABS. Prepared for 38th Annual Mtg of the American Physical Society Div of Plasma Physics, Denver, CO, Nov 11–15, 1996.

Kirkwood, R. K., Observation of Multiple Mechanisms for Stimulating Ion Waves in Ignition Scale Plasmas, Lawrence Livermore National Laboratory, Livermore, CA, UCRL-JC-124651 ABS. Prepared for 38th Annual Mtg of the American Physical Society Div of Plasma Physics, Denver, CO, Nov 11–15, 1996.

Kirkwood, R. K., MacGowan, B. J., Montgomery, D. S., Afeyan, B. B., Kruer, W. L., Moody, J. D., Estabrook, K. G., Back, C. A., Glenzer, S. H., Blain, M. A., Williams, E. A., Berger, R. L., and Lasinski, B. F., *Effect of Ion Wave Damping on Stimulated Raman Scattering in High-Z Laser Produced Plasmas*, Lawrence Livermore National Laboratory, Livermore, CA, UCRL-JC-124019 Rev. 1; *Phys. Rev. Lett.* 77(13), 2706–2709 (1996).

Kirkwood, R. K., Wharton, K., Afeyan, B., Back, C., Berger, R., Blain, M., Estabrook, K., Glenzer, S., Kruer, W., MacGowan, B., and Moody, J., Experimental Investigation of the Electromagnetic Decay Instability, Lawrence Livermore National Laboratory, Livermore, CA, UCRL-JC-124854 ABS. Prepared for 38th Annual Mtg of the American Physical Society Div of Plasma Physics, Denver, CO, Nov 11–15, 1996.

Kopf, D., Keller, U., Emanuel, M. A., Beach, R. J., Skidmore, J. A., and Weingarten, K. J., 1-W Continuous-Wave Diode-Pumped Cr:LiSAF Laser, Lawrence Livermore National Laboratory, Livermore, CA, UCRL-JC-124870 ABS & SUM. Prepared for 1996 Intl Quantum Electronics Conf, Sydney, Australia, Jul 14–19, 1996.

P-8 UCRL-LR-105821-96-4

Kruer, W. L., *Deflection, Spraying and Induced Scattering of Intense Laser Beams in Plasmas*, Lawrence Livermore National Laboratory, Livermore, CA, UCRL-JC-123551 ABS Rev. 1. Prepared for 1996 Intl Conf on Plasma Physics, Nagoya, Japan, Sept 9–13, 1996.

Kruer, W. L., *Deflection, Spraying and Induced Scattering of Intense Laser Beams in Plasmas*, Lawrence Livermore National Laboratory, Livermore, CA, UCRL-JC-123551. Prepared for 1996 *Intl Conf on Plasma Physics, Nagoya*, Japan, Sept 9–13, 1996.

Kruer, W. L., Afeyan, B. B., Wilks, S. C., and Chou, A. E., *Strongly-Driven Laser Plasmas with Self-Consistent Electron Distributions*, Lawrence Livermore National Laboratory, Livermore, CA, UCRL-JC-124491 ABS Rev. 1. Prepared for *38th Annual Mtg of the American Physical Society Div of Plasma Physics*, Denver, CO, Nov 11–15, 1996.

Kruer, W. L., and Hammer, J. H., *Laser Beam Deflection in Nonlinearly-Steepened Flow Profiles*, Lawrence Livermore National Laboratory, Livermore, CA, UCRL-JC-124447. Submitted to *Plasma Phys. and Controlled Fusion*.

#### L

Lambert, S. M., Overturf, G. E., Wilemski, G., Letts, S. A., Cook, R. C., and Schroen-Carey, D., Fabrication of Low-Density Foam Shells from Resorcinol-Formaldehyde Aerogel, Lawrence Livermore National Laboratory, Livermore, CA, UCRL-JC-124663. Submitted to J. of Applied Polymer Science.

Landen, O. L., Hammer, J. A., Suter, L. J., Orzechowski, T. J., Weiland, T., Perry, T. S., Bauer, J., Bach, D., Ward, R., Hammel, B. A., Kilkenny, J. D., and Wallace, R. J., Long Duration Indirect-Drive Experiments at Nova, Lawrence Livermore National Laboratory, Livermore, CA, UCRL-JC-124675 ABS. Prepared for 38th Annual Mtg of the American Physical Society Div of Plasma Physics, Denver, CO, Nov 11–15, 1996.

Langer, S. H., Keane, C. J., and Scott, H. A., Yield and Emission Line Ratios from ICF Target Implosions with Multi-Mode Rayleigh—Taylor Perturbations, Lawrence Livermore National Laboratory, Livermore, CA, UCRL-JC-124484 ABS Rev. 1. Prepared for 38th Annual Mtg of the American Physical Society Div of Plasma Physics, Denver, CO, Nov 11–15, 1996.

Lasinski, B. F., Cohen, B. I., Langdon, A. B., and Williams, E. A., *Stimulated Brillouin Scatter in PIC-Fluid Simulations*, Lawrence Livermore National Laboratory, Livermore, CA, UCRL-JC-124457 ABS Rev. 1. Prepared for *38th Annual Mtg of the American Physical Society Div of Plasma Physics*, Denver, CO, Nov 11–15, 1996.

Latkowski, J. F., Sanz, J., and Vujic, J. L., *The Impact of Pulsed Irradiation upon Neutron Activation Calculations for Inertial and Magnetic Fusion Energy Power Plants*, Lawrence Livermore National Laboratory, Livermore, CA, UCRL-JC-123559. Prepared for *American Nuclear Society 12th Topical Mtg on the Technology of Fusion Energy*, Reno, NV, Jun 16–20, 1996.

Lawson, J. K., Seppala, L. G., Smith, I. C., and Thompson, C. E., Beamlet Schlieren Diagnostic and Experiments, Lawrence Livermore National Laboratory, Livermore, CA, UCRL-JC-124516 ABS. Prepared for 2nd Annual Intl Conf on Solid-State Lasers for Application to Inertial Confinement Fusion, Paris, France, Oct 22–25, 1996.

Lerche, R. A., Ress, D., and Fisher, R. K., Efficient, High-Spatial Resolution Neutron Detector for Coded Aperture Imaging of ICF Targets, Lawrence Livermore National Laboratory, Livermore, CA, UCRL-JC-124660 ABS. Prepared for 38th Annual Mtg of the American Physical Society Div of Plasma Physics, Denver, CO, Nov 11–15, 1996.

Letts, S., Bittner, D., Collins, G. W., and Monsler, E., Generation of Uniform Solid HD Layers inside Spherical Capsules Using Infra-Red Illumination, Lawrence Livermore National Laboratory, Livermore, CA, UCRL-JC-125140 ABS. Prepared for 11th Target Fabrication Specialists' Mtg, Orcas Island, WA, Sept 8–12, 1996.

Letts, S., Buckely, S., and Schroen-Carey, D., *Analysis of the Effect of pH on Poly(Vinyl Phenol)*, Lawrence Livermore National Laboratory, Livermore, CA, UCRL-JC-125134 ABS. Prepared for *11th Target Fabrication Specialists' Mtg*, Orcas Island, WA, Sept 8–12, 1996.

Letts, S., Buckley, S. R., Fearon, E. M., Hamilton, K. E., Vu, D., Wilemski, G., Cook, R. C., and Schroen-Carey, D., Role of Reactant Transport in Determining the Properties of NIF Shells Made by Interfacial, Lawrence Livermore National Laboratory, Livermore, CA, UCRL-JC-125125 ABS. Prepared for 11th Target Fabrication Specialists' Mtg, Orcas Island, WA, Sept 8–12, 1996.

Levedahl, W. K., and Lindl, J. D., Energy Scaling of Inertial Confinement Fusion Targets for Ignition and High Gain, Lawrence Livermore National Laboratory, Livermore, CA, UCRL-JC-120200 Rev. 1. Submitted to Intl Atomic Energy Agency/Nuclear Fusion.

Lindl, J. D., and Marinak, M. M., *Progress on the Physics of Ignition for Radiation Driven Inertial Confinement Fusion (ICF) Targets*, Lawrence Livermore National Laboratory, Livermore, CA, UCRL-JC-124004. Prepared for *16th Intl Atomic Energy Agency Fusion Energy Conf*, Montreal, Canada, Oct 7–11, 1996.

Logan, B. G., Lindl, J. D., and Meier, W. R., *Inertial Fusion Energy Development Approaches for Direct and Indirect-Drive*, Lawrence Livermore National Laboratory, Livermore, CA, UCRL-JC-123788. Prepared for 16th Intl Atomic Energy Agency Fusion Energy Conf., Montreal, Canada, Oct 7–11, 1996.

#### M

MacGowan, B. J., Back, C. A., Blain, M. A., Berger, R. L., Canaud, B., Glenzer, S. H., Hinkel, D. E., Kirkwood, R. K., Lasinski, B. F., Montgomery, D. S., Moody, J. D., Munro, D. H., Powers, L. V., Rousseaux, C., and Williams, E. A., The Effect of Smoothing by Spectral Dispersion on Laser Scattering and Beam Propagation in Large-Scale-Length Plasmas Relevant to National Ignition Facility Hohlraums, Lawrence Livermore National Laboratory, Livermore, CA, UCRL-JC-124656 ABS. Prepared for 38th Annual Mtg of the American Physical Society Div of Plasma Physics, Denver, CO, Nov 11–15, 1996.

Mapoles, E. R., Sater, J., Pipes, J., and Monsler, E., *Smoothing of Deuterium-Tritium Ice by Electrical Heating of the Saturated Vapor*, Lawrence Livermore National Laboratory, Livermore, CA, UCRL-JC-124938. Submitted to *Physical Review B*.

Mapoles, E. R., Sater, J., Pipes, J., and Monsler, E., Smoothing of Solid DT ICF Targets by Electrical Heating, Lawrence Livermore National Laboratory, Livermore, CA, UCRL-JC-125122 ABS. Prepared for 11th Target Fabrication Specialists' Mtg, Orcas Island, WA, Sept 8–12, 1996.

Mapoles, E., and Burmann, J., Cryogenic Testing of Liquid and Solid Layering Cells, Lawrence Livermore National Laboratory, Livermore, CA, UCRL-JC-125137 ABS. Prepared for 11th Target Fabrication Specialists' Mtg, Orcas Island, WA, Sept 8–12, 1996.

Mapoles, E., and Pipes, J. W., Conceptual Design of an In Situ System for Cryogenic Hohlraum Assembly, Lawrence Livermore National Laboratory, Livermore, CA, UCRL-JC-125131 ABS. Prepared for 11th Target Fabrication Specialists' Mtg, Orcas Island, WA, Sept 8–12, 1996.

Marinak, M. M., and Hatchett, S. P., 3-D Hydrodynamic Effects of Pointing and Power Balance Errors on Nova Capsule Implosions, Lawrence Livermore National Laboratory, Livermore, CA, UCRL-JC-124672 ABS. Prepared for 38th Annual Mtg of the American Physical Society Div of Plasma Physics, Denver, CO, Nov 11–15, 1996.

Marinak, M. M., Haan, S. W., Tipton, R. E., and Zimmerman, G. B., *Three-Dimensional Simulations of National Ignition Facility Capsule Implosions*, Lawrence Livermore National Laboratory, Livermore, CA, UCRL-JC-123783 ABS Rev. 2. Prepared for 38th Annual Mtg of the American Physical Society Div of Plasma Physics, Denver, CO, Nov 11–15, 1996.

Marshall, C. D., Speth, J. A., and Payne, S. A., Penetrating Radiation Impact on NIF Final Optic Components, Lawrence Livermore National Laboratory, Livermore, CA, UCRL-JC-124523 ABS. Prepared for 2nd Annual Intl Conf on Solid-State Lasers for Application to Inertial Confinement Fusion, Paris, France, Oct 22–25, 1996.

McEachern, R., Honea, E., and Collins, G., Surface Roughness Scaling of Beryllium Thin Films, Lawrence Livermore National Laboratory, Livermore, CA, UCRL-JC-125132 ABS. Prepared for 11th Target Fabrication Specialists' Mtg, Orcas Island, WA, Sept 8–12, 1996.

Meier, W. R., Developing Inertial Fusion Energy—Where Do We Go from Here? Lawrence Livermore National Laboratory, Livermore, CA, UCRL-JC-123079 SUM. Prepared for 12th Topical Mtg on the Technology of Fusion Energy, Reno, NV, Jun 16–20, 1996.

Meier, W. R., and Abdou, M. A., *Chamber Technology Concepts for Inertial Fusion Energy*, Lawrence Livermore National Laboratory, Livermore, CA, UCRL-JC-125147 ABS. Prepared for *4th Intl Symp on Fusion Nuclear Technology*, Tokyo, Japan, Apr 6–11, 1997.

P-10 UCRL-LR-105821-96-4

Meier, W., Moir, R., Monsler, M., Petzoldt, R., and Unites, W., *Target Design, Fabrication and Injection Considerations for Inertia l Fusion Energy*, Lawrence Livermore National Laboratory, Livermore, CA, UCRL-JC-125120 ABS. Prepared for 11th Target Fabrication Specialists' Mtg, Orcas Island, WA, Sept 8–12, 1996.

Merkuliefv, Y., Startsev, S., and Cook, R., Simulation of High Temperature Formation of Large (2 mm) Polystyrene Shells from Solid Granules, Lawrence Livermore National Laboratory, Livermore, CA, UCRL-JC-125126 ABS. Prepared for 11th Target Fabrication Specialists' Mtg, Orcas Island, WA, Sept 8–12, 1996.

Milam, D., Hunt, J. T., Manes, K. R., Sell, W. D., and Williams, W. H., *Modeling of Filamentation Damage Induced in Silica by 351-nm Laser Pulses*, Lawrence Livermore National Laboratory, Livermore, CA, UCRL-JC-124925 ABS. Prepared for *Symp on Optical Materials for High Power Lasers '96*, Boulder, CO, Oct 7–9, 1996.

Moir, R. W., *IFE Power Plant Design Strategy*, Lawrence Livermore National Laboratory, Livermore, CA, UCRL-JC-123287. Submitted to *Fusion Technology*.

Molau, N. E., Brand, H. R., Kozlowski, M. R., and Shang, C. C., 2-1/2-D Electromagnetic Modeling of Nodular Defects in High-Power Multilayer Optical Coatings, Lawrence Livermore National Laboratory, Livermore, CA, UCRL-ID-124808.

Moody, J. D., MacGowan, B. J., Kirkwood, R. K., Montgomery, D. S., Berger, R. L., Hinkel, D. E., Shepard, T. D., and Williams, E. A., *Experimental Studies of Beam Deflection through an Exploding Foil Plasma*, Lawrence Livermore National Laboratory, Livermore, CA, UCRL-JC-121486 ABS Rev. 1. Prepared for 38th Annual Mtg of the American Physical Society Div of Plasma Physics, Denver, CO, Nov 11–15, 1996.

Moon, S. J., and Eder, D. C., *Target Considerations for Inner-Shell Photo-Ionized X-Ray Lasing*, Lawrence Livermore National Laboratory, Livermore, CA, UCRL-JC-123798. Prepared for *5th Intl Conf on X-Ray Lasers*, Lund, Sweden, Jun 10–14, 1996.

Murray, J. E., Estabrook, K. G., Van Wonterghem, B. M., Milam, D., Sell, W. D., Boley, C., Feit, M. D., and Rubenchik, A. M., *Preventing Spatial Filter Pinhole Closure with the Pinholes Required to Control Beam Breakup for the NIF*, Lawrence Livermore National Laboratory, Livermore, CA, UCRL-JC-124524 ABS. Prepared for 2nd Annual Intl Conf on Solid-State Lasers for Application to Inertial Confinement Fusion, Paris, France, Oct 22–25, 1996.

Murray, J. E., Milam, D., Sell, W. D., Estabrook, K. G., Feit, M. D., and Rubenchik, A. M., *Maximum Background Pressure in Spatial Filters for High Power Lasers*, Lawrence Livermore National Laboratory, Livermore, CA, UCRL-JC-124866 ABS. Prepared for 2nd Annual Intl Conf on Solid-State Lasers for Application to Inertial Confinement Fusion, Paris, France, Oct 22–25, 1996.

#### N

Newton, M., Larson, D., Ullery, G., Hulsey, S., Test, P., Wilson, M., Harjes, C., and Anderson, B., Component Development for the NIF Power Conditioning System, Lawrence Livermore National Laboratory, Livermore, CA, UCRL-JC-124376 ABS. Prepared for 2nd Annual Intl Conf on Solid-State Lasers for Application to Inertial Confinement Fusion, Paris, France, Oct 22–25, 1996.

Nguyen, H. T., Shore, B. W., Britten, J. A., Bryan, S. J., and Perry, M. D., *High-Efficiency Transmission Gratings Fabricated in Bulk Fused Silica*, Lawrence Livermore National Laboratory, Livermore, CA, UCRL-JC-123585 ABS Rev. 1. Prepared for 2nd Annual Intl Conf on Solid-State Lasers for Application to Inertial Confinement Fusion, Paris, France, Oct 22–25, 1996.

Norton, M. A., Murray, J. E., Boley, C. D., Milam, D., Sell, W. D., Feit, M. D., and Rubenchik, A. M., *Development of Long-Lifetime, Low-Contamination Beam Dumps for NIF*, Lawrence Livermore National Laboratory, Livermore, CA, UCRL-JC-124863 ABS. Prepared for 2nd Annual Intl Conf on Solid-State Lasers for Application to Inertial Confinement Fusion, Paris, France, Oct 22–25, 1996.

#### 0

Orzechowski, T. J., Afeyan, B., Berger, R. L., Kirkwood, R. K., Kruer, W. L., Kornblum, H. N., MacGowan, B. J., Montgomery, D. S., Moody, J. D., Powers, L. V., Rosen, M. D., Springer, P. S., Suter, L. J., Wallace, R. J., and Blain, M. A., *Energetics of High-Temperature Laser Driven Hohlraums*, Lawrence Livermore National Laboratory, Livermore, CA, UCRL-JC-124657 ABS. Prepared for 38th Annual Mtg of the American Physical Society Div of Plasma Physics, Denver, CO, Nov 11–15, 1996.

Overturf III, G., Lambert, S., Wilemski, G., Letts, S., Cook, R., and Schroen-Carey, D., Fabrication of Low-Density Foam Shells from Resorcinol-Formaldehyde Aerogel, Lawrence Livermore National Laboratory, Livermore, CA, UCRL-JC-124663 ABS. Prepared for 11th Target Fabrication Specialists' Mtg, Orcas Island, WA, Sept 8–12, 1996.

#### P

Page, R., DeLoach, L., Schaffers, K., Patel, F., Beach, R., Payne, S., Krupke, W., and Burger, A., *Recent Developments in Cr*<sup>2+</sup>-*Doped II-VI Compound Lasers*, Lawrence Livermore National Laboratory, Livermore, CA, UCRL-JC-122122. Prepared for *Advanced Solid State Lasers* '96, San Francisco, CA, Jan 31–Feb 2, 1996.

Page, R., Schaffers, K. I., Skidmore, J. A., Beach, R. J., Payne, S. A., and Krupke, W. F., *ZnSe:Cr*<sup>2+</sup>, *the "Ti-Sapphire of the Mid-IR,"* Lawrence Livermore National Laboratory, Livermore, CA, UCRL-JC-124436. Submitted to *Optics & Photonics News special issue—Optics in* 1996.

Payne, S. A., Conduction Band States and 5d-to-4f Laser Transition of Rare Earth Ion Dopants, Lawrence Livermore National Laboratory, Livermore, CA, UCRL-JC-124497. Prepared for 2nd Intl Conf on Tunable Solid State Lasers, Warsaw, Poland, Sept 1–4, 1996.

Payne, S. A., Page, R. H., Marshall, C. D., Schaffers, K. I., Bayramian, A. J., and Krupke, W. F., *New Tunable Lasers for Potential Use in LIDAR Systems*, Lawrence Livermore National Laboratory, Livermore, CA, UCRL-JC-124015. Prepared for 1996 Intl Symp on Optical Science, Engineering and Instrumentation, Denver, CO, Aug 4–9, 1996.

Pennington, D. M., Dixit, S. N., Weiland, T. L., Ehrlich, R., and Rothenberg, J. E., *Implementation and Performance of Beam Smoothing on 10 Beams of the Nova Laser*, Lawrence Livermore National Laboratory, Livermore, CA, UCRL-JC-124503 ABS. Prepared for 2nd Annual Intl Conf on Solid-State Lasers for Application to Inertial Confinement Fusion, Paris, France, Oct 22–25, 1996.

Pennington, D. M., Milam, D., and Eimerl, D., Gain Saturation Studies in LG-750 and LG-770 Amplifier Glass, Lawrence Livermore National Laboratory, Livermore, CA, UCRL-JC-124504 ABS. Prepared for 2nd Annual Intl Conf on Solid-State Lasers for Application to Inertial Confinement Fusion, Paris, France, Oct 22–25, 1996.

Pennington, D., *Inertial Confinement Fusion Quarterly Report*, Volume 6, Number 2, Lawrence Livermore National Laboratory, Livermore, CA, UCRL-LR-105821-96-2.

Powers, L. V., Berger, R. L., Kirkwood R. K., Kruer, W. L., Langdon, A. B., MacGowan, B. J., Orzechowski, T. J., Rosen, M. D., Springer, P. T., Still, C. H., Suter, L. J., Williams, E. A., and Blain, M. A., *Analysis of Reduced-Scale Nova Hohlraum Experiments*, Lawrence Livermore National Laboratory, Livermore, CA, UCRL-JC-124680 ABS. Prepared for *38th Annual Mtg of the American Physical Society Div of Plasma Physics*, Denver, CO, Nov 11–15, 1996.

Prasad, M., Shaw, M. J., Milovich, J., and Kershaw, D. S., 3D Unstructured Mesh ALE Hydrodynamics with the Upwind, Discontinuous Finite Element Method, Lawrence Livermore National Laboratory, Livermore, CA, UCRL-JC-122104 Rev. 1. Submitted to J. of Computational Physics.

#### R

Rainer, F., Anderson, A., Burnham, A., Milam, D., and Turner, R., *Lifetime Survivability of Contaminated Target-Chamber Optics*, Lawrence Livermore National Laboratory, Livermore, CA, UCRL-JC-124943 ABS. Prepared for *Symp on Optical Materials for High Power Lasers* '96, Boulder, CO, Oct 7–9, 1996.

Reisman, D., Denney, C., De Groot, J. S., Estabrook, K. G., Hammer, L. H., Sanford, T. W. L., Speilman, R. B., and Toor, A., *Energetics in Imploding Z-Pinches*, Lawrence Livermore National Laboratory, Livermore, CA, UCRL-JC-124688 ABS. Prepared for *38th Annual Mtg of the American Physical Society Div of Plasma Physics*, Denver, CO, Nov 11–15, 1996.

Remington, B. A., Campbell, E. M., Holmes, N. C., Libby, S. B., and Teller, E., *Evolution of High Energy-Density Physics: from Nuclear Testing to the Superlasers*, Lawrence Livermore National Laboratory, Livermore, CA, UCRL-JC-124258 Rev. 2. Submitted to *Laser and Particle Beams*.

Remington, B. A., Glendinning, S. G., Kalantar, D. H., Budil, K. S., Landen, O. L., Hammel, B. A., Marinak, M. M., Weber, S. V., Keane, C. J., Haan, S. W., Rubenchik, A., Wallace, R., Key, M. H., Knauer, J. P., Ofer, D., Hsing, W. W., Galmiche, D., Blain, M. A., Wood-Vasey, W. M., and Shvarts, D., *Hydrodynamic Instability Experiments on the Nova Laser*, Lawrence Livermore National Laboratory, Livermore, CA, UCRL-JC-123775. Prepared for *16th IAEA Intl Conf on Plasma Physics and Controlled Nuclear Fusion Research*, Montreal, Canada, Oct 7–11, 1996.

P-12 UCRL-LR-105821-96-4

Remington, B. A., Glendinning, S. G., Kalantar, D. H., Budil, K. S., Marinak, M. M., Weber, S. V., Colvin, J., Griswold, D., Knauer, J. P., Key, M., Hsing, W. W., Galmiche, D., Rubenchik, A., Kane, J., Arnett, W. D., and Wood-Vasey, W. M., *Laser-Driven Hydrodynamics Experiments at Nova*, Lawrence Livermore National Laboratory, Livermore, CA, UCRL-JC-124480. Prepared for 26th Anomalous Absorption Conf, Fairbanks, AK, Aug. 26–30, 1996.

Remington, B. A., Glendinning, S. G., Kane, J., Castor, J., Rubenchik, A., Colvin, J., Drake, R. P., London, R., Liang, E., and McCray, R., *Hydrodynamics Experiments on Supernovae and on Nova—the Laser*, Lawrence Livermore National Laboratory, Livermore, CA, UCRL-JC-124949 ABS. Prepared for 38th Annual Mtg of the American Physical Society Div of Plasma Physics, Denver, CO, Nov 11–15, 1996.

Remington, B. A., Kalantar, D. H., Woolsey, N., Colvin, J., Griswold, D., Cauble, R., Lee, R., Wark, J. S., Hauer, A., and Rubenchik, A., *Nova Experiments on Hydrodynamics and Instabilities in the Solid State*, Lawrence Livermore National Laboratory, Livermore, CA, UCRL-JC-124549 ABS. Prepared for 38th Annual Mtg of the American Physical Society Div of Plasma Physics, Denver, CO, Nov 11–15, 1996.

Ress, D., and Lerche, R. A., Recent Results from the Nova Neutron Microscope, Lawrence Livermore National Laboratory, Livermore, CA, UCRL-JC-124542 ABS. Prepared for 38th Annual Mtg of the American Physical Society Div of Plasma Physics, Denver, CO, Nov 11–15, 1996.

Rhodes, M. A., Fochs, S. N., and Alger, T. W., 1×2 *Prototype PEPC for the NIF*, Lawrence Livermore National Laboratory, Livermore, CA, UCRL-JC-124514 ABS. Prepared for 2nd Annual Intl Conf on Solid-State Lasers for Application to Inertial Confinement Fusion, Paris, France, Oct 22–25, 1996.

Rothenberg, J. E., *Electro-Optic Deflectors as a Method of Beam Smoothing for Inertial Confinement Fusion*,
Lawrence Livermore National Laboratory, Livermore,
CA, UCRL-JC-124507 ABS. Prepared for 2nd Annual
Intl Conf on Solid-State Lasers for Application to Inertial
Confinement Fusion, Paris, France, Oct 22–25, 1996.

Rothenberg, J. E., Improved Beam Smoothing with SSD Using Generalized Phase Modulation, Lawrence Livermore National Laboratory, Livermore, CA, UCRL-JC-124508 ABS. Prepared for 2nd Annual Intl Conf on Solid-State Lasers for Application to Inertial Confinement Fusion, Paris, France, Oct 22–25, 1996.

Rothenberg, J. E., and Weber, S. V., The Impact of Beam Smoothing Method on Direct Drive Target Performance for the National Ignition Facility, Lawrence Livermore National Laboratory, Livermore, CA, UCRL-JC-124509 ABS. Prepared for 2nd Annual Intl Conf on Solid-State Lasers for Application to Inertial Confinement Fusion, Paris, France, Oct 22–25, 1996.

Rothenberg, J. E., Moran, B. D., Wing, R. R., and Van Wonterghem, B. M., *Performance of Smoothing by Spectral Dispersion on Beamlet*, Lawrence Livermore National Laboratory, Livermore, CA, UCRL-JC-124506 ABS. Prepared for 2nd Annual Intl Conf on Solid-State Lasers for Application to Inertial Confinement Fusion, Paris, France, Oct 22–25, 1996.

Rotter, M., McCracken, R., Erlandson, A., and Guenet, M., *Gain Measurements on a Prototype NIF/LMJ Amplifier Pump Cavity*, Lawrence Livermore National Laboratory, Livermore, CA, UCRL-JC-124518 ABS. Prepared for 2nd Annual Intl Conf on Solid-State Lasers for Application to Inertial Confinement Fusion, Paris, France, Oct 22–25, 1996.

Rubenchik, A., Kane, J., Wood-Vasey, M., Glendinning, S. G., and Remington, B. A., On Interface Instabilities in Expanding Plasmas, Lawrence Livermore National Laboratory, Livermore, CA, UCRL-JC-124676 ABS. Prepared for 38th Annual Mtg of the American Physical Society Div of Plasma Physics, Denver, CO, Nov 11–15, 1996.

Runkel, M., and Kozlowski, M., Large Area Damage Testing of Conventionally Grown KD\*P at 351 nm on the Beamlet Laser, Lawrence Livermore National Laboratory, Livermore, CA, UCRL-JC-124535 ABS. Prepared for 2nd Annual Intl Conf on Solid-State Lasers for Application to Inertial Confinement Fusion, Paris, France, Oct 22–25, 1996.

Rushford, M. R., Dixit, S. N., Thomas, I. M., Martin, A. M., and Perry, M. D., Large Aperture Kinoform Phase Plates in Fused Silica for Spatial Beam Smoothing on Nova and the Beamlet Lasers, Lawrence Livermore National Laboratory, Livermore, CA, UCRL-JC-124511 ABS. Prepared for 2nd Annual Intl Conf on Solid-State Lasers for Application to Inertial Confinement Fusion, Paris, France, Oct 22–25, 1996.

#### S

Saculla, M., and Letts, S., *Advances in Bouncer Pan Technology*, Lawrence Livermore National Laboratory, Livermore, CA, UCRL-JC-125136 ABS. Prepared for *11th Target Fabrication Specialists' Mtg*, Orcas Island, WA, Sept 8–12, 1996.

Sahin, S., Moir, R. W., and Sahinaslan, A., *Radiation Damage in Liquid-Protected First-Wall Materials for IFE-Reactors*, Lawrence Livermore National Laboratory, Livermore, CA, UCRL-JC-125149. Submitted to *Fusion Technol*.

Sanchez, J. J., and Giedt, W., *Thermal Design of Cylindrical Hohlraums for the NIF*, Lawrence Livermore National Laboratory, Livermore, CA, UCRL-JC-125141 ABS. Prepared for 11th Target Fabrication Specialists' Mtg, Orcas Island, WA, Sept 8–12, 1996.

Sanchez, J. J., and Letts, S., *High Strength Plastics May Reduce Cryogenic Requirements for the NIF*, Lawrence Livermore National Laboratory, Livermore, CA, UCRL-JC-125142 ABS. Prepared for *11th Target Fabrication Specialists' Mtg*, Orcas Island, WA, Sept 8–12, 1996.

Schroen-Carey, D., Letts, S., Buckley, S., Cook, R., and Lambert, S., Characteristics of Barrier Layers Produced on R/F Foam Shells by Acid Chloride Interfacial Polymerization, Lawrence Livermore National Laboratory, Livermore, CA, UCRL-JC-125127 ABS. Prepared for 11th Target Fabrication Specialists' Mtg, Orcas Island, WA, Sept 8–12, 1996.

Shepard, T. D., Landen, O. L., Lindl, J. D., Rosen, M. D., and Suter, L. J., *High-Z Foil Acceleration Using Hydrodynamic Pressure of Radiatively Heated Matter*, Lawrence Livermore National Laboratory, Livermore, CA, UCRL-JC-124853 ABS. Prepared for *38th Annual Mtg of the American Physical Society Div of Plasma Physics*, Denver, CO, Nov 11–15, 1996.

Shore, B. W., Feit, M. D., Perry, M. D., Rubenchik, A., and Stuart, B., *Brief Intense Laser Fields in Bulk Matter*, Lawrence Livermore National Laboratory, Livermore, CA, UCRL-JC-124040. Previously released for *Seminar on Quantum Optics and Strong-Field Phenomena in Atoms and Molecules, of 5th Intl Workshop on Laser Physics LPHY96*. Submitted to *Laser Physics*.

Skidmore, J. A., Emanuel, M. A., Freitas, B., Beach, R. J., Bibeau, C., Honea, E. C., Page, R. H., Sutton, S. B., and Payne, S. A., *High-Power Laser Diode-Pumped Yb:YAG, Tm:YAG, and Cr:ZnSe Laser Systems*, Lawrence Livermore National Laboratory, Livermore, CA, UCRL-JC-124910 ABS. Prepared for *Society of Photo-Optical Instrumentation Engineers Optoelectronics* '97, San Jose, CA, Feb 8–19, 1997.

Stephens, R., and Collins, G., *Analysis of Performance of Integrating Sphere for IR Enhanced DT Ice Layering*, Lawrence Livermore National Laboratory, Livermore, CA, UCRL-JC-125128 ABS. Prepared for *11th Target Fabrication Specialists' Mtg*, Orcas Island, WA, Sept 8–12, 1996.

Still, C. H., Berger, R. L., Langdon, A. B., Powers, L. V., Willims, E. A., and Young, P. E., *Nonlinear Laser Filamentation Simulation in 3D*, Lawrence Livermore National Laboratory, Livermore, CA, UCRL-JC-124679 ABS. Prepared for *38th Annual Mtg of the American Physical Society Div of Plasma Physics*, Denver, CO, Nov 11–15, 1996.

Stolz, C. J., Furr, J. S., Wu, Z. L., Krupka, R., Lu, Y., and Kuo, P. K., *Study of Defects in HfO*<sub>2</sub>/*SiO*<sub>2</sub> *Multilayer Coatings Using Photothermal Microscopy*, Lawrence Livermore National Laboratory, Livermore, CA, UCRL-JC-124924 ABS. Prepared for 28th Annual Symp on Optical Materials for High Power Lasers, Boulder, CO, Oct 7–9, 1996.

Stolz, C., Genin, F., Reitter, T. A., Bevis, R. P., von Gunten, M. K., and Hue, J., Effect of SiO<sub>2</sub> Overcoat Thickness on Laser Damage Morphology of HfO<sub>2</sub>/SiO<sub>2</sub> Brewster's Angle Polarizers at 1064 nm, Lawrence Livermore National Laboratory, Livermore, CA, UCRL-JC-124875 ABS. Prepared for 28th Annual Symp on Optical Materials for High Power Lasers, Boulder, CO, Oct 7–9, 1996.

Stone, G., Cloud, M., Salazar, M., Bush, H., Gobby, P., and Townsend, J., *Operation of Five Atmosphere Gas Filled Targets at Nova*, Lawrence Livermore National Laboratory, Livermore, CA, UCRL-JC-125133 ABS. Prepared for *11th Target Fabrication Specialists' Mtg*, Orcas Island, WA, Sept 8–12, 1996.

Stout, E., Miller-Kamm, V., Spann, J., and Van Arsdall, P., A Prototype Distributed Object-Oriented Architecture for Image-Based Automatic Laser Alignment, Lawrence Livermore National Laboratory, Livermore, CA, UCRL-JC-124381 ABS. Prepared for 2nd Annual Intl Conf on Solid State Lasers for Application to Inertial Confinement Fusion, Paris, France, Oct 22–25, 1996.

Strobel, G. L., and Haan, S. W., Non-Linear Growth Factor Analysis of NIF Capsule Hydrodynamic Instabilities, Lawrence Livermore National Laboratory, Livermore, CA, UCRL-JC-124546 ABS. Prepared for 38th Annual Mtg of the American Physical Society Div of Plasma Physics, Denver, CO, Nov 11–15, 1996.

P-14 UCRL-LR-105821-96-4

Suter, L. J., Forward Emitters for Increased Coupling of Laser Produced X-Rays to Targets, Lawrence Livermore National Laboratory, Livermore, CA, UCRL-JC-124659 ABS. Prepared for 38th Annual Mtg of the American Physical Society Div of Plasma Physics, Denver, CO, Nov 11–15, 1996.

Sutton, S. B., and Marshall, C. D., *Thermal Recovery of NIF Amplifiers*, Lawrence Livermore National Laboratory, Livermore, CA, UCRL-JC-124528 ABS. Prepared for 2nd Annual Intl Conf on Solid-State Lasers for Application to Inertial Confinement Fusion, Paris, France, Oct 22–25, 1996.

#### T

Takeuchi, K., Final Report for "Item 1: Preliminary Refractory Testing," Lawrence Livermore National Laboratory, Livermore, CA, UCRL-CR-121348.

Takeuchi, K., Final Report for "Item 3: Development of a Direct Batch Charging Method," Lawrence Livermore National Laboratory, Livermore, CA, UCRL-CR-121349.

Takeuchi, K., Final Report for "Item 4: Evaluation of Improved Refractory Melter Concept," Lawrence Livermore National Laboratory, Livermore, CA, UCRL-CR-121347.

Tietbohl, G. L., and Sommer, S. C., Design Guidelines for Mirror Support Systems in Large Lasers, Lawrence Livermore National Laboratory, Livermore, CA, UCRL-JC-124522 ABS. Prepared for 2nd Annual Intl Conf on Solid-State Lasers for Application to Inertial Confinement Fusion, Paris, France, Oct 22–25, 1996.

Tobin, M., Karpenko, V., Anderson, A., Wilemski, G., Burnham, A., Gerassimenko, M., Bernat, T., Peterson, P., Tokheim, R., Seaman, L., Curran, D., and Schirmann, D., *Target Emissions and Their Effects on the National Ignition Facility*, Lawrence Livermore National Laboratory, Livermore, CA, UCRL-JC-124526 ABS. Prepared for 2nd Annual Intl Conf on Solid-State Lasers for Application to Inertial Confinement Fusion, Paris, France, Oct 22–25, 1996.

Tobin, M., Latkowski, J., Singh, M., and Karpenko, V., *The Impacts of Neutron Emissions on the Use of the National Ignition Facility (NIF)*, Lawrence Livermore National Laboratory, Livermore, CA, UCRL-JC-124527 ABS. Prepared for 2nd Annual Intl Conf on Solid-State Lasers for Application to Inertial Confinement Fusion, Paris, France, Oct 22–25, 1996.

Tobin, M., Sanchez, J., Pittenger, L., Dipeso, G., Serduke, F., Anderson, A., Peterson, P., Latkowski, J., and Bernat, T., *Cryogenic Target Integration and Radiation Protection of Near Target Components on NIF*, Lawrence Livermore National Laboratory, Livermore, CA, UCRL-JC-125139 ABS. Prepared for *11th Target Fabrication Specialists' Mtg*, Orcas Island, WA, Sept 8–12, 1996.

Tobin, M., Tokheim, R. E., Seaman, L., Cooper, T., Lew, B., Curran, D. R., Sanchez, J., and Anderson, A., Calculating the Shrapnel Generation and Subsequent Damage to First Wall and Optics Components for the National Ignition Facility, Lawrence Livermore National Laboratory, Livermore, CA, UCRL-JC-124947. Prepared for Proceedings of the American Nuclear Society, 12th Topical Mtg on the Technology of Fusion Energy, Reno, NV, Jun 16–20, 1996.

Turner, R. E., Landen, O. L., Kornblum, H. N., Amendt, P., Decker, C., Hammel, B. A., Morales, R., Suter, L. J., Wallace, R. J., Murphy, T. J., Gobby, P., Hauer, A. A., Knauer, J., Marshall, F. J., Bradley, D., Keck, R., Kelly, J., Kremens, R., Seka, W., and Soures, J. M., *Indirect Drive Measurements on Omega*, Lawrence Livermore National Laboratory, Livermore, CA, UCRL-JC-124665 ABS. Prepared for 38th Annual Mtg of the American Physical Society Div of Plasma Physics, Denver, CO, Nov 11–15, 1996.

Turner, R., Anderson, A., Estabrook, K., Gerassimenko, M., and Serduke, F., *Fabrication of Low-Density Foam Shells from Resorcinol-Formaldehyde Aerogel*, Lawrence Livermore National Laboratory, Livermore, CA, UCRL-JC-125117 ABS. Prepared for *11th Target Fabrication Specialists' Mtg*, Orcas Island, WA, Sept 8–12, 1996.

#### V

Van Wonterghem, B. M., Murray, J. E., Auerbach, J. A., Burkhart, S. C., Caird, J. A., Henesian, M., Penko, F., and Wegner, P., High Fluence 1 to Performance Test Using 20 ns Ignition Shaped Pulses on the Beamlet Prototype Laser, Lawrence Livermore National Laboratory, Livermore, CA, UCRL-JC-124865 ABS. Prepared for 2nd Annual Intl Conf on Solid-State Lasers for Application to Inertial Confinement Fusion, Paris, France, Oct 22–25, 1996.

Van Wonterghem, B., Murray, J. R., Campbell, J. H., Speck, D. R., Barker, C. E., Smith, I. C., Browning, D. F., and Behrendt, W. C., *Performance of a Prototype, Large-Aperture Multipass Nd-Glass Laser for Inertial Confinement Fusion*, Lawrence Livermore National Laboratory, Livermore, CA, UCRL-JC-125150. Submitted to *Applied Optics, Optical Society of America*.

Van Wonterghem, B., Wegner, P. J., Lawson, J. K., Auerbach, J. M., Henesian, M. A., Barker, C. E., Thompson, C. E., Widmayer, C. C., and Caird, J. A., Recent Performance Results of the National Ignition Facility Beamlet Demonstration Project, Lawrence Livermore National Laboratory, Livermore, CA, UCRL-JC-123080 DR. Prepared for American Nuclear Society 12th Topical Mtg on the Technology of Fusion Energy, Reno, NV, Jun 16–20, 1996.

Van Wonterghem, B., Wegner, P. J., Lawson, J. K., Auerbach, J. M., Henesian, M. A., Barker, C. E., Thompson, C. E., Widmayer, C. C., and Caird, J. A., Recent Performance Results of the National Ignition Facility Beamlet Demonstration Project, Lawrence Livermore National Laboratory, Livermore, CA, UCRL-JC-123080. Prepared for American Nuclear Society 12th Topical Mtg on the Technology of Fusion Energy, Reno, NV, Jun 16–20, 1996.

Vann, C. S., and Post, R. F., Reverser Architecture in a Laser Fusion Driver, Lawrence Livermore National Laboratory, Livermore, CA, UCRL-JC-124525 ABS. Prepared for 2nd Annual Intl Conf on Solid-State Lasers for Application to Inertial Confinement Fusion, Paris, France, Oct 22–25, 1996.

#### W

Weber, S. V., Simulations of Laser Imprint for Nova and Vulcan Experiments and for Ignition Capsules, Lawrence Livermore National Laboratory, Livermore, CA, UCRL-JC-124547 ABS. Prepared for 38th Annual Mtg of the American Physical Society Div of Plasma Physics, Denver, CO, Nov 11–15, 1996.

Weber, S. V., Glendinning, S. G., Kalantar, D. H., Remington, B. A., Rothenberg, J. E., Key, M. H., and Knauer, J. P., Laser Imprint and Implications for Direct Drive Ignition with the National Ignition Facility, Lawrence Livermore National Laboratory, Livermore, CA, UCRL-JC-123315. Prepared for 24th European Conf on Laser Interaction with Matter, Madrid, Spain, Jun 3–7, 1996.

Wegner, P. J., Van Wonterghem, B. V., Barker, C. E., Caird, J. A., Dixit, S. N., Henesian, M. A., Hunt, J. T., Seppala, L. G., and Thompson, C. E., *Third-Harmonic Performance of the Beamlet Prototype Laser*, Lawrence Livermore National Laboratory, Livermore, CA, UCRL-JC-124529 ABS. Prepared for 2nd Annual Intl Conf on Solid-State Lasers for Application to Inertial Confinement Fusion, Paris, France, Oct 22–25, 1996.

Wharton, K., Kirkwood, R., Afeyan, B., Back, C., Berger, R., Blain, M., Estabrook, K., Glenzer, S., Kruer, W., MacGowan, B., and Moody, J., Measurement of Near-WpLight as Evidence of the Electromagnetic Decay Instability, Lawrence Livermore National Laboratory, Livermore, CA, UCRL-JC-124881 ABS. Prepared for 26th Annual Anomalous Absorption Conf, Fairbanks, AK, Aug, 26–30, 1996.

Wharton, K., Zakharenkov, Y., Brown, C., Hammel, B., Joshi, C., Moody, J., Offenberger, A., Perry, M., Wilks, S., and Yanovsky, V., *Investigation of the Conversion of Laser Energy to Relativistic Electrons at Intensities of 1020 W/cm*<sup>2</sup>, Lawrence Livermore National Laboratory, Livermore, CA, UCRL-JC-124295 ABS Rev. 1. Prepared for 38th Annual Mtg of the American Physical Society Div of Plasma Physics, Denver, CO, Nov 11–15, 1996.

Wilcox, R. B., and Browning, D. F., A Tunable, Single Frequency, Fiber Ring Oscillator at 1053 nm, Lawrence Livermore National Laboratory, Livermore, CA, UCRL-JC-124515 ABS. Prepared for 2nd Annual Intl Conf on Solid-State Lasers for Application to Inertial Confinement Fusion, Paris, France, Oct 22–25, 1996.

Wilcox, R. B., and Browning, D. F., Integrated Optic Modulator and Splitter Damage at 1053 nm, Lawrence Livermore National Laboratory, Livermore, CA, UCRL-JC-124928 ABS. Prepared for 28th Annual Symp on Optical Materials for High Power Lasers, Boulder, CO, Oct 7–9, 1996.

Wilks, S. C., Freeman, R. Hartmann, F., Kerman, A., Langdon, A. B., and Woodworth, J., Foil-Terminated Free Wave Acceleration, Lawrence Livermore National Laboratory, Livermore, CA, UCRL-JC-124454 ABS Rev. 1. Prepared for 38th Annual Mtg of the American Physical Society Div of Plasma Physics, Denver, CO, Nov 11–15, 1996.

Williams, E. A., Glenzer, S., Back, C. A., Berger, R. L., and Estabrook, K. G., *Non-Local Transport and Plasma Heating by a Probe Laser Beam*, Lawrence Livermore National Laboratory, Livermore, CA, UCRL-JC-124677 ABS. Prepared for *38th Annual Mtg of the American Physical Society Div of Plasma Physics*, Denver, CO, Nov 11–15, 1996.

P-16 UCRL-LR-105821-96-4

Wood, B., Runkel, M., Yan, M., Staggs, M., De Yoreo, J., and Kozlowski, M., *Investigations of Laser Damage in Rapidly Grown KDP Crystals*, Lawrence Livermore National Laboratory, Livermore, CA, UCRL-JC-124534 ABS Rev. 1. Prepared for *28th Annual Symp on Optical Materials for High Power Lasers*, Boulder, CO, Oct 7–9, 1996.

Wood, B., Runkel, M., Yan, M., Staggs, M., De Yoreo, J., and Kozlowski, M., *Investigations of Laser Damage in Rapidly Grown KDP Crystals*, Lawrence Livermore National Laboratory, Livermore, CA, UCRL-JC-124534 ABS. Prepared for 2nd Annual Intl Conf on Solid-State Lasers for Application to Inertial Confinement Fusion, Paris, France, Oct 22–25, 1996.

Woodworth, J. G., and Meier, W. R., *Target Production for Inertial Fusion Energy*, Lawrence Livermore National Laboratory, Livermore, CA, UCRL-JC-117396 Rev. 1. Submitted to *Fusion Technol*.

Wu, C. H., Meister, C. F., Zory, P. S., and Emanuel, M. A., *Microsecond-Long Lasing Delays in Thin P-Clad InGaAs QW Lasers*, Lawrence Livermore National Laboratory, Livermore, CA, UCRL-JC-124871. Prepared for *IEEE Lasers and Electro-Optics Society '96*, Boston, MA, Nov 18–21, 1996.

#### Y

Yan, M., Hutcheon, I. D., Torres, R., Staggs, M., Runkel, M., De Yoreo, J., and Zaitseva, N. P., *Investigation of Impurities and Laser Induced Damage in Rapidly Grown KDP*, Lawrence Livermore National Laboratory, Livermore, CA, UCRL-JC-124919 ABS. Prepared for 28th Annual Symp on Optical Materials for High Power Lasers, Boulder, CO, Oct 7–9, 1996.

Yan, M., Torres, R., Hutcheon, I., Staggs, M., De Yoreo, J., and Zaitseva, N., *Impurity Segregation and Its Effects on the Optical Properties of KH*<sub>2</sub>*PO*<sub>4</sub>, Lawrence Livermore National Laboratory, Livermore, CA, UCRL-JC-123594 ABS Rev. 1. Prepared for 2nd Annual Intl Conf on Solid-State Lasers for Application to Inertial Confinement Fusion, Paris, France, Oct 22–25, 1996.

#### Z

Zacharias, R. A., Bliss, E. S., Davis, D. T., Decker, D. E., Miller, J. L., Toeppen, J. S., and Van Wonterghem, B., Optics Damage Inspection for Large Laser Systems, Lawrence Livermore National Laboratory, Livermore, CA, UCRL-JC-124380 ABS. Prepared for 2nd Annual Intl Conf on Solid-State Lasers for Application to Inertial Confinement Fusion, Paris, France, Oct 22–25, 1996.

Zaitseva, N. P., De Yoreo, J., DeHaven, M., Vital, R. L., Carman, M. L., Spears, R., Montgomery, K., James, L., Atherton, L. J., and Rozsa, R., *Rapid Growth of Large-Scale (20–50 cm) KDP Crystals*, Lawrence Livermore National Laboratory, Livermore, CA, UCRL-JC-124011 ABS Rev. 1. Prepared for 2nd Annual Intl Conf on Solid-State Lasers for Application to Inertial Confinement Fusion, Paris, France, Oct 22–25, 1996.

Zapata, L., Guenet, J., McCracken, R., Horvath, J., Rotter, M., Pollock, G., Guenet, M., Grebot, E., Seznec, S., and Erlandson, A., Large Aperture Diagnostic System for Gain and Wavefront Measurements on NIF/LMJ Prototype Amplifiers, Lawrence Livermore National Laboratory, Livermore, CA, UCRL-JC-124519 ABS. Prepared for 2nd Annual Intl Conf on Solid-State Lasers for Application to Inertial Confinement Fusion, Paris, France, Oct 22–25, 1996.